# Fabrication and validation of an intraneural interface tailored for optic nerve stimulation

## Eleonora BORDA

École
polytechnique
fédérale
de Lausanne

2022

Success is not final.
Failure is not fatal.
It is the courage to continue that counts.
— Wiston Churchill

To my grandma

# Acknowledgements

My journey towards this PhD thesis would not have been possible without the help of many people who supported me professionally and personally and to whom I'm forever grateful.

First of all, I would like to thank Prof. Diego Ghezzi for giving me the opportunity to work in the Laboratory of Neuroengineering on such a multidisciplinary project, spanning from fabrication, characterization, in-vivo testing and data analysis. He helped me to overcome the ups and downs of this PhD even when I was in my most negative attitude. He was available any time I stepped in his office with (many) questions and problems as well as through the different means of communications that we put in place thanks also to an unexpected historical time. I would like to express my gratitude also for having let me experiment outside the labs with little entrepreneurial projects that helped me shape my next steps in life.

I would like to thank the jury members: Professor Van de Ville, Professor Micera, Professor Tybrandt and Professor Wong. Three of them have inspired the work I have performed during my thesis through their publications and innovative ideas. They all agreed to review the work and provided valuable comments and corrections.

To make this thesis possible I had to learn how to properly work in a cleanroom facility and I had the chance to do it while being supported by the amazing team of the Neural Microsystems Platform at Campus Biotech. None of my devices would have seen the light of the day if it wasn't for Anthony, Valerian and Michael. A special thanks goes to Anthony and Valerian who made sure I could complete my "exotic" projects with the best support ever. When I was down, they always had a word to make me feel better, when the results were not coming, they believed in me and the projects the way I even did not. They gave me the wings to "fly" in the cleanroom space and accomplish the mission.

I also had the chance to work in another bigger cleanroom facility, the EPFL Center of MicroNanoTechnology (CMi). While I felt in my little bubble in Geneva when working in the cleanroom, CMi was "a big city" with a lot of traffic, plenty of brilliant researchers testing

their processes on the many machines. So, it was scary at times to be using these important machines. What if I break it? What if hundreds of users cannot use it because of me? It took me some time before getting comfortable and confident and for this I thank CMi staff, particularly, Niccolò, Giovanni and Jeoffrey, and the PhD students I exchanged quick with while waiting for my turn or the end of a process.

Working in Geneva at Campus Biotech has been a wonderful experience, everything needed from fabrication till in-vivo testing in just one place. I am grateful for all the staff members of the different facilities that are there to help us researchers to solve the most challenging questions. Aside from the lab facilities, Fondation Campus Biotech also tried to make our life a bit more balance d, providing a gym and organizing social events (until it was possible). A big thanks goes to Roberto for making me re-discover the beauty of philosophy that I thought I had forgotten after starting my studies in engineering.

Being every day on campus, before COVID-19, I had the chance to meet and closely work with brilliant PhDs, who quickly became friends with whom taking coffees, learning French, exchange about science and life or partying. Crossing them in corridors, especially our neighbors from LSBI helped in sharing the high s and lows of a PhD. Bastien (my French tandem as well), Emanuele, Andreas, Jerome, Sabri, Flavio, I thank you for the wild parties after the monthly aperos. I thank Q for the lunches talking about super cool projects on Parkison and extreme hiking paths around Switzerland. From the LSBI, the list is long: Valentina, I thank you for the endless discussion s in the cleanroom, your kindness and friendship; Nicolas, I thank you for having thought me so much about entrepreneurship; Ludovic, I thank you for the nice moments in the lab complaining about the PhD; Florent, I thank you for sharing the ups and downs of a PhD; Outman, I thank you for sharing your creatives ideas and your optimisms; Ivan, so many mechanical characterizations would have not been possible without you! We were all part of a big family of fab addicted people and sharing with them success and problems helped my projects moving forward.

And now comes the LNE family. I never felt any of them, past and present members, as just colleagues. This made me come in to the office with a different perspective. They have all contributed immensely to my PhD thesis and it has been a pleasure to work with every one of them. We shared offices and labs but also gym sessions, climbing, skiing, partying, dinners, game nights and more. Laura, thank you for being so wise, for your patience and for having shared with me the pain of Medprint. Marta, well, your passions for microfab is of an inspiration, thank you for introducing me to it, since my lab immersion during the Master program, thank you for sharing the stories about your rabbits during lunches and for having left me with OSTE (). Paola, thank you for having worn my shiniest dress with heels, you know it means a lot to me. Naig, thank you for teaching me the rule of "one glass of alcohol with one glass of water". Vivien, thank you for being there throughout all the experiments with the rabbits and for having showed up with the Moscow mules the day of my private defense, much needed! Adele, you are my right arm, extension of my brain, twin, sister, best co-president one could ever ask for, my immense gratitude goes to you for having shared with me every single day of happiness and tears of this PhD. Charles, thank you for having taught me that having me thought that anything is possible in life during your career path. Jake, oh well man,

# Abstract

Technological progress in materials science and micro-engineering along with new discoveries in neuroscience have contributed to restore lost or impaired sensory functions by closely interfacing with the nervous system. Electronic devices have begun to be integrated within the body to artificially reproduce or record the electrical encoding of neural signals, the language of the nervous system. This has allowed us to restore the impaired communication between the missing or defective organ and the brain. As evidence of this, cochlear implants have returned hearing to thousands of people world wide. On the other hand, there is no suitable solution yet for 43 millions people who are currently blind. Nevertheless, several research groups and companies are trying to tackle this issue. The preferred approach has been to stimulate the retina, the neural portion of the eye. For retinal degeneration, it is a convenient solution due to being in close proximity with the defective cells, the photo-receptors, and the possibility to accommodate a large amount of electrodes inside the eye space with a less invasive surgery. So far, different devices have demonstrated the capability of restoring a certain degree of artificial vision, however, with limited success in delivering meaningful improvements in daily life activities. This is because, unlike hearing, vision is an extremely complex sense and requires higher stimulation resolution. Limitations of retinal prostheses have pushed further the investigation of other targets along the visual pathway, such as the optic nerve, the thalamus and the visual cortex. Among these, our group has started to explore the possibility of stimulating the optic nerve. The main advantages are the direct stimulation of the axon fibers and the access to the entire visual field with only one device. It is also interesting because it could work for those patients who are not eligible for retinal prostheses, due to severe eye trauma or retinal detachment, and it does not require optical transparency.

In this thesis, we investigate stimulation strategies and materials to improve the outcome of optic nerve prostheses and make them one step closer to a viable option for blind patients. We

first propose the use of machine learning algorithms to classify cortical activity upon electrical stimulation of the optic nerve. Two approaches are developed, a support machine vector (SVM)-based classifier that can identify distinct stimuli, and a linear regression model. This latter approach is also capable of predicting separate stimuli without prior knowledge about the testing set, resulting in an improved extrapolation capability compared to the classifier. Secondly, we investigate a strategy to achieve higher spatial selectivity of the optic nerve stimulation. Combining the use of computational models and the possibility to micro-fabricate thin-film electrodes in a multi-layer fashion, we design a three-dimensional (3D) multi-layer concentric bipolar (CB) configuration and fabricate a modified version of the OpticSELINE, previously proposed by our group. We validate the efficacy of the novel design during in-vivo experiments on rabbits and find that cortical activation is reduced when using the 3D multilayer CB electrodes compared to the classic monopolar configuration used in intraneural electrodes. In parallel, we explore the use of novel polymers, namely Off-Stoichiometry Thiol-Ene Epoxy (OSTE+), to design conformable neural interfaces. OSTE+ resins have recently been developed for microfluidics applications, however their chemistry makes them a suitable candidate for easy integration in cleanroom processes and they showsuperior adhesion properties with respect to standard thin films currently in use. Hence, we characterize their usability as substrate and encapsulation for neural interfaces in-vitro and in-vivo. Lastly, we propose an alternative fabrication technique, ink-jet printing of platinum on flexible substrates, for neurophysiology applications. Altogether, the findings highlighted in this thesis will hopefully lead to a more in-depth investigation of the optic nerve prosthesis and can also be relevant for other applications in the field of neuroprosthetics.

**Key words:** Blindness, optic nerve prosthesis, artificial vision, electrical stimulation, neuro-prosthetics, conformable neural interfaces, OSTE+ polymers, additive manifacturing, spatial selectivity, rabbit, in-vivo, machine learning

# Sommario

I progressi tecnologici nella scienza dei materiali e nella microingegneria insieme alle nuove scoperte nelle neuroscienze hanno contribuito a ripristinare le funzioni sensoriali perse o compromesse interfacciandosi strettamente con il sistema nervoso. I dispositivi elettronici hanno cominciato a essere integrati nel corpo per riprodurre artificialmente o registrare la codifica elettrica dei segnali neurali, il linguaggio del sistema nervoso. Questo ha permesso di ripristinare la comunicazione compromessa tra l'organo mancante o difettoso e il cervello. Come prova di ciò, gli impianti cocleari hanno restituito l'udito a migliaia di persone in tutto il mondo. D'altra parte, non esiste ancora una soluzione adeguata per le 43 milioni di persone che sono attualmente cieche. Tuttavia, diversi gruppi di ricerca e aziende stanno cercando di affrontare questo problema. L'approccio preferito è stato quello di stimolare la retina, la parte neurale dell'occhio. Per la degenerazione retinica, è una soluzione conveniente grazie alla vicinanza con le cellule difettose, i fotorecettori, e la possibilità di ospitare una grande quantità di elettrodi all'interno dello spazio oculare con un intervento meno invasivo. Finora, diversi dispositivi hanno dimostrato la capacità di ripristinare un certo grado di visione artificiale, tuttavia, con un successo limitato nel fornire miglioramenti significativi nelle attività della vita quotidiana. Questo perché, a differenza dell'udito, la visione è un senso estremamente complesso e richiede una risoluzione di stimolazione più elevata. Le limitazioni delle protesi retiniche hanno spinto ulteriormente l'indagine di altri punti di interesse lungo il percorso visivo, come il nervo ottico, il talamo e la corteccia visiva. Tra questi, il nostro gruppo ha iniziato a esplorare la possibilità di stimolare il nervo ottico. I principali vantaggi sono la stimolazione diretta delle fibre assoniche e l'accesso all'intero campo visivo con un solo dispositivo. È anche interessante perché potrebbe funzionare per quei pazienti che non sono eleggibili per le protesi retiniche, a causa di gravi traumi oculari o distacco di retina, e non richiede trasparenza ottica.

In questa tesi, abbiamo studiato strategie di stimolazione e materiali per migliorare il risultato

delle protesi del nervo ottico e renderle un passo più vicine a un'opzione praticabile per i pazienti ciechi. In primo luogo abbiamo proposto l'uso di algoritmi di apprendimento automatico per classificare l'attività corticale su stimolazione elettrica del nervo ottico. Sono stati sviluppati due approcci, un classificatore basato su una macchina di supporto vettoriale (SVM) in grado di identificare stimoli distinti e un modello di regressione lineare. Quest'ultimo approccio è anche in grado di prevedere stimoli distinti senza una conoscenza preliminare del set di test, con una migliore capacità di estrapolazione rispetto al classificatore. In secondo luogo, abbiamo studiato una strategia per ottenere una maggiore selettività spaziale della stimolazione del nervo ottico. Combinando l'uso di modelli computazionali e la possibilità di microfabbricare elettrodi in film sottili con multistrati, abbiamo progettato una configurazione bipolare concentrica (CB) tridimensionale (3D) multistrato e abbiamo fabbricato una versione modificata dell' OpticSELINE, precedentemente proposta dal nostro gruppo. Abbiamo validato l'efficacia del nuovo design durante esperimenti in vivo sui conigli e abbiamo trovato che l'attivazione corticale è ridotta quando si utilizzano gli elettrodi 3D multistrato CB rispetto alla classica configurazione monopolare utilizzata negli elettrodi intraneurali. In parallelo, abbiamo esplorato l'uso di nuovi polimeri, cioè Off-Stoichiometry Thiol-Ene Epoxy (OSTE+), per progettare interfacce neurali conformabili. Le resine OSTE+ sono state recentemente sviluppate per applicazioni di microfluidica, tuttavia la loro chimica li rende un candidato adatto per una facile integrazione nei processi di camera bianca e mostrano proprietà di adesione superiori rispetto ai film sottili standard attualmente in uso. Quindi, abbiamo caratterizzato la loro usabilità come substrato e isolante per interfacce neurali in-vitro e in-vivo. Infine, abbiamo proposto una tecnica alternativa di fabbricazione, stampa a getto d'inchiostro di platino su substrati flessibili, per applicazioni di neurofisiologia. Complessivamente, i risultati evidenziati in questa tesi si spera portino a un'indagine più approfondita della protesi del nervo ottico e possano essere rilevanti anche per altre applicazioni nel campo della neuroprotesi.

**Parole chiave:** Cecità, protesi del nervo ottico, visione artificiale, stimolazione elettrica, neuroprotesi, interfacce neurali conformabili, polimeri OSTE+, manifattura additiva, selettività spaziale, coniglio, in-vivo, apprendimento automatico

# Contents

# List of Figures

# List of Tables

# 1 Advances in visual prostheses: engineering and biological challenges

Authors: Eleonora Borda[1], and Diego Ghezzi[1]

[1] Medtronic Chair in Neuroengineering, Center for Neuroprosthetics, Institute of Bioengineering, School of Engineering, École Polytechnique Fédérale de Lausanne, Switzerland

Authors contributions: E.B. wrote the manuscript. D.G. edited the manuscript.

## 1.1 Abstract

Vision is an extraordinary sense through which we can appreciate the beauty of the world we live in, gain invaluable knowledge and communicate with others using visual expression and arts. On the contrary, blindness is a threatening medical condition disrupting the life of affected people and their families. Therefore, restoring sight is one of the open challenges of our society. Today, the synergistic convergence of science and technology holds the potential to provide blind patients with artificial vision using visual prostheses: a type of implantable medical device able to reactivate visual neurons using electrical stimulation. Although clinical trials showed that vision restoration is still far away, significant technological advances make visual prostheses a valuable solution for blind patients. This review is not only a description of the state-of-the-art. Instead, it provides the reader with an update on recent developments, a critical discussion of the open challenges, and an overview of promising future directions.

## 1.2   Introduction

An estimated 596 million people suffered from distance vision impairment worldwide in 2020, of which 43 million being blind[1]. Moreover, due to an increase in life expectancy, the number of blind people will predictably increase to 61 million by 2050[1,2]. Blindness dramatically affects educational and employment opportunities[2], causing physical and mental comorbidities[3], especially in low- and middle-income settings where most essential services and specific government-supported aids may be lacking. In the case of older adults, vision impairment can also contribute to social isolation, difficulty in walking, a higher risk of falls and injuries, and a greater likelihood of early entry into nursing or care homes[4]. The high degree of disability that people with severe vision impairments encounter can as well directly impact family members, friends and other carers. Lastly, vision impairment poses an enormous global financial burden for society, with an estimated cost of productivity loss[4], as high as 16.5 billion USD in the United States of America. Given these reasons, the hope that neurotechnology will restore vision, at least partially, is stronger than ever.

In the visual system, information flows from the retina to the visual cortices. Damage anywhere along this pathway might result in an interruption of the signal flow, causing blindness. Today, different vision restoration strategies have been proposed and are currently under investigation. Prospective approaches, like gene and cell therapies or optogenetics, only focus on the retina[5,6], and they are ineffective when pathologies irremediably damage the retina or the optic nerve[7,8]. Visual prostheses bypass the damaged segment of the visual path and electrically stimulate the downstream surviving visual neurons to induce artificial vision. As such, there are compelling reasons to pursue the development of visual prostheses. With multiple devices granted FDA approval and CE mark for clinical use and many others in preclinical and clinical validation, visual prostheses represent a viable therapeutic solution to improve mobility and daily-life activities in blind individuals.

This review describes advances and challenges in visual prostheses. We provide an overview of the visual system to help familiarise the reader with its complexity. Next, we describe different types of visual prostheses, highlighting their strengths and weaknesses and suitability for specific kinds of blindness. Afterwards, we identify the open challenges currently limiting the development of the field. We conclude with an outlook on the road to market and what has been learned from the first generation of clinically approved visual prostheses.

## 1.3   Vision, blindness and artificial vision

Visual information is first processed spatially, temporally and chromatically in the retina, the neural portion of the eye (Figure1.1a). There are five types of neurons in the retina spread across three layers: photoreceptors (rods and cones) in the outer nuclear layer (ONL), horizontal cells (HCs), bipolar cells (BCs) and amacrine cells (ACs) in the inner nuclear layer (INL), and retinal ganglion cells (RGCs) in the ganglionic layer (GL). A vertical neural circuit

composed of photoreceptors, BCs and RGCs converts light into neural signals (Masland 2012). Synaptic connections between photoreceptors and BCs occur in the outer plexiform layer (OPL) and between BCs and RGCs in the inner plexiform layer (IPL). HCs and ACs laterally modulate the information process at the level of photoreceptors and RGCs, respectively. Cones are responsible for high acuity and colour vision, while rods allow us to see at low light. Then, the visual information travels to higher visual centres via the optic nerve, which is composed of the axons of RGCs (Figure 1.1b). The optic nerve, like the retina, is part of the central nervous system. Axons are myelinated and three meningeal layers (pia mater, arachnoid and dura mater) cover the nerve. At the optic chiasm, axons from the nasal retina cross the medial plane and project to the contralateral hemisphere, while axons from the temporal retina project to the ipsilateral hemisphere. The partial decussation of the nerve fibres organises the visual representation of each hemifield in the contralateral brain hemisphere (Figure1.1b). After the optic chiasm, the axons of the same side form the optic tract and connect the retina to the various visual targets. Axons driving structured visual information reach the dorsal lateral geniculate nucleus (LGN) in the thalamus. Relay neurons in the LGN send their axons to the primary visual cortex (V1), located in the occipital pole. As the initial stage of cortical processing, V1 integrates information about rapidly changing stimuli, high acuity, and colour vision. Higher-level processing, such as object recognition and spatial relations between objects in the visual field, occurs in other visual areas via the ventral and dorsal streams.
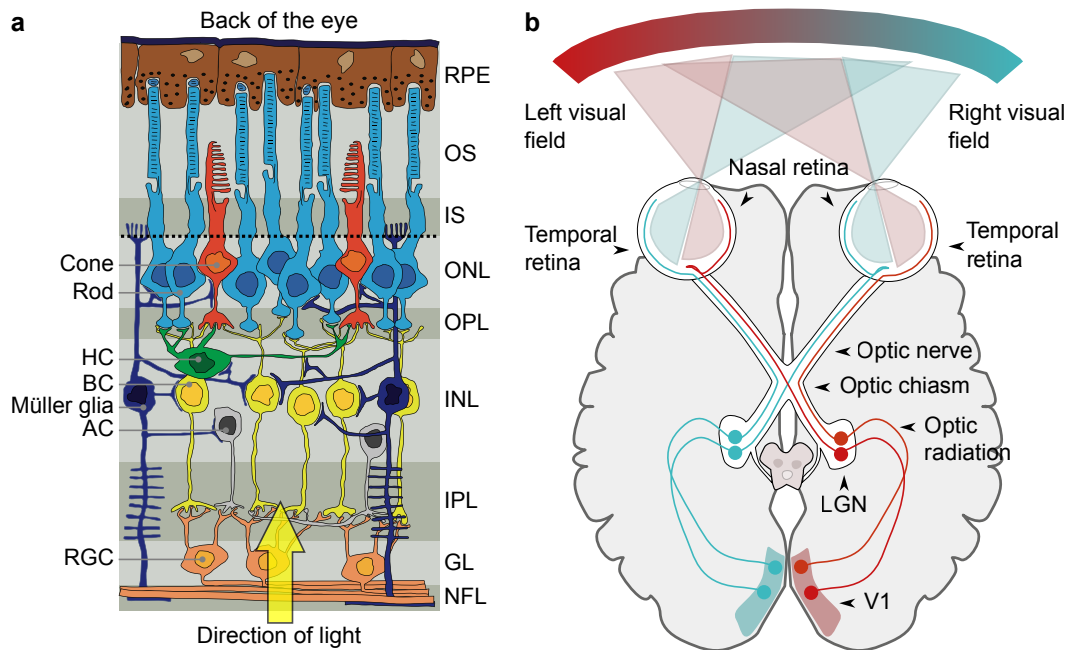
Figure 1.1: Layered structure of the retina. RPE: retinal pigmented epithelium; OS: outer segment; IS: inner segment; ONL: outer nuclear layer; OPL: outer plexiform layer; INL: inner nuclear layer; IPL: inner plexiform layer; GL: ganglionic layer; NFL: nerve fibre layer; OLM: outer limiting membrane; HC: horizontal cell; BC: bipolar cell; AC: amacrine cell; RGC: retinal ganglion cell. The original image has been obtained by the authors from the Wikimedia website where it was made available by  under a CC BY-SA 3.0 licence. It is included and adapted within this article on that basis. It is attributed to Peter Hartmann. (https://commons.wikimedia.org/wiki/File:Retina layers.svg). (b), Drawing of the visual system. LGN: lateral geniculate nucleus; V1: primary visual cortex. The original image has been obtained by the authors from the Wikimedia website where it was made available by Miquel Perello Nieto under a CC BY-SA 4.0 licence. It is included and adapted within this article on that basis. It is attributed to Miquel Perello Nieto. (https://commons.wikimedia.org/wiki/File:Human visual pathway.svg).

Two metrics assess the quality of vision or the presence of visual impairment: visual acuity and visual field. Visual acuity determines the sharpness of vision. A healthy subject can recognise an octotype on a Snellen chart when it subtends 5 minutes of arc (Figure 1.2a). This value corresponds to a minimum angle of resolution (MAR) of 1 minute of arc or a 5-μm separation on the retina[9]. Cone density, which is not homogeneous across the visual field, is directly related to our visual acuity. The maximal visual acuity is in the centre of the fovea and drops rapidly with increased eccentricity (Figure 1.2b). The other parameter used to define the quality of vision is the visual field size. A normal visual field for one eye spans approximately 60 degrees nasally to 107 degrees temporally and from 70 degrees above the horizontal meridian to 80 degrees below (Figure 1.2c).

Vision loss generally occurs when the visual acuity or the visual field size decreases. The
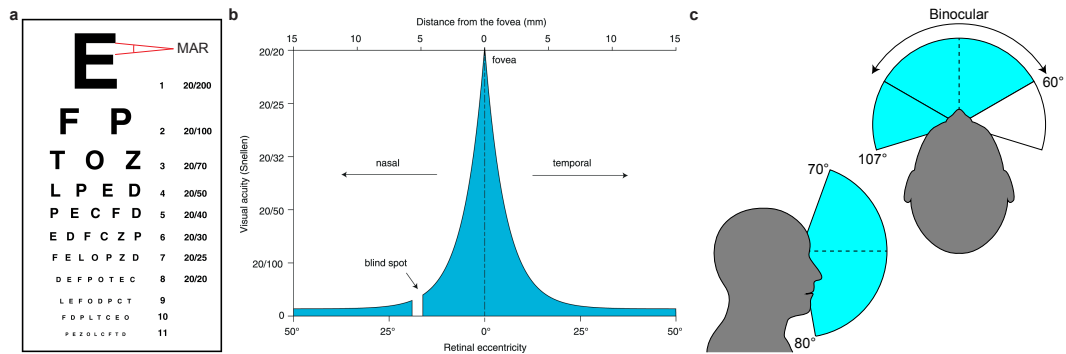
Figure 1.2: (a), Snellen chart to assess visual acuity. The MAR is the minimum angle of resolution corresponding to the smallest recognisable gap in the octotype. Image adapted from Anatomy Physiology, Connexions Website, CC-BY. (b),Quantification of the visual acuity as function of the retinal eccentricity (or the distance from the fovea). Image from[10], CC-BY. (c), Horizontal (top image) and vertical (bottom image) visual field size. For the horizontal size, the cyan area corresponds to the visual field of the left eye and the white area corresponds to the visual field of the right eye. The binocular area is indicated by the arrows. The dashed lines are the vertical and horizontal meridia respectively.

World Health Organisation defines blindness as visual acuity of less than 3/60 (20/400) or a corresponding visual field loss of less than 20° (diameter) in the better eye with the best possible correction. Although more than 50% of blindness cases worldwide can be prevented or treated, such as cataract (33.4%), uncorrected refractive error (20.9%) and trachoma (1.4%), others suffer from incurable pathologies such as macular degeneration (6.6%), glaucoma (6.6%) or diabetic retinopathy (2.6%)[11]. Overall, any type of disease occurring along the entire visual pathway due to genetic, degenerative, traumatic or environmental reasons can cause blindness.

Benjamin Franklin proposed in 1752 the idea of using electricity to restore sight[12]. A few years later, in 1755, Charles LeRoy evoked visual disturbances in a blind volunteer by delivering electric current pulses through a wire coiled around his head[13]. Despite this demonstration of electrical stimulation of the visual system, the systematic exploration of the occipital cortex via electrical stimulation started only after World War I. In 1918, Löwenstein and Borchardt induced flickering perception in the opposite half of the visual field by stimulation in one occipital pole[14]. Then, Krause (1924) and Foerster (1929) induced small evoked flickering visual percepts in different locations of the visual field by moving the stimulated point[15,16]. These experiments demonstrated the possibility of electrically inducing the perception of bright white/yellow dots (called phosphenes). Phosphenes are the building blocks of artificial vision[17]. Blind people perceive the world by combining multiple phosphenes in a meaningful manner (Figure 1.3a). Initially, phosphenes might be irregular and difficult to interpret, but it is assumed that neuroplasticity triggered by learning and rehabilitation will improve artificial vision over time (Figure 1.3b).
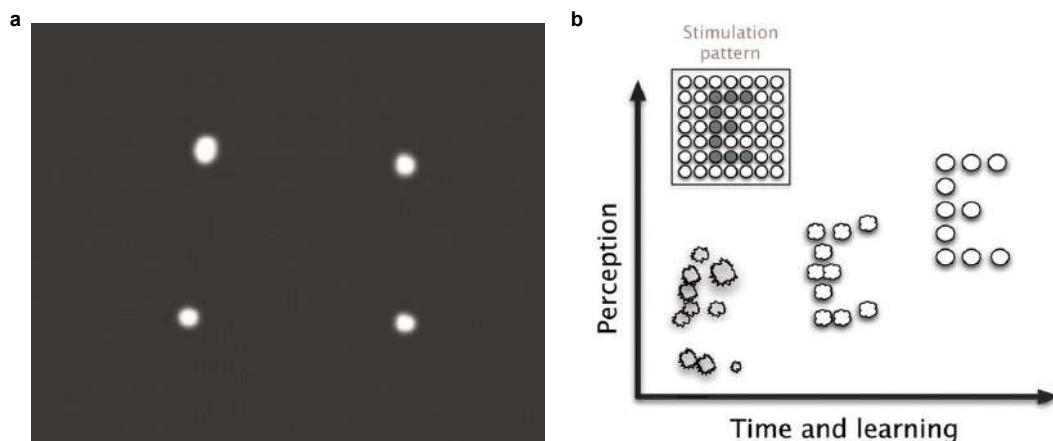
Figure 1.3: (a), Phosphenes arranged as a square generated by stimulating four electrodes simultaneously. Image from[18], CC-BY. (b), Neuroplasticity improves perception over time. Image from[18], CC-BY.

## 1.4   Neuroprostheses for artificial vision through electrical stimulation.

Visual prostheses are classified into four categories based on the location along the visual pathway (Figure 1.4a). Accordingly, this section describes the current approaches to visual prostheses, organised by position following the natural flow of information: retina, optic nerve, LGN, and V1 (Figure 1.4b). We will discuss each approach's main advantages, drawbacks, and clinical applications. Most of the work to date has been focused on retinal stimulation, which quickly became the preferred strategy since it uses the downstream natural process of visual information. The optic nerve is also a target to elicit phosphenes and could have a broader range of applications than retinal prostheses. The LGN in the thalamus has potential for individuals with either retinal or optic nerve pathologies. Similarly, the visual cortex is a target for all blindness, but cortical injuries and stroke. The population of blind patients that could benefit from prostheses increases by moving the surgical placement from the retina to the cortex. However, at the same time, there is also an increase in surgical complexity and risks.

### 1.4.1   Retinal prostheses

Retinal prostheses aim to electrically stimulate the surviving retinal neurons. Therefore, they can offer artificial vision only to blind patients with outer retinal diseases, causing the progressive loss of retinal photoreceptors. These diseases are the major causes of incurable blindness in the western world[19]. They include retinitis pigmentosa (RP), macular dystrophies (e.g. Stargardt disease) and age-related macular degenerations (AMD). Macular degeneration affects retinal cones and results in blurred or no vision in the centre of the visual field (Figure 1.4c). In contrast, peripheral vision remains preserved in most cases. AMD is the most

preeminent pathology amongst outer retinal diseases. Unlike AMD, RP is a set of rare inherited retinal rod-cone dystrophies, causing loss of night vision and the constriction of the visual field (tunnel vision), later followed by cone dysfunction and eventually total blindness (Figure 1.4c)[5,20].

Retinal prostheses have quickly become the leading device among visual prostheses. Several devices have been commercialised[21–23] thanks to their relative ease of implantation and lower surgical risks compared to other approaches. Besides the ease of surgical accessibility, they can also profit from the retinotopic organisation and early positioning in the visual pathway[24,25].

Retinal prostheses can be implanted in three locations (Figure 1.4d). Epiretinal prostheses are anchored to the retina's inner surface, subretinal prostheses are inserted between the retina and the RPE, and suprachoroidal prostheses are implanted between the choroid and the sclera. Consequently, the retina can be electrically stimulated either from the ganglionic layer (as in epiretinal prostheses) or the inner nuclear layer (as in subretinal and suprachoroidal prostheses). The device position (epiretinal, subretinal or suprachoroidal) and the characteristics of the electrical pulses (such as duration and waveform) determine which cell population is predominantly activated[26,27]. Subretinal and suprachoroidal prostheses primarily activate BCs, whose membrane depolarisation triggers synaptic release causing the glutamatergic excitation of RGCs. This mechanism is known as network-mediated stimulation since RGCs are indirectly stimulated via their presynaptic network. Epiretinal prostheses with short (e.g. less than 1 ms) and rectangular pulses directly activate RGCs. However, the network-mediated stimulation is also possible from an epiretinal device if long (more than 8 ms) or non-rectangular pulses are used[27–29]. For more extensive reading about retinal prostheses, we refer the reader to previous review articles[30–34].

### 1.4.1.1   Epiretinal prostheses

The implantation of epiretinal prostheses relies on a surgical approach familiar to vitreoretinal surgeons. Epiretinal surgery allows the placement of sizable devices for artificial vision in a large portion of the visual field[37,38]. Wide artificial vision is crucial for totally blind people to perform everyday visual tasks such as general orientation, safe ambulation, obstacle avoidance and object recognition[39]. Moreover, another advantage of epiretinal implants is the facilitation of heat dissipation via the vitreous[40]. The main surgical drawback is the requirement of one or more retinal tacks to anchor the prosthesis to the retina, which could cause retinal damage. Retinal tacks also lose mechanical stability over time, which can increase the distance between electrodes and the retina and, in consequence, increase the current required for retinal stimulation and reduce resolution[41–43].

Epiretinal stimulation remains an open challenge. Although the electrodes are close to RGCs, they are not directly in contact with their somas. In fact, the NFL composed by the axons converging to the optic disc is in between electrodes and cell bodies (Figure 1.4d). Due to axonal activation, phosphenes often appear with an elongated shape distorting the image
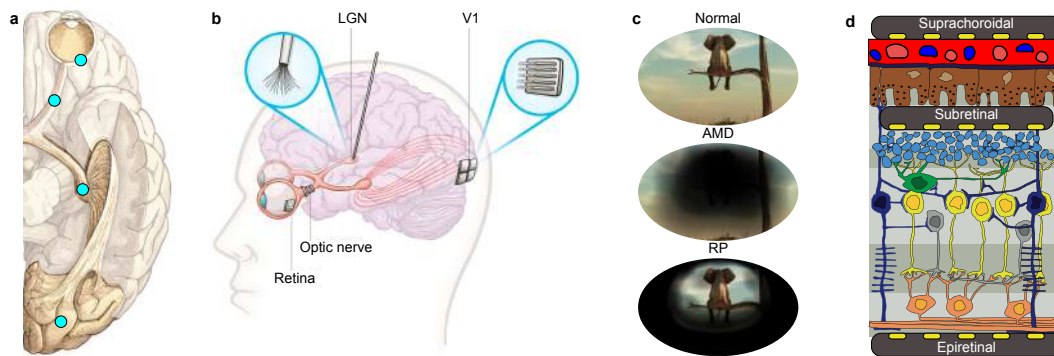
Figure 1.4: (a), The cyan circles show the possible locations for visual implants along the visual pathway: retina, optic nerve, LGN, and V1. (b), Illustration of the four categories of visual prostheses. Image adapted with permission from[35]. (c), Illustration of vision in a sighted (top), AMD (middle) and RP (bottom) subject. Image adapted with permission from[36]. (d), Epiretinal, subretinal and suprachoroidal placement of retinal implants. Subretinal prostheses might be separated from target cells (BCs) by remaining debris following photoreceptor degeneration, represented by circles (in light blue). The original image has been obtained by the authors from the Wikimedia website where it was made available by  under a CC BY-SA 3.0 licence. It is included and adapted within this article on that basis. It is attributed to Peter Hartmann. (https://commons.wikimedia.org/wiki/File:Retina layers.svg).

perceived by the patient[44]. A way to mitigate this phenomenon is to use long and non-rectangular pulses that will preferentially induce network-mediated stimulation, resulting in a more localised activation[45].

So far, only two epiretinal implants have received commercialisation approval for RP patients: the Argus® II (Second Sight Medical Products Inc; CE mark and FDA approval) in Figure 1.5a and the IRIS® II (Pixium Vision SA; CE mark)[32,46]. Both devices are now out of production. A third device is currently under clinical evaluation (NR600, Nano Retina, Rainbow Medical Group). The implant is a wireless light-powered prosthesis with three-dimensional penetrating electrodes to stimulate BCs from the epiretinal side.

### 1.4.1.2   Subretinal prosthesis

Subretinal prostheses are inserted between the retina and the RPE (Figure 1.4d). Therefore, they do not need fixation with retinal tacks and have greater mechanical stability. On the other hand, subretinal surgery is more delicate due to the adhesive junctions between the retina and the RPE[47]. Subretinal prostheses directly stimulate the remaining inner retinal layer and use its processing capability. For this reason, these prostheses might also provide higher visual acuity and more naturalistic perception[48]. However, the presence of debris due to photoreceptor degeneration might increase the distance from the electrodes to BCs and reduce resolution and stimulation efficiency[49]. A major constraint in subretinal prostheses however is the maximum size of the implant, which is limited by the risk of retinal detachment.

Devices have a size providing a maximum restored visual angle of about 10 °, suitable only for applications where a small part of the visual field is lost, such as AMD[48,50]. For totally blind patients, like in RP or severe forms of AMD, a much wider visual field would be required to allow the patient to perform everyday tasks.

Subretinal prostheses have been pioneered in the early 90's by the artificial silicon retina (ASR, Optobionics): an array of photovoltaic diodes coupled to capacitive electrodes. Six RP patients have been implanted with the ASR device[51]. However, visual improvements were likely due to a generalised neurotrophic effect rather than a direct effect from electrical stimulation. Today, only one subretinal prosthesis, the Alpha IMS implant (Figure 1.1b) and its successor Alpha AMS (Retina Implant AG), have received marketing approval (CE mark)[52,53]. Unfortunately, the company dissolved in 2019. The subretinal prosthesis PRIMA (Pixium Vision SA) is currently in clinical evaluation for AMD patients (Figure 1.5c,d)[48,50].

### 1.4.1.3   Suprachoroidal prosthesis

The third location is the suprachoroidal space, between the choroid and the sclera (Figure 4d). This location reduces the risk of retinal damage compared to the other two approaches since it does not require intravitreal manipulation[54]. However, a high risk of subretinal and suprachoroidal haemorrhage has been reported during preclinical and clinical evaluation[55–57]. Like subretinal prostheses, they have good mechanical stability without fixation with retinal tacks[56,58] and, like epiretinal prostheses, they have good heat dissipation capacity and allow the insertion of large arrays[57]. Suprachoroidal prostheses aim at the stimulation of BCs, but the considerable distance between the electrodes and the retina is a major issue. The presence of choroid, RPE, and debris of photoreceptors makes the selective stimulation of BCs extremely difficult, leading to poor spatial resolution[59,60]. Due to the considerable distance from BCs, high current amplitudes are required for retinal stimulation, possibly leading to damage due to overstimulation[46,61].

Two clinical trials are ongoing in RP patients, one in Australia (Bionic Vision Technologies)[57] and one in Japan (Osaka University)[58]. The results showed that implanted patients could localise static objects, light or trajectories, despite the poor visual acuity. In Australia, the second generation of the suprachoroidal prosthesis with more electrodes is currently under clinical assessment[55].

### 1.4.2   Optic nerve prostheses

When severe damage to the eye or the retina occurs (as traumatic eye injury or retinal detachment), or the lack of optical transparency prevents vitreoretinal surgery, retinal prostheses are no longer suitable. Optic nerve prostheses are an attractive solution to overcome the exclusion criteria of retinal implants (Figure 1.4b). Moreover, the relatively small diameter of the optic nerve facilitates the electrical stimulation of a wide visual field[63]. In 1998, a group in
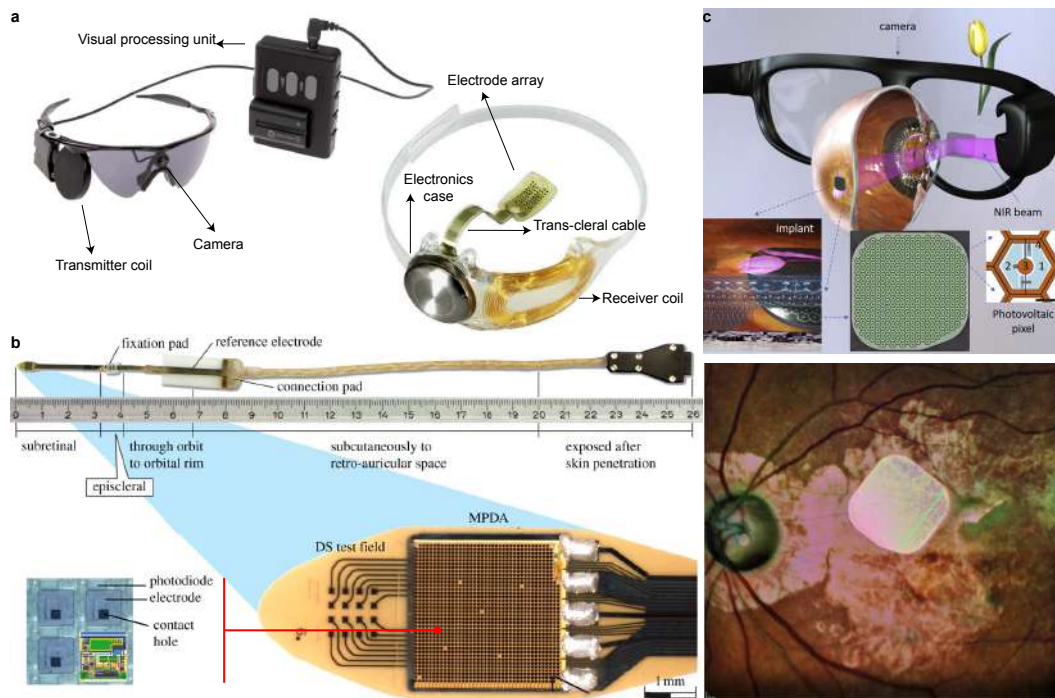
Figure 1.5: (a), The Argus® II system. Image adapted from[62], CC BY. (b), The Alpha-IMS subretinal prosthesis. Image adapted from[52], CC BY. (c), The PRIMA Bionic Vision System composed of the PRIMA photovoltaic retinal prosthesis and the wereable projecting glasses with camera. Image adapted from[48], CC BY.(d), d, Fundus image of the PRIMA implant placed below the macula of one patient with atrophic AMD. Image adapted from[48], CC BY.

Leuven (Belgium) was the first to propose a prototype of optic nerve prosthesis in humans[64]. They implanted a self-sizing spiral cuff with four electrodes in the intracranial segment of a blind subject suffering from RP. The patient reported phosphenes and described them by their position, shape, number of dots, colour and dimension. The results showed excellent retinotopic correspondence between the quadrant of the visual field in which the phosphene appeared and the electrode used. After a few months of training, the patient distinguished line orientations and identified characters despite having only four electrodes[64–66]. The research proved that optic nerve stimulation elicits phosphenes in the entire visual field with some degree of selectivity. However, phosphenes were irregular in shape and not stable over time. The lack of stable phosphene could be attributed to the lack of mechanical stability of the cuff device[67]. The other challenge presented by existing cuff devices is to selectively activate specific fibres, including those in the central portion of the nerve, to improve the resolution of artificial vision[68]. Therefore, intraneural arrays were implemented to increase fibre selectivity (Figure 1.6a). Three platinum wires were implanted in the optic disc of an RP patient eliciting phosphenes in three distinct positions for each electrode[69]. Unfortunately, functional vision tests were not performed. Recently, a few groups have developed optic nerve prostheses based on intraneural electrode arrays. The C-Sight project tested an optic nerve prosthesis based on four stiff electrodes to stimulate the intra-orbital segment of the nerve in rabbits and cats[70–72].

However, this implant is too rigid compared to the nerve tissue and is therefore unsuitable for chronic implantation. Another group has validated a thin and flexible intraneural electrode array called OpticSELINE (Figure 1.6b). Results in rabbits showed that the selective activation of different portions of the optic nerve induced spatially organised cortical activation patterns in the rabbit's V1[63,73,74]. These are promising steps towards developing a more focused optic nerve stimulation. However, the long-term functionality of the device and the biocompatibility should be tested before moving into human application[68].
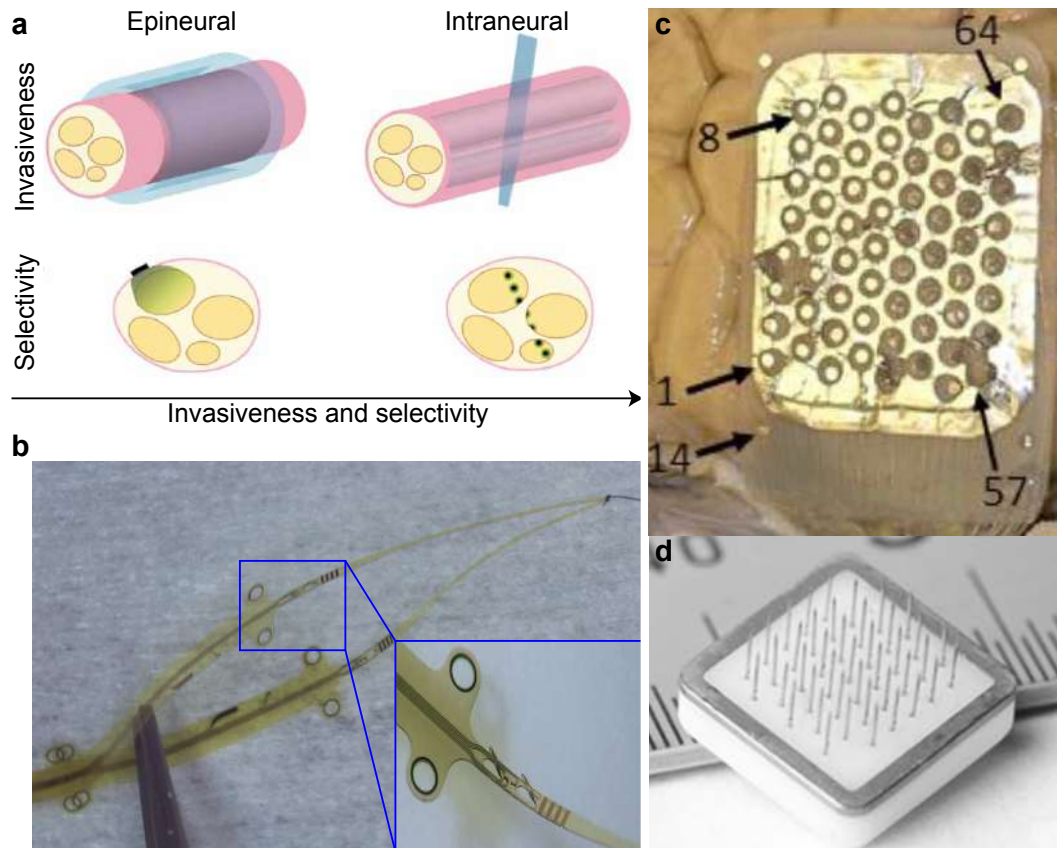


Figure 1.6: (a), Sketch of epineural and intraneural nerve prostheses. Epineural are less invasive than intraneural, but also less selective. Image adapted from Paggi et al., 2021[75], CC-BY. (b), Picture of the OpticSELINE. Image adapted with permission from Gaillet et al., 2020[73]. (c), Picture of the epicortical array explanted after 36 years from one of Dobelle's patients. Image adapted from TOwle et al., 2020[76], CC BY. (d), Picture of one module of the GENNARIS intracortical visual prostheses developed at the Monash Vision Group. Image adapted from Lewis et al., 2016[77], CC BY.

### 1.4.3   Thalamic prostheses

The LGN is a stratified compact structure in the thalamus receiving input from the optic nerve and relaying information to the primary visual cortex[7]. Given its deep location, only recently

have visual prostheses targeting the LGN been investigated thanks to advances in deep brain stimulation (Figure 1.4b). Three main advantages drive the interest in the LGN. First, it can help patients who lost the optic nerve, for example, due to glaucoma or ocular trauma. Second, it is possible to cover a wide visual field with an overrepresentation of the foveal region, thus restoring possibly high-acuity artificial vision[78]. However, since the LGN is located after the optic chiasm, a bilateral implant is required to cover both hemifields. Third, LGN presents retinotopic organisation and well-defined physical separation of the parvocellular and magnocellular pathways, respectively relaying information about small, slow, colourful things (parvocellular; high spatial frequency information; low temporal frequency information) and large, fast, and colourless things (magnocellular; low spatial frequency; high temporal frequency)[35,79]. Therefore, it might encode a more naturalistic perception. In animals, LGN microstimulation produced simple discrete visual percepts[80] and visual cortical responses similar to those elicited by natural vision[81]. So far, there have been very few preclinical studies in animals conducted to test the stimulation efficacy[80,82,83]. With future advancements from the technological point of view, LGN visual prostheses could start to carve their way into a feasible solution for patients[84].

### 1.4.4 Cortical prostheses

After the pioneering experiments of Löwenstein and Borchardt[14], Krause[15] and Foerster[16], cortical prostheses were the first ones to be developed among visual implants.

The first cortical prosthesis had only four intracortical electrodes[85,86] but was able to evoke some visual percepts in the subject[77]. Some years after, Brindley and Lewin (1968) proposed the first permanently implanted cortical prosthesis, consisting of an epineural array of eighty electrodes implanted over the occipital cortex[87,88]. The volunteer, a blind subject with glaucoma, perceived phosphenes and recognised simple patterns. A second subject was implanted a few years later with a bilateral device. He recognised patterns induced by sequential activation of electrodes corresponding to the Braille alphabet[89]. At the same time, Dobelle started a long-term project to develop a portable cortical visual prosthesis. Initial results in the first set of subjects were promising[90–92], but the project suddenly closed after the bilateral implantation of 16 blind volunteers between 2002 and 2004.

A cortical prosthesis offers the advantage of artificial vision in most conditions of blindness, excluding traumatic brain injuries and stroke[7]. On the other hand, the complexity of the visual cortex with neurons specifically tuned for specific cues[93] could hinder the ability to evoke simple uniformly shaped phosphenes. Stimulation paradigms adapted explicitly for each patient might also be required[94]. This aspect becomes even more critical when considering the effect of neuroplasticity, which is the ability of the nervous system to change its activity in response to intrinsic or extrinsic stimuli by reorganising its structure, functions, or connections[95]. Indeed, researchers demonstrated that visual perception and performance in solving visual tasks could improve with learning and time[96,97].

Cortical prostheses follow two main approaches: epicortical arrays placed on the cortical surface (Figure 1.6c) or intracortical electrodes penetrating the cortical layers (Figure 1.6d). Epicortical prostheses are less invasive since they do not penetrate the brain, as confirmed by a post-mortem study on a patient implanted by Dobelle, who retained the epicortical array for 36 years (Figure 1.6c)[76]. However, the current amplitudes required to elicit a phosphene is much higher than with intracortical electrodes because of the distance and the resistive nature of the tissue between the electrodes and the neurons[98]. This distance reduces the spatial resolution of artificial vision[99], and high currents might be unsafe due to the risk of seizures[77]. Intracortical prostheses are more invasive but take advantage of the close contact between the electrodes and the neurons to provide a more selective stimulation at much lower current amplitudes[100,101]. Therefore, evoked phosphenes are smaller and closer. However, the implantation technique requires pneumatic insertion tools that limit the area reachable with the device to only the occipital pole. Contrary to epineural implants, intraneural electrodes cannot be placed in the interhemispheric fissure, where a large portion of the visual field is mapped[102]. In this case, phosphenes are evoked only in a few degrees of the visual field. Therefore, placing the electrodes in higher visual areas where spatial representation is still preserved[24,98] could be a possible solution to enlarge the visual field.

Four projects are currently in clinical evaluation. The Orion I (Second Sight Medical Products Inc) is a flexible electrode array already implanted in six subjects. However, due to the high current intensities required to elicit phosphenes, this approach might induce seizures, as reported by one subject[103,104]. The other three are intracortical prostheses. The GENNARIS (Monash Vision Group) consists of 11 modules with 43 electrodes each (Figure 1.6d)[105]. The CORTIVIS (Miguel Hernández University of Elche) uses a Utah array with 100 electrodes[106]. The ICVP (Illinois University of Technology) is developing a wireless floating microelectrode array with 16 microelectrodes[107]. For more extensive reading about cortical prostheses, we refer the reader to previous review articles[35,108,109].

## 1.5   Current challenges and potential solutions

Visual prostheses have been an incredible breakthrough leading to artificial vision in several blind patients suffering from RP, AMD, glaucoma, or other traumatic injuries). So far, retinal prostheses have reached marketing approval[53,110,111], and other devices are in preclinical and clinical testing. However, artificial vision still does not offer the patient the possibility of regaining fully functional vision[96]. Quantitative limitations in artificial vision are a product of both technological and biological challenges, which will be addressed in the following paragraphs, together with potential solutions.

### 1.5.1    Quantitative limitations

#### 1.5.1.1    Visual field size

Everyday experience shows that the visual angle size has primary importance in mapping and interacting with the environment, consequently affecting one's understanding of layout space, walking distance evaluation, identify-and-reach tasks, spatial cognition, and attention. Many studies have highlighted that restoring a large visual field is necessary to make artificial vision helpful in everyday life[39,112–116]. Studies under simulated prosthetic vision identified a visual angle of 30-35 ° as the minimal requirement for mobility and daily tasks (Figure 1.7)[39,117–120]. However, this number might underestimate the real needs of implanted patients due to the perceptual and behavioural learning required to adapt to artificial vision[121,122]. The entire visual field is mapped over the anatomical area in all the structures mentioned (retina, optic nerve, LGN and V1). Therefore, as a rule of thumb, enlarging the visual field means having electrodes covering a wider tissue area.
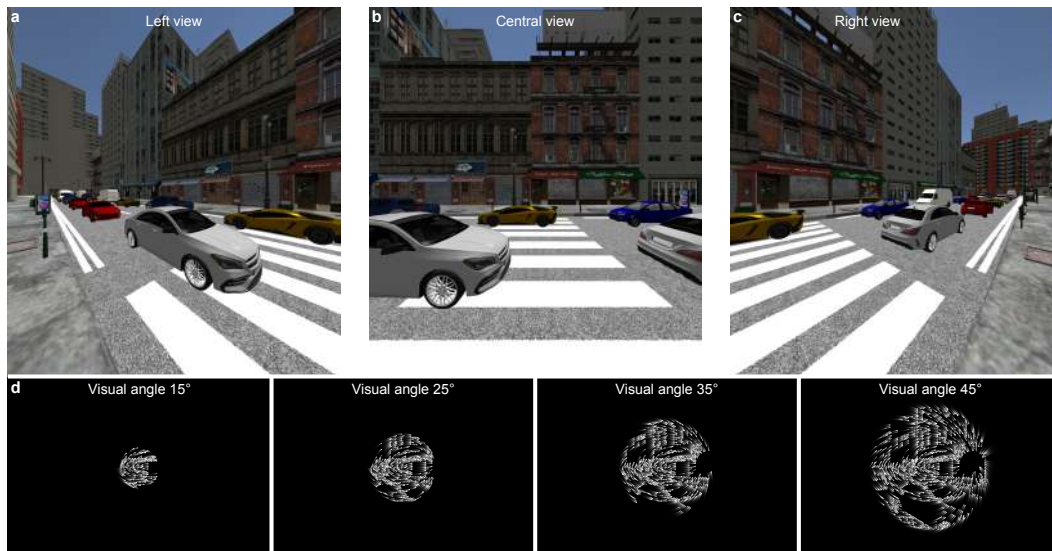


Figure 1.7: (a-c), Virtual reality views of a busy street with cars: left view (a), central view (b) and right view (c). (d), Image rendering is simulated prosthetic vision of the busy street with cars at increasing visual angles. Images adapted from Thorn et al., 2020[39], CC-BY.

In retinal prostheses, wide coverage of the retina remains an open challenge. Moreover, it is possible only for epiretinal and suprachoroidal implants. Subretinal prostheses are typically small in size, since large subretinal implants might encounter considerable difficulty in the surgical placement and represent a high risk of retinal detachment[30]. Multiple PRIMA devices have been placed in the rabbit eye to increase the visual angle [122]. However, it remains unclear if this tiling procedure will be feasible in patients. On the other hand, the surgical fixation to the retina is another open challenge for wide epiretinal implants [123].

Larger prostheses might also require larger and potentially riskier incisions to insert the device

and from which the connection cable will have to exit the eye to connect with the stimulator. Nevertheless, the main issue with wider prostheses is the limited number of electrodes usually available in the array. In conventional visual prostheses, the electrode number and electrode density are limited by the implantable pulse generator, the cable from the pulse generator to the array, and the feedlines in the array. A fixed electrode number reduces the electrode density if electrodes are spread over a wider surface area, which might worsen visual resolution[123]. One way to overcome this problem in retinal prostheses is to use wireless photovoltaic technology where each pixel converts incident light into electrical stimulation[124–127]. In retinal stimulation, photovoltaic technology is intuitive since the retina is designed to absorb the light entering from the pupil. Photovoltaic retinal stimulation is achieved using artificial light projected into the eye (using a projection system as in augmented reality goggles) and absorbed by a semiconductor layer embedded into the stimulating electrodes. This wireless solution avoids a trans-scleral cable which are known to limit the maximum number and density of electrodes on the device and to induce post-operative complications such as eye inflammation or leakage through the incision. To this aim, POLYRETINA is a high-density wide-field epiretinal prosthesis containing 10'498 photovoltaic pixels distributed over an active area of approximately 43 °[37,128,129]. Yet, an open challenge for both subretinal (PRIMA) and epiretinal (POLYRETINA) photovoltaic implants is projecting wide-angle images through the pupil necessary to increase the visual field size.

Both the optic nerve and LGN are compact, making it easier to access the entire visual field of one eye (optic nerve) or a whole hemifield (LGN) with a single implant. However, their small size is a challenge for implant and electrode miniaturisation, particularly when targeting the optic nerve. An epiretinal implant like POLYRETINA on the other hand can have more than 10'000 electrodes over 43 ° (approximately 140 mm$^2$), that is an area ten times larger than the total cross-area of the optic nerve. Most of the primary visual cortex surface lies in the interhemispheric area and the calcarine fissure[79], creating a hurdle for developing wide-angle cortical prostheses. Although placing the electrodes in higher visual areas[24,98] could be a possible solution to enlarge artificial vision.

### 1.5.1.2   Spatial resolution

The visual angle is certainly not the only barrier. Object identification and recognition require devices that are able to provide a high enough resolution during artificial vision. In other words, increasing spatial resolution means increasing the number of separable phosphenes per unit area evoked in the patient's visual field. Another challenge threatening artificial vision lies in the capability of the device to stimulate multiple independent phosphenes to create form perception.

So far, most studies regarding spatial resolution have been conducted with retinal implants. Clinical trials showed that the best visual resolution was achieved using subretinal prostheses. The highest visual acuities reported to date, as measured with the Landolt-C test, were 20/460 with the subretinal implant PRIMA (in AMD patients)[48] and 20/546 with the subretinal implant

Alpha-AMS (in RP patients) (Zrenner et al. 2017). Grating acuities reported in the literature range from 20/1260 with the epiretinal Argus® II implant to 20/364 with the subretinal Alpha-AMS implant[53]. This comparison shows that subretinal prostheses have so far provided better resolution than epiretinal prostheses. This result is primarily due to two factors. First, the Argus® II implant had a significant separation between electrodes (575 μm), about 5 to 8 times higher than PRIMA and Alpha-AMS. A larger electrode separation will inevitably lead to a lower resolution. Second, the Argus® II implant stimulates RGCs directly. Therefore, evoked phosphenes are distorted (resulting in an elongated shape) due to unwanted axonal stimulation in nerve fibre bundle trajectories[110,130,131]. Two approaches have been proposed to improve resolution in epiretinal stimulation. One solution would be to selectively activate individual RGCs by establishing a one-to-one connection between RGCs and electrodes[132]. Also, high stimulation frequency allows discrimination among RGC types [136]. Otherwise, increasing the pulse duration[45] or using non-rectangular pulses[133] facilitates network-mediated stimulation. Sinusoidal electrical stimuli in epiretinal configuration allowed the classification of overlapping but spatially displaced objects in explanted retinas[134]. Epiretinal prostheses with higher pixel density and targeting network-mediated stimulation might overcome these issues and provide high resolution. POLYRETINA reported ex-vivo a spatial resolution of 120 μm (or 20/480) equivalent to the electrode separation[135]. The two approaches to avoid axonal stimulation (selective direct stimulation and epiretinal network-mediated stimulation) point towards different directions, and today they seem mutually exclusive. However, this is an important research question that needs to be addressed in epiretinal stimulation.

Subretinal implants are further away from the GL,, and usually induce circular phosphenes. However, patients might still experience arcuate and linear phosphenes when high current amplitudes are used[136], most probably due to direct RGC activation. A similar effect has also been observed with suprachoroidal implants, where the subjects described geometrically complex percepts[137].

Reducing the size of the electrode is necessary to increase electrode density. However, the electrode size is not the only limiting factor, and further reducing the electrode diameter might not correlate to better resolution[138]. On the other hand, the denser the electrodes, the higher is the risk of cross-talk between electrodes. Visual prostheses could benefit from current-steering approaches that would limit the extent of the activated tissue during stimulation, reducing the risk of cross-talk and increasing the spatial selectivity. A common approach is to use bipolar stimulation through two close electrodes, as shown in retinal[139–141], optic nerve[74], and thalamic prostheses[142]. Different groups demonstrated that spatially organised phosphenes are induced by applying current-steering or modulating current amplitudes[65,72,73]. Despite these results, the selective activation of a few optic nerve fibres by each electrode remains an open challenge. Another example of nonspecific activation can also be found when stimulating the visual cortex. In animal studies, researchers have found that stimulation activates interconnected neurons distant from the electrode, even at low currents[143].

From the perceptual point of view, each electrode should evoke a reproducible phosphene located in a region of the visual field. The stimulation parameters play a crucial role in the characteristics of phosphenes, such as brightness, duration, size or colour. Generally, short trains of charge-balanced biphasic pulses evoke individual phosphenes[144]. Whether the stimulation through multiple electrodes is synchronous[145] or sequential[89,97,146], each electrode should excite selectively only a specific subset of neurons, different from those stimulated by neighbouring electrodes. When the stimulation resolution is low, as it is for the Argus® II or epicortical visual prostheses, it has been shown that phosphenes might fuse into a blob during synchronous activation of multiple electrodes. The sequential activation of electrodes is an attractive strategy allowing form vision in patients[89,97]. Future developments in field-steering technology will be beneficial to improve stimulation therapies not only for visual prostheses but in general for the neuroprosthetics field.

### 1.5.1.3   Temporal resolution

Artificial vision can also be hampered by poor temporal resolution. A significant limitation in artificial vision is phosphene fading[147–149], a perceptual phenomenon similar to the Troxler effect, which affects retinal prostheses and makes continuous perception above flicker fusion nearly impossible. In sighted humans, the Troxler effect is prevented by various ocular micro-movements (tremors, drifts and microsaccades) that refresh a static image and limit retinal adaptation[150,151]. Retinal prostheses can avoid fading if three criteria are met[152]. First, natural or artificial light must activate the electrodes, so that eye micro movements can effectively shift the stimulated area of the retina, like for Alpha IMS/AMS[53], PRIMA[48] and POLYRETINA[37,153]. Second, high-density electrode arrays are required to ensure high-resolution stimulation to move the projected image by one or two electrodes over the prosthesis leading to stimulation of different retinal areas. Third, patients must have preserved their physiological ocular micromovements, such as for AMD patients. However, this ideal case is rarely reached and has only been reported for the PRIMA device[48] and some patients with Alpha IMS, most likely with preserved eye movements[154]. Contrarily, patients implanted with Argus® II, IRIS® II and EPI-RET 3 prostheses were instructed to perform large body and head movements to scan the visual scene and refresh the stimulation pattern on their retina. Such large movements made the experience of artificial vision physically and mentally tiring. Therefore, several groups have developed an interest in exploring compensatory stimulation strategies to reduce retinal desensitisation and avoid fading[129,155,156] and tested them with sighted subjects under simulated prosthetic vision[157].

Another limitation is the maximal frame frequency and the possibility of reaching flicker fusion (30 Hz or above). So far, flicker fusion has been achieved only for the PRIMA device in AMD patients[48]. Patients with other retinal prostheses were more comfortable with lower frame frequencies (between 1 to 20 Hz), most likely due to the process of perceptual fading. The retina has been widely studied, and much knowledge has also been gained thanks to the many patients who have been implanted. Meanwhile, little is known about other visual

targets. Stimulation approaches, such as dynamic current steering, have been investigated and proved to be a helpful strategy for recognising shapes[89,97] and while dynamic current steering combined with high-density electrode arrays holds promises of improvement in cortical prostheses[100], more needs to be known about safe stimulation frequency limits and the possibility of reproducing flicker fusion. As such, it is essential to successfully translate visual prostheses into clinics to understand how to modulate spatiotemporal stimulations to generate individual phosphenes and combine them into perceived objects and visual scenes[144].

### 1.5.2   Technological challenges

#### 1.5.2.1   Electrode-tissue interface

The electrode-tissue interface is one of the most critical elements of a neural interface[158] from a mechanical, chemical and electrical point of view.

Electrodes should be close to and have a comparable dimension of target neurons to achieve high-resolution stimulation, ideally down to a single neuron[96]. However, decreasing the electrode size imposes constraints on the electrode material to maintain low impedance and high charge injection capacity. In the last 20 years, advances like carbon-based materials and nanomaterials have been explored to improve the performance at the electrode-tissue interface[158–160]. Conductive polymers have been widely used in implantable devices as they are considerably softer than metals, flexible and conformable, and have a high charge injection capacity[161–163]. Exceeding the charge injection limit of electrodes will cause irreversible damage to both electrodes and tissue. Since the charge injection limit is a property of a material, smaller electrodes can safely deliver less charge compared to larger electrodes. Smaller electrodes have higher charge density stimulation threshold and lower dynamic range, as shown in explanted ratinas[164,165]. These results have important implications for high-density prostheses.

In the last 20 years, advances like carbon-based materials and nanomaterials have been explored to improve the performance at the electrode-tissue interface[159,160,166,167]. Conductive polymers have been widely used in implantable devices for research as they are considerably softer than metals, flexible and conformable, and have a high charge injection capacity[162,163,166,168]. The use of polymer-based coatings in visual prostheses could be beneficial to allow smaller and denser electrodes [33]. Among carbon-based materials, graphene-based materials emerge in neural interfaces, given their outstanding electrical and optical properties[169]. Recently, the safety and biocompatibility of graphene electrodes for retinal implants has been assessed [169]. Nanomaterials for neural stimulation have also been developed thanks to the latest advancement in nano-engineering[170]. In addition, these novel materials are compatible with flexible and stretchable substrates and cleanroom microfabrication processes. In conclusion, reducing the electrode size will allow visual prostheses to significantly increase the number of electrodes in the array, which might translate into higher

visual acuity and improved visual function for the patients.

Another crucial element of the electrode-tissue interface is the biological response. It has been shown that all biocompatible materials used so far provoke an inflammatory response and some degree of foreign body reaction[171]. For visual prostheses, regardless of whether they are epineural or intraneural, matching the neural tissue mechanical properties with the implanted ones would help in improving the long-term stability and efficacy of the stimulation[172]. In particular, for epineural prostheses, when the target tissue covers a wide area (like in the retina or the visual cortex), the choice of the substrate plays an important role. Exploiting conformable or foldable substrates has two advantages: ease of insertion during the surgical procedure and improved contact with the neural tissue[173]. Minimally invasive surgical insertion is crucial for epiretinal prostheses, where having a large implant in order to cover a greater visual field would mean having to create a wider incision with associated risks. To overcome this issue, POLYRETINA is a foldable and injectable photovoltaic epiretinal prosthesis that can be safely delivered with a 5-mm size cut through the sclera and conform better to the curvature of the eye[37]. Accessibility is also an issue for cortical prostheses since most of the visual field is mapped in the interhemispherical area and the calcarine sulcus. The surgical procedure is just one aspect of the challenge. The prosthesis should conform to the shape and curvature of the cortical surface. Soft, flexible or conformable arrays like those developed for auditory brain stem stimulation could offer a potential solution to ensure better coverage of the target area[174]. An injectable ultra-thin electrode mesh could be a possibility to overcome the issue for an intracortical approach[175]. Besides, advancements from the material side should be followed by solutions for hermetic packaging to ensure robust isolation barriers over long periods[176].

### 1.5.2.2   Image processing and advanced encoding strategies

In general, a visual prosthesis is composed of a camera worn on glasses, capturing the visual information and sending it in real-time to a signal-processing unit that elaborates the translation of the image into a sequence of stimulation patterns. Visual information processing is an essential step to convert a visual scene into patterns of spatiotemporal stimulation[109]. Traditional computer vision approaches, such as edge detection, contrast enhancement, and difference of Gaussian, have been tested in retinal prostheses and proved limited usefulness in daily life[177–179].

Recent studies in healthy subjects under simulated prosthetic vision have investigated other solutions such as saliency detection and object recognition[180]. Saliency detection extracts a region or object of interest by computing from image features, and it can be divided into three types: feature-based, region-based and object-based. This method works efficiently for image or static object recognition tasks. However, due to the complexity of saliency calculation, real-time performance is the limiting factor for visual prostheses[181–184]. Machine learning approaches, such as convolutional neural networks[185] and deep learning[186,187], could recognise multiple objects in complex scenes, helping navigation, obstacle

avoidance and target object finding. A drawback of these methods is the high training cost required for good accuracy. Once the visual information has been pre-processed and features have been extracted, a personalised spatiotemporal stimulation strategy should be provided. Such a customised approach is needed because phosphenes maps are specific to each patient and might change over time. Machine learning could also play a role in optimising stimulation parameters to create more naturalistic electrical stimulation patterns, as shown for optic nerve[188] and cortical[189] prostheses. Last, the conceptual idea of multi-area cortical stimulation has been recently proposed to help create high visual acuity, colour and motor perception to provide a more naturalistic perception[98]. Combining machine learning and multi-area stimulation will require further experimental investigation and advancements from the hardware and software sides.

Similar to other neuromodulation therapies[190], researchers are also considering and exploring bi-directional and closed-loop feedback approaches for retinal[34,191–194] and cortical[100,195] prostheses. This combination would allow such prostheses to automatically adjust the stimulation parameters and improve the performance over time. Most of the image processing algorithms and the closed-loop approaches have been tested so far in-silico or in-vitro. The challenge for the future will then be to determine their efficacy in real-world settings. One additional parameter to consider when designing closed-loop feedback will be voluntary and involuntary eye movements. They have been shown to affect spatial localisation of the phosphene elicited by electrical stimulation of the retina[196] and the medial occipital lobe[101], even after years of blindness.

### 1.5.2.3   Wireless power and data transmission

Neurostimulation has been routinely performed with electrodes wired to an electric pulse generator. Leads-wires breakage is common[46] and leads to malfunctioning or not functioning of the device. Moreover, cables and connectors apply mechanical forces on the implant and the tissue, causing long-term scarring[197]. New methodologies of wireless modulation of the nervous system have recently started to gain attention.

Photovoltaic technologies have emerged to provide artificial vision in retinal implant recipients[48]. It is a convenient strategy for retinal prostheses as the retina is specifically made to absorb light entering from the pupil[17]. In particular, new developments in organic bioelectronics and photovoltaics showed superior features in conformability, flexibility and stretchability[37] compared to silicon-based technology. One important key factor to consider in organic photovoltaics technology is the light conversion efficiency of the materials. It is necessary to find efficient materials to reduce the electrode size and offer better resolution while maintaining a sufficient output current for stimulation[167]. While photovoltaic prostheses[37,48] rely only on passive light-to-charge conversion from projected images, the NR600 implant (Nano Retina, Rainbow Medical Group) uses infra-red laser light projected onto photovoltaics elements to power an image detector collecting natural light from the eye optics and a processing unit converting the image into patterned electrical stimulations.

While light-based technologies are convenient for retinal implants,they are not well suited for other visual prostheses which do not have a natural transparent window to light. Thus, other wireless data and power transfer solutions can be used[197].

Among the approaches under investigation, inductive power transfer seems to be the preferred solution for high-resolution intra-cortical stimulation[198] due to the small distance between the transmitter and the receiver. The GENNARIS system (Monash Vision Group) uses inductive power transfer from a single transmitter coil to transmit data and power to 11 implanted receiver with 43 electrodes each[105].

### 1.5.3   Biological challenges

Another significant limiting factor for better artificial vision is the insufficient understanding of the neural visual code in blind individuals and the effect of visual deprivation and plasticity[199].

In general, a prosthesis is validated for its efficacy in animal models. However, it remains unclear whether experimental animals are appropriate models to predict efficacy in humans. Preclinical trials are performed either on sighted[73,100,200–202] or blind[128,203] animal models. Even when blind animal models are used, it is difficult to establish how well they reflect human diseases. For example, most of our knowledge comes from rodents with genetic mutations leading to an RP-like form of blindness. These rodents show a significant remodelling of the retinal circuits after photoreceptor degeneration[204]. Yet, there are divergent opinions about the integrity of retinal circuits in humans. While some studies reported their anatomical and functional preservation[205,206], others highlighted the remodelling and reorganisation of the synapses, particularly in RP patients, but also in advanced dry forms of AMD[207–209]. In addition, the extent of retinal remodelling might be extremely variable from patient to patient. Variability could also be found in the residual oculomotor behaviour, cellular preservation along the visual pathway, and remaining neuroplasticity. Last, motor strategies, mental representations and associative perceptions that can be affected by visual field loss[210,211] are impacted by each patient's history of blindness[121]. For example, in patients affected by retinal degenerations, the synaptic reorganisation might jeopardise the efficacy of the electrical stimulation[124–127]. Given the unpredictable nature of these plastic events, if stimulation parameters are not adapted accordingly, they might distort evoked phosphenes. Therefore, candidates for visual prostheses must be carefully screened. Among other criteria, the selection for retinal prostheses is based on retinal imaging to verify structural integrity[153] and corneal stimulation with lens electrodes to verify the retinal excitability[120,130,153]. Additional criteria should be considered since these tests are not informative on the functional preservation of the retinal circuits.

The success of visual prostheses strongly depends on our understanding of the adaptive and compensatory changes occurring within the brain[212] and the role of perceptual learning. Psychophysical testing and personalised visual rehabilitation strategies should be challenged to improve the outcome of artificial vision. In addition to measures of quantitative visual func-

tion such as acuity, field size, motion detection and localisation, other measures of qualitative functional vision will also be required for a more accurate depiction of a person's abilities with a visual prosthesis. These are commonly described as orientation and mobility or activities of daily living[46]. The downside of these tests is the limited translatability out of a controlled laboratory environment. On the other hand, it is hard to evaluate real-world functional assessment and self-reports due to their highly subjective and non-standardized nature[213]. Virtual, mixed and augmented reality could help create virtually controlled but highly complex environments[61,214]. These simulations can be helpful to gain an insight into what would be the real-world performance for an implanted subject. Augmented reality settings simulating prosthetic vision could help compare the accuracy of virtual reality prediction and patient performance. Additionally, the cognitive fatigue reported so far by users has discouraged them from using the implant long-term[213]. Hence, this mental effort should also be included in a standardised evaluation by mapping body movements, head scans[157], eye movements, decision time and pupillary measures[215].

Finally, designing a multisensory rehabilitation based on gamification in the short-term[121] and supported with a pharmacological enhancement of synaptic plasticity through serotonin uptake inhibitors administration[216–218] could also improve the capacity of patients to make practical use of their devices in the long-term.

## 1.6   Road to market: what to learn from the first generation of clinically approved visual prostheses

In the last 30 years, significant efforts have been made to develop and commercialise visual prostheses. However, the only systems currently approved for clinical use target the retina and patients affected only by RP. These are the Argus® II (Second Sight Medical Products Inc), the IRIS® II (Pixium Vision SA) and the Alpha-IMS/AMS (Retinal Implant AG). None of them are still on the market. The number of people affected by RP is estimated to be about 1.5-2 million[219], but only 12% of these have a visual acuity worse than counting fingers and 0.5% have no perception of light[220]. So far, retinal prostheses have been implanted in end-stage RP patients which are not enough to make a profitable market[221]. The potential market size is also drastically reduced considering that some of these patients might have other complications leading to exclusion according to criteria set for each device. Companies have had to face economic problems related to limited market size, cost of research and development, regulatory approval, and low acceptance of the device by clinicians and patients[222]. Second Sight Medical Products leveraged the existing Argus® II technology and developed Orion I, a surface grid for subdural stimulation of the primary visual cortex. Orion I has been accepted as a breakthrough device by the FDA and has already been tested in 6 completely blind subjects for 19 months with positive outcomes. Pixium Vision focused on the PRIMA device to address geographic atrophy in AMD patients[48,50]. Two early feasibility studies are active in Europe and the United States of America simultaneously. This double strategy must comply with two different regulatory approval procedures, one from the FDA and one for CE certification in

Europe[222].

Medical device regulation is another crucial step for any kind of neuroprosthetic device. It has been implemented to protect patients' safety by using only sufficiently tested devices before entering the market. Currently, the FDA offers pre-submission processes that allow early dialogue with the assessment body and simplify the path for innovative devices. On the other hand, Europe has not yet defined streamlined processes to obtain the CE mark for complex devices such as visual prostheses, even though new regulations have been implemented since 2020[222].

The device cost needs to be discussed to make visual prostheses available while keeping the company profitable. The Argus® II ranged from 115'000 EUR in Europe to 150'000 USD in the United States of America, excluding surgery, hospitalisation, and rehabilitation. A patient implanted with the Argus® II estimated that the total cost of device, surgery and rehabilitation was 497'000 USD[223]. Companies should therefore find agreements with insurances or governments to reimburse these costs, provided that the benefits for visual prosthesis recipients lead to a tangible reduction in health care costs[47].

Finally, Second Sight Medical Products and Retinal Implant AG discontinued their products. The Argus® II was approved for clinical use in many countries with more than 350 users worldwide. The device is now obsolete, and users declared not having technical support if their implant will stop working[221]. Despite being justified by financial elements, this outcome remains ethically unacceptable and solutions must be found to ensure clinical and technical support to existing patients. Nevertheless, several groups continue to run successful clinical trials[79] and pursue commercial development. Despite the long, unpredictable and costly road to market, they could take advantage of this favourable moment in which neurotechnology is receiving great financial attention. Neurotechnology is a rapidly growing field, with several new companies entering the business. Unfortunately, not all these companies will succeed. Learning from previous experiences will help neurotech entrepreneurs to develop a sustainable business.

## 1.7   Conclusion

Restoring vision is the grand challenge that many research groups and companies are trying to solve. Although remarkable engineering progress has been made since the very first prototype of a visual prosthesis[86], results from the clinical use of commercially available retinal prostheses showed that for now, patients affected by retinal degeneration could only expect a form of vision substitution (artificial vision) rather than vision restoration[213].

Visual prostheses should provide higher resolution and wider angle to substantially help the patients to perform daily activities autonomously. This goal includes reducing the electrode size and finding biomimetic materials so that wireless electronics can be physically embedded within the neural tissue for a long-term period. Artificial intelligence can play a relevant role

by advancing image processing and encoding steps to fine-tune the stimulation parameters towards a more naturalistic perception. Moreover, prostheses might learn to adapt in a contextually dependent manner and provide the patient information in the most helpful and accurate way possible. The ability to artificially produce a visual perception in blind individuals lies in the present understanding of the visual system, its processing units, and how electrical stimulation along the visual pathways can elicit visual sensations. Undoubtedly, a deeper understanding of the functioning of the visual system in blindness is crucial knowledge to design better visual prostheses. Fundamental neuroscience research in animal models and humans is necessary to close significant knowledge gaps, including understanding the role of visual plasticity and neurorehabilitation, determining the impact of retinal remodelling and deciphering the neural code to restore vision in blind subjects. The combination of these elements will make artificial vision closer to vision.

To accomplish this mission, interdisciplinary teams of clinicians and healthcare providers, materials scientists, engineers, neuroscientists and artificial intelligence experts will have to work hand-in-hand towards the next generation of visual prostheses. Lastly, the joint effort of regulatory bodies in streamlining the approval processes for innovative technologies and investors helping to close the gap from research to market will be essential to make the artificial vision a sustainable solution for those patients still in the dark.

Artificial vision has always been a pioneering research activity in the medical field. Charles LeRoy performed his experiment three decades before Luigi Galvani reported about animal electricity. One of the first permanent cortical stimulators implanted in humans was a visual prosthesis[87]. The Argus® II[110] was among the first implantable microelectrode arrays manufactured with cleanroom processes to be approved by regulatory agencies. The subretinal visual implant Alpha IMS[149] was one of the first CE-approved implantable medical devices with a high-channel-count (1500 pixels) and implantable electronics in contact with the central nervous system. Photovoltaic retinal prostheses[48] were the first example of neurostimulation devices providing fully wireless electrical stimulation to the nervous system without the need for implantable batteries or active electronic units. Certainly, research in visual prostheses will push neurotechnology even further.

## 1.8   Acknowledgements

from Wikipedia/Wikimedia and/or the copyright owner (as appropriate) before using or forwarding the images.

# 2 Thesis scope

**Chapter 1** provided the reader with a general overview of the visual prosthesis landscape, familiarity with the biological system and the common obstacles faced by this field within research and industry. Among the strategies to restore artificial vision described in the previous chapter, this thesis will focus on optic nerve stimulation. The following paragraphs will provide an in-depth description of optic nerve (ON) anatomy and a short overview of interfaces for nerve stimulation with particular attention on the OpticSELINE, the first intraneural electrode array for optic nerve stimulation, and its limitations. The last paragraph will outline the objectives of this thesis which, in summary, aims at developing materials and strategies to improve ON stimulation with an intraneural electrode array approach.

## 2.1 The optic nerve anatomy

The optic nerve is the highway that connects the retinal network and the brain. It has a cylindrical structure and is 35 to 55 mm long containing on average 1 million axons of RGCs[224,225]. Additionally, there are three types of glial cells (non-neuronal cells) that can be found within the optic nerve: oligodendrocytes, that are responsible for the myelination of its axons; astrocytes, providing support to the neural tissue and contributing to create fascicle of RGCs fibers[225–228] and; microglial cells, playing a protective role in case of neural damage[229–232]. The number of fascicles can vary between 400 and 600 depending on the position along the optic nerve[233].

The optic nerve can be divided into four main segments (Figure 2.1a). The optic disc segment, which measures 1 mm in length, is located where the unmyelinated RGC axons exit the

eyeball through a hole in the sclera. This area is filled with a sieve-like structure called the lamina cribrosa (LC) made out of several layers of intermingled collagen fibers. These are mechanosensitive cells that are affected by pressure changes and can cause the fiber nerve damage that occurs in glaucoma[234]. The second one is the intraorbital segment, which extends backwards from the back of the eye to the optic canal for about 25 mm. Here the axons become myelinated, doubling the diameter of the nerve from 1.5 mm to 3 mm. In this tract, the central retinal artery and the central retinal vein enter the optic nerve making it a vulnerable spot in cases of raised intracranial pressure[225]. After the intraorbital segment, the optic nerve passes through the optic canal, forming the intracanalicular segment whose length can vary between 4 to 10 mm. The final 10 mm of the nerve represents the intracranial segment, which is also the least affected by stresses due to eye movements given its position after the optic canal[233]. The optic nerves of both eyes end by meeting at the optic chiasm. Depending on the species, a different portion of optic nerve axons will decussate and combine with the fibers of the opposite eye. In humans and other vertebrate species with a very large binocular visual field, approximately 55% of the fibers crosses the optic chiasm while the remaining 45% continues on the same side (Figure 2.1b)[235,236]. Differently, in species with lateral eyes, such as rodents or rabbits, between 90% and 99% of the fibers decussate and combine with the other side[237] (Figure 2.1c).
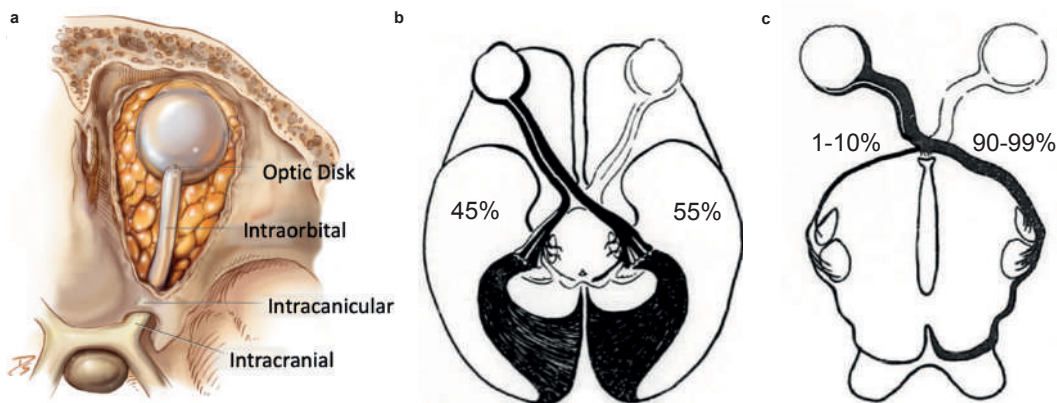


Figure 2.1: (a), Optic nerve's four different anatomical segments: optic disc, intraorbital, intracanicular, and intracranial segments. Segment lengths are respectively approximately 1, 25, 7, and 10 mm long. Adapted from Atlas of Endoscopic Sinus and Skull Base Surgery, 2nd edition, 2019[238]. (b), and (c), Percentage of optic nerve fibers decussation at the optic chiasma for primates and rodents respectively. Adapted from Webvision[239].

Comprehending the visual field map, or retinotopy, of the anatomical target chosen to provide artificial vision is critical when designing a visual prosthesis. Several studies[240–243] have demonstrated that in primates, due to the presence of the fovea, the axonal fibers originating from the macula enter the optic nerve through the temporal side (Figure 2.2a). Therefore, the axons originating from the superior and inferior temporal retinal quadrants enter through the

upper and lower temporal side, while those originating from the nasal retinal quadrants enter through the optic nerve nasal side. The axon's organization gradually shifts toward a central position of the macula by the time the optic nerve reaches the chiasm (Figure 2.2a). Thus it is assumed that in this segment the optic nerve exhibits a retinotopic organization. In addition, the representation of the macular area occupies a greater portion of the optic nerve compared to the periphery, given that 90% of the total number of axonal fibers that constitute the optic nerve originate from the macular area[244]. On the other hand, the spatial organization of the optic nerve of rodents and rabbits has received less attention hence this knowledge is sparse. Regarding rats and mice, it appears that the retinotopy is conserved in the first portion of the optic nerve but lost after that[245,246].

While for rabbits, according to what Lashley reported in 1930 about a study published by Brouwer in 1923[247], fibers might be roughly organized in a retinotopic manner where axons coming from different quadrants of the retina are grouped in corresponding quadrants of the nerve. However, it is unsure whether this is true throughout the length of the nerve. In addition, rabbits lack the presence of the fovea region. They have instead a visual streak (Figure 2.2b) which is a narrow horizontal band that presents high density of RGCs from the nasal to temporal side while steeply decreasing in the vertical direction[248]. The cortical representation of the contralateral visual streak in V1 is asymmetric and does not match the temporo-nasal distribution of the retinal ganglion cell[249]. In fact, the representation of the central and temporal area of the visual streak is located in the tentorial surface, while the nasal end occupies a larger cortical area extending mostly anteriorly (Figure 2.2c).

## 2.2 Overview of interfaces for nerve stimulation

Different approaches have been attempted to stimulate the optic nerve by using peripheral nerve interfaces (PNIs). Conventional PNI designs, represented in Figure 2.3a, are commonly categorized based on invasiveness and selectivity and are thus divided into extraneural and intraneural. Extraneural implants, like cuff electrodes, are a minimally invasive solution since they merely surround the nerve's epineurium and interact with the outer regions of the nerve. Despite this, selectivity is limited due to a large distance between electrodes and axons located in the center of the nerve. Intraneural interfaces instead penetrate the nerve so that the active sites are closer to the fibers. While this allows for a more intimate contact, the penetration also disrupts the nerve fibers and triggers a foreign body reaction.

### 2.2.1 Epineural electrodes

Nerve cuffs have been an effective early strategy to chronically record and stimulate nerve activity from the surface. The implant consists of a cylindrical polymer film that is wrapped around the nerve, with the electrodes contacting the nerve tissue. Although they are the least invasive, they lack fiber-level selectivity, especially towards the center of the nerve, where fibers have higher activation threshold than the ones in the periphery closer to the electrodes[251].
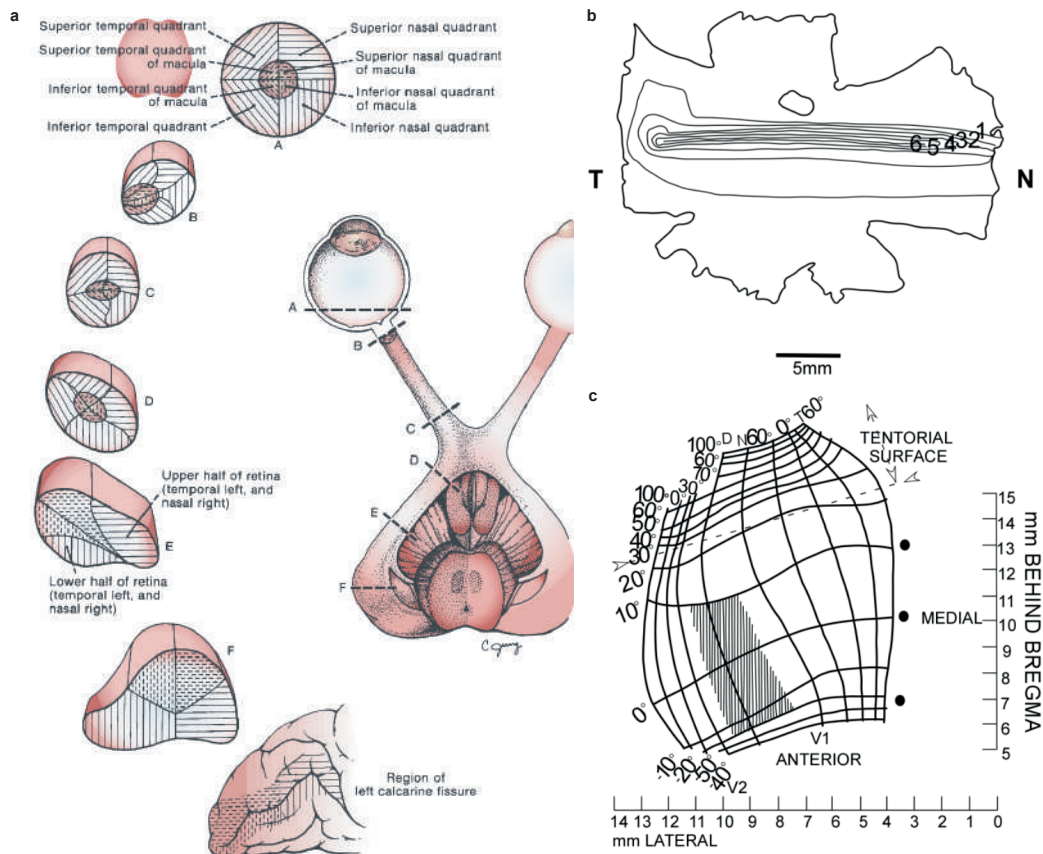
Figure 2.2: (a), Location of visual fibers from the four retinal quadrants and macular area in the optic nerve, optic tract, LGN, and occipital cortex. From DeJong's the Neurologic Examination[233]. (b), Ganglion cells isodensity lines in the retina of the rabbit. Isodensity line numbers indicate the distribution of ganglion cells x 103. From Picanço-Diniz et al., 2011[250].(c), V1 visual field representation in the rabbit. Binocular field is indicated by hatched area. From Picanço-Diniz et al., 2011[250]. T: temporal; N: Nasal.

Flat-interface nerve electrode (FINE) is an advanced form of cuff electrode that by forcing the nerve to remodel into a flatter non-circular configuration improves the selectivity of the stimulation[252]. Although fascicles are closer to the electrode sites since they spread out in the nerve when this is flattened, this reshaping could cause nerve damage.

### 2.2.2 Intraneural electrodes

Two types of flexible thin film-based intraneural electrodes have been developed, the longitudinal intrafascicular electrode (LIFE) and the transverse intrafascicular electrode (TIME). Unlike extraneural electrodes, LIFE and TIME penetrate through the nerve membranes making them in direct contact with the axons. They consist of a double side electrode array based on a PI substrate that is pulled longitudinally or transversely through the nerve using a needle with a

loop of suture thread[75]. These configurations allow better selectivity and a lower stimulation threshold[253]. On the other hand, potential movements of the electrodes within the nerve could affect fiber recruitment during stimulation and recording capabilities on a long-term scale. The highest selectivity in peripheral nerve stimulation and recording is obtained with the Utah slanted electrode array (USEA). This interface is characterized by high microprobe density. By penetrating the nerve, it can place a large number of microelectrodes at multiple depths adjacent to different fibers[254]. The high invasiveness and the use of materials that are stiffer than the nerve tissue makes the USEA less suitable for chronic implantation.
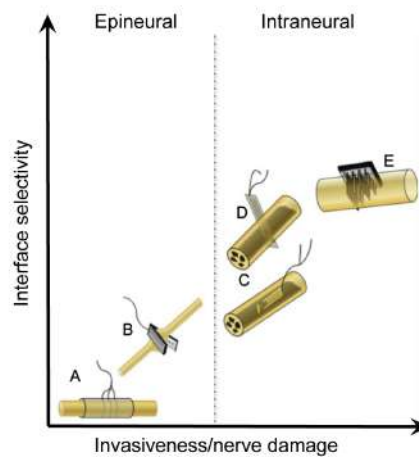


Figure 2.3: (a), Peripheral nerve interfaces classified according to their invasiveness and selectivity. Sketches are representative of the cuff electrode (A), the FINE (B), the LIFE (C), the TIME (D), and the Utah slanted array (E). Adapted from Del Valle et al., 2013[255].

*Self-opening intraneural electrode (SELINE)*

The self-opening neural interface (SELINE) has been developed as an evolution of TIME electrodes to prevent relative movement of the active sites and reduction of the signal-to-noise ratio when it increases the distance between electrodes and axons due to implant motion or interposition of scar tissue[256]. In fact, the novelty of this neural interface is the three-dimensional geometry. On each side of the electrodes, there are two wings with active sites that open out within the tissue. After insertion through a needle, the flexible polyimide-based structure is gently pulled back to open the wings and anchor them. This three-dimensional geometry has two advantages that have been demonstrated in-vitro and in-vivo. It increases mechanical stability of the electrode (extraction force tests and evaluation of the response from stimulation) and provides access to more axons inside the nerve[256]. Furthermore, Wurth et al. demonstrated functionality and bio-integration of a SELINE implant in the peripheral nerve environment over extended durations (6 months) in rodents[257].

## 2.3   Optic nerve stimulation state of the art

In 1998, the group led by C. Veraart was the first to propose a prototype optic nerve prosthesis in humans[64]. They implanted a 4-contact self-sizing spiral cuff epineural electrode in the intracranial segment of a blind subject suffering from retinitis pigmentosa. The stimulation protocol consisted in charge balanced single pulses and pulse trains applied mono- or bipolar between two contacts of the cuff. After few months of training, the patient was asked to describe the phosphene characteristics, such as shape, number of dots, color, dimensions, etc. The results showed a good retinotopic correspondence between the quadrant of the visual field in which the phosphene was perceived and the contact of the cuff electrode used for a given stimulation. Moreover, the reported position of the phosphenes covered a significant portion of the visual field, about 85° vertically and 60° horizontally. Thus, they proved that the optic nerve stimulation could potentially be used to elicit phosphenes in the whole visual field with some degree of selectivity. In 2000, the same group performed a second study on the same patient. The results showed that the patient was able to distinguish line orientations as well as shapes and symbols despite using only 4 electrodes[65,66]. However, the greatest drawbacks of this epineural approach is that phosphenes are irregular in shape and localization.

Sakagushi et al.[69] also conducted a study in human, but using three platinum wire electrodes implanted in the optic disk of the patient. The results showed that they were able to elicit phosphenes in three clearly distinct positions for each electrode. This suggests that a better control on the phosphene's characteristic can be achieved while stimulating in closer contact with the targeted tissues[69].

Following this approach, the C-Sight project is testing an optic nerve prosthesis to stimulate the intra-orbital region with a 4-filament electrode. They employ penetrating platinum-iridium electrodes that have been implanted and assessed in acute experiments on rabbits and cats[70–72].

*Self-opening intraneural electrode for optic nerve stimulation (OpticSELINE)*

Despite the promising results, these type of implants are too stiff with respect to the nerve tissue inducing a large mechanical mismatch and making them unsuitable for chronic implantation. Great efforts have been made in our group to optimize a surgical procedure to implant a modified version of the previously described SELINE electrode array[256,257], called OpticSELINE[73] (Figure 2.4a), for the stimulation of the optic nerve. The OpticSELINE is a flexible polyimide-based structure with twelve stimulating electrodes (six electrodes per side, area of 0.008 mm2) in the active area. Each wing carries two electrodes (two wings per side) and two more electrodes are located on each side of the main body. The dimensions of the OpticSELINE were chosen in accordance with the anatomical structure of the rabbit optic nerve. In this study, electrical and mechanical characterization of the implant was performed, followed by optimization of the stimulation parameters, such as pulse width and duration, to allow flexibility in stimulation paradigms.

By changing the current amplitude, it was also possible to modulate the magnitude of the cortical activation (Figure 2.4c and d) recorded with an ECoG array placed on the primary

visual cortex (Figure 2.4b). In addition, a classification algorithm showed that some components of the ECoG signal originating from the stimulation through different electrodes were meaningfully distinct, suggesting that the electrical stimulation indeed stimulates different portions of the nerve. In fact, most of these meaningful components are segregated in a small portion of the optic nerve, localized around single electrodes or in some cases a few neighboring ones (Figure 2.4e). However, spatial shifts of the cortical activity upon stimulation with different electrodes were not found.
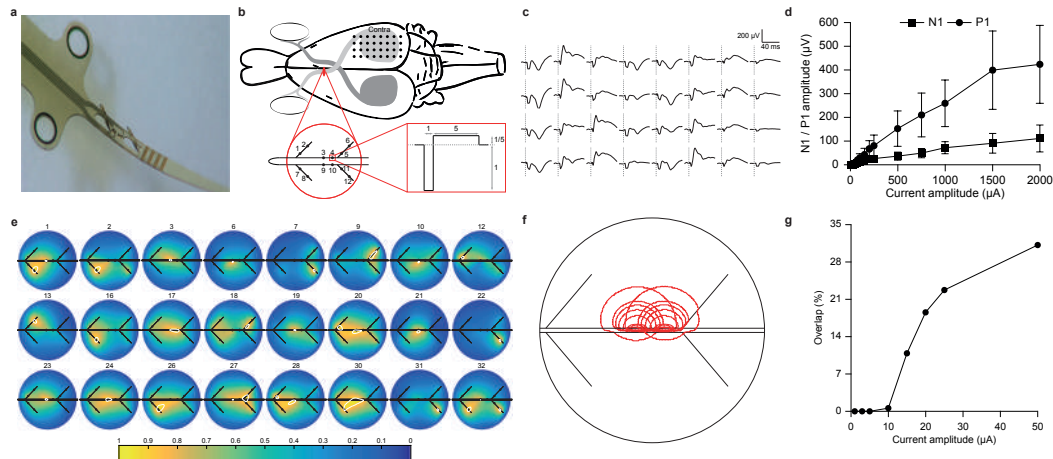


Figure 2.4: (a), Magnified view of one side of the OpticSELINE, showing the active area with the two wings, the six electrodes and the alignment bars. (b), Schematic diagram (top view) of the placement of the ECoG array (black dots) over the rabbit visual cortex and the OpticSELINE in the rabbit optic nerve (red dot). The electrodes are labeled with a number and the enlarged red box shows the biphasic current pulse used in the stimulation protocol. (c), Example of electrical evoked potentials (EEPs) to a current pulse of 250 μA and 150 μs delivered from electrode 4. The dashed lines represent the stimulus onset. (d), Mean N1 (squares) and P1 (circles) for current pulses of 150 μs as a function of the current amplitude. (e), Individual distribution maps of each meaningful component (visible meaningful activation) of the ECoG signals within the optic nerve. Representative example from N = 1 rabbit with a current amplitude of 750 μA. (f), Overlay of the activated area with a probability higher than 90% at increasing current amplitudes for two neighboring electrodes. The higher the current, the greater the overlapping activated area. g, Percentage of overlap of the activated areas from two neighboring electrodes as a function of the current amplitude. All images are adapted from Gaillet et al., 2020[73].

A powerful tool to better understand and predict the effect of new electrode's designs and operating mechanisms inside nerves is the combination of mathematical models of neurons and finite element analysis (FEA) of the implant as also shown in studies on peripheral nerve stimulation[258–260]. In fact, measuring the fiber recruitment during in-vivo stimulation of ON is a challenging task, a hybrid FEA numerical model and NEURON simulation environment was implemented to obtain the activation probability of the fibers located around a stimulating electrode. The model showed that internal and external fibers could be activated, however,

upon stimulation of two neighboring electrodes, the activated areas started fusing above amplitude currents of 10 μA (Figure 2.4f and g). Hence, this limits the dynamic range of the intraneural stimulation requiring a different strategy to enhance selectivity.

## 2.4 PNIs Challenges

### 2.4.1 Selectivity

Selectivity in PNIs can be classified as functional and spatial[261]. Small fibers require a higher current threshold for activation compared to big ones[262]. Consequently, larger fibers are also activated when targeting smaller ones. Current methods to functionally select diameter-specific fibers include optimized stimulation waveforms[262] and high frequency stimulation to block fiber activation[263,264]. The latter was also tested with the OpticSELINE and showed that at 1 kHz the N1 threshold was reduced[73].

Spatial selectivity, instead, refers to the ability to stimulate axons in a predefined and limited volume[75]. A possible solution could be to increase the number of active sites along the interface, however this comes with technical and physical barriers, such as reducing the electrode size, affecting impedance, and crosstalk. To work around these limitations, multipolar configurations can be exploited to achieve localized stimulation. Examples of such an approach have been shown in cuff electrodes where tripolar configurations can target more superficial fascicles[265–267]. Despite numerous tests in extraneural implants, no multipolar electrodes have been tested on intraneural interfaces thus far.

### 2.4.2 Foreign body reaction (FBR)

As also seen in **Chapter 1**, the choice of materials and fabrication methods employed for neural interfaces is key in obtaining safe, reliable and long-term functionality. Selectivity risks being worsened by the FBR as threshold currents increase over time due to the growing scar tissue interposed between electrode and axons[75]. Static and rigid implants are not suitable for following the natural micro- and/or macroscopic motion of the neural tissues. This is why there is a surge in research into more compliant materials that aim at causing minimal growth of inflammatory tissue. A promising approach involves the manufacturing of soft and stretchable electrically conductive composites embedded in an elastomer matrix[268–271]. So far, the most common material used for fabrication of PNIs is PDMS. However, it presents challenging steps in the microfabrication process, especially for the encapsulation of the active sites. This is particularly relevant in applications where reducing electrode size is important to enhance selectivity but space is limited, as for the OpticSELINE.

### 2.4.3 Longevity

The long-term viability of intraneural electrode arrays is still an open question. Numerous examples of longevity in extraneural electrodes in-vitro and in-vivo have been published, however, only fewer are available for implants such as TIME or SELINE[75]. Before reaching FDA or CE mark for these implants, issues of delamination, corrosion, and swelling need to be addressed. PI is the most common material used so far for intraneural electrode arrays and different groups have started to address the delamination issue by using Si-C[272,273].

Advancements in materials for neural implants will help in optimizing future optic nerve prostheses. The ability to control the size of the activated portion of the nerve as well as the type of fibers will be very useful to design efficient image reconstruction algorithms and therefore effective patterns of stimulation. Optic nerve prosthesis will most probably lack high-density distribution of electrodes, as compared to retinal implants due to anatomical constraints. This is why it is unlikely that the image reconstruction algorithms implemented for an optic nerve prosthesis will be based on image pixelation. Instead, spatial and functional selectivity will help to create a combination of phosphenes of various sizes and shapes for a higher quality of artificial vision.

## 2.5 Thesis structure

In light of the promising results obtained with the OpticSELINE, we decided to address some of the limitations presented in our first version of the implant. Thus, the general objective of this thesis and so the "fil rouge" of the following chapters is the investigation of stimulation strategies and materials to improve the outcome of ON prostheses and make them one step closer to a viable option for blind patients. In addition, the findings reported here could also be relevant for other applications in the field of neuroprosthetics.

**Chapter 3** (Figure 2.5a) will propose an advanced way to analyze visual evoked potentials (VEP) and electrical evoked potentials (EEP) by using two machine learning algorithms, a classifier based on a support vector machine (SVM) algorithm and a linear regression model based on a wide variety of features, instead of the commonly used P1 peak extracted from the ECoG signal traces. These approaches allowed us to demonstrate that the cortical activities elicited by the electrical stimulation of ON were indeed distinct. In addition, such machine learning algorithms could be useful to evaluate new optic nerve implants prototypes and patterns of stimulation.

**Chapter 4** (Figure 2.5b) will introduce an intraneural electrode array, designed to enhance spatial selectivity in ON. Taking inspiration from the field of retinal prosthesis, we developed a 3D concentric bipolar electrode configuration. This design confines the electrical field generated by the stimulation and it saves space given that the feed lines are on two separated layers. Thus, it is especially convenient for intraneural electrodes like the OpticSELINE where there is a clear spatial constraint. Therefore, we first assessed in-silico the number of activated

fibers with monopolar and bipolar stimulation. We then optimized the fabrication process for bilayer electrodes arrays, previously developed by[274] to include the 3D concentric bipolar configuration and characterized the electrochemical properties before in-vivo experiments. Finally, we compared the spreading of cortical activation between monopolar and bipolar stimulation.

In **Chapter 5** (Figure 2.5c), a proof of concept study using off-stoichiometric thiol-ene epoxy (OSTE+) thermosets to fabricate a conformable and compliant ECoG array will be presented. Such polymers have first been developed for rapid prototyping of microfluidic chips less permeable to gas in alternative to PDMS[275]. They are photo-patternable and, by adjusting the stoichiometry of the constituting monomers, the Young's modulus can be decreased down to a few MPa. Given these properties and their biocompatibility, they offer an alternative to poly(dimethylsiloxane) (PDMS) and polyimide (PI) substrates for neural interfaces. In this chapter, we described the mechanical properties of OSTEMER 324 Flex (OSTE+ Flex), chosen for its flexible and deformable behavior. Taking advantage of its good adhesion to metal and compatibility with established wafer-scale technologies, we designed and optimized a process-flow to fabricate a conformable, transparent multilayer ECoG. The study will be concluded by acute in-vivo experiments and biocompatibility tests over 6 weeks after implantation. These promising results can open the way to the introduction of OSTE+ Flex as substrate and encapsulation material for intraneural electrode arrays for optic nerve stimulation.

More recently, additive manufacturing has started to become an attractive solution for neural interfaces[276]. The work presented in **Chapter 6** (Figure 2.5d) shows the fabrication of the first all-printed electrocorticography arrays made by inkjet printing of platinum and screen printing of polyimide. Mechanical and electrical characterization of the multi-electrode array (MEA) is provided along with in-vivo evaluation of the recording performances. These technologies that so far have been mostly used for wearable flexible applications[277] hold the potential to increase the versatility of designs, accommodate large area processes and be cost-effective. Considering the current version of the OpticSELINE is a polyimide-based looped electrode array, ink-jet printing on large flexible PI foils could help in designing double-side implants without the need of using wafers bigger than 4 inch that are usually less suitable for non-industrial clean-rooms. Thus, with improvements in feature resolution, ink-jet printing of metallic conductors could be used for applications such as the OpticSELINE.

Finally, a conclusion chapter, **Chapter 7**, summarizes the achievements and reports the limitations and future perspectives of the developed technologies.
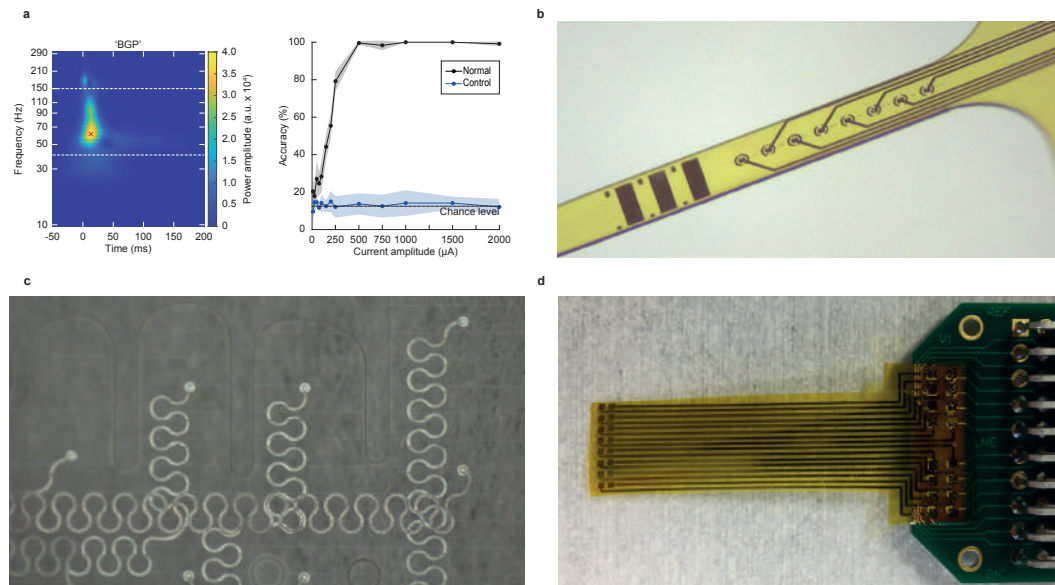
Figure 2.5: (a), Left: Broad gamma power (BGP) response upon electrical stimulation in one recording channel. Right: average classification accuracy as a function of the stimulation current amplitude of all the electrodes. From Gaillet et al., 2021[63]. (b), Picture of the Flat OpticSELINE active area with 8 3D concentric bipolar electrodes (central electrodes with 40 μm diameters) from Borda et al., 2022[74]. (c), Picture of one side of the conformable OSTE+ Flex ECoG array (electrodes are 40 μm in diameter). (d), Picture of the all-printed (PI/Pt) ECoG array (electrodes diameter of 250 μm) connected to a printed circuit board (PCB) from Borda et al., 2020[278].

# 3 A machine-learning algorithm correctly classifies cortical evoked potentials from both visual stimulation and electrical stimulation of the optic nerve

Authors: Vivien Gaillet[1], Eleonora Borda[1], Elodie Geneviève Zollinger[1], and Diego Ghezzi[1]

[1] Medtronic Chair in Neuroengineering, Center for Neuroprosthetics, Institute of Bioengineering, School of Engineering, École Polytechnique Fédérale de Lausanne, Switzerland

## 3.1  Abstract

*Objective.* Optic nerve's intraneural stimulation is an emerging neuroprosthetic approach to provide artificial vision to totally blind patients. An open question is the possibility to evoke individual non-overlapping phosphenes via selective intraneural optic nerve stimulation. To begin answering this question, first, we aim at showing in preclinical experiments with animals that each intraneural electrode could evoke a distinguishable activity pattern in the primary visual cortex.

*Approach.* We performed both patterned visual stimulation and patterned electrical stimulation in healthy rabbits while recording evoked cortical activity with an electrocorticogram array in the primary visual cortex. Electrical stimulation was delivered to the optic nerve with the intraneural array OpticSELINE. We used a support vector machine algorithm paired to a

linear regression model to classify cortical responses originating from visual stimuli located in different portions of the visual field and electrical stimuli from the different electrodes of the OpticSELINE.

*Main results.* Cortical activity induced by visual and electrical stimulation could be classified with nearly 100% accuracy relative to the specific location in the visual field or electrode in the array from which it originated. For visual stimulation, the accuracy increased with the separation of the stimuli and reached 100% for separation higher than 7 degrees. For electrical stimulation, at low current amplitudes, the accuracy increased with the distance between electrodes, while at higher current amplitudes, the accuracy was nearly 100% already for the shortest separation.

*Significance.* Optic nerve's intraneural stimulation with the OpticSELINE induced discernible cortical activity patterns. These results represent a necessary condition for an optic nerve prosthesis to deliver vision with non-overlapping phosphene. However, clinical investigations will be required to assess the translation of these results into perceptual phenomena.

## 3.2  Introduction

Blindness is a medical condition impairing the quality of life of the affected people and their relatives; hence it represents a high medical, economic and social cost for society. While therapies are available for several pathologies causing vision loss and blindness, some others currently have no treatment[279]. Among these diseases, retinitis pigmentosa is a set of inherited retinal rod-cone dystrophies with a prevalence of about 1:4,000 individuals causing the progressive loss of rod photoreceptors, loss of night vision and the constriction of the visual field (tunnel vision), later followed by cone dysfunctions and eventually profound blindness[280]. The degeneration of retinal photoreceptors characterises retinitis pigmentosa. Consequently, the other retinal neurons (i.e. bipolar cells, amacrine cells and retinal ganglion cells) are generally considered to be preserved and to form a functional network that can be activated via electrical stimulation evoking the sensation of discrete points of light called phosphenes. Artificial vision is the perception of the world using an ensemble of these phosphenes. Retinal prostheses have been extensively investigated in animal experiments[37,124,126,127,281–283] and in retinitis pigmentosa patients to fight blindness[46,47,61]. However, none of these devices is available in clinics today, and the few that were available have been discontinued.

Large clinical studies with retinal implants in retinitis pigmentosa patients showed a large performance variability[284–286]. The number of functional electrodes able to elicit phosphenes with the Argus® II retinal implant was variable, as low as 5 out of 60[284]. Postoperative outcomes were also variable, from just phosphenes perception to object recognition and reading capability[284]. Similar variable outcomes were observed in retinitis pigmentosa patients implanted with the Alpha-IMS/AMS subretinal prostheses, ranging from just light perception to restoration of partial visual acuity[285]. Variable perceptual outcomes could be attributed to the advance stage of retinal degeneration. In late-stage retinitis pigmentosa patients, post-

mortem retina analysis revealed that 78% of bipolar cells and 30% of retinal ganglion cells are spared, while it was the case for only 5% of photoreceptors[205,206,287,288]. However, there are divergent opinions about the functional integrity of retinal circuits. While some studies reported the anatomical and functional preservation of retinal ganglion cells in both humans and animal models[205,289,290], some others documented the remodelling and reorganisation of the synapses in the inner nuclear layer[207,208], which might compromise the efficacy of electrical stimulation[204,291–293]. The deafferentation of bipolar cells caused by photoreceptors' death is followed by a negative plasticity period, which is not fully understood. Changes in synaptic connectivity might form aggregates of synaptic connexions between survival cells, known as microneuromas, which are presumably the source of the spontaneous retinal hyperactivity[204,292,294]. These plastic events might create connectivity loops, reducing the retinal excitability and impairing the ability to encode visual information with retinal implants[295]. Retinal network-mediated stimulation in retinitis pigmentosa patients is also subjected to rapid phosphene's fading due to static adaptation and bipolar cells' desensitisation[133,203]: a phenomenon requiring cognitively exhausting large head and body movements to counteract it. Therefore, bypassing the retinal network might be an attractive strategy to reduce the variability in retinal stimulation. One approach was developed by the AV-DONE project based on an intrapapillary electrode array[296,297]. A retinitis pigmentosa patient implanted with three wires reported the perception of distinguishable phosphenes upon stimulation of the optic disc[69].

Long-term mechanical stability of epiretinal prostheses is another critical element leading to an increase in the stimulation threshold associated with the increase of the electrode-to-retina distance[41,43]. Also, several exclusion criteria limit the eligibility for retinal prostheses, as appeared from enrolment criteria in several clinical trials, and here summarised: retinal detachment or trauma, sub-macular choroidal neovascularization, extremely thin conjunctiva, too small or too long axial length, corneal ulcers, abnormalities in the typical curvature of the retina, eyeball trauma, and corneal opacity or lack of optical transparency preventing adequate visualisation of the inner structures of the eye or impeding the correct placement of the device. Retinal prostheses might not be limited by all those criteria simultaneously since some of them might apply only to specific implants. However, optic nerve's direct electrical stimulation appears an attractive strategy to circumvent all the above-mentioned limitations in a single step. Another consideration is the restored visual angle. Previous studies pointed out that retinitis pigmentosa patients will benefit from the restoration of a wide visual angle[39,119]. Although some wide-field retinal prostheses are under development[37,123,128,129,298], optic nerve's stimulation is attractive because its relatively small diameter facilitates the electrical stimulation of a wide visual field.

Early studies on optic nerve's stimulation were performed in retinitis pigmentosa patients[65,299]. The first subject received a 4-contacts self-sizing cuff electrode around the intracranial segment of the optic nerve. Following psychophysical testing, the subject correctly identified basic shapes and character-like symbols, even if the phosphenes were reported as unstable, possibly due to the device's movement caused by the poor anchorage of the cuff electrode.

Following these results, the C-sight project proposed an optic nerve prosthesis based on a few (3 to 5) penetrating rigid and stiff microelectrodes and tested the concept in preclinical experiments[70,72]. An optic nerve prosthesis (OpticSELINE) was also proposed by our group[73]. Compared to other approaches, the OpticSELINE provides higher mechanical stability due to its three-dimensional anchoring wings, better mechanical compliance because of thin-film microfabrication on polymeric materials and higher electrodes' number because of the high integration capacity of cleanroom processes. Despite early clinical studies in humans[65,69,299] and preclinical experiments in animals[70,72,73], optic nerve stimulation is not mature yet for clinical use. Several technical improvements and validations are still required, such as electrode miniaturisation, increase of the electrodes' number and density, long-term biocompatibility assessment in the optic nerve and demonstration of localised and non-overlapping phosphenes when multiple electrodes are activated simultaneously or in rapid succession. A necessary, but not sufficient, step towards this latter goal is to show that the stimulation through different electrodes induces distinguishable cortical activity patterns, suggesting that different fibres of the optic nerve are recruited.

Preclinical studies in animals often rely on the peak-to-peak analysis of electrocorticogram (ECoG) recordings to determine the portion of the visual cortex activated by the stimulation. However, ECoG recordings with microelectrodes are often limited by low spatial resolution. A recent report found that the cortical tissue around an ECoG electrode that contributes to its activity is approximately 3-mm in diameter[300], most likely because of the volume conduction of the potentials. The mapping of spatially organised cortical activity patterns in relatively small animals could be hindered, if not prohibited, by this physical limitation. On the other hand, a previous study presenting letters to a rhesus monkey demonstrated that machine-learning algorithms might overcome this problem since they benefit from the information of the whole spectrogram of ECoG recordings[301]. Therefore, we propose a machine-learning approach not relying exclusively on the peak-to-peak amplitude but encompassing the whole signal spectrogram to correctly classify and predict the ECoG signal originating from patterned visual stimulation and optic nerve's intraneural electrical stimulation. First, we validated the algorithms using patterned visual stimuli. Then, we demonstrated that the cortical signals evoked by electrical stimulation from different electrodes of the OpticSELINE were correctly classified and predicted.

These results represent a leap forward for intraneural optic nerve stimulation towards an artificial vision. Also, this approach might have wide use in neuroprosthetics for the preclinical validation of visual prostheses and other sensory prostheses.

## 3.3 Materials and methods

### 3.3.1 Animal handling and surgery

Animal experiments were performed according to the authorisation GE519 approved by the Département de l'Emploi, des Affaires Sociales et de la Santé, Direction Générale de la Santé of the Republique et Canton de Genève (Switzerland). Female rabbits (>16 weeks, >2.5 kg) were premedicated 30 min before the transfer to the surgical room with an intramuscular injection of xylazine (3 mg kg$^{-1}$; Rompun® 2%, 20 mg ml$^{-1}$, 0.15 ml kg$^{-1}$), ketamine (25 mg kg$^{-1}$; Ketanarkon® 100 mg ml$^{-1}$, 0.25 ml kg$^{-1}$) and buprenorphine (0.03 mg kg$^{-1}$; Temgesic® 0.3 mg ml$^{-1}$, 0.1 ml kg$^{-1}$). Rabbits were left under 100% O2. 10 to 15 min after premedication, a 22G catheter was placed in the ear's marginal vein. Local anaesthesia was provided to the throat (Xylocaine 10%, spray push). The rabbit was intubated with a 3.5-mm tracheal tube with a balloon and ventilated (7 ml kg$^{-1}$, rate: 40/min, positive end-expiratory pressure: 3 cm of H20). Eye gel (Lacrigel) was placed on the eye to protect it from drying. Anaesthesia and analgesia were provided intravenously with propofol (10 mg kg$^{-1}$ $^{-1}$; 20 mg ml$^{-1}$, 0.5 ml kg$^{-1}$ h$^{-1}$) and fentanyl (0.005 mg kg$^{-1}$ h$^{-1}$; 0.05 mg ml$^{-1}$, 0.1 ml kg$^{-1}$ h$^{-1}$). Rabbits were placed on a heating pad at 35 °C for the entire surgery. The depth of anaesthesia was monitored continuously throughout the procedure, including heart rate, temperature and pulse oximetry. Fluid supplementation was administered intravenously to prevent dehydration (physiological solution 20-35 ml kg$^{-1}$, IV). The rabbit's head was shaved and secured gently within a stereotactic frame (David Kopf Instruments). Before cortical skin incision, lidocaine (6 mg kg$^{-1}$; Lidocaine 2%, 20 mg ml$^{-1}$, 0.3 ml kg-1) was injected subcutaneously at the surgical sites. After 5 min, the skin was opened and pulled aside to clean the skull with cotton swabs. A craniotomy was made to expose the visual cortex. A 32-channel epidural ECoG array (E32-1000-30-200; NeuroNexus) was placed over V1. For electrical stimulation, a frontotemporal craniotomy was made to access the optic nerve. The intraneural electrode array was inserted in the optic nerve in the pre-chiasmatic area. The surgical implantation was performed by piercing the nerve with a needle (nylon black DLZ 4,8-150 10/0, FSSB) and by guiding the intraneural electrode array transversally into the nerve. All rabbits were euthanised at the end of the acute recording procedures while still under anaesthesia, with an intravenous injection of pentobarbital (120 mg kg$^{-1}$).

### 3.3.2 Electrophysiological recording and stimulation

For patterned visual stimulation, white rectangles were projected (ML750ST; Optoma) on a reflective screen placed approximately 90 cm away from the rabbit. The projected area covered 28 x 44 degrees of the visual field, and the full luminance of the projector was 530 cd m$^{-2}$. Rectangles of 1/4th of the screen's size (14 x 22 degrees) were projected in 10 different locations along the horizontal meridian separated by 2.2 degrees. Each stimulus lasted for 16 ms (based on the projector frame rate). Sixty flashes were presented for each stimulus location. For patterned electrical stimulation, two microelectrode arrays were used: Flat-OpticSELINE and OpticSELINE. The OpticSELINE was previously described by our group[73].

**Chapter 3**

**A machine-learning algorithm correctly classifies cortical evoked potentials from both visual stimulation and electrical stimulation of the optic nerve**

Briefly, it is a polyimide-based looped microelectrode array. Six microelectrodes (0.0078-mm$^2$ area) are located on each side of the OpticSELINE, with a reference electrode and a ground electrode placed outside the active area. Two three-dimensional flaps extend from both sides of the main body and carry two electrodes each; two more electrodes are located on each side of the main body. The dataset with the OpticSELINE was obtained from the previous experiment[73], during which only the six electrodes on the top side were used for stimulation. The Flat-OpticSELINE is a modified version of the OpticSELINE. The array is a single polyimide strip with a linear and planar distribution of eight electrodes (40-μm diameter, 160-μm pitch, 0.0013-mm$^2$ area) with a reference electrode and a ground electrode placed outside the active area. The microelectrode array was attached to a current stimulator (IZ2MH; Tucker-Davis Technologies). Optic-nerve stimulation was performed with 150-μs biphasic cathodic-first current pulses (asymmetric: 750-μs anodic phase at one-fifth of the cathodic amplitude) at various cathodic current amplitudes (10, 25, 50, 75, 100, 150, 200, 250, 500, 750, 1,000, 1,500 and 2,000 μA) delivered in a scrambled manner. For each electrode and current amplitude, 30 stimuli were delivered with the Flat-OpticSELINE and 10 with the OpticSELINE. For cortical recordings, an ECoG array composed of 32 (4 × 8) platinum electrodes with a diameter of 200 μm and a pitch of 1 mm (E32-1000-30-200; NeuroNexus) was placed over V1 contralateral to the stimulated eye and connected to an amplifier (PZ5; Tucker-Davis Technologies) via a 32-channel analogue head stage (ZIF-Clip Analog Headstage; Tucker-Davis Technologies). Data were filtered between 0.1 and 500 Hz and digitised at 12 kHz. Epochs synchronous to the stimulation's onset (from –100 ms to +750 ms) were then extracted from the data stream and analysed with MATLAB (MathWorks).

### 3.3.3   Signal processing and feature extraction

The ECoG signal was band-pass filtered between 3 and 500 Hz, then offset by a value equal to the average voltage of the 100-ms preceding the stimulus's onset. The signal spectrogram was computed with a built-in MATLAB function (continuous 1-D wavelet transform) using the Morlet wavelet to extract the frequency bands from 10 to 300 Hz. The wavelet power was obtained by squaring two times the magnitude of the wavelet transform. The wavelet power was then normalised by subtracting the average power of the 100 ms before the stimulus's onset and then dividing the result by the same value for each frequency bands (baseline-correction). Nine classes of features were extracted from the time course portion from 5 ms after the stimulus's onset (to remove the stimulus artefact that occurs between 0 to 4 ms) to 100 ms after the stimulus. The continuous features named 'Time' and 'Slope' consist of the time course itself ('Time') and its derivative ('Slope'). The punctual features named 'PA' and 'PL' consisted of the VEP signal's peak amplitude ('PA') and the positive peak's latency ('PL'). The broad-band gamma power ('BGP') was obtained by averaging the frequency bands from the wavelet power ranging from 40 to 150 Hz. The punctual features in the frequency domain named 'Power Amplitude', 'Power Frequency' and 'Power Timing' correspond respectively to the maximum value of the power wavelet spectrogram, its frequency and its timing. Finally, the wavelet power spectrogram was down-sampled in the time axis from 12 kHz down to 1200

Hz and used as the continuous feature named 'Power'.

### 3.3.4 Classification

For patterned visual stimulation and patterned electrical stimulation with the Flat-OpticSELINE, both a classification and a linear regression were performed. For patterned electrical stimulation with the OpticSELINE, only the classification was performed. The classification was performed in MATLAB using a support vector machine algorithm (SVM), determining the hyperplane in the feature space that maximises the margins (the projection of the data points on the hyperplane). The SVM algorithm was used with the MATLAB error-correction output codes allowing the SVM classifier to be used on a multi-class data set. No kernel function was used. We ran 6-fold cross-validation, where 5/6 of the observations were used for training (training set) and 1/6 for testing (testing set). The classification was repeated on 6 different pairs of training and testing sets. The final classification accuracy score was the average of the 6 trials. Features' selection was performed on the training set only. We first conducted the classification on all the stimuli at once for patterned visual stimulation and patterned electrical stimulation with the Flat-OpticSELINE. Then, we computed the classification accuracy between pairs to evaluate the impact of the distance between stimuli or electrodes on the classification accuracy. For patterned electrical stimulation with the OpticSELINE, the classification was conducted on all the stimuli at once only.

### 3.3.5 Linear regression

The correlation coefficient between the features and the stimuli' location was computed, and a regression model was built with the features with the highest absolute correlation coefficient value. The model takes the form of $y = \beta 0 + \beta 1 X1 + \beta 2 X2 + \beta 3 X3 + \ldots + \beta n Xn + \varepsilon$, where X1 to Xn are the features used as input, $\beta 0$ to $\beta n$ are the weights of the features, $\varepsilon$ is the error term, and y is the predicted location of the rectangle's centre or the electrode's position. The observations were split into training and testing sets of a size equal to 5/6 and 1/6 of the total number of observations, which was repeated 60 times for patterned visual stimulation and 30 times for patterned electrical stimulation with the Flat-OpticSELINE to gradually shift the testing sets by an increment equal to the number of stimulations. The average model predictions and the root-mean-square error (RMSE) were reported as the average values of the different splits.

## 3.4 Results

### 3.4.1 Classification of visual responses

We took advantage of patterned visual stimulation to validate the SVM classification algorithm on ECoG recordings (Figure 3.1). An anaesthetised rabbit was placed in front of a screen (Figure 3.1a), and white flash stimuli (14 x 22 degrees rectangles) were projected on dark

background in 10 different locations along the horizontal meridian (red dots in Figure 3.1b). Visually evoked potentials (VEPs) elicited by patterned visual stimulation (Figure 3.1c) were detected using the ECoG electrode array placed over V1 contralateral to the stimulated eye. Strong patterned flash stimulation was selected among the various stimuli used in vision research to mimic the strong and fast activation induced by electrical stimulation as closely as possible. Flashes and electric pulses are both fast transients, not physiological in normal vision. Also, electrical stimulation elicits phosphenes, and a focalised flash is the closest stimulus to a phosphene. Despite these similarities, electrically evoked responses do not necessarily match visually evoked responses since electrical stimulation bypasses both phototransduction and the retinal network. Also, flashes are two orders of magnitude longer than electric pulses (16 ms and 150 µs, respectively).
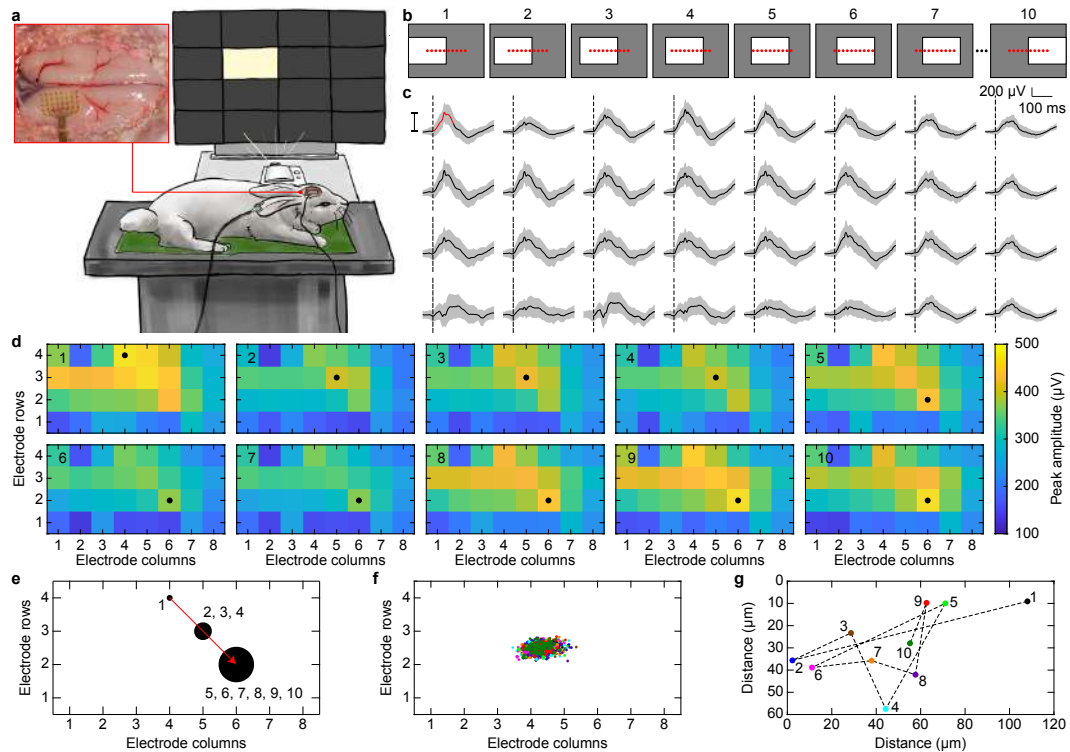
Figure 3.1: (a) Sketch of the experimental setup for visual stimulation. An anaesthetized rabbit is placed in front of the screen on which the light stimuli are projected. The red square shows an enlarged picture of the ECoG recording electrode array placed over V1 (post-mortem image). (b) Schematic representations of the patterned visual stimulation. The red dots are the centre of the white rectangles. (c) Representative example of the 32 VEPs recorded with the ECoG electrode array upon presentation of one visual stimulus. The black trace is the average of 60 repetitions, while the s.d. is the gray area. The trace in the top left corner shows the quantification of the peak-to-peak amplitude in the early portion of the signal (100 ms). The black dashed lines are the light stimulus onset. (d) Averaged activity maps among the 60 repetitions obtained for each visual stimulus location. In each map, the number in the upper left corner indicates the stimulus location, while the black circle indicates the leading channel. (e) Map of the channels identified as leading channels. The black circles' size is proportional to the number of times the electrode is identified as the leading channel. The numbers next to the circles correspond to the stimulus locations leading to the electrode being identified as the leading channel. The red arrow identifies the leading channel's shift. (f) Distributions of the centres of the activity map. Each circle corresponds to a single activity map upon one visual stimulus (60 circles for each stimulus location). Each colour corresponds to one stimulus location as in (g). (g) Shifts of the average centre of the activity maps. Each circle is the average of the centres originating from a stimulus location. The numbers correspond to the stimulus location associated to a colour code.

One of the most commonly used approaches to determine what part of the visual cortex is activated by a stimulus is measuring the leading channel's shift[72], which is the electrode with

the highest peak-to-peak amplitude. This approach has been successfully used to determine retinotopic organisation in the visual cortex when paired with intracortical recordings. However, the low spatial resolution of ECoG microelectrodes might be inadequate for this task. In our dataset, we computed the activity map for each visual stimulus in each location as the peak-to-peak amplitude for each recording electrode. The 60 activity maps corresponding to a stimulus location have been averaged (Figure 3.1d), revealing that 3 leading channels appeared out of the 10 stimulus locations upon patterned visual stimulation (Figure 3.1e). The shift in the leading channel is coherent with the stimulus's shift (from temporal to nasal) according to previously reported visual maps[302–304]. However, the limited spatial resolution of the recording system and analysis method provides only three hot-spots, which are not enough to identify distinguishable pattern of activation for each stimulus location. Therefore, we evaluated the whole activity maps. First, we computed the distribution of the centre of mass for each activity map (Figure 3.1f), and they resulted in overlapping distributions lacking significant clustering. Then, we computed the average centre of the distributions and evaluated the shift, which is in the order of one hundred microns and occurring in directions not coherent with the visual stimulus's horizontal motion. These results indicate that the cortical activity map measured by the ECoG electrode array was not affected by the visual stimulus's location.

The shifts of both the leading channel and the centre of mass alone are not a good estimator of the cortical activity pattern's modulation upon variation of the stimulus location when recordings are made with ECoG microelectrodes, since they are both based only on the signal peak-to-peak amplitude. Therefore, we sought an alternative method encompassing more exhaustive information about the elicited cortical signal to identify the stimulation corresponding to a particular activation pattern in the visual cortex.

We investigated a machine-learning approach to isolate the most informative features leading to a finer analysis of the cortical signals, highlighting differences among signals generated by different stimuli. The hypothesis is that the similarity between signals will decrease when the areas of stimulation within the visual field are further apart, which will be reflected by higher classification accuracy. The machine-learning workflow classified the signal originating from patterned visual stimulation based on two types of features extracted from the 32 VEP time courses: continuous or punctual. The continuous features are the signal time course ('Time', Figure 3.2a in red), its derivative ('Slope', Figure 3.2b in red) and its broad-band gamma power ('BGP', Figure 3.2c). The punctual features, which have a single value per time course, are the peak-to-peak amplitude of the VEP signal ('PA') and the latency of the positive peak ('PL') (Figure 3.2a). In addition to the features derived from the time course, we included features containing information about the frequency domain to broaden the possible features. Therefore, we added continuous features consisting of each pair of time points and the power spectrogram frequency (which was down-sampled by a factor 10 in time). From the power spectrogram, we extracted three punctual features: amplitude ('Power Amplitude'), frequency ('Power Frequency') and timing ('Power Timing') of the maximum of the power spectrogram (red cross in Figure 3.2c). Last, the wavelet power spectrogram was down-sampled in the

time axis from 12 kHz down to 1200 Hz and used as the continuous feature ('Power'). All the features were concatenated in a single matrix for feature selection.

Since specific portions of the signal or some signal features are more informative than others, we applied a feature selection approach on the training set only. The very large number of features made some feature selection approaches computationally expensive, so we opted first to do a pre-selection test by computing the chi-score of all the individual features. We then proceeded to test different features selection algorithms (minimum redundancy maximum relevance, chi-squared test, reliefF and randomly selected features) on the 5% of the features with the highest chi-score (Figure 3.2d). We selected the minimum redundancy maximum relevance (MRMR) algorithm for our future analysis, as this algorithm resulted in the highest classification accuracy. When the number of selected features is disproportionally large compared to the number of observations, overfitting may occur: the RMSE of the training set converges to zero, while the RMSE of the testing set increases drastically. To avoid overfitting, we selected the best 200 features returned by the MRMR algorithm (one-third of the total number of observations) for which the RMSE of the testing set was minimized, and we used them as an input of a support machine vector classifier. The MRMR algorithm returned a classification accuracy 70.67% with 200 features (Figure 3.2d).

In a first step, we conducted the classification on all the stimuli at once (10 locations and 60 repetitions for a total of 600 observations), resulting in an average (± s.d.) classification accuracy of 71.17% ± 1.83% (10-classes classification). Then, to evaluate the impact of the distance (in degrees) between stimuli on the classification accuracy, we computed the classification accuracy between pairs of patterned visual stimuli (2-classes classification), resulting in 90 accuracy values organised into an accuracy matrix (Figure 3.2e). All the values separated by the same distance were averaged and plotted as a function of the distance (Figure 3.2f). We observed an increase in the classification accuracy when the distance between stimulus locations increased. The classification accuracy started from 83.15%, which is higher than the chance level (50%), monotonously increased for the lowest separations, reached 96% for a separation of 5 degrees, and 100% for separation higher than 7 degrees. Visual stimuli are 14 degrees wide, so 100% classification accuracy was reached when the stimuli's overlap was reduced to 50%. This result suggested that the more the visual stimuli were separated, the less similar the VEPs are. In our hypothesis, as the patterned stimulations get further apart and gradually stop overlapping, they will recruit different populations of retinal ganglion cells, leading to the activation of increasingly different groups of neurons in V1. This activation ultimately results in a larger difference between the VEP signals, as they are an integrated summation of those neurons' activity.

### 3.4.2　Classification of electrical responses

We successfully designed a classification algorithm for patterned visual stimulation. Next, we tested it on the optic nerve's intraneural electrical stimulation. First, we took advantage of a

**Chapter 3**

**A machine-learning algorithm correctly classifies cortical evoked potentials from both visual stimulation and electrical stimulation of the optic nerve**
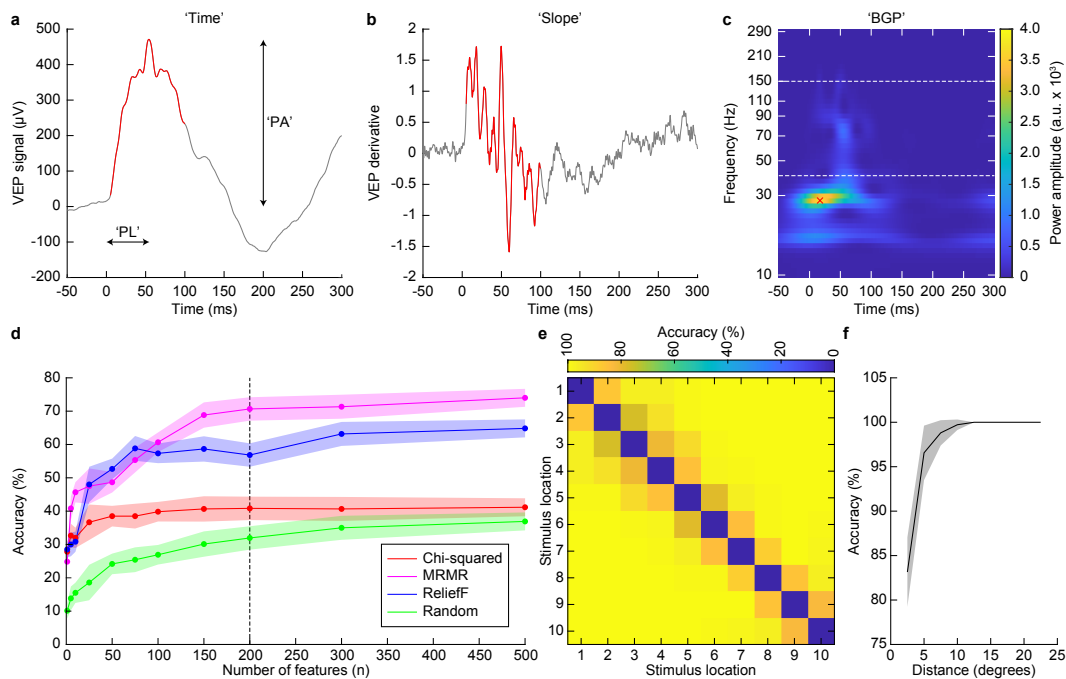


Figure 3.2: (a) Representative VEP signal highlighting the peak-to-peak amplitude and the positive peak latency. The red portion of the signal corresponds to the time course used as a feature from 5 ms to 100 ms. (b) Derivative of the VEP signal in a. The red portion of the signal is the one used as a feature from 5 ms to 100 ms. (c) Representative spectrogram from the VEP signal in a. The white dashed lines indicate the frequency band corresponding to the 'BGP'. The red cross highlights the 'Power Amplitude', the 'Power Frequency' and the 'Power Timing'. (d) Average (± s.d., 6 repetitions) classification accuracy of the feature selection algorithms. The black dashed line highlights the classification accuracy after 200 features. (e) Accuracy matrix for patterned visual stimulation. (f) Average (± s.d.) classification accuracy of the combination of pairs of stimuli as a function of the centre-to-centre distance between visual stimuli.

tailored OpticSELINE (Flat-OpticSELINE) with a linear and planar distribution of 8 electrodes transversally inserted from medial to lateral in the centre of the left optic nerve (Figure 3.3a). The advantage of this linear and flat electrode array is the similarity with the previously tested visual pattern: stimuli varying along a single dimension. Visual stimulation consisted of flashes aligned along the horizontal meridian from temporal to the nasal direction. With the Flat-OpticSELINE also electrical pulses are organised along the central line of the nerve's cross-section. A liner electrodes' distribution does not necessarily mean that phosphenes will occur along the horizontal meridian, since the fibres' retinotopic distribution within the nerve is unknown. However, the liner electrodes' distribution allowed us to compute the classification accuracy as a function of the distance and apply the linear regression model. Electrically evoked potentials (EEPs) were recorded upon biphasic charge-balanced asymmetric current pulses of different current amplitudes ranging from 10 to 2000 uA (Figure 3.3b).
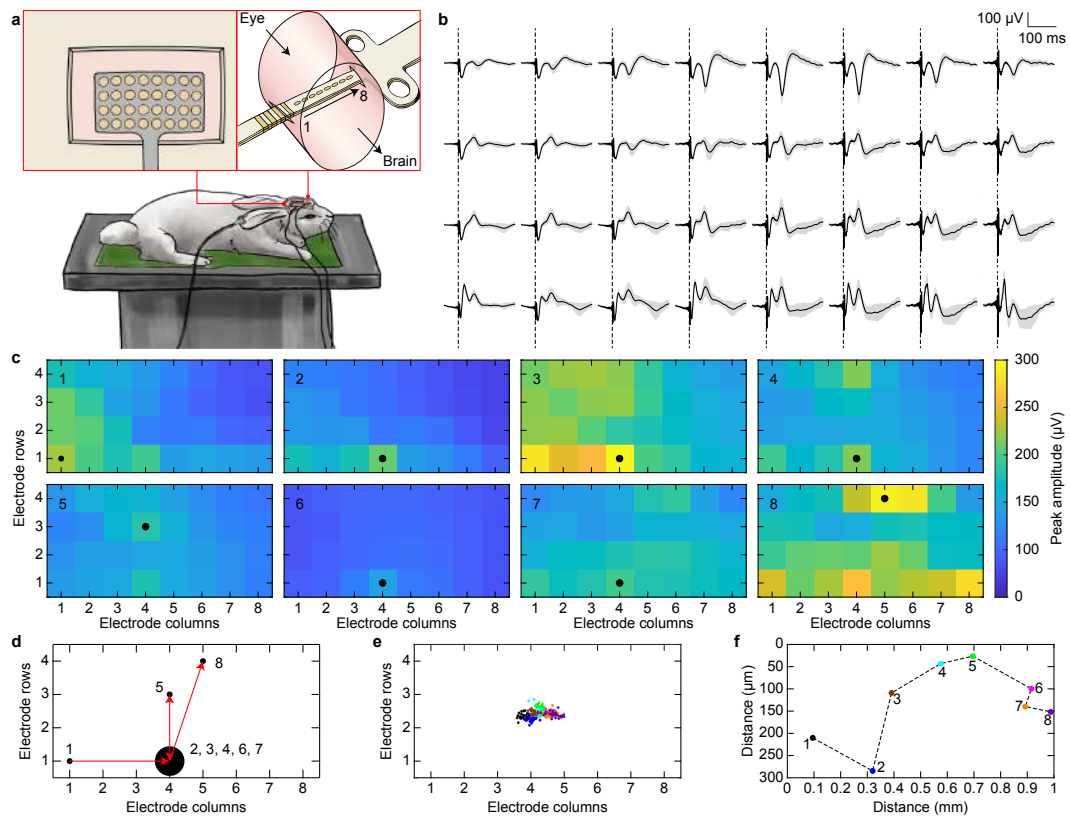
Figure 3.3: (a) Sketch of the experimental setup for electrical stimulation with the Flat-OpticSELINE. The red squares show an enlarged sketch of the ECoG recording electrode array placed over V1 and the Flat-OpticSELINE inserted into the left optic nerve from medial to lateral. The electrode's arrangement is indicated by the black arrow from 1 to 8. (b) Representative example of the 32 EEPs recorded with the ECoG electrode array upon one electric pulse (2000 µA). The black trace is the average of 30 repetitions, while the s.d. is the gray area. The black dashed lines are the stimulus onset. (c) Averaged activity maps among the 30 repetitions obtained for each electrode upon electrical stimulation at 2000 µA. In each map, the number in the upper left corner indicates the electrode, while the black circle indicates the leading channel. (d) Map of the channels identified as leading channels upon electrical stimulation at 2000 µA. The black circles' size is proportional to the number of times the electrode is identified as the leading channel. The numbers next to the circles correspond to the stimulation electrodes leading to the recording electrode being identified as the leading channel. The red arrows identify the shift of the leading channel. (e) Distributions of the centres of the activity map upon electrical stimulation at 2000 µA. Each circle corresponds to a single activity map upon one electric stimulus (30 circles for each electrode). Each colour corresponds to one stimulus location as in (f). (f) Shifts of the average centre of the activity map upon electrical stimulation at 2000 µA. Each circle is the average of the centres originating from one electrode. The numbers correspond to the electrode associated to a colour code.

First, we computed the activity maps for each stimulation electrode and each current amplitude (Figure 3.3c). From the maps, we computed the shift in both the leading channel

(Figure 3.3d) and the average centre of mass (Figure 3.3e). At low current amplitudes ($\leq 250$ μA), both shifts appear random, but they became structured and reproducible from higher current amplitudes ($\geq 750$ μA). The quantification of the peak-to-peak amplitude from 750 μA revealed 2 to 5 leading channels out of the 8 stimulating electrodes depending on the current amplitude with a clear shift direction. Compared to the shift in VEPs, the direction is opposite, from posterior-lateral (electrode 1) to anterior-medial (electrode 8), which might be coherent with the insertion of the array from the medial to the lateral side of the nerve: electrode 1 is lateral, and electrode 8 is medial. Again, the limited spatial resolution of the recording system and analysis method provides only 2 to 5 hot-spots, which are not enough to identify distinguishable cortical activity patterns for each electrode. The distributions of the centre of mass for each activity map appeared more clustered and separated than the ones from VEPs (Figure 3.3e). Consequently, the shift of the average centre of the distributions from posterior-lateral (electrode 1) to anterior-medial (electrode 8) is larger than the one from VEPs. This larger shift and higher clustering could be justified since visual stimuli cover a small portion of the visual field, while electrodes spanned the entire optic nerve cross-section. We could hypothesise that electrodes induced phosphenes in region of the visual filed which are more distant than the visual stimuli.
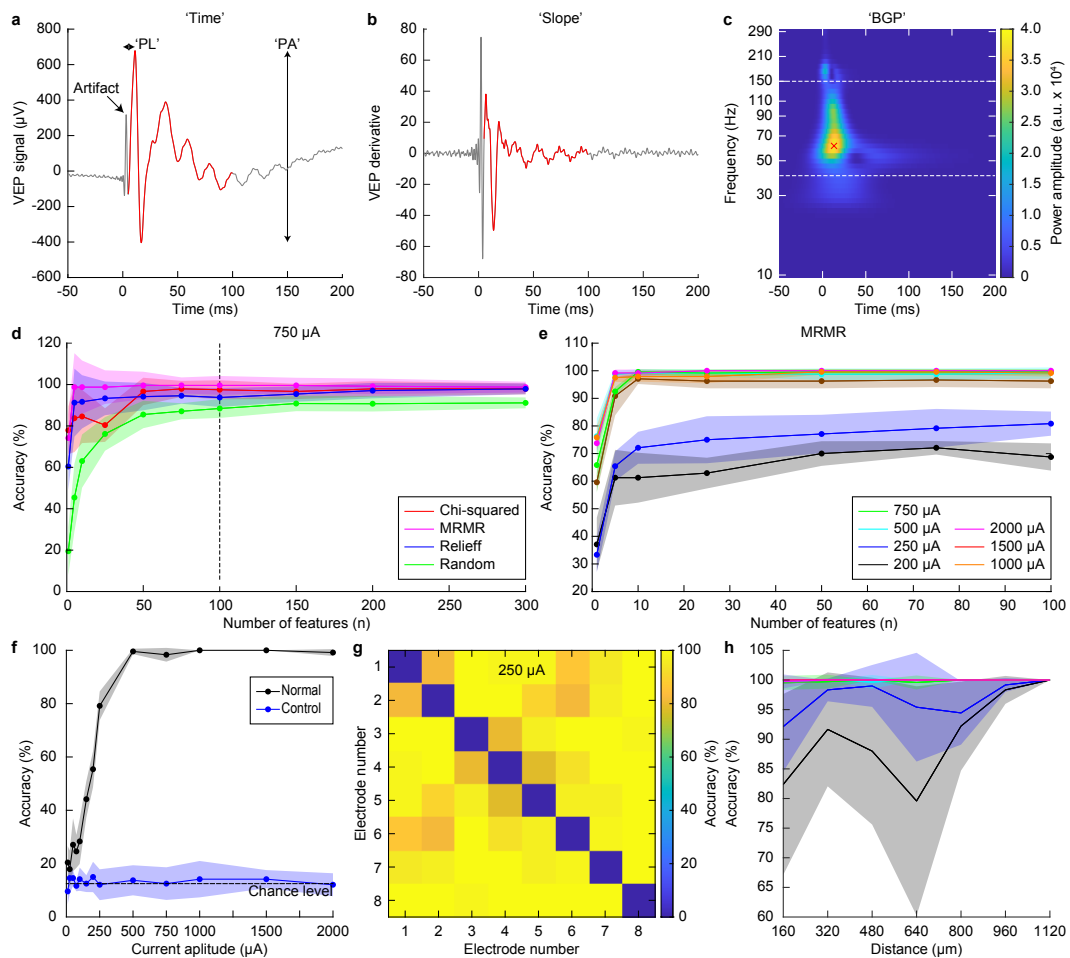
Figure 3.4: (a) Representative EEP signal highlighting the peak-to-peak amplitude and the latency of the positive peak. The red portion of the signal corresponds to the time course used as features from 5 ms to 100 ms. (b) Derivative of the EEP signal in a. The red portion of the signal is the one used as features from 5 ms to 100 ms. (c) Representative spectrogram from the EEP signal in a. The white dashed lines indicate the frequency band corresponding to the 'BGP'. The red cross highlights the 'Power Amplitude', the 'Power Frequency' and the 'Power Timing'. (d) Average (± s.d., 6 repetitions) classification accuracy of the feature selection algorithms for a stimulation current amplitude of 750 μA. The dotted line highlights the classification accuracy after 100 features. (e) Average (± s.d., 6 repetitions) classification accuracy of the MRMR feature selection algorithm for the stimulation current amplitudes from 200 μA to 2,000 μA. (f) Average (± s.d.) classification accuracy as a function of the stimulation current amplitude of all the electrodes (black). The blue circles and line show the classification accuracy when labels of the observations were scrambled. (g) Accuracy matrix for the optic nerve's intraneural electrical stimulation at 250 μA. (h) Average (± s.d.) classification accuracy of the combination of electrodes' pairs as a function of the centre-to-centre distance at increasing current amplitudes (from 200 to 2,000 μA) for the optic nerve's intraneural electrical stimulation. Colour code is as in panel e.

Chapter 3

**A machine-learning algorithm correctly classifies cortical evoked potentials from both visual stimulation and electrical stimulation of the optic nerve**

For EEPs, we implemented the same classification workflow used for VEPs with the machine-learning algorithm. The features used and the feature selection method remained unchanged (Figure 3.4a-c), but due to the lower number of repetitions (30 instead of 60), we selected only the 100 best scoring features to avoid overfitting using the MRMR algorithm (Figure 3.4d,e). In a first step, we conducted the classification on all the stimuli at once (8-classes classification) for each current amplitude: 8 electrodes and 30 repetitions for a total of 240 observations (Figure 3.4f, black). The classification accuracy started around 20% for low current amplitudes (from 10 to 75 µA), slightly above the chance level (12.5% for 8 electrodes). This low correlation accuracy is justified since those current amplitudes correspond to the threshold to elicit a detectable EEP. The correlation accuracy linearly increased by increasing the current amplitude and reached nearly 100% from 500 µA. As a control experiment, the observations' labels were randomly scrambled before the classification in both the training and testing sets, and the classification accuracy remained rightfully close to chance level regardless of the current amplitude (Figure 3.4f, blue). Overall, the machine-learning algorithm correctly classified cortical activity patterns based on the electrode in the array from which they were evoked in the entire range of current amplitudes above the activation threshold for EEP. Then, to evaluate the impact of the separation between electrodes on the classification accuracy of the elicited cortical activations, we computed the classification accuracy between pairs of electrodes (2-classes classification), resulting in 56 accuracy values organised into an accuracy matrix for each current amplitude (Figure 3.4g). All the values separated by the same distance were averaged and plotted as a function of the distance (Figure 3.4h). The classification accuracy with the machine-learning algorithm returned an increasing classification accuracy as a function of the electrode distance. The increase was marked for intermediate current amplitudes (200 and 250 µA), while at higher current amplitudes, the accuracy was quickly reaching 100%. For lower current amplitudes (below 150 µA), we could not find a clear relation between classification accuracy and electrode separation, probably because of the very low cortical activity elicited by such low currents.

The machine-learning algorithm returned an excellent classification accuracy for intraneural electrical stimulation with the Flat-OpticSELINE. Therefore, we generalised the approach and used the method to classify EEPs originating from the standard OpticSELINE having flaps distributing electrodes over the nerve's cross-section. For this classification, we used a dataset obtained from previous experiments[73]. Briefly, the optic nerves of four rabbits were implanted with the OpticSELINE, and the six electrodes of the top shank were used for electrical stimulation. EEPs were collected with the same ECoG arrays (Figure 3.5a). For each of the four rabbits, we classified the time courses of the EEPs originating from the optic nerve's stimulation using the six electrodes of the upper part of the OpticSELINE as a function of the current amplitude (Figure 3.5b). We conducted the classification on all the stimuli at once for each current amplitude: 6 electrodes and 10 repetitions for a total of 60 observations. The machine-learning algorithm showed a very high classification accuracy for three rabbits, close to 100% from 200 µA. In one rabbit (bottom left panel in Figure 3.5b), the classification accuracy was increasing with a slower slope, probably because higher currents were required

to elicit detectable EEPs and the signal-to-noise ratio of the cortical responses was low. The average accuracy among the four rabbits started around 20% for low current amplitudes (10 and 25 µA), which is slightly above the chance level (16.6% for 6 electrodes). Then, the classification accuracy rapidly increased until reaching a plateau at 100% for the higher current amplitudes (Figure 3.5c).
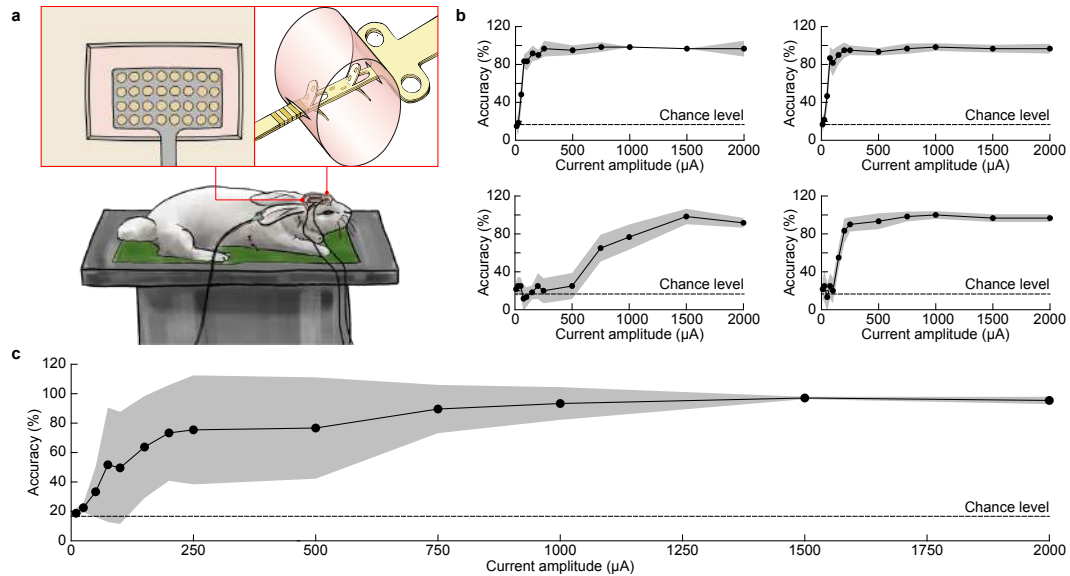


Figure 3.5: (a) Sketch of the experimental setup for electrical stimulation with the OpticSELINE. The red squares show an enlarged sketch of the ECoG recording electrode array placed over V1 and the OpticSELINE. (b) Average (± s.d.; 6 repetitions) classification accuracy as a function of the stimulating current for each rabbit. (c) Mean (± s.d.; n = 4 rabbits) classification accuracy as a function of the current amplitude.

### 3.4.3   Linear regression of patterned visual and electrical stimulation

While the classification algorithm could classify cortical patterns originating from visual and electrical stimuli in different locations with high accuracy, the classifier had one limitation. If giving as input to the classifier a novel signal from an unknowing origin, it would only associate it with one of the classes of signals already encountered in its training phase, but it would not extrapolate the actual location of the stimulus eliciting that signal. This limitation motivated us to build a linear regression model to improve the predictive capacity when presented with a new signal of unknown origin, using the features with the highest individual $R2$ scores: 200 for patterned visual stimulation and 100 for patterned electrical stimulation.

For patterned visual stimulation, the prediction of the model was close to the actual centre of the rectangles (Figure 3.6a), with an average (± s.d.) RMSE of 2.72 ± 0.60 degrees (Figure 3.6d), equivalent to 12.45% of the full range of possible positions. The model performed better for the central locations, while the performance slightly decreased at the extremities. The adjusted $R2$ score of 0.86 suggested that the linear model is a good fit for patterned visual

**Chapter 3**

**A machine-learning algorithm correctly classifies cortical evoked potentials from both visual stimulation and electrical stimulation of the optic nerve**

stimulation. To validate the model further, we performed two control experiments. First, we randomly scrambled the labels of the stimulus's centres in both the training and testing sets (scrambled condition), where all stimuli corresponding to one location have been randomly assigned to another location (e.g. location 1 at -11 degrees was renamed +11 degrees). The linear regression model had a worst performance to predict the positions of the stimuli (Figure 3.3b), with an average (± s.d.) RMSE of 6.29 ± 2.16 degrees (Figure 3.3e) and very large variation in the average difference. Second, we removed one location from the training set, and we trained on the 9 remaining locations. The testing set was composed only by the location that was left out from the training set (left-out condition). The linear regression model correctly predicted the missing stimulus position (Figure 3.3c), with an average (± s.d.) RMSE of 2.90 ± 0.96 degrees (Figure 3.3f).
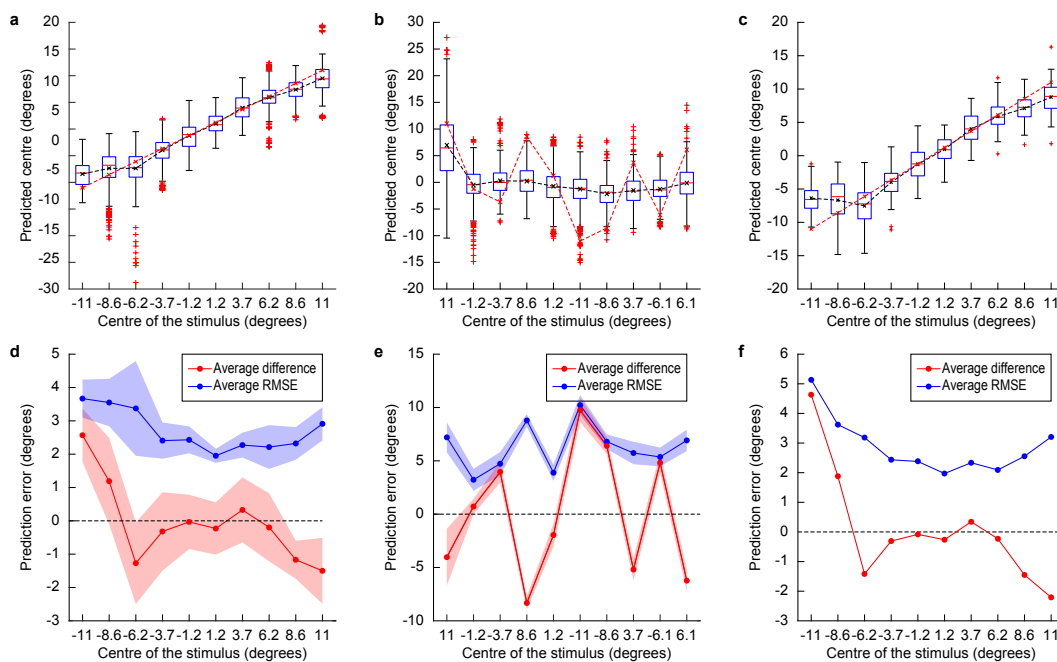


Figure 3.6: (a,b,c) Quantification of the averaged predicted centre locations (black dashed line) and their actual locations (red dashed line) for the three conditions: normal (a), scrambled (b) and left-out (c). In each box: the red line is the median, the box extremities are the 1st (q1) and 3rd (q3) quartiles, the whiskers are q1 + 1.5 × (q3 – q1) and q3 + 1.5 × (q3 – q1) and the red crosses outside of the whiskers are the outliers. (d,e,f) Average difference between the predicted and the actual locations (red) and RMSE of the predicted locations (blue) for the three conditions: normal (d), scrambled (e) and left-out (f). In panels (d,e) the shaded area is the s.d. In the left-out condition (f), the RMSE is computed only once for each excluded stimulus, so the s.d. cannot be computed.

Next, we fitted the linear regression model on the features extracted from the EEPs (Figure 3.7). The model had the best fit for 1,000 uA (Figure 7a,b) according to the adjusted R2 (0.91) and the average RMSE (0.68). Overall, among the various current amplitudes, the model had an adjusted R2 between 0.01 and 0.91, increasing with the current amplitude and an

average RMSE between 3.24 and 0.65, decreasing with the current amplitude (Figure 3.7c). In the scrambled condition, the linear regression was worst (Figure 3.7d), with an average (± s.d.) RMSE of 2.06 ± 0.53 (Figure 3.7e). However, it can be noted that while some electrodes are not accurately predicted, other they still are despite the random scrambling. A similar behaviour was observed at all current amplitudes (Figure 3.7f). In the left-out condition, the linear regression model correctly predicted the missing electrode position (Figure 3.7g), with an average (± s.d.) RMSE of 1.06 ± 0.74 (Figure 3.7h). Overall, among the various current amplitudes, the model had an average RMSE between 4.06 and 1.06, decreasing with the current amplitude (Figure 3.7i).

Our approach used nine classes of features from both the time domain and the frequency domain classified in two major categories: punctual and continuous. Therefore, we investigated which feature's types was most informative. We repeated the linear regression model for both patterned visual stimulation and patterned electrical stimulation. We computed the correlation coefficient between the features and the stimuli' locations based on the whole datasets to be more descriptive (i.e. on the total number of observations instead of the 5/6th of the training sets' observations). Then, we selected the 200 (for patterned visual stimulation) and 100 (for patterned electrical stimulation) features with the highest correlation coefficient value (Figure 3.8). For patterned visual stimulation, the 200 selected features were from only two types: 'Slope' (51.5%) and 'Power' (48.5%), both continuous features. This result indicates that continuous features might be more informative than punctual features, like the peak-to-peak amplitude. Patterned electrical stimulation revealed a remarkably similar behaviour. Among all the current amplitudes, 6 types of features were cumulatively selected: 'Time' (8.5%), 'Slope' (12.5%), 'Power Timing' (0.2%), 'Power Amplitude' (0.2%), 'BGP' (19.2%) and 'Power' (59.4%). Continuous features (99.6%) were largely predominant compared to punctual features (0.4%). Features in the frequency domain were mostly selected (79%) compared to features in the time domain (21%). The most informative feature was the 'Power' feature (59.4%).

## 3.5   Discussion

Optic nerve stimulation has advantages compared to epiretinal stimulation. However, one of the key open questions in preclinical studies is tose detect distinguishable cortical patterns upon selective activation of the nerve fibres. Computational and experimental methods showed that intraneural electrodes could selectively activate different sets of fibres within the optic nerve[73]. Also, high-frequency pulse trains with a variable number of pulses could modulate the cortical responsivity without affecting the optic nerve's activated area. Building on this evidence, our results showed that a machine-learning algorithm could correctly classify electrically evoked cortical potentials originating from the microelectrodes of the OpticSELINE array.

First, we showed that approaches relying only on the peak-to-peak amplitude alone are not powerful enough to distinguish the stimulus's location inducing the cortical activation due to

the low spatial resolution of ECoG microelectrodes. This result motivated the development of a new signal analysis approach based on a SVM classification algorithm, and we took advantage of patterned visual stimulation for its validation. We designed the stimulation pattern to test conditions in which the visual field's stimulated portions are close and overlapping, thus more difficult to distinguish from one another. We hypothesised that the further apart the visual field's stimulated portion would be, the less similar the signal originating from their activation would be. Therefore, the visual stimuli were aligned over the horizontal meridian to precisely quantify their centre-to-centre separation. The SVM classification method confirmed the hypothesis, showing an increase in classification accuracy with increased centre-to-centre separation, reaching 100% accuracy for stimuli with less than 50% overlap.

After demonstrating the efficiency of the SVM classification approach on patterned visual stimulation, we tested it on the optic nerve's intraneural electrical stimulation. First, we used a simplified intraneural electrode array (Flat-OpticSELINE). As for visual stimulation, we found an increase in classification accuracy with increased centre-to-centre separation between the stimulating electrodes. However, the performance of the SVM classification method was much better for electrical stimulation than visual stimulation, with nearly 100% classification accuracy from the smallest separation distance above 500 µA. The better performance on electrical stimulation can be explained since the visual stimuli cover a small portion of the visual field, while electrodes spanned the entire optic nerve. We could hypothesise that electrodes induced phosphenes in region of the visual filed which are more distant than the visual stimuli. Because of this difference, a quantitative comparison between visual and electrical stimulation could not be performed. However, both modalities showed the same qualitative behaviour. This result also highlighted the classification accuracy's dependence on the current amplitude, with higher accuracy at higher amplitudes. Higher current amplitudes activate a larger portion of the nerve, increasing the overlap between neighbouring electrodes. We hypothesised that the classification accuracy still increases because the nerve's activated portion remains sufficiently different, leading to distinguishable cortical patterns. Also, the higher is the current amplitude, the higher is the signal-to-noise ratio of the recorded signal, and the lower is the variability among trials, leading to better classification.

To generalise the approach, we implemented the SVM classification algorithm to EEPs induced by the OpticSELINE intraneural array, where the electrodes are not distributed in line but cover the cross-section of the nerve. The algorithm returned similar results, with a nearly 100% classification accuracy above 200 µA of current stimulation in three out of the four rabbits tested. According to the Shannon criteria[305], the OpticSELINE can safely deliver current pulses up to 500 µA (k = 1.85). In one animal, the classification accuracy increased with a slower slope as a function of the current. This result was explained since, in that experiment, higher currents were required to elicit detectable EEPs, and the signal-to-noise ratio of the cortical responses was low. The classification accuracy's dependency with the signal-to-noise ratio makes the classification algorithm relative to the stimulation strength. Thus, an increase in classification accuracy could be linked to a larger separation between the stimuli only when the stimuli are comparable in strength: that is to say, the same illuminated surface for visual

58

stimuli or the same current amplitude for electrical stimulation.

The SVM algorithm provided only a qualitative estimation of the distance separating two stimuli: a low accuracy score was associated with a small distance between the stimuli, while a high accuracy score indicated that the stimuli were further apart. However, it cannot predict how far apart the stimuli were since after a small distance between the electrodes, the classification accuracy reached a plateau at 100% of accuracy, and increasing the distance between stimuli further could note improve it. Also, for electrical stimulation with the Flat-OpticSELINE above 500 μA, the classification accuracy reached 100% from the smallest separation distance. Therefore, we applied a regression model to add a predictive capacity. We selected a linear model as it is a simple approach matching the type of stimuli used, which vary along a single dimension. This choice relies on the assumption that some features are linearly related to the stimuli' coordinates. We obtained several features with a large correlation coefficient, which allowed us to build a successful regression model for both visual and electrical patterned stimulation. The linear regression model performed better for patterned visual stimulation than patterned electrical stimulation, because in visual stimulation the stimuli remained located in a small and central portion of the visual field. The approximation of linearity is less accurate for patterned electrical stimulation since electrodes are located through the whole size of the optic nerve, and the evoked phosphenes might not be all linearly organised. In this condition, a more complex machine-learning algorithm such as convolutional neural networks could provide better results since it would not impose any assumption on linearity or any other type of regression.

The linear regression models for both patterned visual and electrical stimulation revelated that continuous features are the most informative. Punctual features appeared only sporadically in pattered electrical stimulation and resulted in not being very informative. Punctual features compress the cortical signal into a single value, which does not appear to be informative enough for prediction models. Features from both time and frequency domains were selected. However, spectral features appeared to be the most robust, especially the 'Power' feature. Among features in the time domain, 'Slope' was the most selected. It is noteworthy that the signal's derivative ('Slope') was mostly selected and not the signal itself ('Time'). This result might be explained by the trial-to-trial variation of the signal (e.g. voltage offset), which is removed in the derivative, making the 'Slope' more consistent between repetitions. Among features in the frequency domain, it appears that the 'Power' feature is the most informative. BGP or similar frequency ranges have been used to successfully classify cortical signals in V1 upon visual stimulation[301] and electrical stimulation of the retina[306]. From this dataset and results, the whole spectrum ('Power' feature) is more informative than its partition ('BGP'). The BGP might results in a loss of information compared to the whole spectrum.

The successful design of these two algorithms shows that the cortical activities elicited by the electrical stimulation are indeed distinctively different. The linear regression model then shows that they are meaningfully different, as it highlights features that vary in a linear manner, which can be expected from cortical activity patterns resulting from the stimulation

of a gradually shifted portion of the visual field.

## 3.6   Conclusion

The machine-learning approach based on a SVM classification algorithm showed that the cortical activity patterns induced by the optic nerve's intraneural stimulation with the OpticSELINE could be successfully classified. Like patterned visual stimulation, intraneural electrodes might selectively recruit different optic nerve portions leading to different visual phosphenes. These results represent a necessary, although not sufficient, condition for an optic nerve prosthesis to deliver vision with non-overlapping phosphene. It must be noted that this analysis and results cannot provide information about perceptual phenomena. Also, in late-stage retinitis pigmentosa patients, only 30% of retinal ganglion cells might be spared, and the retina's hyperexcitability might affect the reliability of artificial vision via optic nerve's stimulation. These assessments will require further clinical investigation.

## 3.7   Acknowledgment
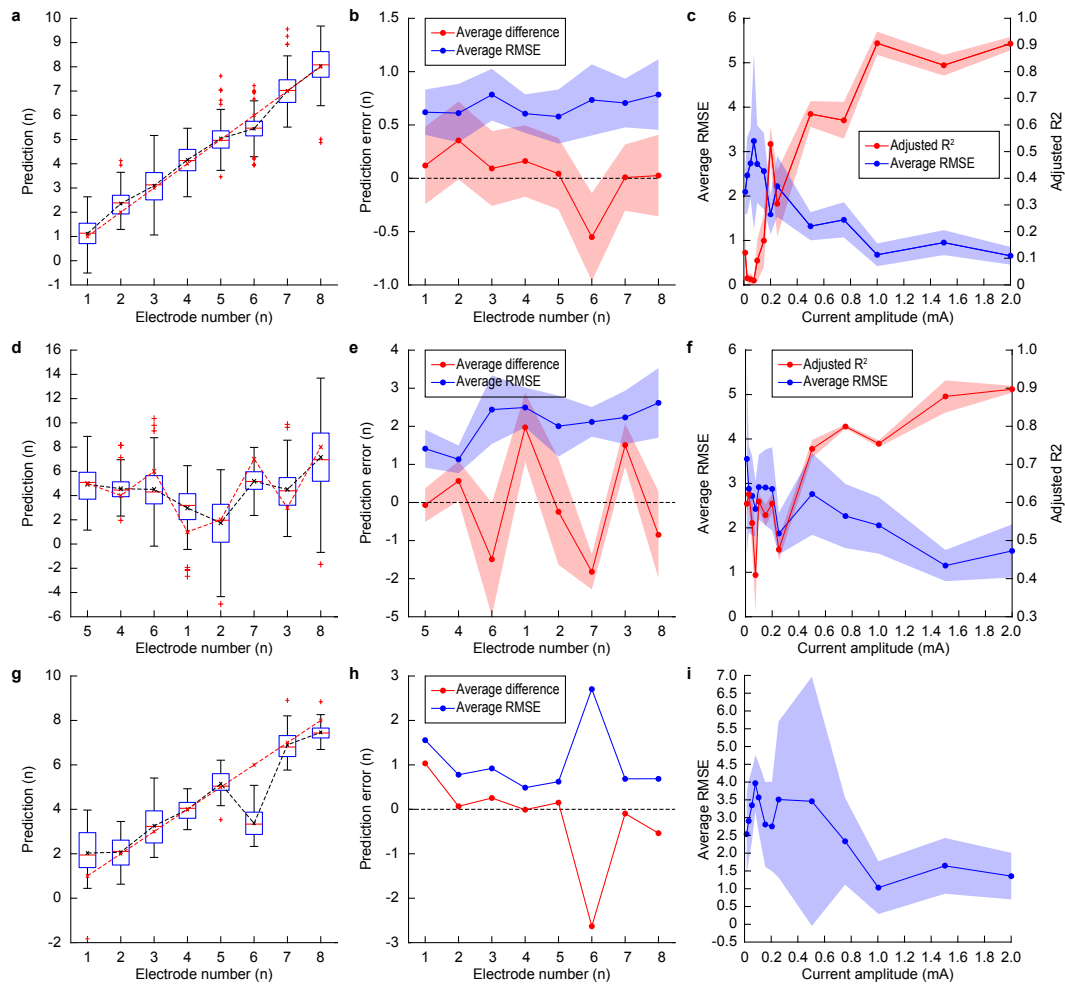
Figure 3.7: (a,d,g) Quantification of the averaged predicted centre locations (black dashed line) and their actual locations (red dashed line) upon electrical stimulation at 1,000 µA for the three conditions: normal (a), scrambled (d) and left-out (g). In each box: the red line is the median, the box extremities are the 1st (q1) and 3rd (q3) quartiles, the whiskers are q1 + 1.5 × (q3 − q1) and q3 + 1.5 × (q3 − q1) and the red crosses outside of the whiskers are the outliers. (b,e,h) Average difference between the predicted and the actual locations (red) and RMSE of the predicted locations (blue) upon electrical stimulation at 1,000 µA for the three conditions: normal (b), scrambled (e) and left-out (h). In panels (b,e) the shaded area is the s.d. In the left-out condition (h), the RMSE is computed only once for each excluded stimulus, so the standard deviation cannot be computed. (c,f,i) Average (± s.d.) RMSE (blue) and adjusted R2 coefficient (red) of the model as a function of the stimulating current amplitudes for the three conditions: normal (c), scrambled (f) and left-out (i). In the left-out condition (i), the adjusted R2 coefficient cannot be computed since it requires the variance of the testing set labels, which is null since the testing set is only composed of observations with the same label.

**Chapter 3**

**A machine-learning algorithm correctly classifies cortical evoked potentials from both visual stimulation and electrical stimulation of the optic nerve**

| Stimulus condition | Feature type | | | | | |
|---|---|---|---|---|---|---|
| | BGP | Time | Power | Slope | PT | PA |
| VEP | 0 | 0 | 48.5 | 51.5 | 0 | 0 |
| EEP 10 µA | 100 | 0 | 0 | 0 | 0 | 0 |
| EEP 25 µA | 100 | 0 | 0 | 0 | 0 | 0 |
| EEP 50 µA | 48 | 4 | 40 | 8 | 0 | 0 |
| EEP 75 µA | 2 | 2 | 95 | 1 | 0 | 0 |
| EEP 100 µA | 0 | 0 | 100 | 0 | 0 | 0 |
| EEP 150 µA | 0 | 0 | 98 | 0 | 0 | 2 |
| EEP 200 µA | 0 | 41 | 0 | 59 | 0 | 0 |
| EEP 250 µA | 0 | 0 | 95 | 5 | 0 | 0 |
| EEP 500 µA | 0 | 63 | 37 | 0 | 0 | 0 |
| EEP 750 µA | 0 | 0 | 100 | 0 | 0 | 0 |
| EEP 1000 µA | 0 | 0 | 91 | 9 | 0 | 0 |
| EEP 1500 µA | 0 | 0 | 75 | 24 | 1 | 0 |
| EEP 2000 µA | 0 | 0 | 41 | 57 | 2 | 0 |
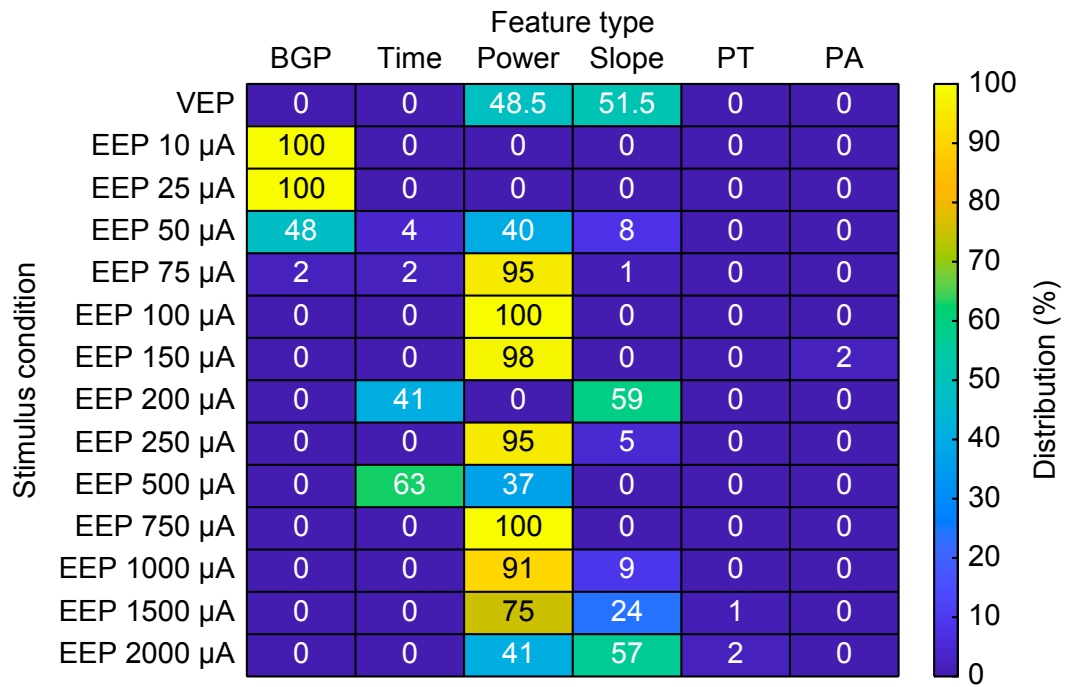
Figure 3.8: Distribution of the selected feature's types. Numbers in each box correspond to the exact percentage value. PT corresponds to 'Power Timing' and PA to 'Power Amplitude'.

# 4 Three-dimensional multilayer concentric bipolar electrodes enhance the selectivity of optic nerve stimulation

Authors: Eleonora Borda[1], Vivien Gaillet[1], Marta Jole Ildelfonsa Airaghi Leccardi[1], Elodie Geneviève Zollinger[1], Ricardo Camilo Moreira[1] and Diego Ghezzi[1]

[1] Medtronic Chair in Neuroengineering, Center for Neuroprosthetics, Institute of Bioengineering, School of Engineering, École Polytechnique Fédérale de Lausanne, Switzerland

## 4.1 Abstract

*Objective.* Intraneural nerve interfaces often operate in a monopolar configuration with a common and distant ground electrode. This configuration leads to a wide spreading of the electric field. Therefore, this approach is suboptimal for intraneural nerve interfaces when selective stimulation is required.

*Approach.* We designed a multilayer electrode array embedding three-dimensional concentric bipolar electrodes. First, we validated the higher stimulation selectivity of this new electrode array compared to classical monopolar stimulation using simulations. Next, we compared them in-vivo by intraneural stimulation of the rabbit optic nerve and recording evoked potentials in

the primary visual cortex.

*Main results.* Simulations showed that three-dimensional concentric bipolar electrodes provide a high localisation of the electric field in the tissue so that electrodes are electrically independent even for high electrode density. Experiments in-vivo highlighted that this configuration leads to evoked responses with lower amplitude and more localised cortical patterns due to the fewer fibres activated by the electric stimulus in the nerve.

*Significance.* Highly focused electric stimulation is crucial to achieving high selectivity in fibre activation. The multilayer array embedding three-dimensional concentric bipolar electrodes improves selectivity in optic nerve stimulation. This approach is suitable for other neural applications, including bioelectronic medicine.

## 4.2   Introduction

The treatment for several neurological disorders and traumatic injuries, such as Parkinson's disease, epilepsy, deafness, blindness, amputation, chronic pain and spinal cord injury, among others, relies on the electrical stimulation of the central and peripheral nervous system[307]. Interfaces to the nervous system traditionally consist of microelectrode arrays placed on (epineural) or inside (intraneural) the tissue. Microelectrodes deliver current or voltage pulses to stimulate neuronal cells and recover lost functions.

The number of electrodes in the array varies depending on the application, from few units (e.g. deep brain stimulation)[308] to few tens (e.g. cochlear implants)[309], or even hundreds or thousands (e.g. retinal prostheses)[37,129]. Regardless of the number of electrodes, neural interfaces share the same principle: electrodes should be electrically independent without stimulation cross-talk among neighbours. In other words, each electrode should excite selectively a specific subset of cells or fibres, different from those stimulated by neighbouring electrodes. For example, a visual prosthesis should have as many electrically independent electrodes as possible so that each electrode induces a spatially isolated visual percept in the subject, called phosphene. Artificial vision consists of perceiving the world using an ensemble of these phosphenes[17]. On the other hand, a second requirement is to have electrodes as dense as possible to increase the theoretical resolution of the restored image (as the number of pixels per unit of area). Although these two concepts work in theory, there is a constraint in practice: a trade-off between density and independence must be found. Increasing the electrode density increases the risk of having a stimulation cross-talk among neighbouring electrodes. In such a case, two electrodes could induce the same phosphene, or two close phosphenes could fuse[90,99].

The configuration used for electrical stimulation plays a significant role in this balance. Most clinical neural interfaces function in a monopolar configuration with a common and distant return ground placed several millimetres away[52,57,310,311]. When the current is injected into the stimulating electrode, the electric field spreads to the common and distant ground, not

allowing the confinement of the electrical stimulation around the electrode and resulting in the activation of a large portion of the neural tissue[312]. Other stimulation configurations were widely investigated in cochlear implants and visual prostheses, including bipolar, hexapolar and multipolar[140]. In addition to these configurations, the concentric bipolar (CB) is an attractive strategy. Each stimulating electrode has a concentric return electrode, and the electric field is localised between the two electrodes[140].

Compared to the monopolar configuration, the main disadvantage of a conventional CB configuration is that two feedlines are required for each electrode pair, composed of the stimulating electrode and the concentric return electrode. Two feedlines increase the space occupied on the array and, consequently, the size of the implant. This paper reports the design, simulation and validation of a novel intraneural electrode array based on three-dimensional (3D) multilayer CB electrodes fabricated using a previously described 3D multilayer technology[274]. This multilayer process allows placing electrodes on separate layers and overlaying the feedlines. Therefore, each electrode pair occupies the same space on the array as the monopolar configuration. This advantage is beneficial for intraneural interfaces where the nerve size is an important constraint to the total size of the array. Hence, we validated this technology in the context of intraneural optic nerve stimulation. Our research group recently proposed a new intraneural electrode array (OpticSELINE) for artificial vision via optic nerve electrical stimulation[63,73]. However, the selective activation of a few optic nerve fibres by each electrode was still an open challenge. The array of 3D multilayer CB electrodes proposed here improves the selectivity of the intraneural stimulation.

Beyond optic nerve stimulation and artificial vision, we believe that the high-spatial stimulation selectivity of this electrode array can be exploited in other neural applications, including bioelectronic medicine.

## 4.3   Methods

### 4.3.1   Electrode array modelling

A finite element analysis (FEA) was performed in COMSOL Multiphysics (Version 5.3), using a stationary current study with the AC/DC module. The electrode array (5 x 5 electrodes, 80-μm diameter and 100-μm pitch) was simulated inside a 1-cm height and 2-cm wide cylinder filled with saline (saline box). A circular ground electrode (1-cm diameter) was placed concentrically with the simulated array (Figure 4.1a). The electrodes were modelled in platinum (Pt), while the substrate and superstrate were modelled in polyimide (PI). Meshing was performed with tetrahedral nodes. Simulations were performed under static conditions. Current conservation was assumed following the continuity equation. Electrodes were modelled with the geometrical and electrical parameters reported in Table 4.1.

| Geometrical parameters | | | | | | |
|---|---|---|---|---|---|---|
| | Central electrode | | | Return electrode | | Wall |
| Monopolar | 80 | 6 | 5027 | - | - | - |
| 3D multilayer CB | 40 | 12 | 1257 | 6 | 6 | 1395 | 14 |
| Electrical parameters | | | | | | |
| | Platinum | | Polyimide | | Saline | |
| Conductivity [S m$^{-1}$] | 8.9 x 10$^6$ | | 6.67 x 10$^{-18}$ | | 1 | |
| Relative permittivity | - | | 3.4 | | 80 | |

Table 4.1: Geometrical and electrical parameters for the model.

### 4.3.2 Hybrid FEA-NEURON modelling of optic nerve stimulation

The hybrid FEA-NEURON simulation was performed as previously described[73]. The optic nerve model was built in COMSOL with the geometrical and electrical parameters reported in Table 4.2. The optic nerve and the meningeal layers were modelled as concentric cylinders. The axonal compartment was 1.5 mm in diameter. The pia was approximated by a contact impedance due to its small thickness, and cerebrospinal fluid was placed between the pia and the dura. A saline box (4.5-mm diameter and 5-mm length) surrounded the optic nerve. Except for the axons, which have higher longitudinal conductivity, the other domains have isotropic conductivity. A single monopolar or 3D multilayer CB electrode was modelled as described above and placed in the optic nerve centre. A ground electrode was placed in the saline box. The size of the saline box and the mesh were optimised to respect the hypothesis of ground condition at infinity. The mesh size was reduced close to the electrode to detect the rapid change in the electric field.

| Axons | | | Pia | | Cerebrospinal fluid | | Dura | | Saline |
|---|---|---|---|---|---|---|---|---|---|
| Radius [μm] | Transversal conductivity [S m$^{-1}$] | Longitudinal conductivity [S m$^{-1}$] | Thickness [μm] | Conductivity [S m$^{-1}$] | Thickness [μm] | Conductivity [S m$^{-1}$] | Thickness [μm] | Conductivity [S m$^{-1}$] | Conductivity [S m$^{-1}$] |
| 750 | 0.08 | 0.5 | 10 | 0.016 | 100 | 1.7 | 300 | 0.06 | 1.7 |

Table 4.2: Geometrical and electrical parameters for the optic nerve model. Saline conductivity was adjusted to 37 °C.

The axon fibre model was implemented in NEURON (Version 7.4) as McNeal's cable model. Briefly, only the nodes of Ranvier were active segments, while the myelinated segments were approximated by a perfect insulator. The geometrical parameters of the axon model were obtained from previous work[313]. Each axon model was a modified Hodgkin-Huxley model[314]. Each node of Ranvier contained five currents: fast sodium current, fast potassium current, persistent sodium current, slow potassium current, and leak current. The electrical properties of the axon model were obtained from previous work[315]. An axon is activated if an action potential travels to both ends. For an axon of a given diameter and shift (the relative distance separating its central node of Ranvier from the centre of the stimulating electrode), its probability of being activated by the stimulation was either 0 or 1. To determine the probability for a specific pair of coordinates in the nerve cross-section to contain an axon activated by a given electrical stimulus, 42 combinations of 6 shifts and 7 diameters were

considered. Shifts ranged from 0, if the electrode was aligned with the central node of Ranvier, to 0.5, if the electrode was aligned with the centre of the myelinated segment, with steps of 0.1 since any shift is as likely as the others. On the contrary, the 7 diameters do not have the same probability of occurring: some will contribute more than others to the final activation probability. Instead of computing the activation probability for specific diameters with a constant interval and weighting these values by their frequency of occurrence, we computed the frequency distribution of axon diameters and multiplied it by the squared diameters. Then, we divided the distribution into 8 bins of 12.5% each, effectively doing the weighting before computing the probability values. Last, the 42 probability values were averaged to obtain the final activation probability by a given electrical stimulus for a given pair of coordinates in the nerve cross-section. For each current amplitude (2, 3, 5, 10, 20, 25, 50, 75, 100, 150, 200, 250, 500, 750, 1000, 1500 and 2000 µA) and configuration (monopolar and 3D multilayer CB) tested, an activation probability matrix was obtained by sampling every 40 µm × 40 µm pair of coordinates over the cross-section of the nerve. Then, they were sampled with higher resolution at the locations where a large change in the activation probability was present. The total number of fibres activated for each current amplitude and configuration was computed by multiplying each activation probability in the matrix by the number of fibres present in the sampled area (averaged fibre density in the rabbit optic nerve is 0.19 fibres $µm^2$,[73]) and summing up all the values. Activation probability maps were obtained by interpolating the activation probability matrix with a resolution of 1 x 1 µm2 using the cubic 2D-interpolation function in MATLAB (MathWorks).

### 4.3.3 Array microfabrication

The Flat-OpticSELINE[63] is a modified version of the OpticSELINE[73] without protruding wings. Therefore, it is equivalent to a transverse intrafascicular multichannel electrode (TIME) array. The Flat-OpticSELINE electrode array contains 8 CB electrode pairs fabricated with a 3D multilayer process. The detailed process flow is available in[274]. Briefly, a Ti/Al release layer (10/100 nm) was deposited using a magnetron sputter onto 4-inch Si wafers. The deposition of a PI layer (PI2611 HD MicroSystems GmbH) of 12 µm was obtained by spin-coating at 1000 rpm, soft-baking at 65 °C (5 min) and 95°C (5 min), as well as hard-baking at 200°C (1 hr) and 300°C (1 hr) both under nitrogen atmosphere. The electrodes Ti/Pt (15/300 nm) were made by magnetron sputtering onto oxygen plasma-treated PI layers, followed by photolithography and chlorine-based dry etching. The central electrodes were 40 µm in diameters with 15-µm wide interconnects. After photoresist removal, the substrates were coated again with 6 µm of PI (2000 rpm), as just described. The metallisation and PI encapsulation were repeated for the top layer, with a PI thickness of 6 µm. A 14-µm thick layer of positive photoresist was spin-coated and patterned by photolithography to open the electrodes and the pads for the connector in both layers. The PI layers were directionally dry-etched using oxygen plasma until the openings reached all the electrode layers (Pt was used as etch stop material). The remaining layer of photoresist was dissolved in acetone. The top layer electrodes had a 6-µm width ring shape, and 15-µm wide interconnects overlaid to the bottom ones. The Flat-OpticSELINE

was then shaped by laser cutting and released from the wafer by Al anodic dissolution. After release, the arrays were inserted into a ZIF connector placed on a customised printed circuit board. Last, the electrodes were electroplated with platinum black (PtB), using a solution containing 1% of platinum chloride H2PtCl6 · 6H2O, 0.01% of lead acetate Pb(COOCH3)2 · 3H2O and 0.0025% of HCl[316]. An LCR meter (4263A, Hewlett Packard) was used for deposition at 800 mV and 100 Hz.

### 4.3.4   Electrochemistry

Electrochemical impedance spectroscopy (EIS) was performed with a potentiostat (Compact-Stat, Ivium Technologies). The arrays were soaked in phosphate-buffered saline (pH 7.4) at room temperature with a Pt counter wire and an Ag/AgCl reference wire. The potential was set at 50 mV, and the impedance magnitude and phase were measured between 1 Hz and 1 MHz. Cyclic voltammetry (CV) was performed with the same setup and three-electrodes configuration used for EIS. The applied voltage was scanned between 0.6 and 0.8 V at 50 mV s$^{-1}$. CV was repeated for six cycles. The first cycle was discarded, and the remaining five were averaged.

### 4.3.5   Animal handling and surgery

Animal experiments were performed according to the authorisation GE519 approved by the Département de l'Emploi, des Affaires Sociales et de la Santé, Direction Générale de la Santé of the Republique et Canton de Genève (Switzerland), as previously described[63]. Two female Chinchilla Bastard rabbits (>16 weeks, >2.5 kg) were premedicated 30 min before the transfer to the surgical room with an intramuscular injection of xylazine (3 mg kg$^{-1}$; Rompun® 20 mg ml$^{-1}$, 0.15 ml kg$^{-1}$), ketamine (25 mg kg$^{-1}$; Ketanarkon® 100 mg ml$^{-1}$, 0.25 ml kg$^{-1}$) and buprenorphine (0.03 mg kg$^{-1}$; Temgesic® 0.3 mg ml$^{-1}$, 0.1 ml kg$^{-1}$). Rabbits were placed on a heating pad at 35 °C. A 22G catheter was placed in the ear marginal vein 15 min after premedication. Local anaesthesia was provided to the throat (Xylocaine 10%, spray push). The rabbit was intubated with an endotracheal tube with balloon (3.5 mm) and ventilated (7 ml kg$^{-1}$, rate: 40 min$^{-1}$, positive end-expiratory pressure: 3 cm of H2O). Eye gel was placed on the eye to protect it from drying. Anaesthesia and analgesia were provided intravenously with propofol (10 mg kg-1 h$^{-1}$; 20 mg ml$^{-1}$, 0.5 ml kg$^{-1}$ h$^{-1}$) and fentanyl (0.005 mg kg$^{-1}$ h$^{-1}$; 0.05 mg ml$^{-1}$, 0.1 ml kg$^{-1}$ h$^{-1}$). Body temperature, heart rate, blood pressure, and oxygen saturation were monitored continuously during the procedure. Saline was administered intravenously to prevent dehydration. The rabbit head was shaved and secured to a stereotactic frame (David Kopf Instruments). Lidocaine (6 mg kg$^{-1}$; Lidocaine 20 mg ml$^{-1}$, 0.3 ml kg$^{-1}$) was injected subcutaneously at the surgical sites. After 5 min, the skin was opened and pulled aside to clean the skull with cotton swabs. A craniotomy was made to expose the visual cortex. The dura was removed, and an electrocorticography (ECoG) array was placed over V1 (E32-1000-30-200; NeuroNexus). The ECoG array was composed of 32 (4 × 8) Pt electrodes with a 200-μm diameter and a 1-mm pitch. A temporal craniotomy was made to access the optic nerve.

The Flat-OpticSELINE was inserted in the intracranial portion of the nerve by piercing the nerve with a needle (nylon black DLZ 4,8-150 10/0, FSSB) and guiding the Flat-OpticSELINE transversely into the nerve. Rabbits were euthanised at the end of the procedure with an intravenous injection of pentobarbital (120 mg kg$^{-1}$).

### 4.3.6 Electrophysiological recording and stimulation

The ECoG array was connected to the amplifier using a 32-channel analogue head stage for cortical recordings (PZ5; Tucker-Davis Technologies). The Flat-OpticSELINE was attached to a current stimulator (IZ2MH; Tucker-Davis Technologies). Optic nerve stimulation was performed with asymmetric biphasic cathodic-first current pulses (cathodic phase 150 µs; anodic phase 750 µs at one-fifth of the cathodic amplitude; interphase gap 20 µs) at various cathodic current amplitudes (10, 25, 50, 75, 100, 150, 200, 250, 500, 750, 1000, 1500 and 2000 µA). Each stimulus was composed of a single current pulse or a pulse train of 2, 3 or 4 pulses delivered at 1 kHz. Within the train, pulses had the same current amplitude. 52 conditions were generated by combining the current amplitudes (13) and the number of pulses in the train (1, 2, 3 or 4) for each of the 8 stimulating electrodes. A total of 416 stimuli were delivered in a randomised manner. The stimulation protocol was repeated 30 times (Rabbit 1) and 15 times (Rabbit 2) for both monopolar and 3D multilayer CB configurations.

### 4.3.7 Signal processing

Electrically evoked cortical potentials (EEPs) were filtered from 3 to 100 Hz and sampled at 24 kHz. Then, epochs synchronous to the stimulus onset (from –200 to +300 ms) were extracted from the data stream. Before data analysis in MATLAB, EEPs were visually inspected and manually rejected when presenting noisy signals. Afterwards, epochs were down-sampled to 2.4 kHz. An unsupervised approach based on Gaussian Mixture Model (GMM) clustering was used to classify electrodes exhibiting significant EEPs. For each rabbit, 25-ms long epochs after the stimulus onset were concatenated to perform dimensionality reduction with principal components analysis (PCA). The first two PCs were chosen to run the GMM clustering algorithm. The Davies-Bouldin index was used to select the optimal number of clusters. Templates for each cluster were plotted, and those presenting a flat signal were classified as electrodes not exhibiting a significant EEP (non-responsive electrodes). Only recording electrodes showing a significant EEP (responsive electrodes) were considered for further analysis. EEP peak-to-peak amplitudes were computed as the difference between P1 and N1 peaks. A normalised weighted distance was calculated using equation 4.1 to quantify how significantly responses spread across the visual cortex when changing the stimulus parameters[306]:

$$D = \frac{\sum_i r_i d_i}{\sum_i r_i} \tag{4.1}$$

Where $r_i$ is the EEP peak-to-peak amplitude in responsive electrode $i$, and $d_i$ is the cortical distance in mm from the responsive electrode $i$ to the weighted mean centre $\vec{x}_0$ among the

responsive electrodes, as in equation 4.2. $r_i$ is zero for the non-responsive electrodes.

$$d_i = |\vec{x}_i - \vec{x}_0| \tag{4.2}$$

### 4.3.8   Statistical analysis and graphical

Statistical analysis and graphical representation. Statistical analysis and graphical representation were performed with Prism 8 (Graph Pad). The D'Agostino & Pearson omnibus normality test was performed to justify the choice of the statistical test. In plots, p-values were reported as: * $p < 0.05$, ** $p < 0.01$, *** $p < 0.001$, and **** $p < 0.0001$.

## 4.4   Results

### 4.4.1   Hybrid FEA-NEURON modelling

Monopolar configuration is predominantly used in neural stimulation (Figure 4.1b,c). In this case, each electrode has a common and distant return electrode placed several millimetres away. Upon current injection, the electric field spreads from the stimulating electrodes to the common and distant return ground, resulting in an unconfined electrical activation of the neural tissue. We modelled by FEA a 5 x 5 microelectrode array (80-μm diameter and 100-μm pitch) in monopolar configuration. The simulation confirmed that the electric field spread widely (Figure 4.1d,e). Therefore, we designed a CB configuration with a 3D feature to achieve focal stimulation (Figure 4.1f,g). The central and the concentric return electrodes are placed in a multilayer configuration on two layers separated by 6 μm[274]. Moreover, they are independently controlled and referenced to a distal ground. The central electrode is the stimulating electrode (cathodic first), and the return injects a current of opposite polarity (anodic first). Therefore, the electric field is localised from the central electrode to the concentric electrode working as a local independent return. The return coefficient α (from 0.5 to 1) defines the proportion between the current injected into the central electrode, and the current returned to the concentric return. For α = 0.5, the CB stimulation is balanced, and the total current is returned to the concentric electrode. For α > 0.5, only a fraction of the current is returned to the concentric electrode, while the remaining current is returned to the distant ground (Ig). Finally, for α = 1, the system works in the monopolar configuration, and the total current is returned to the distant ground (Ig = I). FEA simulations confirmed that the local return electrode localised the electric field (Figure 4.1h,i).
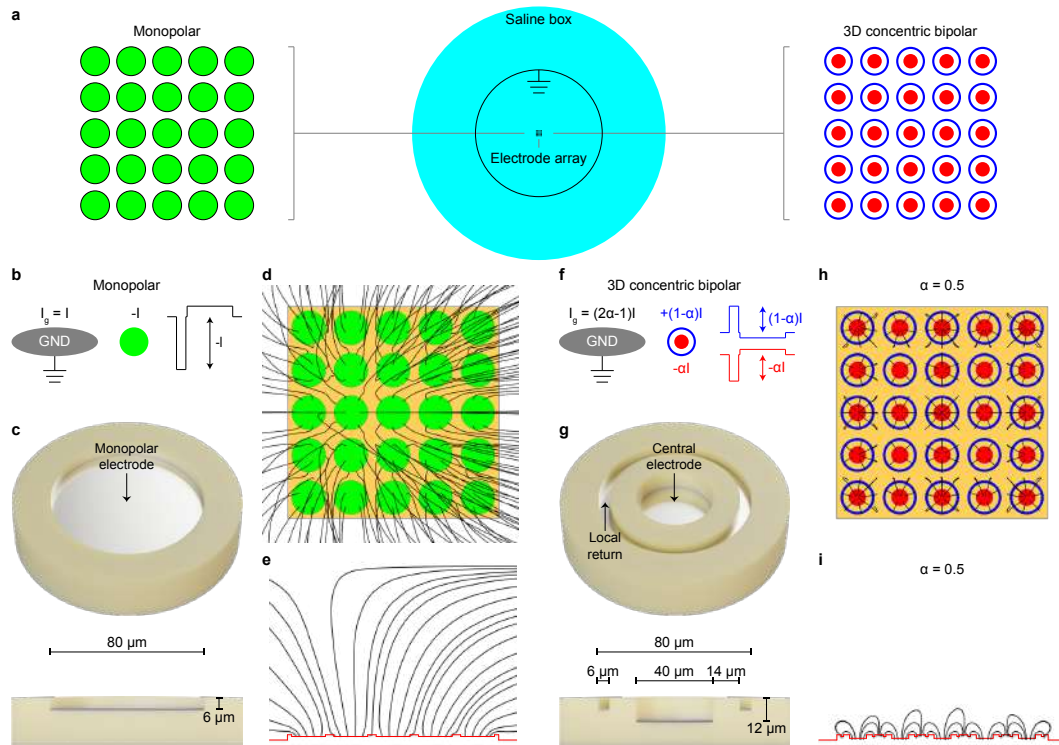
Figure 4.1: (a) Sketch of the FEA simulation. The electrode array (5 x 5 electrodes, 80-µm diameter and 100-µm pitch) is inside a 1-cm height and 2-cm wide saline box. A circular ground electrode (1-cm diameter) is placed concentrically with the electrode array. (b) Monopolar configuration: the current is injected into one electrode (negative for cathodic stimulation) with a faraway common ground. (c) Tilted top view (top) and side view (bottom) of a monopolar electrode. The encapsulation material (PI) is yellow, and the electrode (Pt) is gray. (d,e) Top view (d) and side view (e) of the electric field computed by FEA simulation for the monopolar configuration (all electrodes are active). (e) 3D multilayer CB configuration: the current is injected between the central electrode (cathodic, $-\alpha I$) and the concentric return electrode (anodic, $+(1-\alpha)I$), both referenced to the distal ground ($I_g = (2\alpha-1)I$). (g) Tilted top view (top) and side view (bottom) of a 3D multilayer CB electrode. (h,i) Top view (h) and side view (i) of the electric field computed by FEA simulation for the 3D multilayer CB configuration ($\alpha = 0.5$, all electrodes are active).

To further analyse the performance of CB electrodes and ensure that neighbouring electrodes do not have crosstalk, we repeated the simulation activating different electrodes of the array: central electrode only (Figure 4.2a, left), all electrodes (Figure 4.2a, middle) or all electrodes but with the central electrode off (Figure 4.2a, right). The electric potential profiles were obtained along the midline (dashed black line in Figure 4.2a) in planes at increasing distances from the surface of the array (sketch in Figure 4.2a, middle). When only one electrode is active, the electric potential profile obtained by FEA simulations has a Gaussian shape for both the monopolar configuration (Figure 4.2b, left) and the 3D multilayer CB configuration (Figure 4.2c, left). However, for the monopolar configuration, the lateral spreading of the

electric potential increases as the distance from the electrode increase (Figure 4.2b, left), while it remains sharp for the 3D multilayer CB configuration (Figure 4.2c, left) even on a plane located 100 μm away from the electrode. When all the 25 electrodes are activated, the electric potential profile obtained for the monopolar configuration (Figure 4.2b, middle) is widened and increased in amplitude due to potential summation. The contribution of each electrode is barely distinguishable only at a distance of 10 μm from the electrode surface. Further away, the electric potential fuse. When switching off the central electrode, the electric potential in monopolar configuration remains blurred due to the electrode cross-talk (Figure 4.2b, right). The contrast between the central off electrode and the surrounding active electrodes may not be enough for discrimination. Thus, the electrodes in monopolar configuration cannot be considered electrically independent unless for a much lower density. Conversely, the 3D multilayer CB configuration allows sharp discrimination of the electric potential induced by each electrode at every distance (Figure 4.2c, middle). Also, we observed a maximal contrast in the electric potential drop when the central electrode is switched off (Figure 4.2c, right). In this condition, the electrodes are electrically independent, even for high electrode density.
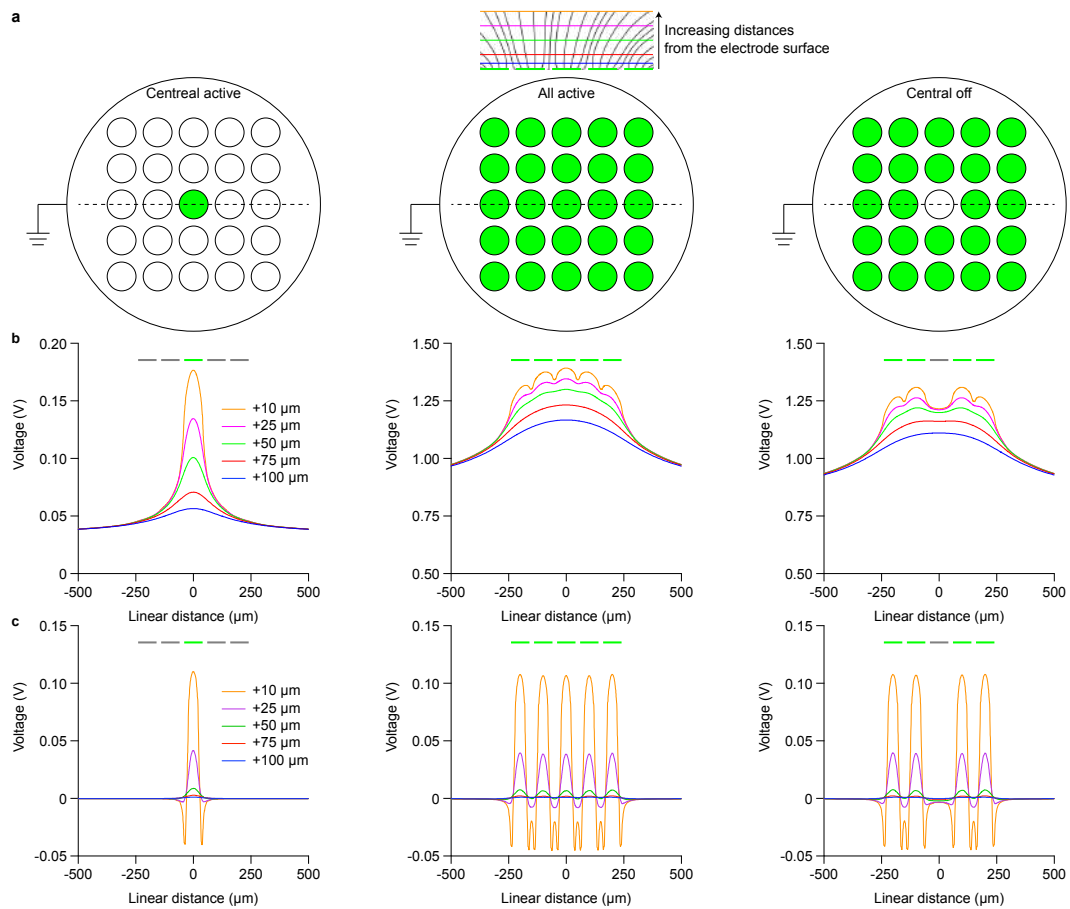
Figure 4.2: (a) Sketch of FEA simulations performed for three patterns: central electrode on (left), all electrodes on (middle) and all electrodes on but central electrode off (right). The electric potentials were measured along the dashed line and at various distances from the electrode surface: +10, +25, +50, +75, and +100 μm. (b) The plot of the electric potential obtained with the monopolar configuration and a current injected of I = -100 μA for the three patterns in (a). (c) The plot of the electric potential obtained with the 3D multilayer CB configuration ($\alpha = 0.5$) and a current injected of -50 μA in the central electrode and +50 μA in the return electrode for the three patterns in (a). In all panels, the green/gray bars show the position of the active (green) and inactive (gray) electrodes.

FEA simulations showed that the 3D multilayer CB configuration focuses the electric potential laterally and vertically. The electric potential decreases substantially with the distance from the electrode surface. This decrease is due to the lateral shunting effect of the concentric return electrode. Thus, the stimulation is localised vertically to a few tens of micrometres from the electrode surface, which is not the case for the monopolar configuration. This feature is useful when a small area around the electrode has to be stimulated, such as optic nerve stimulation for artificial vision. However, measuring the recruitment of nerve fibres in-vivo is a challenging task. Therefore, we implemented a hybrid FEA-NEURON model. First, the electric field generated by the electrical stimulation was computed using FEA simulation for the monopolar

and the 3D multilayer CB configuration ($\alpha = 0.5$). For a better comparison, the dimension of the central cathode was 40 μm in both configurations. Thus, the monopolar configuration is equivalent to the 3D multilayer CB configuration with $\alpha = 1$. Then, the activation probability of the fibres upon electrical stimulation for one electrode located in the centre of the nerve was obtained in NEURON. The model showed that the nerve area activated by one electrode in the 3D multilayer CB configuration ($\alpha = 0.5$) is more confined than the monopolar configuration (Figure 4.3a). Besides the size of the activated area, also the shape is different between the two conditions. The activated area is circular around the central electrode in the monopolar configuration. For low current amplitudes, the shape is not symmetrical to the horizontal plane because the electrode is exposed towards the upper part of the nerve, and the PI substrate reduces the stimulation in the lower part of the nerve. At higher current amplitudes, the activation area becomes more symmetric because of the large spreading of the electric field. In the 3D multilayer CB configuration, the localisation of the electric potential due to the concentric return electrode blocks the activation of the nerve below the plane of the electrode array. This result is crucial to enhance selectivity in TIME arrays. Usually, TIME arrays have electrodes on both sides[73,311] , and 3D multilayer CB electrodes can provide lateral selectivity of the stimulated area even at high current amplitudes. Interestingly, the activated area has a 'three-leaf clover' shape for 3D multilayer CB electrodes. This shape is caused by the anodic activation from the concentric return electrode. The quantification of the total number of activated fibres revealed that a 3D multilayer CB electrode activated about 40 times fewer fibres than a monopolar electrode (Figure 4.3b,c). Also, for 3D multilayer CB electrodes, we found that the return coefficient $\alpha$ linearly modulates the number of activated fibres (Figure 4.3d).
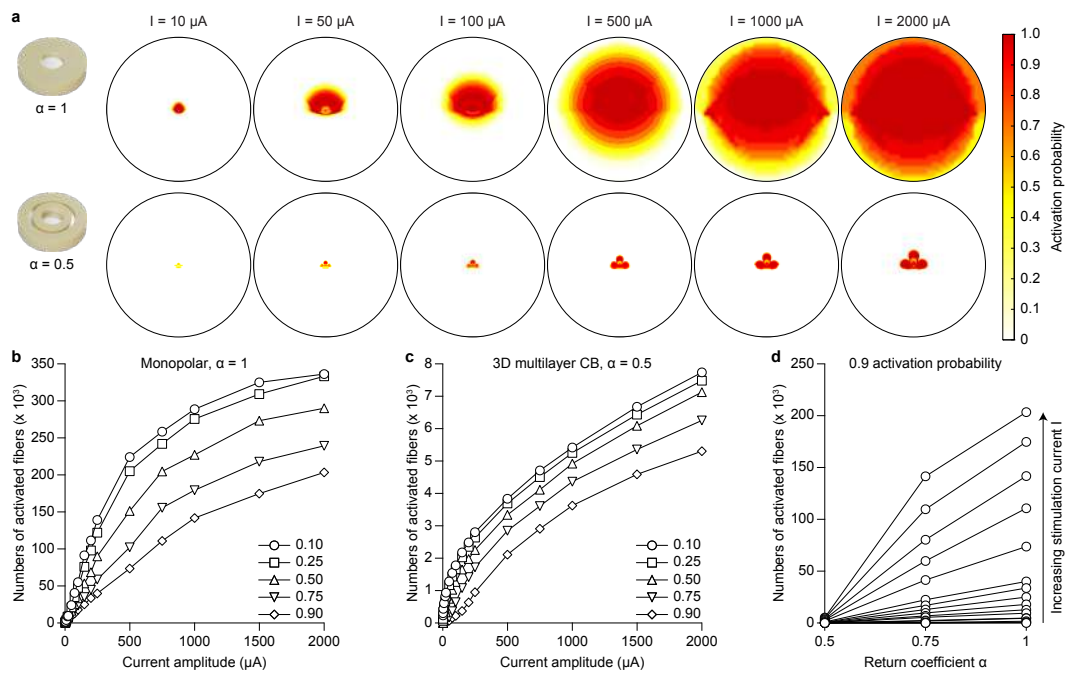
Figure 4.3: (a) Probability activation maps in the optic nerve upon current pulses at increasing current amplitudes from a monopolar electrode ($\alpha = 1$, top) and a 3D multilayer CB electrode ($\alpha = 0.5$, bottom). The black circles correspond to the optic nerve (diameter of 1500 µm). (b,c) The number of fibres activated by a single pulse as a function of the current amplitude from a monopolar electrode (b) and a 3D multilayer CB electrode (c). The quantification was made for 5 activation probabilities (higher than 0.1, 0.25, 0.5, 0.75 and 0.9). (d) The number of fibres activated with a probability higher than 0.9 by a single current pulse as a function of the return coefficient $\alpha$ for increasing current amplitudes. Each set of connected circles refers to one current amplitude. Simulated current amplitudes are 2, 3, 5, 10, 20, 25, 50, 75, 100, 150, 200, 250, 500, 750, 1000, 1500 and 2000 µA.

To further assess the higher selectivity in 3D multilayer CB electrodes, we compared two current amplitudes having a similar total activation probability across the entire nerve section (4.8% percentage change between the two configurations), which is the sum of all the values in the activation probability matrix sampled with a resolution of 1 x 1 µm2. The amplitude is 20 µA for the monopolar configuration and 2000 µA for the 3D multilayer CB (Figure 4.4a). It must also be clarified that a similar total activation probability corresponds to a similar number of activated fibres. Then, we computed the cumulative distribution of all the activation probabilities within the two maps (Figure 4.4b). The 3D multilayer CB configuration (red line) contains a higher proportion of high activation probabilities than the monopolar configuration (black line), visible from the left shift of the curve and the steeper increase. For instance, in the 3D multilayer CB configuration, 60% of the area is activated at a probability higher than 0.9 (dashed gray line), while only 40% in the monopolar configuration. This result shows that when the same averaged number of fibres are activated (similar total activation probability across the entire nerve section), the 3D multilayer CB configuration activates fibres (both

small and large) in a smaller area close to the electrode. On the contrary, the monopolar configuration activates a more diffuse area. Indeed, despite the total activation probability across the entire nerve section being similar (4.8% percentage change), the total activated area (black contour in the maps) is larger by a 30.4% percentage increase in the monopolar configuration. The peripheral area with low activation probabilities visible in the monopolar configuration is associated with the activation of larger fibres away from the electrode since they have a lower activation threshold compared to smaller fibres.
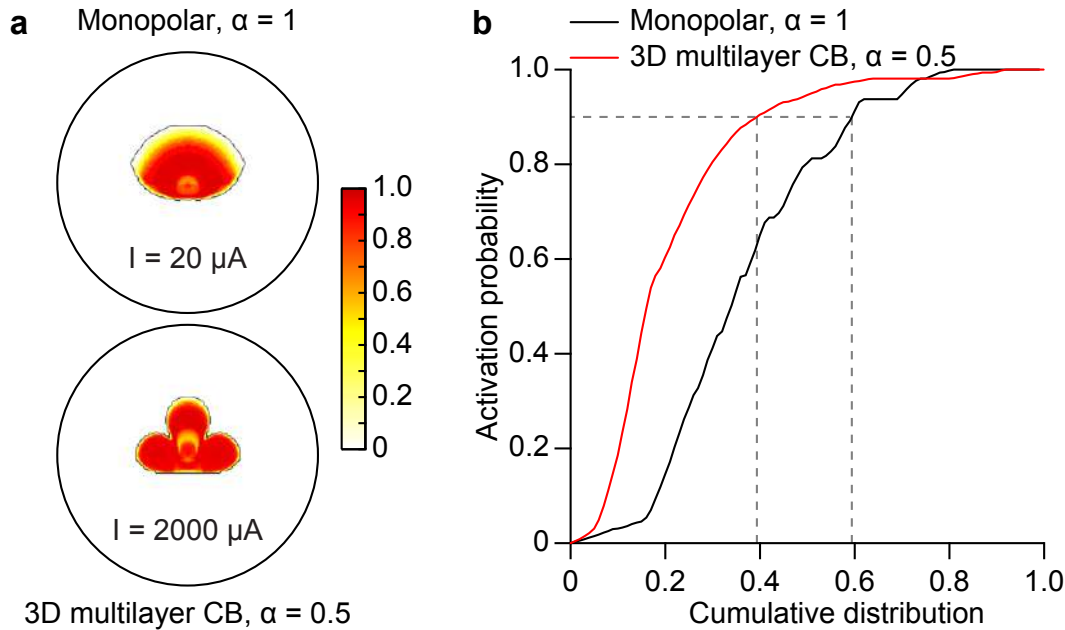


Figure 4.4: (a) Magnified view of two activation maps, corresponding to 20 μA for the monopolar electrode (α = 1, top) and 2000 μA for the 3D multilayer CB electrode (α = 0.5, bottom). The black contour delimits the total activated area (non-zero activation probability). The black circles correspond to a portion of the nerve with a diameter of 750 μm. The colour scale is the activation probability. (b) Plot of the activation probability as a function of the cumulative distribution of the non-zero activation probabilities within the activation matrix for the monopolar (α = 1, black) and the 3D multilayer CB (α = 0.5, red) configurations. Dashed gray lines highlighted the cumulative distribution at an activation probability of 0.9.

### 4.4.2   Flat-OpticSELINE microfabrication and characterisation

We fabricated a Flat-OpticSELINE electrode array with 8 3D multilayer CB electrodes having a 40-μm diameter and a 160-μm pitch (Figure 4.5a). Electrodes are placed in two layers to reduce the space occupied by the feedlines: the central electrodes are in the bottom layer (Figure 4.5a, gray), and the concentric return electrodes are in the top layer (Figure 4.5a, black). Feedlines from the same electrode pair are overlaid. Electrodes were coated with PtB (Figure 4.5b,c). EIS and CV showed that the impedance magnitude and phase at 1 kHz decreased (p < 0.0001 for both, two-tailed Wilcoxon matched-pairs signed rank test) and the charge storage

capacity (CSC) increased (p < 0.0001, two-tailed Wilcoxon matched-pairs signed rank test) for both central and return electrodes after coating with PtB (Figure 4.5d-f).
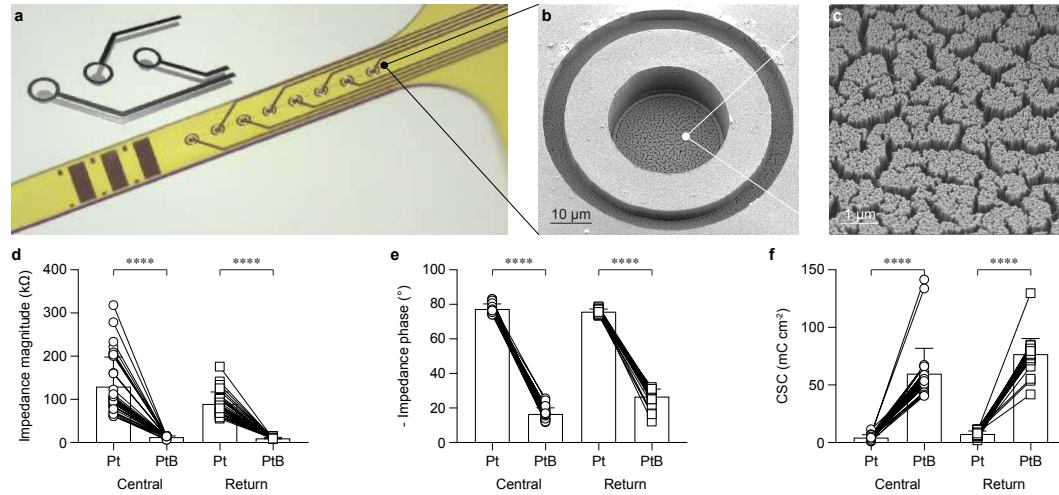


Figure 4.5: (a) Picture of a Flat-OpticSELINE with 8 3D multilayer CB electrodes. The sketch shows the electrode positions in the two planes. Central electrodes are in gray, and concentric return electrodes are in black. (b) Scanning electron microscope image of one 3D multilayer CB electrode. (c) Magnified scanning electron microscope image of the PtB coating. (d) Quantification of the impedance magnitude at 1 kHz before (circles) and after (squares) coating with PtB for both the central and return electrodes. (e) Quantification of the impedance phase at 1 kHz before (circles) and after (squares) coating with PtB for the central and return electrodes. (f) Quantification of the total charge storage capacity before (circles) and after (squares) coating with PtB for the central and return electrodes. In panels d-f, bars show the mean ± s.d.

### 4.4.3 Electrophysiological validation in-vivo

The Flat-OpticSELINE with 3D multilayer CB electrodes was transversally inserted in the optic nerve, and EEPs were recorded upon electrical stimulation with biphasic charge-balanced asymmetric current pulses of different current amplitudes ranging from 10 to 2000 μA (Figure 4.6a). EEPs were detected using an ECoG electrode array placed over V1 contralateral to the implanted optic nerve. In each experiment, EEPs were recorded from both monopolar ($\alpha$ = 1) and the 3D multilayer CB ($\alpha$ = 0.5) configurations (Figure 4.6b,c). After dimensionality reduction through PCA, significant responses to electrical stimulation were classified using a GMM clustering algorithm (Figure 4.6d). For each cluster, we then plotted the template responses. Clusters that appeared near the origin of the axes in the PCs space contained those responses that exhibited no stimulus-related modulation and showed a flat template (Figure 4.6d, red). Therefore, the other clusters were considered to contain significant responses (Figure 6d, green and blue). Last, we applied a detection algorithm to determine N1 and P1 peaks and compute the EEP peak-to-peak amplitudes.
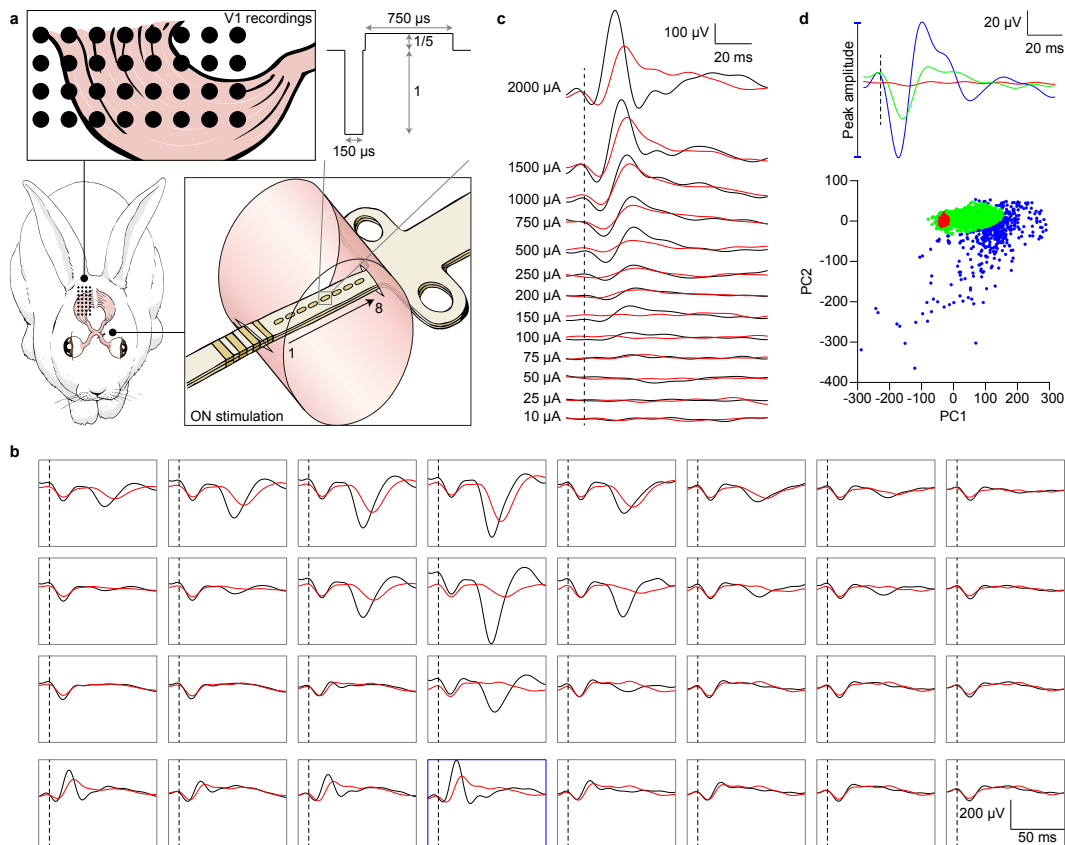
Figure 4.6: (a) Sketch of the experiment. (b) Representative examples of EEPs recorded upon monopolar ($\alpha = 1$, black) and the 3D multilayer CB ($\alpha = 0.5$, red) stimulations from the same electrode at the maximum current amplitude (2000 µA). The 4 x 8 boxes correspond to the arrangement of the 32 electrodes in the ECoG array. The dashed black lines show the onset of the electric stimulus. The blue box identifies the recording channel highlighted in panel c. (c) Representative example of EEPs recorded by one electrode (blu box in b) upon monopolar ($\alpha = 1$, black) and the 3D multilayer CB ($\alpha = 0.5$, red) stimulations at increasing current amplitudes. The dashed black line shows the onset of the electric stimulus. (d) Bottom: PC1-PC2 space after GMM Clustering (k = 3). Top: template responses from each cluster.

The mean EEP peak-to-peak amplitudes for all the recording and stimulating electrodes in both conditions, monopolar ($\alpha = 1$) and 3D multilayer CB ($\alpha = 0.5$), showed a monotonic growth as a function of the current amplitude (Figure 4.7a). It was also apparent that EEP peak-to-peak amplitudes became higher than zero, starting from a current amplitude of 150 µA for the monopolar configuration and 250 µA for the 3D multilayer CB. A linear regression fitting showed that the slopes of the two lines are significantly different ($p < 0.0001$), confirming the prediction of the hybrid FEA-NEURON model. Next, we assessed at which current amplitude each stimulating electrode elicited a significantly different averaged EEP peak-to-peak amplitude between the monopolar ($\alpha = 1$) and the 3D multilayer CB ($\alpha = 0.5$) configurations using the Kolmogorov-Smirnov test (Figure 4.7b). From 150 µA, an increasing

number of stimulating electrodes appeared to elicit a significantly different EEP. While from 1500 μA, all the stimulating electrodes (8 per rabbit) showed a significant difference between monopolar ($\alpha = 1$) and the 3D multilayer CB ($\alpha = 0.5$) configurations.
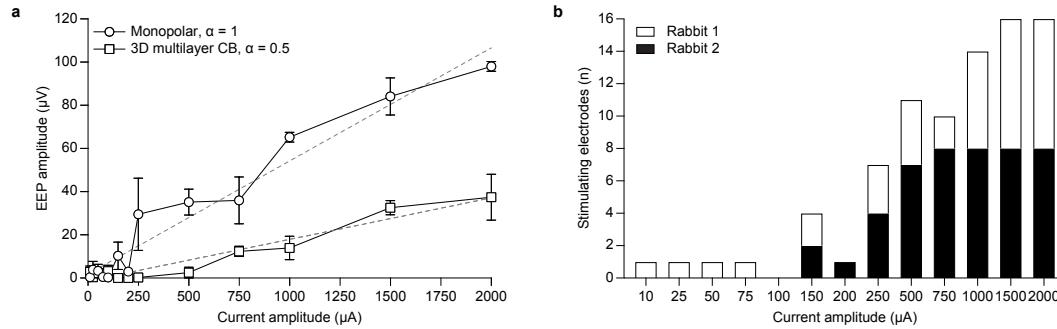


Figure 4.7: (a) Quantification of the mean (± s.e.m., N = 2 rabbits) EEP peak-to-peak amplitudes for all the recording and stimulating electrodes in monopolar ($\alpha = 1$, circles) and the 3D multilayer CB ($\alpha = 0.5$, squares) configurations. The dashed grey lines are linear regressions. For monopolar configuration: slope = 0.0524, R squared = 0.9140. For 3D multilayer CB configuration: slope = 0.0192, R squared = 0.8488. Both slopes are significantly non-zero ($p < 0.0001$). (b) Quantification of the number of stimulating electrodes that present a significant difference ($p < 0.05$, Kolmogorov-Smirnov test) in the averaged EEP peak-to-peak amplitude at different current amplitudes between monopolar ($\alpha = 1$) and the 3D multilayer CB ($\alpha = 0.5$) configurations.

The previous analysis compared the averaged EEP peak-to-peak amplitudes in both monopolar ($\alpha = 1$) and 3D multilayer CB ($\alpha = 0.5$) configurations, but it did not consider the spatial extent of the evoked response. Qualitatively, the evoked cortical response spread across more recording channels for increasing current amplitudes. However, it remained more localised when the 3D multilayer CB configuration was used instead of the monopolar configuration (Figure 4.8a). To quantify this difference, we computed two indexes: (1) the number of responsive electrodes (Figure 4.8b,d) and (2) the normalised weighted distance (Figure 4.8c,e). Results showed that fewer recording electrodes had a significant response in the 3D multilayer CB configuration compared to the monopolar configuration (Figure 4.8b,d). Polling the data of two rabbits together, one curve cannot fit both sets ($p < 0.0001$, F = 13.86, DFn = 4, DFd = 44) indicating that the two curves are significantly different (Figure 4.8d). Similarly, the normalised weighted distance was smaller, at every current amplitude, for the 3D multilayer CB configuration (Figure 4.8c,e). Polling the data of two rabbits together, one curve cannot fit both sets ($p < 0.0001$, F = 11.80, DFn = 4, DFd = 44) indicating that the two curves are significantly different (Figure 4.8e).
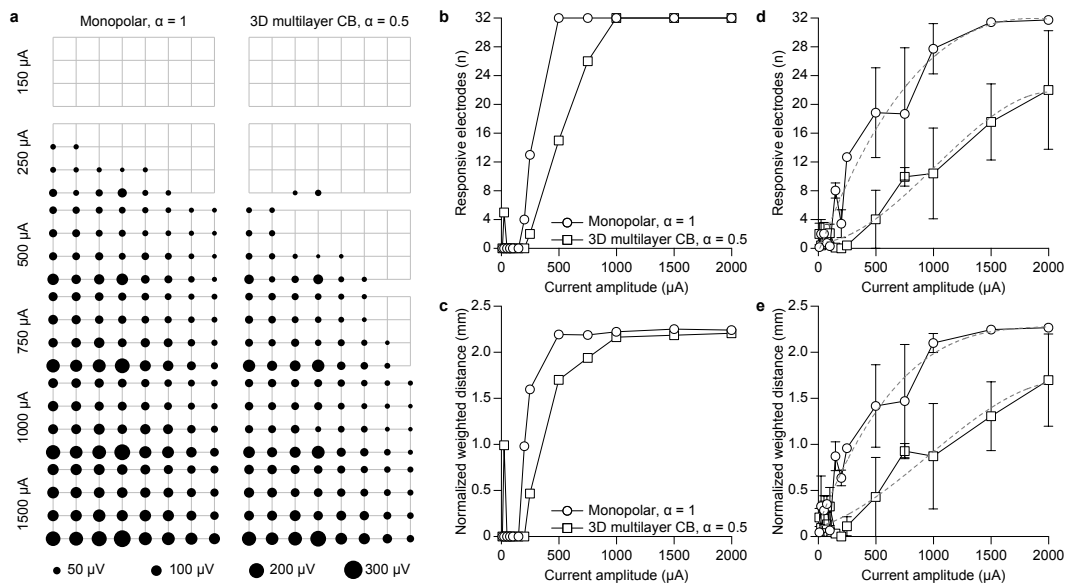
Figure 4.8: Quantification of the cortical activation spreading upon electrical stimulation of the optic nerve in monopolar vs 3D CB configurations

(a) Activation maps for one stimulating electrode in monopolar ($\alpha = 1$) and the 3D multilayer CB ($\alpha = 0.5$) configurations. The size of the circles corresponds to the EEP peak-to-peak amplitudes. Only responsive electrodes are shown. The grey grid highlights the electrode positions. (b) Quantification of the number of responsive electrodes as a function of the current amplitude in monopolar ($\alpha = 1$, circles) and the 3D multilayer CB ($\alpha = 0.5$, squares) configurations. Representative example for one stimulating electrode in one rabbit. (c) Quantification of the normalised weighted distance as a function of the current amplitude in monopolar ($\alpha = 1$, circles) and the 3D multilayer CB ($\alpha = 0.5$, squares) configurations. Representative example for one stimulating electrode in one rabbit. (d) Quantification (mean ± s.e.m) of the number of responsive electrodes as a function of the current amplitude in monopolar ($\alpha = 1$, circles) and the 3D multilayer CB ($\alpha = 0.5$, squares) configurations across all the stimulation electrodes (n = 8 electrodes) and animals (N = 2 rabbits). The dashed grey lines are the third-order polynomial (cubic) regressions. For monopolar configuration: R squared = 0.8873. For 3D multilayer CB configuration: R squared = 0.7785. (e) Quantification (mean ± s.e.m) of the normalized weighted distance as a function of the current amplitude in monopolar ($\alpha = 1$, circles) and the 3D multilayer CB ($\alpha = 0.5$, squares) configurations across all the stimulation electrodes (n = 8 electrodes) and animals (N = 2 rabbits). The dashed grey lines are the third-order polynomial (cubic) regressions. For monopolar configuration: R squared = 0.8725. For 3D multilayer CB configuration: R squared = 0.7306.

Last, we investigated the possibility of modulating the cortical responsivity by changing the return coefficient $\alpha$ or increasing the number of pulses in the train (Figure 4.9). When changing the return coefficient, the linear regression fitting showed that the slopes of the two lines ($\alpha = 0.5$ vs. $\alpha = 0.75$) were significantly different (p = 0.0394 for 1 pulse; p < 0.0001 for 2 pulses; p <

0.0001 for 3 pulses; p < 0.0001 for 4 pulses). This result confirms the prediction of the hybrid FEA-NEURON model (Figure 4.3d). Similarly, when increasing the number of pulses in the train, the linear regression fitting showed that the slopes of the four lines were significantly different (p = 0.0035 for $\alpha = 0.5$; p < 0.0001 for $\alpha = 0.75$). This result confirms the previous finding that the cortical activation can be modulated in amplitude by increasing the number of pulses instead of changing the current intensity[73]. More pulses in the train increased the EEP peak-to-peak amplitude by increasing the probability of fibre activation via a mechanism of temporal summation resulting from the repeated activation of the same few fibres and not by the enlargement of the activated area of the nerve.
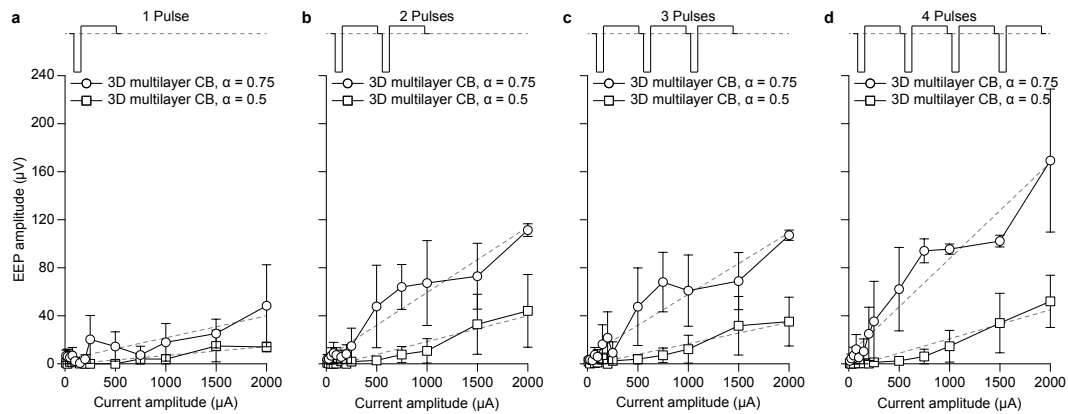


Figure 4.9: Quantification (mean ± s.e.m., N = 2 rabbits) of the EEP peak-to-peak amplitudes across all the recording and stimulating electrodes in the 3D multilayer CB configuration with return coefficient $\alpha = 0.75$ (circles) and $\alpha = 0.5$ (squares) for trains with 1 pulse (a), 2 pulses (b), 3 pulses (c) and 4 pulses (d) at 1 kHz pulse rate. The dashed gray lines are linear regressions. All slopes are significantly non-zero (p < 0.0001).

## 4.5   Discussion

In this article, we proposed a 3D multilayer CB electrode array that enhances the selectivity of optic nerve stimulation. We first investigated the effectiveness of 3D multilayer CB configuration in reducing the number of fibres activated by electrical stimulation with a hybrid FEA-NEURON model. Then, we assessed in-vivo the spread of neural activation in the visual cortex compared to monopolar stimulation. These findings are consistent with previous evidence that local return stimulation can be used to restrict the electrical activation of neurons by shaping the electric field[317,318]. Other approaches have been proposed to localise electrical stimulation. A first approach, called quasi-monopolar (QMP), has a distant ground electrode and a plane of hexapolar return electrodes surrounding each stimulating electrode. Each electrode in the array is alternatively used as a stimulating electrode or as part of the hexapolar return. This approach has been implemented in a suprachoroidal prosthesis under development by Bionic Vision Technologies[312,319], but several disadvantages have been identified[320]. QMP requires complex current injection schemes at each of the hexapolar electrodes, and the

electrodes in the external perimeter of the array cannot be used for QMP stimulation. Also, the QMP configuration is suitable for large surface electrode arrays (e.g. retinal prostheses or ECoG arrays) and not for intraneural electrode arrays. Last, complex stimulation patterns at high resolution cannot be easily obtained since, for every stimulating electrode, the six surrounding electrodes are used as a return. A second option is the ground plane configuration, where a highly conductive local ground plane provides focalisation of the currents[321,322]. Compared to the QMP configuration, its main advantage is that it requires fewer feedlines, which is necessary for arrays with many electrodes (e.g. > few hundreds). Besides this advantage, it has several limitations. First, it requires a highly conductive surface (> 5,000 S m$^{-2}$). A metallic ground plane exposed to the extracellular medium is not advantageous because of the risk of delamination, it makes the device not transparent (if necessary), and it may crack due to the implant bending necessary in most surgical insertions. Last, a ground plane surrounding each electrode of the array limits the final electrode density.

A 3D multilayer CB electrode provides a stimulation configuration that strongly reduces crosstalk between electrodes. The multilayer process allows placing concentric electrodes on different layers and patterning the feedlines from the same electrode overlaid. Therefore, each electrode pair occupies the same space on the array as the monopolar configuration. However, because the two electrodes are independently controlled, the number of pads will be doubled compared to the monopolar configuration.

In the study, we compared monopolar and 3D multilayer CB configurations using a hybrid FEA-NEURON model of the optic nerve. The results showed a substantial reduction in fibres activated with the 3D multilayer CB electrode. However, measuring the fibre activation upon electrical stimulation in the optic nerve remains an open challenge due to the limited space available in the intracranial segment, where the array is currently implanted. In addition to the stimulating array, another electrode array should be inserted for recordings to validate simulations. Future works may address this challenge ex-vivo combining stimulation and recording on explanted optic nerves**eva** (Evans et al. 2010). Here, we choose to measure the activation in the visual cortex. Thus, we could infer that a lower peak-to-peak amplitude of the EEPs with the 3D multilayer CB configuration is associated with fewer fibres activated in the optic nerve.

To select significant EEPs, we first used PCA as a feature extraction method. We selected the first two principal components representing more than 95% of the variance[323]. EEPs were clustered according to a GMM algorithm: an unsupervised method used to cluster unlabeled data with advantages over the more classic k-means. The most important advantage is that GMM accounts for the data variance and can handle oblong clusters. The dimensionality reduction and clustering of the EEPs were automatic and relatively assumption-free[324], enabling a straightforward classification of significant EEP without defining a priori punctual features, such as latency or amplitude. Indeed, we already showed that punctual features appeared to be not informative enough for prediction models[63]. Hence, this classification allowed us to compare how significant electrically evoked responses spread across the cortex with changing

stimulus parameters and electrode configuration.

Consistent with a previous study on suprachoroidal stimulation[325], the 3D multilayer CB configuration activated smaller EEPs and a smaller area on the cortex than the monopolar electrodes. We then quantified the activated area by computing the response spread across the visual cortex. We showed it increased with increasing current amplitudes for both monopolar, as presented in[306], and 3D multilayer CB configurations. However, on average, the extent of this spatial spread was significantly lower for the 3D multilayer CB configuration. Moreover, we also find that the current threshold for cortical activation with the 3D multilayer CB configuration was higher than for monopolar. It is possible that the signal-to-noise ratio and the spatial resolution of the ECoG array used in this study were not sufficient to record EEP upon activation of a small number of fibres, such as with low current amplitude in 3D multilayer CB configuration. Therefore, future works should employ recording solutions with higher spatial resolution. High-density intracortical microelectrodes arrays (e.g. Utah array) placed in multiple locations of the visual cortex could help assess the performance of the 3D multilayer CB configuration at low currents. Alternatively, fast three-dimensional functional imaging tools[326,327] could also provide better spatial resolution in cortical recordings.

Last, we observed that the modulation of the return coefficient $\alpha$ could increase the number of fibres activated and the EEP peak-to-peak amplitude. It must be noted that we designed 3D multilayer CB electrodes where the area of the central and return electrodes are almost identical. Thus, further work could investigate electrodes having different surface areas to optimise the stimulation efficiency.

## 4.6 Conclusions

Spatial selectivity in neuromodulation refers to interacting with neurons in a predefined and limited volume of tissue[75]. This ability is key in avoiding side effects and improving outcomes for neurological treatments. Highly localised electrical stimulation is an attractive solution to reach spatial selectivity. Here, we proposed a feasibility study of a 3D multilayer CB configuration carried out in the optic nerve. However, this approach could be extended to other applications. For example, in retinal prostheses, this configuration could help to increase spatial resolution. In cortical stimulation with surface electrodes, activation of a confined area in the somatosensory cortex could improve sensory feedback giving higher spatial discrimination in the corresponding perceived body parts[28]. A higher spatial resolution would be equally important in cortical visual prostheses, like the Orion I device[97]. Moreover, stimulation selectivity applies to peripheral nerve stimulation as well. For instance, it could help limit the side effects of unspecific vagus nerve stimulation and improve the treatment of pathological conditions[328,329]. Lastly, the 3D multilayer CB configuration could better modulate bladder functions in spinal cord injured patients[330]. In any case, spatially precise electrical stimulation requires a microscopic understanding of the anatomical and functional organisation of the target tissue, which is often missing, like for the optic nerve. This knowledge

might provide a further step toward personalised bioelectronic medicine.

## 4.7 Acknowledgments

# 5 Conformable neural interface based on off-stoichiometry thiol-ene-epoxy thermosets

Authors: Eleonora Borda[1], Marta Jole Ildelfonsa Airaghi Leccardi[1], Danashi Imani Medagoda[1], Elodie Geneviève Zollinger[1] and Diego Ghezzi[1]

[1] Medtronic Chair in Neuroengineering, Center for Neuroprosthetics, Institute of Bioengineering, School of Engineering, École Polytechnique Fédérale de Lausanne, Switzerland

## 5.1 Abstract

Off-stoichiometry thiol-ene-epoxy (OSTE+) thermosets have recently gained attention for the rapid prototyping of microfluidic chips because they show low permeability to gases and little absorption of dissolved molecules, they allow direct low-temperature dry bonding without surface treatments, they have a low Young's modulus, and they can be manufactured via UV polymerisation. The compatibility with standard clean-room processes and the outstanding mechanical properties make OSTE+ an excellent candidate as a novel material for neural implants. Here we exploit OSTE+ to manufacture a conformable multilayer microelectrocorticography array with 16 platinum electrodes coated with platinum black. The mechanical properties allow device conformability to curved surfaces such as the brain. The

low permeability and strong adhesion between layers improve the stability of the device. Acute experiments in mice show the multimodal capacity of the array to record and stimulate the neural tissue by smoothly conforming to the mouse cortex. Devices are not cytotoxic, and immunohistochemistry stainings reveal only modest foreign body reaction after two and six weeks of implantation. This work introduces OSTE+ as a promising material in the field of implantable neural interfaces.

## 5.2 Introduction

The nervous system is an extraordinarily complex system capable of receiving, processing and sending a large amount of information simultaneously across multiple central and peripheral regions. Any damage in these areas, caused by illness, genetic disorders or traumatic injuries, might lead to transient or permanent deficits in sensory, cognitive or motor abilities. Advances in neural interfaces[160,166,167,331–333] have contributed to a better understanding of the underlying mechanisms of the nervous system[334,335] and to improving several therapeutic solutions[259,336–339].

One of the main challenges for neural interfaces is to reduce the foreign body response[340] and preserve their long-term functioning[75,341]. A glial scar is traditionally described as a passive barrier that encapsulates the device, alters the tissue-electrode interface, and impairs neural sensing and stimulation[342–344]. The mechanical mismatch between a neural implant, which is often fabricated with stiff materials, and the soft neural tissue is a crucial limitation inducing neural damage and glial scar formation[172]. The neural tissue is dynamic and subject to deformations caused, for example, by blood pulsation, respiratory pressure, and natural body movements[172,345]. By contrast, most neural interfaces are static. On the other hand, activated microglia and macrophages release soluble factors that can accelerate electrode corrosion and degradation[346]. However, the biological response of the tissue is not the only source of failure. The material and mechanical integrity of the neural interface should also be considered[344]. Electrode corrosion and insulation failure are just two examples that can hinder the long-term stability and performance reliability of these devices[343].

A large body of research in neural interfaces is addressing this issue by investigating novel materials and less invasive surgical approaches. On the contrary, clinical-grade neural implants have undergone only minor changes in the past 70 years[347]. In general, they have large electrode paddles with thick platinum-iridium electrodes and stainless-steel wires embedded in a millimetre-thick silicone matrix[172]. Moreover, a large part of the manufacturing process is done manually. Because of the manufacturing processes and geometrical characteristics, these implants lack important features, such as a high electrode density to improve spatial resolution[348], and low implant stiffness to match the elastic modulus of the neural tissue[73,128,166,257,349–351]. Polyimide (PI), parylene-C and SU-8 are widely used in neural implants because they are biochemically and thermally stable, and processable with silicon-based microfabrication technologies[352–354]. Ultra-thin layers of these materials improved

device flexibility achieving relatively long-term integration within the neural tissue[355]. However, when excessively bent, they permanently fold, preventing a tight interface with the nervous tissue[356]. Moreover, the relatively high Young's modulus (GPa range) and limited elastic deformation[268] make them less suitable for complying with the small and large movements of the nervous tissue[357]. Elastomers such as polydimethylsiloxane (PDMS), on the other hand, exhibit a Young's modulus three orders of magnitude lower (MPa range) and a much broader elastic regime under strain than PI, parylene-C and SU-8. PDMS has been widely used for conformable and soft interfaces placed on the surface of the spinal cord, brain, retina, and peripheral nerves[37,268–270,358,359]. However, despite the superior mechanical properties, micropatterning on PDMS with conventional clean-room processes is an open challenge[360]. Most recently, ultra-soft materials (kPa range), like hydrogels, have also been investigated not only as a conductive coating for electrodes[163] but also as biocompatible substrates matching the mechanical properties of the neural tissue[361,362]. Similarly to PDMS, the microstructuring process of hydrogels and their integration with functional materials are still at an early stage[363]. Moreover, it is still unclear if reducing Young's modulus of neural implants to this degree would have any benefits in chronically implanted devices[364].

So far, materials for neural implants have been characterised either by excellent compliance with clean-room processes (e.g. PI, parylene-C and SU-8) but high mechanical mismatch with the nervous tissue or, on the contrary, high mechanical compliance but poor manufacturing compatibility (e.g. PDMS and hydrogels). Off-stoichiometry thiol-ene-epoxy (OSTE+) thermosets have been developed for the rapid prototyping of biocompatible microfluidic chips with low permeability to gases and little absorption of dissolved molecules[365–367]. OSTE+ is based on the versatile UV-curable thiol–ene chemistry which provides off-stoichiometry ratios to enable one-step surface modifications, tunable mechanical properties (from GPa to MPa at physiological temperature), and leakage-free sealing via direct UV-bonding[275,368]. In this way, OSTE+ films are patterned with photolithographic techniques and covalently linked via the epoxy- and thiol-binding chemistry without any adhesion enhancing method (e.g. plasma activation). The versatile properties of OSTE+ make them a promising material for neural interfaces[368] encompassing the features of previously used materials, such as excellent compliance with clean-room processes (e.g. PI, parylene-C and SU-8), high mechanical compliance (e.g. PDMS) and, in addition, low permeability to gases and molecules.

Based on the aforementioned reasons, we exploited OSTE+ to fabricate a conformable multi-layer micro-electrocorticography (μECoG) array. We characterised mechanical and electro-chemical properties as well as showed the multimodal capacity of the implant to record and stimulate the brain in-vivo. Then, we performed an immunohistochemical analysis after two and six weeks of implantation to assess the foreign body response caused by the implanted conformable multilayer OSTE+ μECoG array. This work shows that OSTE+ is a promising material for implantable neural interfaces.

## 5.3    Materials and methods

### 5.3.1    OSTE+

OSTEMER 324 Flex (Mercene Labs) was prepared by mixing the two components in a 1.24:1 ratio.

### 5.3.2    Mechanical characterization

OSTEMER 324 Flex mix was spin-coated (1000 rpm, 60 s) onto 4-inch silicon (Si) wafers previously coated with a sacrificial layer in poly(4-styrene-sulfonic acid) (PSS; 561223, Sigma Aldrich). Thiol-ene photopolymerization was performed under UV light (365 nm, 2 min; Gia-Tec). This step was repeated five times to reach a thickness of 150 µm. Samples were then baked overnight at 95 °C to complete the thiol-epoxy thermal polymerization from the thiol excess. Once fully cured, samples were cut by laser (10 J; WS Turret200, Optec Laser Systems) and released in deionized water. Mechanical properties of OSTEMER 324 Flex samples were determined by dynamic mechanical and thermal analysis (DMTA; DMA Q800, TA Instruments) and tensile testing (MTS Systems Corporation). DMTA was operated using a 150-µm thick sample at a thermal ramping of 0.2 °C s$^{-1}$ and a measurement frequency of 1 Hz. For the tensile test, 150-µm thick dog-bone shaped samples (ASTM D412) were mounted in the MTS grips and the crosshead speed was set at 1% of the length between the grips (in mm s$^{-1}$). The displacement and the corresponding force during the test were recorded automatically using the MTS TestSuite™ TW Software (MTS Systems Corporation). The elastic modulus was then calculated as the slope of the curve between 10% and 30% strain (linear regime) using MATLAB (MathWorks), while the elongation at break was defined as the strain with the highest stress value before fracture. Cyclic stress-strain curves were obtained with the same machine by setting in advance the applied percentage of strain. PI samples for the tensile test were prepared by spin-coating PI (PI2611, HD MicroSystems) on a 4-inch Si wafer (1500 rpm, 60 s), soft-baking at 65 °C (5 min) and 95 °C (5 min), and hard-baking at 200 °C (1 hr) and 300 °C (1 hr) both in a nitrogen atmosphere. Samples were cut by laser and peeled off the wafer. PI thickness was 8 µm.

### 5.3.3    Resolution and stability tests

A 30-µm thick layer of OSTEMER 324 Flex was spin-coated (1000 rpm, 60 s) onto a PSS-coated 4-inch Si wafer, cured under UV light (2 min) and baked overnight at 95 °C. Photolithography with a 10-µm thick photoresist (AZ 10XT) was performed to pattern platinum (Pt) lines of different sizes and shapes. Soft-baking was performed at 60 °C to avoid cracks on the photoresist due to the softening of OSTEMER 324 Flex at high temperature. Pt was deposited by DC magnetron sputtering (150 nm) followed by lift-off in propylene glycol monomethyl ether acetate (PGMEA, Sigma-Aldrich) during sonication (20 min). To fully encapsulate the metal layer, OSTEMER 324 Flex was spin-coated (6-µm thick, 2500 rpm, 60 s), cured under UV light (2 min) and

baked overnight at 95 °C. Samples were then laser-cut and released in deionized water. PI samples were prepared as follows. A titanium/aluminium (Ti/Al, 10/100 nm) release layer was evaporated directly onto a 4-inch Si wafer. A 12-µm thick PI layer was obtained by spin-coating (1000 rpm, 60 s), soft-baking at 65 °C (5 min) and 95 °C (5 min), and hard-baking at 200 °C (1 hr) and 300 °C (1 hr) both in a nitrogen atmosphere. Ti/Pt lines were fabricated by DC magnetron sputtering (15/300 nm) onto PI treated with oxygen plasma (200 W, 20 s), followed by photolithography and chlorine-based dry etching (Corial 210 RIE). The wafer was coated again with a 6-µm thick layer of PI (2000 rpm, 60 s). Samples were cut by laser and released by Al anodic dissolution. Images of the Pt lines were taken with an optical microscope before encapsulation in both OSTEMER 324 Flex and PI samples. The stability test was performed in a sonication bath (185 W) at 37 °C with samples immersed in deionised water.

### 5.3.4 Adhesion tests

Samples were designed according to the standard test method for peel resistance and adhesives (T-Peel Test, ASTM D1876-08). Structures were 77.5-mm long and 8.3-mm wide. Two samples were manufactured: one to test adhesion between two OSTEMER 324 Flex layers and the other to test between OSTEMER 324 Flex and Pt. In the first sample, two layers of OSTEMER 324 Flex were prepared as previously described (layer thickness of 150 µm). In the second sample, Pt was deposited by DC magnetron sputtering (150 nm) followed by lift-off in PGMEA during sonication (20 min). In both samples, a 25-µm thick PI foil (Kapton) was used to separate the two layers of OSTEMER 324 Flex. Mechanical T-peel tests were performed using the tensile-load frame with a 10 N load cell at a crosshead translation rate of 0.1 mm s-1. The displacement and the corresponding force during the test were recorded automatically using the MTS TestSuite™ TW Software. Tests were performed at room temperature.

### 5.3.5 µECoG array fabrication

OSTE+ EcoG arrays were designed to cover a large surface of the mouse cortex. A PSS sacrificial layer was deposited on a 4-inch Si wafer, followed by spin-coating of a 30-µm thick layer of OSTE+ Flex as previously described. Photolithography with photoresist was performed to pattern Pt as previously described. Electrodes (40 µm in diameter) with 30-µm wide inter-connects with horse-shoe shape ($\vartheta = 45°$, W = 30 µm, R = 90 µm) were manufactured on the bottom layer. A 6-µm thick layer of OSTE+ Flex was spin-coated for encapsulation onto the wafer treated with a short and low power oxygen plasma (30 W, 30 s) and exposed to UV laser (375 nm, 800 mJ cm$^{-2}$) with a maskless aligner (MLA 150, Heidelberg). The OSTE+ Flex layer was developed in ethyl L-lactate (77367, Sigma-Aldrich) for 210 s, rinsed in isopropanol and DI water, dried with a nitrogen gun and cured at 95 °C overnight. The metallization and OSTE+ Flex encapsulation steps were repeated for the top layer. OSTE+ EcoG arrays were then shaped by laser and released from the wafer by PSS dissolution in DI water. After release, the arrays were inserted into a ZIF connector placed on a customized printed circuit board. Last, the electrodes were electroplated with platinum black (PtB), using a solution containing 1% of

platinum chloride $H_2PtCl_6 \cdot 6H_2O$, 0.01% of lead acetate $Pb(COOCH_3)_2 \cdot 3H_2O$ and 0.0025% of $HCl$[74]. An LCR meter (4263A, Hewlett Packard) was used for deposition at 800 mV and 100 Hz.

### 5.3.6   Bending test

Samples for the bending test were fabricated following the same process described for the ECoG array. A customized cycling stretcher was used to perform the bending test with a cyclic compressive force (bending radius 9.1 mm)[278]. The system included a stepping motor and a dedicated mechanics to bend the array. For each test, the stepping motor frequency was set at 0.5 Hz, which resulted in a cycling speed of 10 mm s$^{-1}$. The resistance of the lines was acquired at each cycle and relevant points were then extracted.

### 5.3.7   Electrochemical characterization

Electrochemical impedance spectroscopy (EIS) was performed with a potentiostat (Compact-Stat, Ivium Technologies). The arrays were soaked in phosphate-buffered saline (PBS, pH 7.4) at room temperature with a Pt wire (counter electrode) and an Ag/AgCl wire (reference electrode). The potential was set at 50 mV, and the impedance magnitude and phase were measured between 1 Hz and 1 MHz. Cyclic voltammetry (CV) was performed with the same setup and three-electrodes configuration used for EIS. The applied voltage was scanned between 0.6 and 0.8 V at a rate of 50 mV s$^1$ for six cycles. The first cycle was discarded, and the remaining five were averaged.

### 5.3.8   Animal handling

All experiments were conducted according to the animal autorisation GE/193/19 approved by the Département de l'emploi, des affaires sociales et de la santé (DEAS), Direction générale de la santé de la République et Canton de Genève in Switzerland. All the experiments were carried out during the day cycle. For the entire duration of the experiment, the health condition was evaluated three times a week, and the body weight was controlled once a week. Experiments were performed in adult (> 1-month-old) female C57BL/6J mice (Charles River Laboratories). Mice were kept in a 12 hr day/night cycle with access to food and water ad libitum. White light (300 ± 50 lux) was present from 7 AM to 7 PM and red light (650-720 nm, 80-100 lux) from 7 PM to 7 AM.

### 5.3.9   Acute craniotomy

Mice were anesthetised with an intraperitoneal injection of ketamine (87.5 mg kg$^{-1}$) and xylazine (12.5 mg kg$^{-1}$) mixture. Analgesia was performed by subcutaneous injection of buprenorphine (0.1 mg kg$^{-1}$) and lidocaine (6 mg kg$^{-1}$). Artificial tears were used to prevent the eyes from drying. The temperature was maintained at 37 °C with a heating pad. The depth

of anesthesia was assessed with the pedal reflex. The skin of the head was shaved and cleaned with betadine. Mice were then placed on a stereotaxic frame, and the skin was opened to expose the skull. A squared craniotomy was performed to expose the cortex from bregma to lambda landmarks covering both hemispheres.

### 5.3.10   Acute recording of epileptiform activity

Immediately after surgery, the OSTE+ EcoG array was placed on the cortex and the animal was removed from the stereotaxic apparatus while still under general anesthesia. The OSTE+ EcoG array was then connected to the amplifier using a 32-channel analogue head-stage (RHS headstages Intan). Signals were recorded using the Open Ephys Acquisition Board (sampling frequency 30 kHz). After a baseline period (5 minutes), 20 µl of pentylenetetrazol (PTZ; 50 mg ml$^{-1}$, 45 mg kg$^{-1}$) were injected intraperitoneally to evoke epileptiform activities[369]. Data was analysed in MATLAB. Epochs of 60 seconds were chosen to represent baseline and epileptiform activity. Welch's power spectral density between 0 and 100 Hz was computed in MATLAB.

### 5.3.11   Acute brain stimulation and electromyography

Immediately after surgery, the OSTE+ EcoG array was placed on the cortex to elicit muscle contraction assessed via electromyography (EMG). Two intramuscular needles (working and reference electrodes) were placed in the right gastrocnemius muscle with a ground needle in the contralateral back area. Two electrodes of the implant (cathode and anode), covering the hindlimb motor cortex, were used to deliver cathodic-first biphasic current pulses. Different pulse durations and amplitudes were tested with 10 trials per each condition at a repetition rate of 1 Hz. Signals were amplified (BM623, Biomedica Mangoni), filtered (1–1000 Hz with 50 Hz notch) and digitalised (16584 Hz). Data was analyzed in MATLAB. Data was detrended and bandpass filtered (10 and 1'000 Hz). To obtain the EMG envelope, the full-wave was rectified then smoothed using the root-mean square over a 20-ms window. The area of the envelope was computed to quantify the total muscle activity.

### 5.3.12   Chronic implantation

Mice were anesthetised with an intraperitoneal injection ketamine (87.5 mg kg$^{-1}$) and xylazine (12.5 mg kg$^{-1}$) mixture. Analgesia was performed by subcutaneous injection of buprenorphine (0.1 mg kg$^{-1}$) and lidocaine (6 mg kg$^{-1}$). Artificial tears were used to prevent the eyes from drying. The temperature was maintained at 37 °C with a heating pad. The depth of anaesthesia was assessed with the pedal reflex. The skin of the head was shaved and cleaned with betadine. Mice were then placed on a stereotaxic frame, and the skin was opened to expose the skull. A squared craniotomy was performed to expose the left cortex from bregma to lambda. After craniotomy, animals were divided into sham and implanted groups. The implanted group received the multilayer OSTE+ µECoG array below the dura. A sterile cap was placed in contact

with the skull bone and glued to it from the outside using bone cement. The sterile cap was filled with a silicone polymer (Kwik-Sil, World Precision Instruments). The skin was then sutured around the cap. The sham group did not receive the implant but followed the same surgical protocol, including the sterile cap.

### 5.3.13 Histology

Two and six weeks after implantation, animals were euthanized with an injection of pentobarbital (150 mg kg$^{-1}$). The chest cavity was opened to expose the beating heart, and a needle was inserted in the left ventricle, while the right atrium was cut to allow complete bleeding. The animal was immediately perfused with PBS followed by a fixative solution of 4% paraformaldehyde (PFA) in PBS. At the end of the procedure, the brain was collected and placed in 4% PFA overnight for post-fixation. Brains were cryoprotected in sucrose 30% and frozen in the optimal cutting temperature compound. 30-$\mu$m thick coronal sections of the brain were obtained using a cryostat (Histocom) and placed on microscope slides. Brain sections were washed in PBS, permeabilized with PBS + Triton 0.1% (Sigma-Aldrich), left for 1 hr at room temperature in blocking buffer (PBS + Triton 0.1% + normal goat serum 5%), and incubated overnight at 4 °C with primary antibodies for the glial fibrillary acidic protein (GFAP; 1:1000, Z0334, Dako), ionised calcium-binding adapter molecule 1 (IBA1; 1:500, 019-19741, Wako) and neural nuclei (NeuN; 1:500, ABN90P, Sigma). The day after, the sections were incubated for 2 hr at room temperature with secondary antibodies (Alexa Fluor 647, 1:500), counterstained with DAPI (1:300, Sigma-Aldrich) and mounted for imaging with Fluoromount solution (Sigma-Aldrich). Images were acquired at 20x with a slide scanner microscope (VS120, Olympus). Image quantification was performed in ImageJ. First, a rectangular region of interest was manually selected to represent the area in contact with the implant, and the corresponding area on the other hemisphere. Each image was converted to binary using a threshold algorithm: all pixels whose intensity was above the threshold were assigned the value 1, while the value 0 was assigned to the rest of the pixels. For the three markers, the threshold was defined using the Moment thresholding method in ImageJ. The percentage of the pixels above the threshold was then computed.

### 5.3.14 Citotoxicity

A test on extract was performed on multilayer OSTE+ $\mu$ECoG arrays sterilised by UV exposure. Arrays were incubated in water for 0 (no incubation), 1, 2, 5, 6, and 8 days before the test. For each condition, two arrays were used and the test on each array was replicated three times. The extraction on the samples was performed for 24 hr at 37 °C and 5% CO2 with 1 ml of extraction vehicle for 3 cm2 of device surface. The extraction vehicle was Eagle's minimum essential medium (11090081, Thermo Fisher Scientific) supplemented with 10% foetal bovine serum (10270106, Thermo Fisher Scientific), 1% penicillin-streptomycin (15070063, Thermo Fisher Scientific), 2 mM L-Glutamine (25030081, Thermo Fisher Scientific) and 2.50 $\mu$g ml$^{-1}$ Amphotericin B (15290026, Thermo Fisher Scientific). L929 cells (88102702, Sigma-Aldrich)

were plated in a 96-well plate at a subconfluent density of 7000 cells per well in 100 µl of the same medium. L929 cells were incubated for 24 hr at 37 °C and 5% CO2. After incubation, the medium was removed from the cells and replaced with the extract (100 µl per well). After another incubation of 24 hr, 50 µl per well of XTT reagent (Cell proliferation kit 11465015001, Sigma-Aldrich) were added and incubated for 4 hr at 37 °C and 5% CO2. An aliquot of 100 µl was then transferred from each well into the corresponding well of a new plate, and the optical density was measured at 450 nm by using a plate reader (FlexStation3, MolecularDevices). Clean medium alone was used as a negative control, whereas medium supplemented with 15% of dimethyl sulfoxide (D2650-5X5ML, Sigma-Aldrich) was used as a positive control. Optical density was normalised to the average value of the negative control to determine the cell viability.

### 5.3.15  Statistical analysis and graphical representation

Statistical analysis and graphical representation were performed with Prism 8 (Graph Pad). The D'Agostino & Pearson omnibus normality test was performed to justify the choice of the statistical test. In plots, p-values were reported as: * $p < 0.05$, ** $p < 0.01$, *** $p < 0.001$, and **** $p < 0.0001$.

## 5.4  Results and discussion

### 5.4.1  OSTE+ manufacturing

Among the commercially available OSTE+ polymers, we chose OSTEMER 324 Flex, which differs from other OSTE+ resins in its mechanical properties that make it conformable. After mixing the three monomers with thiol, allyl, and epoxy groups, the viscous resin can be coated onto a wafer surface and the thickness of the layer can be controlled by the spin speed (Figure 5.1a). Then, the fast thiol-ene radical UV polymerization results in a soft solid surface, which is chemically reactive due to the exposed thiol excess and epoxy groups. Last, the slower anionic thermal polymerization allows epoxy groups to react with the remaining thiol groups, thereby stiffening the substrate[368,370,371]. UV polymerisation allows photo-patterning of the film, which acts as a negative photoresist (Figure 5.1b). OSTE+ allows precise patterning of various sizes and shapes with relatively high resolution (about 2 µm). The possibility of UV patterning of OSTE+ is an advantage for the encapsulation step of neural implants if compared to PDMS encapsulation, which is usually done manually[268,358,372] or by reactive-ion etching to obtain smaller features[269] but with the risk of leaving toxic residues[373].

Next, we assessed the resolution of thin metal films on OSTEMER 324 Flex obtained with standard photolithographic techniques. Straight (Figure 5.1c) and horseshoe-shaped (Figure 5.1d) lines of decreasing width from 60 µm down to 5 µm have been patterned with 10-µm thick photoresist. 5-µm lines appears sharply defined on the OSTEMER 324 Flex substrate, which is a largely better resolution that what typically obtained on PDMS[269,374]. Ripples

appeared on the Pt layer because of the stress that builds up between two materials (Pt and OSTEMER 324 Flex) of different modulus and coefficients of thermal expansion, like happening on other elastomeric substrates including PDMS[375,376]. Ripples help increase elastic deformation in the neural interface. Similarly to PI, parylene-C and SU-8, the possibility of using standard photolithography to directly pattern metallic structures ensures high reliability and reproducibility in the fabrication process. Unlike previous studies using thiol-ene-based polymers for neural interfaces, the process presented here is simple and does not require any transfer-by-polymerization process[373,377–379].
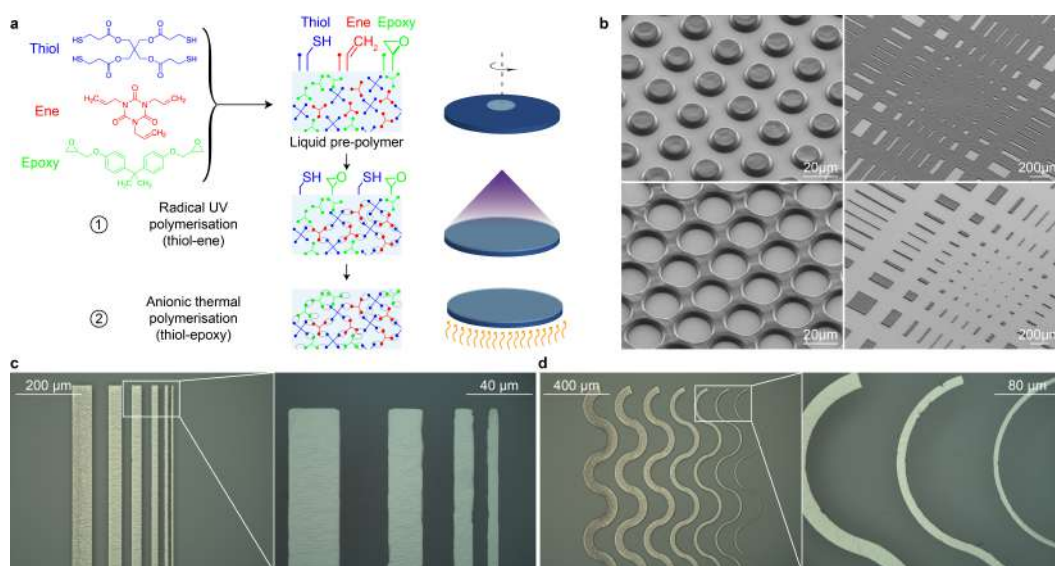


Figure 5.1: (a) Step-by-step procedure to manufacture a spin-coated film of OSTE+. (b) Example of structures obtained with OSTEMER 324 Flex via direct UV exposure of the liquid pre-polymer. The layer thickness is 4 µm. (c,d) Resolution of straight (c) and horseshoe-shaped (d) lines on OSTEMER 324 Flex. Line widths are 60 µm, 40 µm, 30 µm, 20 µm, 10 µm and 5 µm from left to right. The magnifications show line widths 30 µm to 5 µm (c) and 20 µm to 5 µm (d).

### 5.4.2   OSTE+ mechanical characterization

A crucial element for materials used in neural interfaces is flexibility and conformability. Ultrathin layers of PI, parylene-C and SU-8 allows device flexibility. However, the relatively high Young's modulus (GPa range) and limited elastic deformation make them less attractive than elastomers like PDMS (MPa range). OSTEMER 324 Flex closes this gap in neural interfaces having promising mechanical properties.

First, we performed DMTA in one OSTEMER 324 Flex sample (Figure 5.3a). The glass transition temperature (Tg) is 29.2 °C (Figure 5.3a, green circle), lower than the operating body temperature for neural implants (37 °C). This feature is interesting compared to other materials (PI, parylene-C, SU-8 and PDMS) because OSTEMER 324 Flex is stiffer at room tem-

perature (easier insertion) and softens once inserted into the body (reduced mechanical mismatch)[377,378,380,381]. Accordingly, the storage moduli at room (21 °C) and physiological (37 °C) temperatures are respectively 323.7 MPa and 15.2 MPa (Figure 5.3a, red circles). Then, we performed tensile stress/strain tests (Figure 5.3b) to quantify the elastic modulus (Figure 5.3c), stress at break (Figure 5.3d), and elongation at break (Figure 5.3e). OSTEMER 324 Flex samples have an average Elastic modulus of 15.03 ± 1.21 MPa, an average stress at break of 15.70 ± 4.95 MPa and an average elongation at break of 65.88 ± 10.37 % (n = 4 samples, mean ± s.d.).
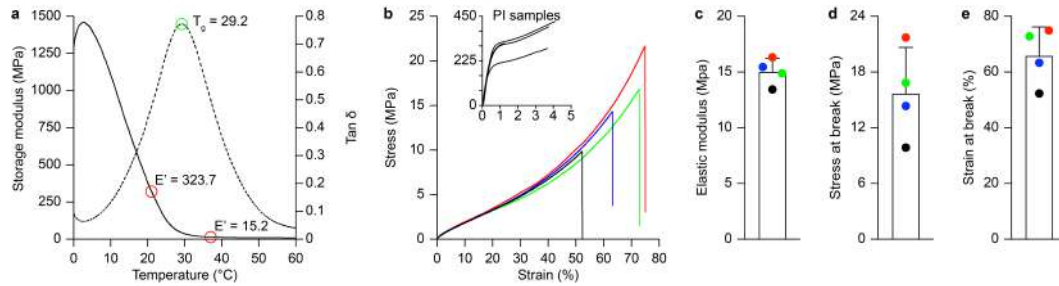


Figure 5.2: (a) DMTA in one OSTEMER 324 Flex sample. The black line is the storage modulus and the dashed line is the tan $\delta$ as a function of the temperature. The green circle highlights the Tg, and the two red circles highlight the storage modulus at 21 and 37 °C. (b) Stress-strain curves of four OSTEMER 324 Flex samples under tensile test at room temperature. The insert shows the stress-strain curves obtained from four PI samples. (c-e) Quantification of the elastic modulus (c), stress at break (d) and strain at break (e) from the four tested samples (n = 4 samples, mean ± s.d.).

For µECoG arrays, it is important to take into consideration the capability of a flexible polymeric substrate to conform with the complex topography of the central nervous system. Therefore, we computed the critical thickness (h) to achieve spontaneous wrapping of an OSTEMER 324 Flex film around a curvilinear body with a given radius of curvature, following equation (1) for an elasto-capillary model [35,73].

$$(1) \ h = \sqrt[3]{\frac{24r^2\gamma(1-v^2)}{E}}$$

The radius of curvature r is 2.3 mm, corresponding to the mouse cortex[353], the elastic modulus E is 15.03 x 106 N m^{-2}, the Poisson's ratio $v$ is assumed 0.4[382], and the cerebrospinal fluid surface tension $\gamma$ is 61 mN m[-1][383]. The threshold value for conformability to a mouse brain is 75.64 µm. Below this thickness, multilayer OSTE+ µECoG arrays naturally conform to the mouse brain without additional pressure. In addition, because of its elastic component, OSTEMER 324 Flex, can conform better than PI to curved surfaces like spheres. For comparison, results from tensile stress/strain tests in conformable PI samples (8-µm thick) are reported in the insert of Figure 5.3b. Based on these results, OSTEMER 324 Flex is a suitable candidate for surface and penetrating brain implants, where the dynamic strain is in the range of 0.01-0.03%[384], or intraneural interfaces for nerves away from joints[385].

### 5.4.3   OSTE+ adhesion strength

The adhesion between layers is a crucial feature to ensure integrity and longevity of a neural interface. A common failure mechanism in neural implants is the delamination between the insulating layers and the conductor, leading to fluid penetration and loss of the device integrity and functionality[273]. Therefore, we performed adhesion T-peel tests to investigate the adhesion strength of OSTEMER 324 Flex samples (Figure **??**). First, we assessed the self-adhesion forces between two OSTEMER 324 Flex layers (Figure **??**a). During a tensile load, the peel force linearly increases with the distance until cohesive fracture occurs in the unbonded portion of the sample before delamination. This result suggests a strong self-adhesion because of the OSTE+ functional groups covalently linked during the anionic thermal polymerisation[275]. Moreover, heating the polymer above the Tg during the anionic thermal curing softens the polymer and allows it conforming to nano and microcavities in the substrate creating a perfect seal. In a neural interface, it is also crucial to verify the adhesion strength also between the encapsulation and the metal electrodes. Therefore, we repeated the T-peel test in samples with a Pt layer between the two OSTEMER 324 Flex layers (Figure **??**b). In this case, the top OSTE+ layer was peeled off because of the weaker adhesion to Pt at an averaged peel force per unit width of $89.22 \pm 8.11$ N m$^{-1}$ (mean $\pm$ s.d., n = 4 samples), which is 30 times higher than the one required to peel Ti sputtered on PI[273]. The peel force per unit width during separation was averaged between 1 and 5 mm of displacement. Ti is commonly used as an adhesion layer for Pt in PI-based implants; OSTEMER 324 Flex showed stronger adhesion to Pt without the need of any intermediated interface nor surface treatment.

Then, we fabricated samples with patterned Pt lines fully embedded in either two layers of OSTEMER 324 Flex or PI to compare the encapsulation capability of the materials. Samples were then immersed in a sonication bath and controlled at various time points. The PI sample shows signs of metal delamination already after 10 s of sonication (Figure **??**e) while the OSTE+ samples remain unaltered even after 90 min (Figure **??**d). This qualitative test demonstrates the superior stability of OSTEMER 324 Flex.
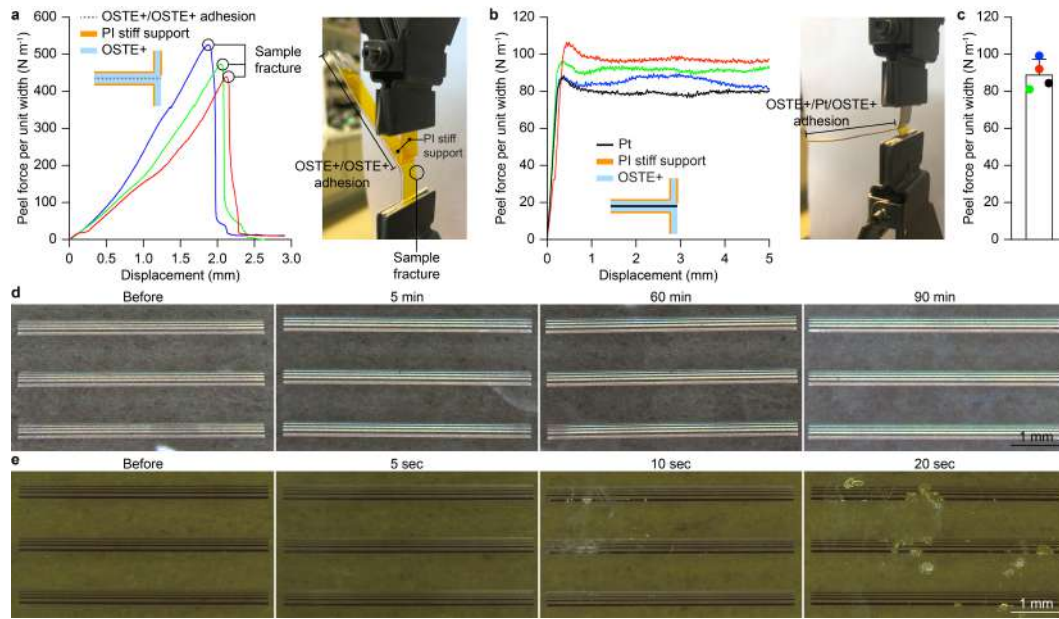
Figure 5.3: (a) T-peel test between two OSTEMER 324 Flex layers. In all three samples a fracture of the samples is observed. The insert represents the cross-section of the sample. The image on the right shows a sample under testing. (b) T-peel test between two OSTEMER 324 Flex layers with a Pt film in between (4 samples). The insert represents the cross-section of the sample. The image on the right shows a sample under testing. (c) Quantification of the averaged peel force per unit width at which layers separate. Each colour corresponds to the samples in (b). (d) Stability test for OSTEMER 324 Flex. Images before sonication and after 5, 60 and 90 min of sonication. (e) Stability test for PI. Images before sonication and after 5, 10 and 20 s of sonication.

### 5.4.4 OSTE+ electrical and electrochemical characterization

Next, we designed and optimised a process-flow to fabricate conformable multilayer OSTE+ µECoG arrays by using established wafer-scale technologies. The implant is designed to covers a large area of the mouse cortex (Figure 5.4a,b) and 16 electrodes are arranged to cover both brain hemispheres (eight electrodes per side) placed in two layers: half in the bottom layer (Figure 5.4a, black) and half in the top layer (Figure 5.4a, grey). Multilayer fabrication is advantageous to not increase the area occupied by feedlines or to manufacture three-dimensional electrodes[74,274]. The total thickness of the device is 42 µm, well below the critical thickness for conformability. At this thickness, OSTEMER 324 Flex has a bending stiffness (B) of 1.10 x 10-7 N m, according to equation (2)[353].

(2) $B = \frac{Eh^3}{12(1-v^2)}$

This value is lower than the bending stiffness for 8 µm-thick PI (4.34 x $10^{-7}$ N m) and 150 µm-thick PDMS (3.75 x $10^{-7}$ N m), while a 42-µm thick OSTE+ array is still easy to handle.

The substrate is 30 µm and each encapsulation is 6 µm. Therefore, metal lines are not located in the neutral plane, potentially causing stress concentration upon bending and torsion during handling and implantation[386]. Hence, a horseshoe pattern was used to reduce the stress in the stiff metal layer as well as allow conformability to the tissue (Figure 5.4a,b). Meander-like patterns have already been investigated by other groups, who found the horseshoe pattern superior over sinusoidal or U-shaped designs[386–388]. We performed measurements of the electrical resistance of the horseshoe lines under bending cycles to evaluate their robustness (Figure 5.4c). The resistance values of bottom and top lines remained stable at least for 105 bending cycles. However, it can be noticed a consistent but small difference between the two layers. The top layer has a 10.05% increase compared to the bottom layer. This small difference might be caused by changes in the Pt microstructure happening on the bottom layer due to the additional heat treatments following the fabrication of the top layer[372], or by small changes in the deposition chamber between the two processes. If, on the one hand, a horseshoe pattern provides flexibility, on the other hand, it reduces the integration density and slightly increases the electrical resistivity. Alternatively, stretchable conductors could be used[268,269].

Direct writing photolithography was used to pattern the electrode openings in both layers (Figure 5.4d,e). The UV polymerization of OSTE+ allows multilayer fabrication and reduces the risk of misalignment, thus ensuring a stable and repeatable process. Electrodes have been coated with Pt-black, which is known to reduce their impedance magnitude as well as increase the total charge storage capacity (CSC) compared to bare Pt[74]. Moreover, no significant difference has been found in the electrochemical properties between bottom and top electrodes (Figure 5.4f-k). The versatility of the fabrication process allows electrode coating with other materials, like sputtered iridium oxide, spin-coated or electrodeposited PEDOT:PSS or a combination of the two[353].
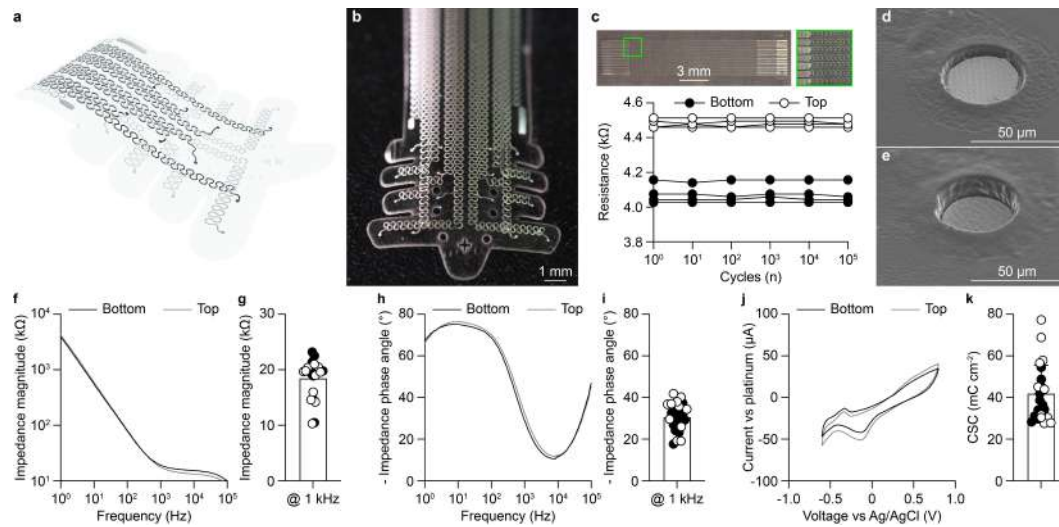
Figure 5.4: (a) Sketch of conformable multilayer OSTE+ µECoG array highlighting the bottom (black) and top (grey) electrode layers. (b) Picture of the conformable multilayer OSTE+ µECoG array. (c) Line resistance as a function of multiple bending cycles (bending radius: 9.1 mm). The white dots are top electrodes (n = 4), whereas the black dots are bottom electrodes (n = 4). The top pictures show the sample used for the bending test. (d,e) Scanning electron microscopy images of 40-µm diameter top (d) and bottom (e) electrodes coated with Pt-black and encapsulated in OSTE+. (f) Plot of the impedance magnitude. The gray line is the average from the top electrodes (n = 11 electrodes from N = 2 arrays) and the black line is the average from the bottom electrodes (n = 12 from N = 2 arrays). (g) Quantification (mean ± s.d.) of the impedance magnitude at 1 kHz. The black circles are bottom electrodes and the white cirlces are top electrodes (p = 0.3237, two-tailed Mann-Whitney test). (h) Plot of the impedance phase angle. The gray line is the average from the top electrodes (n = 11 electrodes from N = 2 arrays) and the black line is the average from the bottom electrodes (n = 12 from N = 2 arrays). (i) Quantification (mean ± s.d.) of the impedance phase angle at 1 kHz. The black circles are bottom electrodes and the white cirlces are top electrodes (p = 0.2239, two-tailed unpaired t test). (j) Plot of the CV. The gray line is the average from the top electrodes (n = 11 electrodes from N = 2 arrays) and the black line is the average from the bottom electrodes (n = 12 from N = 2 arrays). (k) Quantification (mean ± s.d.) of the CSC. The black circles are bottom electrodes and the white cirlces are top electrodes (p = 0.2738, two-tailed unpaired t test).

### 5.4.5 Functional validation in-vivo

Conformable multilayer OSTE+ µECoG arrays were tested for brain recording and stimulation. First, we performed in-vivo brain recordings in an anaesthetised mouse upon induction of epileptiform activity. The conformable multilayer OSTE+ µECoG array was implanted with the electrodes covering both hemispheres of the cortex from lambda to bregma (Figure 5.5a,d). The neural activity was recorded before and after peritoneal injection of the convulsant PTZ, which is routinely used to test anticonvulsants in animals[369,389–391]. The transition between baseline (Figure 5.5a, black) and epileptiform activity (Figure 5.5a, red) after PTZ injection was

clearly detected by the conformable multilayer OSTE+ µECoG array with an excellent signal to noise ratio, thus demonstrating the potential of OSTE+ neural interfaces for monitoring brain activity. Injection of PTZ induced characteristic spike and wave discharges[392], evident in all the 16 spectrograms from top and bottom electrodes (Figure 5.5b). The presence of epileptiform activity is further evidenced by the statistically higher PSD that was observed after PTZ injection (Figure 5.5c).
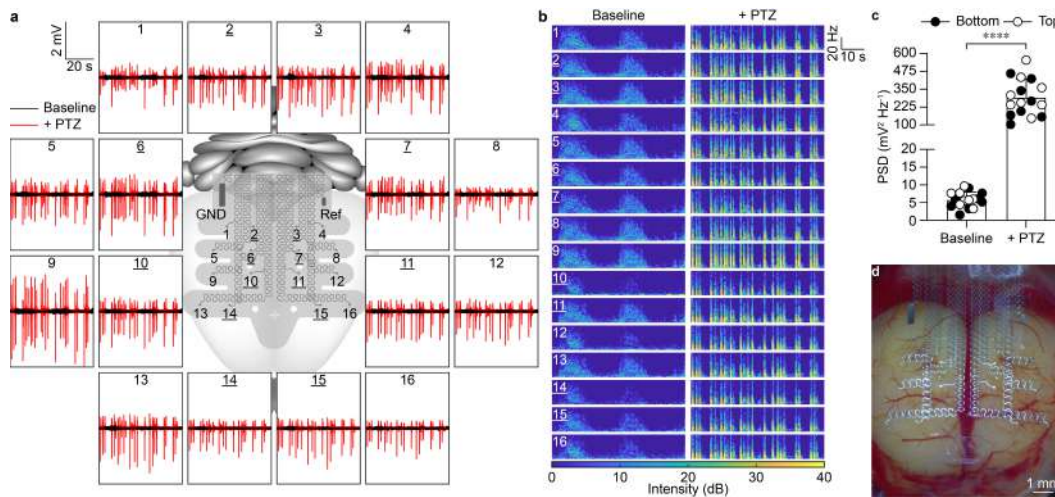


Figure 5.5: (a) The central sketch shows a multilayer OSTE+ ECoG array covering a mouse brain for in-vivo recordings. Medial electrodes (underlined numbers) are in the bottom layer. Around the sketch, representative recordings from each electrode are reported. The black traces are the baseline activity, while the red traces are the epileptiform activity after PTZ injection. Each box corresponds to 60 seconds of recordings. (b) Spectrogram between 0 and 50 Hz from the 16 recordings shown in a. (c) PSD quantification between 0 and 100 Hz from recordings in a. The black circles are bottom electrodes and the white circles are top electrodes (p < 0.0001, two-tailed paired t test). (d) Image of the multilayer OSTE+ ECoG array onto the mouse cortex.

Next, we investigated the performance of conformable multilayer OSTE+ µECoG arrays in brain stimulation in one anaesthetised mouse (Figure 5.66). Two neighbouring electrodes covering the cortical hindlimb motor area have been used for bipolar electrical stimulation to elicit muscle contraction assessed via EMG recordings (Figure 5.6a). Two intramuscular needles were placed in the gastrocnemius muscle, while a ground needle in the contralateral back area. EMG responses appeared upon single cathodic-first biphasic pulses (Figure 5.6b). Then, we extracted the linear envelope of the EMG signal (Figure 5.6c) and computed the iEMG to compare various current amplitudes and pulse durations (Figure 5.6d). As expected, longer pulse durations reduced the current required for inducing robust motor activity.
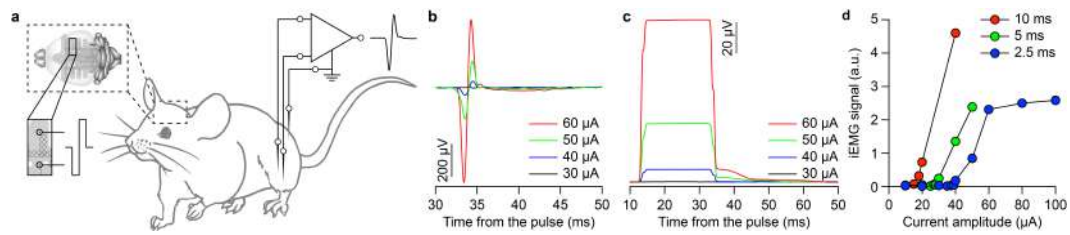
Figure 5.6: (a) Diagram of the stimulation set-up. A pair of electrodes in the µECoG array covering the cortical hindlimb motor area are selected for stimulation. Two needles are in the mouse hindlimb for EMG recordings. A third needle is the ground. (b) EMG responses to increasing current amplitudes from 30 to 60 uA with a 2.5-ms long pulse. (c) EMG envelope calculated using the root-mean square over a 20-ms sliding window from responses in b. (d) Quantification of the iEMG for 2.5 (blue), 5 (green) and 10 (red) ms pulses at increasing current amplitudes.

Overall, we showed that conformable multilayer OSTE+ µECoG arrays are suitable for acute brain recordings and stimulation of neural activity. In future works, in-vivo long-term functionality of conformable multilayer OSTE+ µECoG arrays will necessarily be assessed.

### 5.4.6  OSTE+ biocompatibility

Last, we evaluated the OSTE+ biocompatibility in-vitro and in-vivo.

Previous studies showed that OSTE+ films are non-toxic to cultured cells only after immersion in water for 7 days[371]. Therefore, we assessed the in-vitro cytotoxicity of conformable multilayer OSTE+ µECoG arrays after immersion in water for 1, 2, 5, 6, and 8 days before the test or without immersion (0 days). The results showed no cytotoxicity for all the tested conditions, including the arrays not immersed in water before the test (Figure 5.7a,b). This result might be explained by the several washing steps performed during fabrication which could remove impurities from the residual constituents.
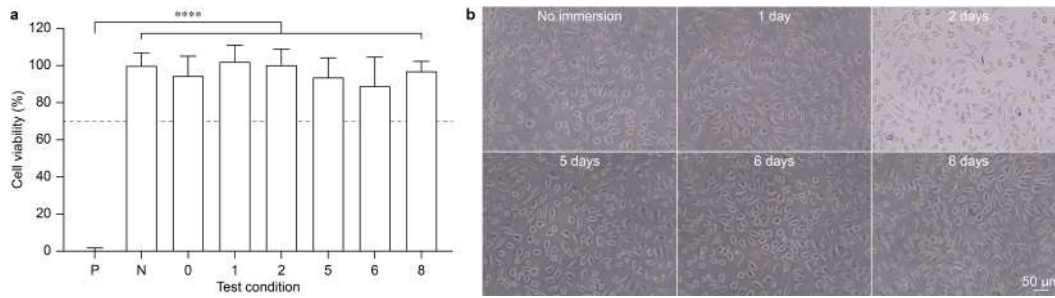
Figure 5.7: (a) Quantification of cell viability in the conditions tested (mean ± s.d.). Positive control (P) 0 ± 1.8% (9 replicas); negative control (N) 100 ± 6.8% (9 replicas); no immersion (0) 94.5 ± 10.5% (2 arrays, 6 replicas); 1 day immersion (1) 102.2 ± 8.8% (2 arrays, 6 replicas); 2 days immersion (2) 100.4 ± 8.4% (2 arrays, 6 replicas); 5 days immersion (5) 93.7 ± 10.5% (2 arrays, 6 replicas); 6 days immersion (6) 89.0 ± 15.6% (2 arrays, 6 replicas); 8 days immersion (8) 97.0 ± 5.3% (2 arrays, 6 replicas). One-way ANOVA: F = 144.1 and p < 0.0001. Tukey's multiple comparisons test: P vs. all other conditions p < 0.0001; all other comparisons are statistically not significant (p = 0.3516 or higher). The dashed grey bar indicates the threshold for cytoxicity. (b) Representative optical images of the cells after the test, for different immersion conditions.

Then, we evaluated the in-vivo biocompatibility of conformable multilayer OSTE+ μECoG arrays by performing chronic implantation and post-mortem histological assays against GFAP, IBA1 and NeuN markers (Figure 5.8). For this analysis, conformable multilayer OSTE+ μECoG arrays have been implanted in one brain hemisphere (operated), leaving the other hemisphere untouched (unoperated). Histological analysis has been performed on coronal brain sections corresponding to the operated area at two time points: two and six weeks after implantation. Images at both two and six weeks post implantation were quantified and statistically compared with a Two-Way repeated measure ANOVA (Factor 1 is the procedure: implanted or sham; Factor 2 is the brain hemisphere: operated or unoperated). For NeuN signals, there are no statistically significant differences at both two (Factor 1: p = 0.4329; Factor 2: p = 0.5359; Interaction: p = 0.3888) and six (Factor 1: p = 0.2382; Factor 2: p = 0.7065; Interaction: p = 0.4628) weeks post implantation (Figure 5.8a,b). Similarly, IBA1 signals are not significantly different at both two (Factor 1: p = 0.4331; Factor 2: p = 0.0701; Interaction: p = 0.1705) and six (Factor 1: p = 0.5754; Factor 2: p = 0.5902; Interaction: p = 0.8532) weeks post implantation (Figure 5.8a,d). GFAP signals are not significantly different at two weeks post implantation (Factor 1: p = 0.4438; Factor 2: p = 0.1805; Interaction: p = 0.4333), but they show a statistically significant difference after six weeks (Factor 1: p = 0.0044; Factor 2: p = 0.2612; Interaction: p = 0.4430) between implanted and sham groups (Figure 5.8a,c). The Šidák's multiple comparison test showed that this difference is associated to the unoperated hemisphere (unoperated sham vs unpoperated implanted: p = 0.099) and not to the operated one (operated sham vs unoperated implanted: p = 0.1006). From these results, we concluded that superficial damage is caused mainly by the surgical procedure as previously observed[393], and conformable multilayer OSTE+ μECoG arrays do not cause significant foreign body reaction in the first six weeks post implantation.
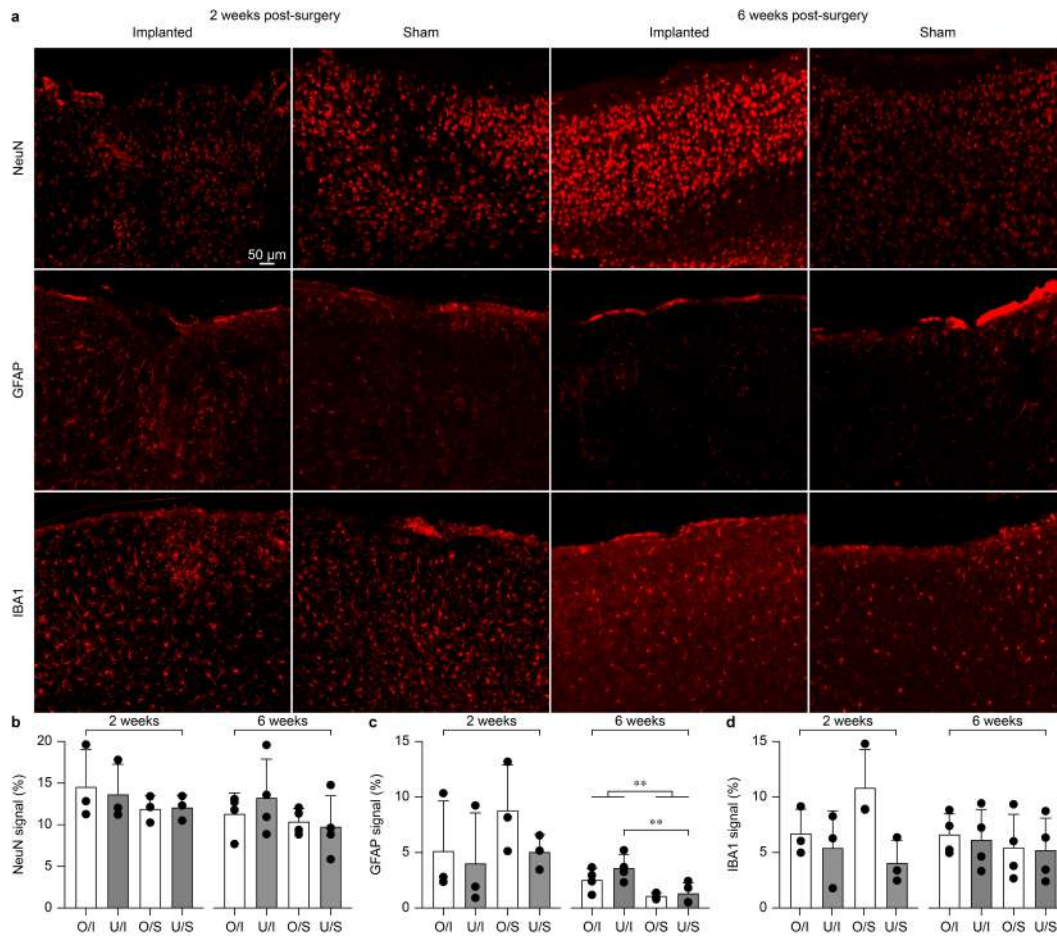
Figure 5.8: (a) Representative images for NeuN, GFAP and IBA1 sampled 2 and 6 weeks after implantation in both implanted and sham mice. Corresponding images for NeuN, GFAP and IBA1 are from the same mouse. Slice were sampled at the level of the operated area. (b-d) Quantification of the NeuN (b), GFAP (c) ans IBA1 (d) signals two (mean ± s.d., n = 3 mice) and six (mean ± s.d., n = 4 mice) weeks after implantation in implanted and sham mice. O/I: operated hemisphere for implanted mice; U/I: unoperated hemisphere for implanted mice; O/S: operated hemisphere for sham mice; U/S: unoperated hemisphere for sham mice.

## 5.5  Conclusions

We exploited a soft and flexible OSTE+ formulation, known as OSTEMER 324 Flex, to develop a conformable neural interface. OSTE+ thermosets have shown tunable mechanical properties by adjusting the stoichiometry of the constituting monomers, they can be manufactured via UV polymerisation and allow direct low-temperature dry bonding without surface treatments[275]. These physicochemical properties result in several advantages compared to other materials used in neural interfaces (PI, SU8, parylene-C or PDMS). OSTE+ shows superior adhesion forces, a necessary feature to improve stability and longevity of neural interfaces[273]. In addition, previous studies have shown that OSTE+ have low permeability

to gases and show low absorption of small molecules: two crucial characteristics to protect thin implants against moisture and ions in long-term chronic applications[348]. Conformable multilayer OSTE+ µECoG arrays are manufactured with standard clean-room manufacturing processes. Compared to PDMS, photolithography on OSTE+ allows reliable patterning to make openings for electrical contacts, otherwise done manually[268,358,372] or by aggressive etching steps[269,373]. Achieved resolution is comparable to other polymeric neural interfaces based on PI, parylene-C or SU-8, but OSTEMER 324 Flex showed superior mechanical and encapsulation properties. A glass transition temperature lower than the body temperature might allow temperature-dependent softening during surgical insertion: an interesting feature for penetrating neural implants[377,380,381,394]. The superior adhesive and encapsulation properties of OSTE+ derives from the two-step polymerisation process, which could be further exploited to expand the device functionality. Reactive groups exposed at the surface allow for surface functionalization. For example, to embed molecules improving biocompatibility and reducing long-term foreign body response. Also, the radical UV polymerisation might be exploited to integrate microfluidics in neural implants for drug release[357]. The electrophysiological and histological in-vivo study showed that OSTEMER 324 Flex is a promising material to build conformable multilayer µEcoG arrays. Given these promising results, future works will focus on long-term in-vivo testing.

### 5.5.1 Acknowledgments

# 6 All-printed electrocorticography array for in-vivo neural recordings

Authors: Eleonora Borda[1], Laura Ferlauto[1], Jürg Schleuniger[2],Alessandro Mustaccio[2],Fabian Lütolf[2],Arnold Lücke[2],Sören Fricke[2],Nenad Marjanović[2], and Diego Ghezzi[1]

[1] Medtronic Chair in Neuroengineering, Center for Neuroprosthetics, Institute of Bioengineering, School of Engineering, École Polytechnique Fédérale de Lausanne, Switzerland
[2] CSEM Muttenz, Switzerland

## 6.1   Abstract

Bioelectronic and neuroprosthetic interfaces rely on implanted micro-electrode arrays to interact with the human body. Printing techniques, such as inkjet and screen printing, are attractive methods for the manufacturing of micro-electrode arrays because they allow flexible, room-temperature, scalable, and cost-effective fabrication processes. In this work, we show the fabrication of all-printed electrocorticography arrays made by inkjet printing of platinum and screen printing of polyimide. Next, we performed mechanical and electrochemical characterizations. As a proof-of-concept, we recorded in-vivo visually evoked cortical potentials in

rabbits upon flash stimulation. Last, we showed that the all-printed printed electrocorticography arrays were not cytotoxic. Altogether our results enable the use of printed micro-electrode arrays for neurological applications.

## 6.2  Main

Micro-electrode arrays (MEAs) are devices essential to interface with electroactive tissues, such as the nervous system and muscles[395]. Several biomedical devices rely on macro- and micro-electrodes to deliver electrical stimuli or to record electrical activity to and from the tissue, such as cardiac pacemakers, deep brain stimulators, cochlear implants, retinal prostheses, and electrocorticography arrays[189,281,396–398]. Medical-grade MEAs are mostly hand-made by skilled technicians, while only a few rely on clean-room processes derived from the silicon industry[310]. Although clean-room processes have high resolution and reproducibility, they constrain the fabrication of medical-grade MEAs mostly because of high production cost and chemical or thermal incompatibility with flexible or elastic substrates. Besides, clean-room processes limit the size of MEAs to the wafer dimension and the number of possible layouts due to expensive lithographic masks. Printing methods can overcome the issues mentioned above since they are based on low-temperature, flexible, cost-effective, and large area processes. Platinum is the material of choice for both recording and stimulation electrodes in most of the medical-grade MEAs because of its mechanical and chemical stability, ease of processing from foils, and its good electrochemical performance[399,400]. Besides, the faradaic reactions are confined to a surface monolayer, therefore often called pseudocapacitive, which is an appealing feature for safe electrical stimulation[401]. Despite the relevance of platinum in the medical field, printed platinum-based MEAs were not yet investigated. In this paper, we report the fabrication, characterization, and validation of a fully-printed, flexible, platinum-based electrocorticography array.

Platinum-based electrocorticography arrays (Figure 6.1a,b) were printed using a commercial platinum precursor ink (16512, Ceimig Limited) on 60-μm thick polyimide foils (PI; Kapton HN, DuPont). Each electrocorticography array consisted of 16 (2 x 8) square electrodes of 450 μm in size with a center-to-center pitch of 1120 μm (Figure 6.1a). Electrodes, tracks, and pads were printed with a single scan resulting in a line thickness of 130.8 ± 39.3 nm (mean ± s.d., n = 18 lines from N = 3 arrays; Figure 6.1c), while the line width was 246 ± 12.8 μm (mean ± s.d., n = 9 lines from N = 3 arrays). After printing and pre-curing (200 °C, 20 min), the line resistance, measured from electrode to pad, was 1.26 ± 0.19 kΩ (mean ± s.d., n = 6 lines from N = 1 array). Such a high resistance would have hampered the capability of the array to detect neuronal activity. Photonic sintering (PS) was performed to reduce the line resistance by a factor of 2.5, lowering it to 515.7 ± 28.4 Ω (mean ± s.d., n = 16 lines from N = 1 array; Figure 6.1d, column 'After PS'). Afterwards, the arrays were encapsulated with a layer of screen-printed PI precursor (HP-1000G2, Hitachi Chemical) having a thickness 4.37 ± 0.93 μm (mean ± s.d., n = 9 measures from N = 2 arrays). In order to expose the electrodes and pads, circular openings were designed in the encapsulation layer with 300-μm and 550-μm nominal

diameters, respectively (Figure 6.1b). The measured apertures were 300.2 ± 23.5 μm for the electrodes and 534.1 ± 18.7 μm for the pads (mean ± s.d., n = 48 measures from N = 3 arrays). After encapsulation, the line resistance was slightly reduced to 495.3 ± 27.1 Ω (mean ± s.d., n = 16 lines from N = 1 array; Figure 6.1d, column 'After PI'; p < 0.0001, two-tailed paired t-test). This reduction might be associated with the additional thermal treatment performed after screen printing. Overall, the average line resistance of the printed electrodes was 477.3 ± 29.9 Ω (mean ± s.d.; n = 16 electrodes, N = 5 arrays; Figure 6.1d, column 'All arrays'). Moreover, the line resistance can be further decreased by printing multiple layers of platinum (Figure 6.1e): this is an established technique that was already shown for feedlines printed in gold[402]. For printed platinum, the line resistance was also reduced coherently with the number of multiple overprints. Indeed, a considerable reduction was observed up to three overprints (42.00% of the initial value with 3 overprints) while a minor decrease was reported with more overprints (28.35% of the initial value with 5 overprints).

Next, the surface roughness of the printed platinum electrodes was measured (Figure 6.1f), which resulted significantly higher than the one of sputtered platinum electrodes (p < 0.0001, two-tailed unpaired t-test; n = 3 electrodes each; Figure 6.1g). This higher surface roughness is a desirable feature for microelectrodes because it should provide better electrochemical performance, due to the increase of the electrochemical surface area.

The choice of PI as substrate material relied mainly on its flexibility, a crucial feature when designing medical MEAs to interface soft tissues like the brain. Thus, we also tested the mechanical robustness of the printed arrays upon cyclic bending. Printed platinum-based electrocorticography arrays were stable upon 100,000 cycles of flexion (bending radius: 9.1 mm; speed: 10 mm s$^{-1}$; Figure 6.1h-i). The line resistance was monitored over cycles, and there was no statistically significant change after each bending cycle (p = 0.2820, one-way ANOVA; Figure 6.1l).
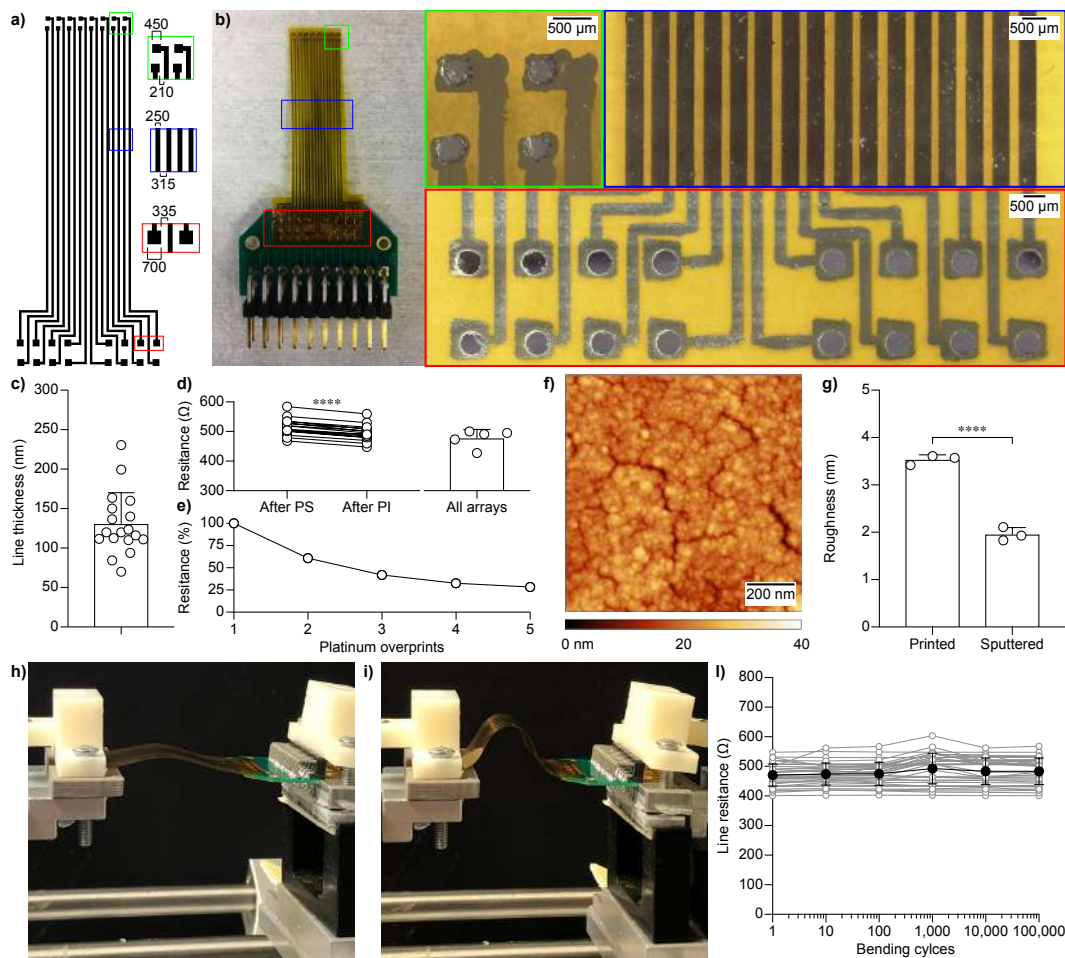
Figure 6.1: Printed platinum-based electrocorticography electrode array. (a) Printing layout. The inserts show the electrodes (green), tracks (blue), and pads (red). The quotes are reported in μm. (b) Picture of an assembled array connected to a printed circuit board. The green, blue, and red boxes show a magnified view of the electrodes (green), tracks (blue), and pads (red). (c) Mean (± s.d.) line thickness measured across n = 18 lines from N = 3 arrays. (d) Line resistance from pad to electrode. Left: comparison of the resistance values after photonic sintering and after PI encapsulation (n = 16 electrodes from N = 1 array). Right, mean (± s.d.) line resistance values across N = 5 arrays. For each array, the values of n = 16 electrodes were averaged together. (e) Normalized line resistance with multiple overprints of platinum. (f) Example of an atomic force microscopy image (1 μm x 1 μm) of a printed platinum electrode. (g) Mean (± s.d.) roughness values for printed (3.533 ± 0.100 nm) and sputtered platinum (1.957 ± 0.142 nm) electrodes obtained from the corresponding images (n = 3 electrodes from N = 1 array for each condition). (h,i) Printed platinum-based electrocorticography electrode array during a bending test in the initial position (h) and final position (i). The bending radius was 9.1 mm, and the bending speed was 10 mm s$^{-1}$. (l) Line resistance variation as a function of multiple bending cycles. The gray dots and lines are individual electrodes (n = 35 electrodes from N = 3 array), while the black dots and line is the mean ± s.d.

To characterize in-vitro the performance of printed platinum-based electrodes in an aqueous environment, we performed electrochemical impedance spectroscopy (EIS) and cyclic voltammetry (CV) (Figure 6.2). The impedance magnitude (Figure 6.2a), the impedance phase (Figure 6.2b), and the CV curves (Figure 6.2c) of printed platinum electrodes (black lines, n = 15 electrodes from N = 1 array) showed a shape qualitatively similar to the one of sputtered electrodes of equivalent surface area (gray line, average of n = 16 electrodes from N = 1 array). However, the impedance magnitude (Figure 6.2a,d) and the impedance phase (Figure 6.2b,e) were significantly lower (p < 0.0001, unpaired t-test) whereas the charge storage capacity (CSC) was significantly higher (p < 0.0001, Mann-Whitney test; Figure 6.2c,f), likely due to the higher roughness of the printed platinum. In MEAs, a higher CSC and a lower impedance magnitude correlate with improved performance during tissue stimulation and recording[401]. The values of the impedance magnitude and phase were taken at 1 kHz, which is reference frequency in neurotechnology. EIS and CV were measured for 5 printed arrays (Figure 6.2d-f, columns 'All arrays'). The results showed that the impedance magnitude, the impedance phase, and the charge storage capacity are reproducible not only within the same array but also between arrays (mean ± s.d., for each of the N = 5 arrays the data from all the n = 15 electrodes were averaged). For printed arrays, only 15 electrodes out of 16 were working during electrochemical experiments. Since the line conductivity was verified for all of the electrodes, this might be associated to the manual bonding procedure of the array to a printed circuit board used to connect the array to the measuring instrumentation (Figure 6.1b).
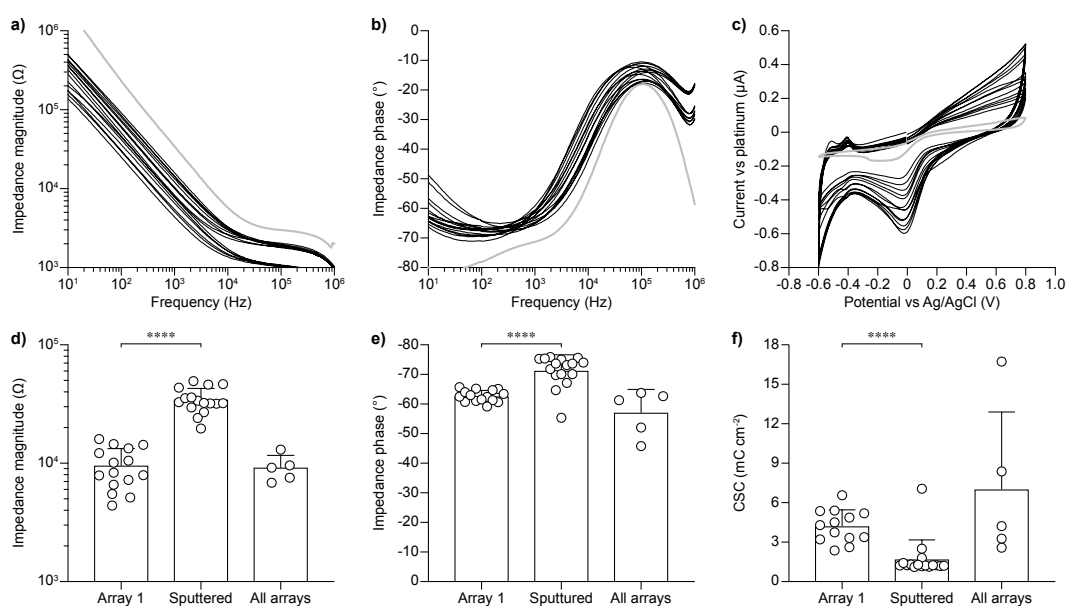
Figure 6.2: Electrochemical characterization of electrocorticography electrode arrays with printed platinum. (a-c) Impedance magnitude (a), impedance phase (b), and cyclic voltammetry (c) measured on a printed array (black lines, n = 15 electrodes from N = 1 array). The gray line is the average from sputtered platinum electrodes of equivalent surface area (300-μm diameter, average of n = 16 electrodes from N = 1 array). (d-f) Quantification (mean ± s.d.) of the impedance magnitude at 1 kHz (d), impedance phase at 1 kHz (e), and charge storage capacity (f) for the n = 15 printed electrodes (columns 'Array 1'), the n = 16 sputtered electrodes (columns 'Sputtered'), and all the printed array (columns 'All arrays'; for each array, the values of the n = 16 electrodes were averaged together). Impedance magnitude: 9,599 ± 3,734 Ω ('Array 1'), 34,531 ± 8,284 Ω ('Sputtered'), 9,248 ± 2,409 Ω ('All arrays'); Impedance phase: -62.70 ± 1.960 ° ('Array 1'), -71.31 ± 5.336 ° ('Sputtered'), -57.13 ± 7.835 ° ('All arrays'); Charge storage capacity: 4.222 ± 1.237 mC cm$^{-2}$ ('Array 1'), 1.713 ± 1.467 mC cm$^{-2}$ ('Sputtered'), 7.034 ± 5.869 mC cm$^{-2}$ ('All arrays').

Next, we provided proof-of-concept evidence about the use of printed platinum-based electrocorticography arrays in-vivo to detect sensory-evoked cortical activity. The printed array was placed onto the visual cortex of an anesthetized rabbit (Figure 6.3a), and visually evoked potentials were recorded upon flash stimulation of the eye contralateral to the recording hemisphere (Figure 6.3b). Recordings showed the appearance of the classical peaks of the visually evoked potentials (Figure 6.3c) with an amplitude modulated by the stimulus luminance (Figure 3d). Besides, the biocompatibility of the printed arrays was also proven. According to ISO 10993-5: Biological Evaluation of Medical Devices, in-vitro cytotoxicity was evaluated via an extraction test on the murine fibroblastic L929 cells[37]. Cell viability was estimated via an XTT assay on triplicate culture wells for each sample. Results on the printed platinum-based electrocorticography arrays showed no cytotoxic effect (sample 1: 100% viability; sample 2: 92.4% viability), while positive control has 0.17% viability and negative control has 100% viability (all numbers are averages of 3 repetitions). Therefore, no cytotoxic effect is demonstrated

for viability above 70% compared to the negative control.
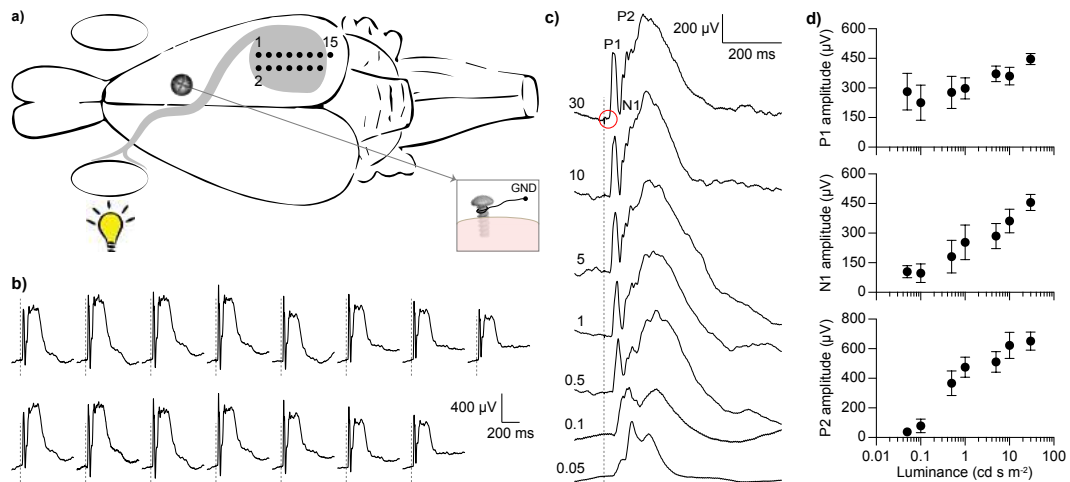


Figure 6.3: Validation in-vivo. (a) Recordings of visually evoked cortical potentials were performed with the printed electrocorticography array covering the visual cortex and a flash stimulation (4 ms, Ganzfeld white LED) in the contralateral eye. (b) Example of responses (synchronous average of 10 repetitions) to a flash illumination of 30 cd s m$^{-2}$. The dashed gray lines show the occurrence of the flash. (c) Example traces obtained from 1 recording channel at increasing flash luminance values. The main peaks (P1, N1, P2) are visible. The dashed line shows the occurrence of the flash. The red circle shows the stimulation artifact. (d) Quantification of the peak amplitudes as a function of the flash luminance. Each data point is the mean (± s.d.) of the 15 recording electrodes. For each electrode, 10 consecutive recordings were averaged.

The main goal of this study was to demonstrate that printed flexible platinum-based electro-corticography arrays can be used in neurophysiological investigations. To do so, the printed geometrical features were kept similar to the ones of conventional electrocorticography ar-rays. However, the minimal resolution that could be achieved with this combination of ink, substrate, and equipment were further investigated (Figure 6.4). A minimum single dot size of about 200 μm with a minimum dot separation of 20 μm was obtained (without in-flight dispensing mode; Figure 6.4a). For lines, a minimum line with of 220 μm with a line spacing of 50 μm was obtained (with in-flight dispensing mode; Figure 6.4b). Last, excellent line stability was also observed for multiple overprints (Figure 6.4c). Printing technology possesses several advantages compared to clean-room microfabrication techniques, such as low-temperature, flexible, cost-effective, and large area processes. These aspects might be relevant for the production of medical-grade MEAs, currently mostly hand-made. In this work, exclusively commercially available materials were employed, which is an advantage for a faster clini-cal translation of these electrocorticography arrays. Printed MEAs were already tested to detect the pressure ulcer in rats and pulse rate and arterial blood oxygenation in humans, but the use of printing techniques for functional materials in biomedical implants is still uncommon[277,403,404]. Concerning MEAs for sensing and stimulating electrogenic tissue, other groups already reported the fabrication of inkjet-printed electrodes for in-vitro applications.

Inkjet-printed gold MEAs were used in-vitro to detect action potentials from cardiomyocyte-like HL-1 cells cultured on top of the device[402]. Uncoated gold is usually a candidate for recording electrodes. However, platinum is a common choice for both recording and stimulating electrodes[400]. Therefore, a printed platinum-based array has the advantage to be more versatile in neurophysiological investigations. Among other materials, inkjet-printed silver / poly(3,4-ethylenedioxythiophene)-poly(styrenesulfonate) were proposed for neuromuscular cartography[405]. To our knowledge, this is the first time that printed flexible platinum-based electrocorticography arrays are used in neurophysiological investigations in-vivo. Further studies will be required to grant the use of printed arrays to monitor or treat neurological disease in humans. Nonetheless, our results represent the first step in this direction.
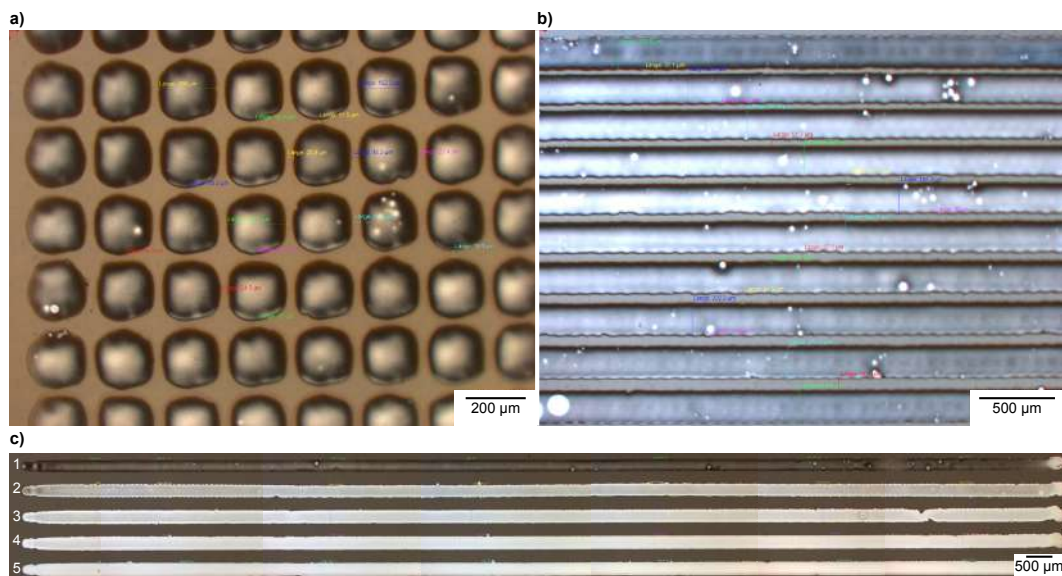


Figure 6.4: Printing resolution. (a) An array of printed single dots. (b) An array of printed single lines. (c) Multiple overprints of 2-cm long platinum lines. The number of overprints is shown on the left.

## 6.3 Experimental section

### 6.3.1 Electrode array printing

Printing was performed on polyimide foils (60-µm thick Kapton HN, DuPont) previously rinsed with isopropyl alcohol. An organometallic non-particulated platinum precursor with 12 wt% platinum metal content was used (16512, Ceimig Limited). The ink was stored at 4 °C. Before use, the ink was filtrated with a PTFE filter with 0.45-µm pore size. A single nozzle inkjet printer (Microdrop Technologies GmbH; Germany) with a 50-µm glass capillary (MDK-140) was used for printing. The printer vacuum chuck was kept at 85 °C, which caused the print head to gradually heat up from room temperature to 40 °C during the printing process. The original layout was discretized to fit a drop spacing of 0.06 mm. Printing was performed with in-flight

dispensing mode (20 mm s$^1$). After printing, the device was pre-cured in a reflow oven at 200 °C for 20 min.

### 6.3.2   Photonic sintering

Photonic sintering was performed with a Pulse Forge 1300 (Novacentrix TX, USA). Three 700-μs pulses were delivered with an interval of 1 ms. The bank voltage was 440 V, corresponding to light energy of 5476 mJ cm$^{-2}$. During light exposure, the samples were cooled by air-flow. The simulation software tool correlates a light pulse into a sintering temperature of approximately 1300 °C.

### 6.3.3   Screen printing

Screen printing was performed with an Aurel VS1520 printer, with the following parameters: print speed 125 mm s$^{-1}$, print type 2 directions print, print gap 2 mm, pressure 10 kg, and squeegee 45 °.  Meshes were manufactured by Koenen GmbH. After printing, the screen-printed layers were heated on a hot plate at 100 °C for 10 min and then cured in reflow oven at 250 °C for 5 min.

### 6.3.4   Electrode arrays with sputtered platinum

Arrays were fabricated as previously described[163]. Briefly, sputtered MEAs were fabricated on 4-inch silicon (Si) wafers (thickness 525 μm) with a titanium-tungsten alloy / aluminum release layer (TiW / Al, 200 nm / 1 μm). A PI layer (HD MicroSystems PI2611, 10 μm) was spin-coated (1400 rpm for 40 s) and then cured by a soft bake (5 min at 65 °C and 5 min at 95 °C) followed by a hard bake (1 hr at 300 °C with nitrogen from 190 °C). A titanium / platinum (Ti / Pt, 5 nm / 150 nm) adhesive / conductive layer was deposited by sputtering (Alliance Concept AC450). A positive photoresist (AZ1512, 2 μm) was deposited by spin-coating and soft baked at 110 °C for 2 min before direct exposure (Heidelberg Instruments MLA150, 405 nm) and development. Electrode shaping and photoresist removal were performed by chlorine dry etching (Corial 210IL) followed by oxygen plasma (500 W for 30 s). MEAs were encapsulated by spin-coating an adhesion promoter (VM651, 1000 rpm for 10 s + 3000 rpm for 30 s), spin-coating and soft baking a first PI layer (PI2611, 10 μm) followed by a second layer (10 μm) and curing (soft and hard bake). Then, a Si hard mask (1 μm) was deposited by sputtering (Alliance Concept AC450), and the photolithography was repeated. Dry etching (Corial 210IL) of Si and eventually PI and photoresist (respectively chlorine and oxygen chemistries) allowed the exposure of Pt pads and electrodes. A final Si dry etching removed the remaining hard mask. The MEAs were cut by a laser cutter (Optec MM200-USP) and released by Al anodic dissolution for 15 hr. Electrodes were 300-μm in diameter.

### 6.3.5   Printed circuit board

MEAs were connected to printed circuit boards using conducting epoxy (EPO-TEK® H20E-FC) placed on the contact pads manually. After, an isolating epoxy (EPO-TEK® 302-3M) was used to ensure a stable connection.

### 6.3.6   Measurements of thickness and electrical resistivity

The thickness was measured with a stylus profilometer (Tencor P-10). The electrical resistivity was measured with a Fluke 73/77 Series III Digital Multimeter.

### 6.3.7   Atomic force microscopy

Surface topography of printed and sputtered platinum electrodes was imaged at room temperature using a Dimension Icon atomic force microscope (Bruker) in PeakForce tapping mode (ScanAsyst Air silicon tip, f0 = 70 kHz, k = 0.4 N m-1). Image processing and roughness evaluation were performed using Gwyddion open-source software.

### 6.3.8   Bending test

A customized cycling stretcher was used to perform the bending test with a cyclic compressive force (bending radius 9.1 mm). The system included a stepping motor and a dedicated mechanics to bend the array. For each test, the stepping motor frequency was set at 0.5 Hz, which resulted in a cycling speed of 10 mm s$^{-1}$. The resistance was measured with a digital multimeter (PeakTech 3690).

### 6.3.9   Electrochemistry

Electrochemical characterizations were performed with a three-electrode (Ag / AgCl reference electrode, Pt counter electrode) potentiostat (Compact Stat, Ivium) in PBS (pH 7.4) at room temperature. Impedance spectroscopy was performed between 10 Hz and 1 MHz with an AC voltage of 50 mV. Cyclic voltammetry was obtained by sweeping a cyclic potential at a speed of 50 mV s-1 between -0.6 V and 0.8 V. For each electrode, the average response over 5 cycles was calculated[37].

### 6.3.10   Animal experiment

Animal experiments were approved by the Département de l'emploi, des affaires sociales et de la santé (DEAS), Direction générale de la santé of the Republique et Canton de Genève (Switzerland, authorization GE1416). The procedure was previously described.(Gaillet et al. 2019) Female New Zealand White rabbits (> 16 weeks, > 2 kg) were sedated with an

intramuscular injection of xylazine (5 mg kg$^{-1}$). Anesthesia and analgesia were provided with an intramuscular injection of an anesthetic mix composed of medetomidine (0.5 mg kg$^{-1}$), ketamine (25 mg kg$^{-1}$), and buprenorphine (0.03 mg kg$^{-1}$). Eye drops were placed on the eye to prevent eye drying. The rabbit was placed on a heating pad at 35 °C for the entire procedure. Oxygen was provided with a mask to prevent hypoxia during the anesthesia. The head was shaved and cleaned with 70% ethanol and betadine. Before cortical skin incision, a mix of lidocaine (6 mg kg$^{-1}$), bupivacaine (2.5 mg kg$^{-1}$), and epinephrine (0.1 mg kg$^{-1}$) was injected subcutaneously on the surgical sites. After 5 minutes, the skin was opened and pulled aside to expose the skull; afterwards, the skull was cleaned with cotton swabs. A craniotomy was made to expose the right visual cortex. The electrocorticography array was placed onto the visual cortex. Light flashes (4 ms) at increasing luminance levels (0.05, 0.1, 0.5, 1, 5, 10, and 30 cd s m$^{-2}$) were delivered using a Ganzfeld stimulator (BM6007B9.5, Biomedica Mangoni) positioned close to the contralateral eye. For cortical recordings, the array was connected to a wireless amplifier (W2100-HS32, Multi Channel Systems) and a data acquisition system (W2100, Multi Channel Systems). Data were filtered (0.1-300 Hz) and sampled at 5 kHz; ten sweeps were averaged for each luminance level. Data analysis was performed in MATLAB (MathWorks). The rabbit was euthanized at the end of the recordings, while still under anesthesia, with an intravenous injection of pentobarbital (120 mg kg$^{-1}$).

### 6.3.11    Cytotoxycity test in-vitro

The test was performed by an accredited company (Medistri SA) as previously described[37]. The test was conducted according to the requirement of ISO 10993-5: Biological Evaluation of Medical Devices, in-vitro cytotoxicity test; ISO 10993-12: Test article preparation and reference materials; USP 35-NF30 (87): Biological Reactivity test, in-vitro; Medistri internal procedure WI 47 and WI 56. Cytotoxycity was assessed on two independent printed platinum-based electrocorticography arrays sterilized with EtO before the test. The test on extraction was performed on each array with a surface area of 6 cm2 and a ratio of the product to extraction vehicle of 3 cm2 ml$^{-1}$. The extraction vehicle was Eagle's Minimum Essential Medium supplemented with fetal bovine serum, penicillin-streptomycin, amphotericin B, and L-glutamine. The extraction was performed for 24 hr at 37 °C. The extract was added on triplicate cultures wells containing a sub-confluent L929 cell monolayer (1:1 dilution). The test samples and the control wells were incubated at 37 °C in 5 % CO2 for 24 hours. Following incubation, the cell cultures were examined for quantitative cytotoxic evaluation. 50 μl per well of XTT reagent was added to the cells then incubated at 37 °C in 5 % CO2 for further 3 to 5 hr. An aliquot of 100 μl was then transferred from each well into the corresponding wells of a new plate, and the optical density was measured at 450nm.

### 6.3.12    Statistical analysis and graphical representation

Statistical analysis and graphical representation were performed with Prism (GraphPad Software Inc.). The normality test (D'Agostino & Pearson omnibus normality test) was performed

in each dataset to justify the use of a parametric or non-parametric test. In each figure, p-values are represented as * $p < 0.05$, ** $p < 0.01$, *** $p < 0.001$, and **** $p < 0.0001$. Data are reported as the mean ± s.d.; n is used to identify the number of electrodes or measures and N is used to identify the number of arrays.

## 6.4   Acknowledgements

# 7 Conclusions and future perspectives

## 7.1 Summary of the performed research

Millions of people worldwide suffer from untreatable blindness. Visual prostheses, interfacing across the retino- calcarine span, can offer a form of artificial vision to help these blind patients in their everyday life activities. Among the different implants currently under investigation, the starting point for this research was the OpticSELINE, a flexible intraneural electrode array to be proposed for the electrical stimulation of the optic nerve. This is why this thesis addresses some technological limitations and proposes possible solutions that could advance ON prostheses and improve the state of the art in artificial vision.

*Chapter 3*

Despite the promising results obtained from the stimulation of the ON with the OpticSELINE, spatial shifts of the cortical activity upon stimulation with different electrodes were not found. For this reason, we developed two machine learning algorithms, a classifier based on an SVM algorithm and a linear regression model based on a wide variety of features, to understand whether the cortical activities elicited by the electrical stimulation were distinct. First we demonstrated the ability of the SVM approach in classifying visual stimuli with increased accuracy when visual stimuli were further apart in the visual field. Then, we tested them on ON stimulation. The SVM algorithm returned nearly 100% classification accuracy from the smallest separation distance between two electrodes above 500 μA for the Flat OpticSELINE and above 200 μA for the OpticSELINE. These results obtained also with the linear regression model confirmed that cortical activities elicited by different stimulation electrodes are indeed distinct and representative of different portions of the visual field. This work opens the

way to the use of machine learning algorithms to automatically detect small changes in cortical activity and help in evaluating novel ON interfaces. What is more, such algorithms could have additional applications in the optimization of stimulation parameters as well as automatization of the calibration of the optic nerve prosthesis once they reach clinical use.

*Chapter 4*

Another limitation that emerged from preliminary work on the OpticSELINE is the limited spatial selectivity of the stimulation. When two or more neighboring electrodes are stimulating at the same time, the respective activated areas within the nerve overlap at increasing current amplitudes. As it is the case for the majority of the neural interfaces, the OpticSELINE worked in monopolar configuration. We therefore developed a novel electrode configuration, namely a 3D multilayer concentric bipolar (CB) configuration, that allowed bipolar stimulation without increasing the size of the implant. First, we compared the performance of the 3D multilayer CB versus the monopolar configuration in-silico, with FEA simulations and a hybrid FEA-NEURON model. The results confirmed the reduced spread of the electric field and focal activation of the nerve fibers when using the 3D multilayer CB configuration. Then, we fabricated a Flat-OpticSELINE electrode array with 8 3D multilayer CB electrodes and validated its functionality in-vivo. We showed that the novel configuration reduced the response spread across the visual cortex. The work presented here can be further optimized by studying the impact of the size between central and return electrode on how this would change the profile of the stimulation or the penetration depth. Another interesting aspect could be the investigation in-vivo of the simultaneous activation of multiple electrodes in monopolar and bipolar.

*Chapter 5*

The success of a neuroprosthesis such as the OpticSELINE is not determined only by its stimulation capabilities but also by the materials chosen to interface with the biological host. This is why parallelly to the development of the 3D multilayer CB configuration we investigated the feasibility of OSTE+ polymers to possibly substitute PI as a flexible but toughsubstrate. Among the commercially available OSTE+ formulations, we chose OSTE+ Flex because of its mechanical properties that makes it flexible and deformable with an elastic modulus closer to the nerve tissue than PI. These are not the only advantages that characterize OSTE+ Flex. It is transparent and thanks to its chemistry can be photo-patterned with UV light and bond covalently to a series of surfaces without the need of extra adhesive layers or plasma treatments. This first proof-of-concept study characterized OSTE+ Flex resin with the aim to design microelectrode arrays and validated its compatibility with cleanroom processes, such as photolithography and sputtering. After having optimized the fabrication steps, we successfully tested an OSTE+ Flex conformable multilayer ECoG array with 40 μm diameter electrodes made of Pt-PtB in acute experiments on mice for recording and stimulation. Finally, we studied the foreign body reaction resulting from the implantation of OSTE+ Flex samples on the mouse cortex over a period of six weeks. The preliminary results showed that there was no significant difference with the sham group where only a craniotomy was performed. A higher

number of samples should be reached to draw more solid conclusions. Moreover, it would be interesting to study the difference between untethered and tethered devices. Despite the need of further characterization for long-term applications, OSTE+ Flex already demonstrated several advantages in manufacturing capability compared to PDMS, making it equally or more amenable to MEMS-based fabrication techniques as PI and parylene-C, while being softer, transparent and showing superior surface adhesion.

*Chapter 6*

The last work presented here shows the possibility to use additive manufacturing to fabricate flexible microelectrode arrays in Pt and PI, two common materials found in several neural interfaces such as the OpticSELINE. The main goal of this study was to prove that all-printed flexible Pt-based ECoG arrays can be used to measure neurophysiological activity in-vivo. We first characterized the mechanical and electrochemical properties of the inkjet printed platinum and screen printed PI. This was followed by in-vivo recording of visually evoked cortical potential in rabbits upon flash stimulation. Printing technologies can be advantageous compared with microfabrication techniques for fast and flexible prototyping, reducing costs and implementing large-area processes. these approaches are just starting to be investigated and used in the neuroprosthetics field but can be promising for 3D microstructure and scaffolds for better biointegration on stretchable matrices.

## 7.2 Future perspectives on optic nerve stimulation

*"From understanding comes innovation…"*
Professor Warren Grill

Innovations in engineering and neuroscience have enabled the development of sophisticated neural implants. Research in optic nerve neurotechnology has tackled significant technical challenges, including reducing the footprint of the electrode arrays, increasing the number of active sites within the nerve, and selective activation of axons. However, significant gaps in knowledge remain in the realm of neuroscience, namely understanding the organization of the fibers and the information they encode. This is particularly true for the animal model used in this work, the rabbit. As animal models, they are relatively inexpensive and easy to handle. They also have a simplified visual system where there is no fovea, but a visual streak, and high percentage of fiber decussation as seen in **Chapter 2**. Because of this, their visual system is also considerably different from the human's both in terms of dimensions and organization. Nevertheless, they could serve as a first step for preclinical tests. We would however need a deeper understanding of the retinotopic mapping of their ON axonal fibers. This knowledge could also be useful to implement a computational model that could estimate the cortical activation patterns expected from the electrical stimulation of the optic nerve. Hence, our results obtained in **Chapter 3** and **4** could be reassessed and better interpreted.

Investigating the retinotopic map of the optic nerve could be achieved in several ways. First,

topical application of dyes on small portions of the retina, followed by immunohistochemistry of the optic nerve would allow the distinction of the axons corresponding to the stained portion of the retina from which the retinotopic map is better known. An alternative approach could consist in recording the compound action potentials from the nerve in response to visual stimuli spanning across the visual field of the rabbit, similarly to what was presented in **3**. An intraneural electrode like the OpticSELINE could be used to get a first grasp of the organization. Having additional information on the position of the implant within the nerve would also be necessary. In fact, the surgical implantation in the intracranial segment, as performed so far, is challenging and depending where the needle first penetrates the nerve, the electrode array could be placed differently for every experiment. High-resolution CT-scan of the explanted nerve with the implant could help acquiring this essential information. Alternatively, electrical impedance tomography[406] could detect transient impedance changes in the axons caused by the opening of ionic channels during propagation of action potentials upon visual stimulation.

While performing the mapping of the nerve, it could be helpful to adapt the recording setup on the visual cortex. So far we used a 32 channels ECoG array. In **3**, even for the most separated and non-overlapping visual stimulation patterns, there was no evident shift in the almost identical cortical maps. This could be due to several factors. The ECoG array was often placed on the frontal part of V1 (Figure chapter 3.1a) that seems to encode for peripheral vision (Figure 2.2b). Visual stimuli were only covering 28 x 44 degrees of the visual field while rabbits are lateral eyed animals. Thus, it is possible the electrodes could detect a general cortical activity generated by the integration of neural signals from a large volume of tissue but not specific for the stimulus presented.

In the future, it would be best to first assess the area of the brain that responds the most to certain visual stimuli, defining the recording implant's receptive field. Besides finding the best position, there are other aspects to consider such as the size of the array, the electrode's density and the level of proximity with the neurons. Several groups working on suprachoroidal prostheses[306,407,408] recorded V1 activity with high-density penetrating electrodes such as the Utah array. It was possible to study local field potential responses as well as neuron's firing patterns. The limiting factors of this approach are related to the restricted size of the Utah array and challenges linked to surgical implantation depending on the target area. Alternatively, Provansal et al.[409] demonstrated the use of functional ultrasound imaging to study V1 activity in rat's brains. This technique could also help in understanding the interaction with upstream visual areas. Lastly, a more challenging option to study the retinotopic organization of the nerve would be stimulating with an intraneural implant in multiple locations and recording the nerve activity with another one to find the corresponding receptive fields. Spatial constrains in-vivo limit the feasibility of this approach, however trying ex-vivo could be a preliminary step.

Non-human primates should eventually be considered to foster artificial vision using ON stimulation. As for many applications in the field of neuroscience, this animal model is the closest to the human in terms of nervous system organization, particularly for the optic

nerve. Their similar configuration shows a magnification of the center of the visual field, they have binocular vision and their visual cortex is more representative of the human one. In addition, access to the optic nerve for chronic experiments could be less challenging than for rabbits. This means that it could be possible to perform studies in awake animals, avoiding the possible side effects of the anesthesia protocols. Behavioral tasks could also be performed to gain insights on how more complex patterns are encoded through the optic nerve to the brain. These experiments could also be carried out with electrical stimulation to understand phosphenes perception, such as coordinates, size, and appearance as shown with cortical prostheses[106].

Acquiring more knowledge about the optic nerve and the visual cortex activity can lead to the creation and validation of computational frameworks that are more representative of the reality of this complex system. So far, hybrid models, such as the one described in **4** and machine learning algorithms[188] are a simplified version of this sensory system. However, they are a powerful tool to test new stimulation protocols, closed-loop systems and rethink the design of future neural interfaces for ON stimulation. In fact, given a more precise knowledge of the organization of the optic nerve, they could provide an estimation of the theoretical elicited visual sensation while varying the number of electrode sites and their distribution in the nerve sections.

The OpticSELINE is a modified version of the SELINE developed for the sciatic nerve, which in principle does not require a high number of stimulating sites. As mentioned in Chapter 1, the use of graphene oxide[410] could help in reducing the electrode size and doubling their number on each device. Hence, if we could implant several OpticSELINEs in a single nerve, this would bring the total number of stimulating sites in the range of the Argus II while covering larger portions of the visual field. However, simulation studies have suggested that a visual prosthesis should elicit between 500 and 1000 of phosphenes in order to allow the patient to read[411]. It is unlikely that with the current design these numbers can be satisfied. On the other hand, it remains to be understood if this number of electrodes would be sufficient for orientation.

While investigating the retinotopic organization, we should explore new design possibilities. A first inspiration can be the MINA (Figure 7.1a), a flexible microneedle nerve array, which is the first high-density penetrating electrode array made with axon-sized silicon microneedles embedded in low-modulus thin silicone[412]. This version could be modified to have microneedles of different height and possibly electrode of the surface of the cuff with a 3D CB configuration to improve superficial selectivity. Alternative materials and fabrication techniques could also be employed. OSTE+ Flex could replace PDMS, Au-coated $TiO_2$ NWs could be transferred on it using a process adapted from Tybrandt et al.[269] (Figure 7.1b). Microneedles could be fabricated using fast micron-scale 3D printing with a resonant-scanning two-photon microscope developed by Gardner Lab[413,414], leveraging the advancement in additive manufacturing. A wireless alternative would consist in having free-standing microneedles all equipped with a transmitter implanted in different zones around the nerve akin to neural dust[415]. Surgical implantation strategies should be studied with skilled neurosurgeons or ophthalmologists

while designing these new devices. Whether the future of ON stimulation will be a hybrid cuff-intraneural electrode array or wireless units singularly controlled, the biocompatibility and longevity of all these options must be assessed.
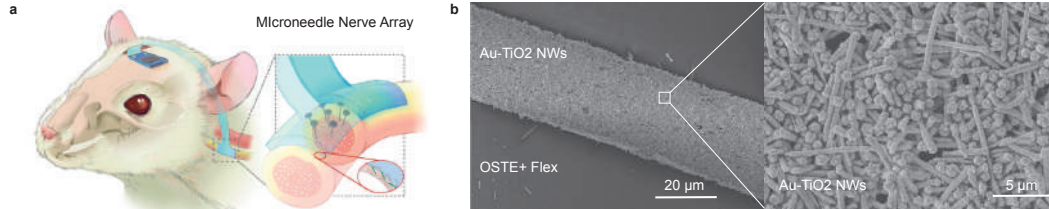


Figure 7.1: (a) Conceptual diagram of a chronically implanted MINA in a rodent autonomic nerve. Adapted from Yan et al. 2022[412] (b) SEM images of Au-TiO$_2$ NWs transfered onto OSTE+ Flex substrate with an almost optimized fabrication developed in our lab.

## 7.3 Opportunities of the developed technologies for bioelectronic interfaces

In the same way that the field of visual prostheses translated advancements from neuropros-thetics into clinical applications, the research presented in this work may contribute to further developments in neural implants targeting other systems. Retinal prostheses could take ad-vantage of the 3D multilayer CB configuration in suprachoroidal or epiretinal approaches to activate a smaller subset of retinal ganglion cells. Peripheral nerve stimulation for touch restoration or vagus nerve regulation could also benefit from strategies for spatially selective activation of nerve fibers. Thin-film based electrode arrays could be fabricated with novel materials that might reveal superior properties to the classic PDMS, PI or Parylene-C. OSTE+ polymers could be engineered to integrate multimodal systems for researchers to study the brain dynamics. The exploration of alternative fabrication processes holds the potential for fast prototyping of new and more complex design integration. Machine learning pipelines are already becoming the standard for data analysis. It is the beauty and mystery of the complex nervous system that drives researchers into pushing the boundaries and finding inspiration within and outside the field.

# Bibliography

1. Burton, M. J. *et al.* The Lancet Global Health Commission on Global Eye Health: vision beyond 2020. *The Lancet Global Health* **9,** e489–e551. ISSN: 2214109X. https://linkinghub.elsevier.com/retrieve/pii/S2214109X20304885 (2022) (Apr. 2021).

2. Bourne, R. *et al.* Trends in prevalence of blindness and distance and near vision impairment over 30 years: an analysis for the Global Burden of Disease Study. *The Lancet Global Health* **9,** e130–e143. ISSN: 2214109X. https://linkinghub.elsevier.com/retrieve/pii/S2214109X20304253 (2022) (Feb. 2021).

3. Court, H., McLean, G., Guthrie, B., Mercer, S. W. & Smith, D. J. Visual impairment is associated with physical and mental comorbidities in older adults: a cross-sectional study. *BMC Medicine* **12,** 181. ISSN: 1741-7015. http://bmcmedicine.biomedcentral.com/articles/10.1186/s12916-014-0181-7 (2022) (Dec. 2014).

4. World Health Organization. *World report on vision* 160 pp. ISBN: 978-92-4-151657-0. https://apps.who.int/iris/handle/10665/328717 (2022) (World Health Organization, Geneva, 2019).

5. Scholl, H. P. N. *et al.* Emerging therapies for inherited retinal degeneration. *Science Translational Medicine* **8.** ISSN: 1946-6234, 1946-6242. https://www.science.org/doi/10.1126/scitranslmed.aaf2838 (2022) (Dec. 7, 2016).

6. Xue, K. & MacLaren, R. E. Correcting visual loss by genetics and prosthetics. *Current Opinion in Physiology* **16,** 1–7. ISSN: 24688673. https://linkinghub.elsevier.com/retrieve/pii/S2468867320300213 (2022) (Aug. 2020).

7. Mirochnik, R. M. & Pezaris, J. S. Contemporary approaches to visual prostheses. *Military Medical Research* **6,** 19. ISSN: 2054-9369. https://mmrjournal.biomedcentral.com/articles/10.1186/s40779-019-0206-9 (2022) (Dec. 2019).

8.  Cehajic-Kapetanovic, J., Singh, M. S., Zrenner, E. & MacLaren, R. E. Bioengineering strategies for restoring vision. *Nature Biomedical Engineering*. ISSN: 2157-846X. https://www.nature.com/articles/s41551-021-00836-4 (2022) (Jan. 31, 2022).

9.  Goetz, G. A. & Palanker, D. V. Electronic approaches to restoration of sight. *Reports on Progress in Physics* **79,** 096701. ISSN: 0034-4885, 1361-6633. https://iopscience.iop.org/article/10.1088/0034-4885/79/9/096701 (2022) (Sept. 1, 2016).

10. Lambertus, S. *et al.* Highly sensitive measurements of disease progression in rare disorders: Developing and validating a multimodal model of retinal degeneration in Stargardt disease. *PLOS ONE* **12** (ed Wedrich, A.) e0174020. ISSN: 1932-6203. https://dx.plos.org/10.1371/journal.pone.0174020 (2022) (Mar. 29, 2017).

11. Bourne, R. R. *et al.* Causes of vision loss worldwide, 1990–2010: a systematic analysis. *The Lancet Global Health* **1,** e339–e349. ISSN: 2214-109X (2013).

12. XXXI. An account of Mr. Benjamin Franklin's treatise, lately published, intituled, Experiments and observations on electricity, made at Philadelphia in America. *Philosophical Transactions of the Royal Society of London* **47,** 202–211. ISSN: 0261-0523, 2053-9223. https://royalsocietypublishing.org/doi/10.1098/rstl.1751.0032 (2022) (Dec. 31, 1752).

13. LEROY, C. Ou l'on rend compte de quelques tentatives que l'on a faites pour guerir plusieurs maladies par l'electricite. *Hist Acad Roy Sciences (Paris) Memoire Math. Phys.* **60,** 87 (1755).

14. Löwenstein, K. & Borchardt, M. Symptomatologie und elektrische Reizung bei einer Schußverletzung des Hinterhauptlappens. *Deutsche Zeitschrift für Nervenheilkunde* **58.** Publisher: Verlag Von FCW Vogel, 264–292 (1918).

15. Krause, F. Die Sehbahn in Chirurgischer Beziehung und die Faradische Reizung des Sehzentrums. *Klinische Wochenschrift* **3,** 1260–1265. ISSN: 0023-2173, 1432-1440. http://link.springer.com/10.1007/BF01735820 (2022) (July 1924).

16. Foerster, O. Beitrage zur pathophysiologie der sehbahn und der spehsphare. *J Psychol Neurol* **39,** 435–463 (1929).

17. Ghezzi, D. Translation of a photovoltaic retinal prosthesis. *Nature Biomedical Engineering* **4,** 137–138. ISSN: 2157-846X. http://www.nature.com/articles/s41551-020-0520-2 (2022) (Feb. 2020).

18. Fernandez, E. Development of visual Neuroprostheses: trends and challenges. *Bioelectronic Medicine* **4,** 12. ISSN: 2332-8886. https://bioelecmed.biomedcentral.com/articles/10.1186/s42234-018-0013-8 (2022) (Dec. 2018).

19. Gregory-Evans, K. & Bhattacharya, S. S. Genetic blindness: current concepts in the pathogenesis of human outer retinal dystrophies. *Trends in Genetics* **14,** 103–108. ISSN: 01689525. https://linkinghub.elsevier.com/retrieve/pii/S0168952598014024 (2022) (Mar. 1998).

20. Hamel, C. Retinitis pigmentosa. *Orphanet journal of rare diseases* **1,** 40. ISSN: 1750-1172 (2006).

21.  Hornig, R. *et al.* in *Artificial sight* 111–128 (Springer, 2007).

22.  Humayun, M. S. *et al.* Interim results from the international trial of Second Sight's visual prosthesis. *Ophthalmology* **119.** ISBN: 0161-6420 Publisher: Elsevier, 779–788 (2012).

23.  Stingl, K. *et al.* Interim results of a multicenter trial with the new electronic subretinal implant alpha AMS in 15 patients blind from inherited retinal degenerations. *Frontiers in neuroscience* **11.** ISBN: 1662-453X Publisher: Frontiers, 445 (2017).

24.  Farnum, A. & Pelled, G. New Vision for Visual Prostheses. *Frontiers in Neuroscience* **14,** 36. ISSN: 1662-453X. https://www.frontiersin.org/article/10.3389/fnins.2020.00036/full (2021) (Feb. 18, 2020).

25.  Ghezzi, D. Retinal prostheses: progress toward the next generation implants. *Frontiers in Neuroscience* **9.** ISSN: 1662-453X. http://journal.frontiersin.org/Article/10.3389/fnins.2015.00290/abstract (2021) (Aug. 20, 2015).

26.  Boinagrov, D., Pangratz-Fuehrer, S., Goetz, G. & Palanker, D. Selectivity of direct and network-mediated stimulation of the retinal ganglion cells with epi-, sub-and intraretinal electrodes. *Journal of neural engineering* **11.** ISBN: 1741-2552 Publisher: IOP Publishing, 026008 (2014).

27.  Chenais, N. A. L., Leccardi, M. J. I. A. & Ghezzi, D. Capacitive-like photovoltaic epiretinal stimulation enhances and narrows the network-mediated activity of retinal ganglion cells by recruiting the lateral inhibitory network. *Journal of Neural Engineering* **16,** 066009. ISSN: 1741-2552 (Oct. 18, 2019).

28.  Lee, B. *et al.* Engineering Artificial Somatosensation Through Cortical Stimulation in Humans. *Frontiers in Systems Neuroscience* **12,** 24. ISSN: 1662-5137. https://www.frontiersin.org/article/10.3389/fnsys.2018.00024/full (2022) (June 4, 2018).

29.  Weitz, A. C. *et al.* Improving the spatial resolution of epiretinal implants by increasing stimulus pulse duration. *Science Translational Medicine* **7.** ISSN: 1946-6234, 1946-6242. https://www.science.org/doi/10.1126/scitranslmed.aac4877 (2022) (Dec. 16, 2015).

30.  Yue, L., Weiland, J. D., Roska, B. & Humayun, M. S. Retinal stimulation strategies to restore vision: Fundamentals and systems. *Progress in Retinal and Eye Research* **53,** 21–47. ISSN: 18731635. http://dx.doi.org/10.1016/j.preteyeres.2016.05.002 (2016).

31.  Barriga-Rivera, A. *et al.* High-amplitude electrical stimulation can reduce elicited neuronal activity in visual prosthesis. *Scientific Reports* **7,** 42682. ISSN: 2045-2322. http://www.nature.com/articles/srep42682 (2021) (May 2017).

32.  Cheng, D. L., Greenberg, P. B. & Borton, D. A. Advances in Retinal Prosthetic Research: A Systematic Review of Engineering and Clinical Characteristics of Current Prosthetic Initiatives. *Current Eye Research* **42,** 334–347. ISSN: 0271-3683, 1460-2202. https://www.tandfonline.com/doi/full/10.1080/02713683.2016.1270326 (2022) (Mar. 4, 2017).

33.  Ayton, L. N. *et al.* An update on retinal prostheses. *Clinical Neurophysiology* **131,** 1383–1398. ISSN: 13882457. https://linkinghub.elsevier.com/retrieve/pii/S1388245719313264 (2022) (June 2020).

34. Tong, W., Meffin, H., Garrett, D. J. & Ibbotson, M. R. Stimulation Strategies for Improving the Resolution of Retinal Prostheses. *Frontiers in Neuroscience* **14,** 262. ISSN: 1662-453X. https://www.frontiersin.org/article/10.3389/fnins.2020.00262/full (2022) (Mar. 26, 2020).

35. Lewis, P. M., Ackland, H. M., Lowery, A. J. & Rosenfeld, J. V. Restoration of vision in blind individuals using bionic devices: A review with a focus on cortical visual prostheses. *Brain Research* **1595,** 51–73. ISSN: 00068993. https://linkinghub.elsevier.com/retrieve/pii/S0006899314015674 (2021) (Jan. 2015).

36. Airaghi Leccardi, M. J. I. Development of a new visual prosthesis for preclinical studies on artificial vision. Publisher: Lausanne, EPFL. http://infoscience.epfl.ch/record/277678 (2022) (2020).

37. Ferlauto, L. *et al.* Design and validation of a foldable and photovoltaic wide-field epiretinal prosthesis. *Nature Communications* **9,** 1–15. ISSN: 20411723 (2018).

38. Schaffrath, K. *et al.* New epiretinal implant with integrated sensor chips for optical capturing shows a good biocompatibility profile in vitro and in vivo. *BioMedical Engineering OnLine* **20,** 102. ISSN: 1475-925X. https://biomedical-engineering-online.biomedcentral.com/articles/10.1186/s12938-021-00938-9 (2022) (Dec. 2021).

39. Thorn, J. T., Migliorini, E. & Ghezzi, D. Virtual reality simulation of epiretinal stimulation highlights the relevance of the visual angle in prosthetic vision. *Journal of Neural Engineering* **17,** 056019. ISSN: 1741-2560, 1741-2552. https://iopscience.iop.org/article/10.1088/1741-2552/abb5bc (2022) (Oct. 1, 2020).

40. Opie, N. L., Burkitt, A. N., Meffin, H. & Grayden, D. B. Heating of the eye by a retinal prosthesis: modeling, cadaver and in vivo study. *IEEE transactions on biomedical engineering* **59.** ISBN: 0018-9294 Publisher: IEEE, 339–345 (2011).

41. Ahuja, A. K. & Behrend, M. R. The Argus™ II retinal prosthesis: factors affecting patient selection for implantation. *Progress in Retinal and Eye Research* **36.** ISBN: 1350-9462 Publisher: Elsevier, 1–23 (2013).

42. Shepherd, R. K., Shivdasani, M. N., Nayagam, D. A., Williams, C. E. & Blamey, P. J. Visual prostheses for the blind. *Trends in biotechnology* **31.** ISBN: 0167-7799 Publisher: Elsevier, 562–571 (2013).

43. Yue, L. *et al.* Ten-year follow-up of a blind patient chronically implanted with epiretinal prosthesis Argus I. *Ophthalmology* **122.** ISBN: 0161-6420 Publisher: Elsevier, 2545–2552. e1 (2015).

44. Humayun, M. S. *et al.* Visual perception in a blind subject with a chronic microelectronic retinal prosthesis. *Vision research* **43.** ISBN: 0042-6989 Publisher: Elsevier, 2573–2581 (2003).

45. Weitz, A. C. *et al.* Improving the spatial resolution of epiretinal implants by increasing stimulus pulse duration. *Science Translational Medicine* **7.** ISSN: 1946-6234, 1946-6242. https://www.science.org/doi/10.1126/scitranslmed.aac4877 (2021) (Dec. 16, 2015).

46. Ayton, L. N. *et al.* An update on retinal prostheses. *Clinical Neurophysiology* **131,** 1383–1398. ISSN: 13882457. https://linkinghub.elsevier.com/retrieve/pii/S1388245719313264 (2022) (June 2020).

47. Mills, J. O., Jalil, A. & Stanga, P. E. Electronic retinal implants and artificial vision: journey and present. *Eye* **31.** ISBN: 1476-5454 Publisher: Nature Publishing Group, 1383–1398 (2017).

48. Palanker, D., Le Mer, Y., Mohand-Said, S., Muqit, M. & Sahel, J. A. Photovoltaic Restoration of Central Vision in Atrophic Age-Related Macular Degeneration. *Ophthalmology* **127,** 1097–1104. ISSN: 01616420. https://linkinghub.elsevier.com/retrieve/pii/S0161642020301895 (2022) (Aug. 2020).

49. Flores, T. *et al.* Optimization of pillar electrodes in subretinal prosthesis for enhanced proximity to target neurons. *Journal of Neural Engineering* **15,** 036011. ISSN: 1741-2560, 1741-2552. https://iopscience.iop.org/article/10.1088/1741-2552/aaac39 (2021) (June 1, 2018).

50. Palanker, D., Le Mer, Y., Mohand-Said, S. & Sahel, J. A. Simultaneous perception of prosthetic and natural vision in AMD patients. *Nature Communications* **13,** 513. ISSN: 2041-1723. https://www.nature.com/articles/s41467-022-28125-x (2022) (Dec. 2022).

51. Chow, A. Y. The Artificial Silicon Retina Microchip for the Treatment of VisionLoss From Retinitis Pigmentosa. *Archives of Ophthalmology* **122,** 460. ISSN: 0003-9950. http://archopht.jamanetwork.com/article.aspx?doi=10.1001/archopht.122.4.460 (2022) (Apr. 1, 2004).

52. Zrenner, E. *et al.* Subretinal electronic chips allow blind patients to read letters and combine them to words. *Proceedings of the Royal Society B: Biological Sciences* **278.** ISBN: 0962-8452 Publisher: The Royal Society, 1489–1497 (2011).

53. Edwards, T. L. *et al.* Assessment of the Electronic Retinal Implant Alpha AMS in Restoring Vision to Blind Patients with End-Stage Retinitis Pigmentosa. *Ophthalmology* **125,** 432–443. ISSN: 01616420. https://linkinghub.elsevier.com/retrieve/pii/S0161642017321796 (2022) (Mar. 2018).

54. Villalobos, J. *et al.* A Wide-Field Suprachoroidal Retinal Prosthesis Is Stable and Well Tolerated Following Chronic Implantation. *Investigative Opthalmology & Visual Science* **54,** 3751. ISSN: 1552-5783. http://iovs.arvojournals.org/article.aspx?doi=10.1167/iovs.12-10843 (2022) (May 29, 2013).

55. Petoe, M. A. *et al.* A Second-Generation (44-Channel) Suprachoroidal Retinal Prosthesis: Interim Clinical Trial Results. *Translational Vision Science & Technology* **10,** 12. ISSN: 2164-2591. https://tvst.arvojournals.org/article.aspx?articleid=2777940 (2022) (Sept. 28, 2021).

56. Eggenberger, S. C. *et al.* Implantation and long-term assessment of the stability and biocompatibility of a novel 98 channel suprachoroidal visual prosthesis in sheep. *Biomaterials* **279,** 121191. ISSN: 01429612. https://linkinghub.elsevier.com/retrieve/pii/S0142961221005482 (2022) (Dec. 2021).

57. Ayton, L. N. *et al.* First-in-human trial of a novel suprachoroidal retinal prosthesis. *PLoS ONE* **9,** 1–26. ISSN: 19326203 (2014).

58. Fujikado, T. *et al.* One-Year Outcome of 49-Channel Suprachoroidal–Transretinal Stimulation Prosthesis in Patients With Advanced Retinitis Pigmentosa. *Investigative Opthalmology & Visual Science* **57,** 6147. ISSN: 1552-5783. http://iovs.arvojournals.org/article.aspx?doi=10.1167/iovs.16-20367 (2022) (Nov. 11, 2016).

59. Petoe, M. A. *et al.* Determining the Contribution of Retinotopic Discrimination to Localization Performance With a Suprachoroidal Retinal Prosthesis. *Investigative Opthalmology & Visual Science* **58,** 3231. ISSN: 1552-5783. http://iovs.arvojournals.org/article.aspx?doi=10.1167/iovs.16-21041 (2022) (June 28, 2017).

60. Shivdasani, M. N. *et al.* Identification of Characters and Localization of Images Using Direct Multiple-Electrode Stimulation With a Suprachoroidal Retinal Prosthesis. *Investigative Opthalmology & Visual Science* **58,** 3962. ISSN: 1552-5783. http://iovs.arvojournals.org/article.aspx?doi=10.1167/iovs.16-21311 (2022) (Aug. 9, 2017).

61. Bloch, E., Luo, Y. & da Cruz, L. Advances in retinal prosthesis systems. *Therapeutic Advances in Ophthalmology* **11,** 251584141881750. ISSN: 2515-8414, 2515-8414. http://journals.sagepub.com/doi/10.1177/2515841418817501 (2022) (Jan. 2019).

62. Farvardin, M. *et al.* The Argus-II Retinal Prosthesis Implantation; From the Global to Local Successful Experience. *Frontiers in Neuroscience* **12,** 584. ISSN: 1662-453X. https://www.frontiersin.org/article/10.3389/fnins.2018.00584/full (2022) (Sept. 5, 2018).

63. Gaillet, V., Borda, E., Zollinger, E. G. & Ghezzi, D. A machine-learning algorithm correctly classifies cortical evoked potentials from both visual stimulation and electrical stimulation of the optic nerve. *Journal of Neural Engineering* **18,** 046031. ISSN: 1741-2560, 1741-2552. https://iopscience.iop.org/article/10.1088/1741-2552/abf523 (2022) (Aug. 1, 2021).

64. Veraart, C. *et al.* Visual sensations produced by optic nerve stimulation using an implanted self-sizing spiral cuff electrode. *Brain Research* **813,** 181–186. ISSN: 00068993. https://linkinghub.elsevier.com/retrieve/pii/S0006899398009779 (2021) (Nov. 1998).

65. Veraart, C., Wanet-Defalque, M. C., Gérard, B., Vanlierde, A. & Delbeke, J. Pattern Recognition with the Optic Nerve Visual Prosthesis. *Artificial Organs* **27,** 996–1004. ISSN: 0160564X (2003).

66. Brelén, M. E., Duret, F., Gérard, B., Delbeke, J. & Veraart, C. Creating a meaningful visual perception in blind volunteers by optic nerve stimulation. *Journal of Neural Engineering* **2.** ISSN: 17412560 (2005).

67. Rathbun, S. D. Chapter 1 restoring vision to the blind: the new age of implanted visual prostheses recent advances in retinal stimulation: clinical applications. *Transl. Vis. Sci. Technol* **3,** 3–13 (2014).

68.  Fried, S. I. & Shivdasani, M. N. Selective activation of the visual cortex. *Nature Biomedical Engineering* **4,** 139–141. ISSN: 2157-846X. http://www.nature.com/articles/s41551-020-0519-8 (2021) (Feb. 2020).

69.  Sakaguchi, H. *et al.* Artificial vision by direct optic nerve electrode (AV-DONE) implantation in a blind patient with retinitis pigmentosa. *Journal of Artificial Organs* **12,** 206–209. ISSN: 1434-7229, 1619-0904. http://link.springer.com/10.1007/s10047-009-0467-2 (2021) (Sept. 2009).

70.  Lu, Y. *et al.* Electrical stimulation with a penetrating optic nerve electrode array elicits visuotopic cortical responses in cats. *Journal of Neural Engineering* **10.** ISSN: 17412560 (2013).

71.  Sun, J., Chen, Y., Chai, X., Ren, Q. & Li, L. Penetrating electrode stimulation of the rabbit optic nerve: parameters and effects on evoked cortical potentials. *Graefe's Archive for Clinical and Experimental Ophthalmology* **251,** 2545–2554. ISSN: 0721-832X, 1435-702X. http://link.springer.com/10.1007/s00417-013-2449-6 (2021) (Nov. 2013).

72.  Yan, Y. *et al.* Electrically evoked responses in the rabbit cortex induced by current steering with penetrating optic nerve electrodes. *Investigative Ophthalmology and Visual Science* **57,** 6327–6338. ISSN: 15525783 (2016).

73.  Gaillet, V. *et al.* Spatially selective activation of the visual cortex via intraneural stimulation of the optic nerve. *Nature Biomedical Engineering* **4,** 181–194. ISSN: 2157-846X. http://www.nature.com/articles/s41551-019-0446-8 (2021) (Feb. 2020).

74.  Borda, E. *et al.* Three-dimensional multilayer concentric bipolar electrodes enhance the selectivity of optic nerve stimulation. *bioRxiv.* Type: 10.1101/2022.03.21.485100, 2022.03.21.485100. https://www.biorxiv.org/content/biorxiv/early/2022/03/22/2022.03.21.485100.full.pdf (2022).

75.  Paggi, V., Akouissi, O., Micera, S. & Lacour, S. P. Compliant peripheral nerve interfaces. *Journal of Neural Engineering* **18,** 031001. ISSN: 1741-2560, 1741-2552. https://iopscience.iop.org/article/10.1088/1741-2552/abcdbe (2022) (June 1, 2021).

76.  Towle, V. L. *et al.* Postmortem investigation of a human cortical visual prosthesis that was implanted for 36 years. *Journal of Neural Engineering* **17,** 045010. ISSN: 1741-2560, 1741-2552. https://iopscience.iop.org/article/10.1088/1741-2552/ab9d11 (2022) (Aug. 1, 2020).

77.  Lewis, P. M. *et al.* Advances in implantable bionic devices for blindness: a review. *ANZ Journal of Surgery* **86,** 654–659. ISSN: 1445-1433, 1445-2197. https://onlinelibrary.wiley.com/doi/10.1111/ans.13616 (2022) (Sept. 2016).

78.  Mullen, K. T., Dumoulin, S. O. & Hess, R. F. Color responses of the human lateral geniculate nucleus: selective amplification of S-cone signals between the lateral geniculate nucleno and primary visual cortex measured with high-field fMRI. *European Journal of Neuroscience* **28,** 1911–1923. ISSN: 0953816X, 14609568. https://onlinelibrary.wiley.com/doi/10.1111/j.1460-9568.2008.06476.x (2022) (Nov. 2008).

79. Abbasi, B. & Rizzo, J. F. Advances in Neuroscience, Not Devices, Will Determine the Effectiveness of Visual Prostheses. *Seminars in Ophthalmology* **36,** 168–175. ISSN: 0882-0538, 1744-5205. https://www.tandfonline.com/doi/full/10.1080/08820538.2021.1887902 (2022) (May 19, 2021).

80. Pezaris, J. S. & Reid, R. C. Demonstration of artificial visual percepts generated through thalamic microstimulation. *Proceedings of the National Academy of Sciences* **104,** 7670–7675. ISSN: 0027-8424. http://www.pnas.org/lookup/doi/10.1073/pnas.0608563104 (2021) (May 1, 2007).

81. Panetsos, F., Sanchez-Jimenez, A., Cerio, E. D. D., Diaz-Guemes, I. & Sanchez, F. M. Consistent phosphenes generated by electrical microstimulation of the visual thalamus. An experimental approach for thalamic visual neuroprostheses. *Frontiers in Neuroscience* **5,** 1–12. ISSN: 16624548 (JUL 2011).

82. Choi, C. W., Kim, P. S., Shin, S. A., Yang, J. Y. & Yang, Y. S. Lateral geniculate body evoked potentials elicited by visual and electrical stimulation. *Korean Journal of Ophthalmology* **28.** Publisher: The Korean Ophthalmological Society, 337–342 (2014).

83. Tangutooru, S. M., Yoon, W. J. & Troy, J. B. *Early design considerations for a thalamic visual prosthesis to treat blindness resulting from glaucoma* in *2nd Middle East Conference on Biomedical Engineering* (IEEE, 2014), 249–252. ISBN: 1-4799-4799-7.

84. Kyada, M. J., Killian, N. J. & Pezaris, J. S. in *Artificial Vision* (ed Gabel, V. P.) 177–189 (Springer International Publishing, Cham, 2017). ISBN: 978-3-319-41874-2 978-3-319-41876-6. http://link.springer.com/10.1007/978-3-319-41876-6_14 (2022).

85. Button, J. C. Electronics brings light to the blind. *Radio Electron* **29,** 53–55 (1958).

86. Button, J. & Putnam, T. Visual responses to cortical stimulation in the blind. *J Iowa Med Soc* **52,** 17–21 (1962).

87. Brindley, G. S. & Lewin, W. S. The sensations produced by electrical stimulation of the visual cortex. *The Journal of physiology* **196.** ISBN: 0022-3751 Publisher: Wiley Online Library, 479–493 (1968).

88. Brindley, G. S. Sensations produced by electrical stimulation of the occipital poles of the cerebral hemispheres, and their use in constructing visual prostheses. *Annals of the Royal College of Surgeons of England* **47.** Publisher: Royal College of Surgeons of England, 106 (1970).

89. Donaldson, P. Experimental visual prosthesis. *Proceedings of the Institution of Electrical Engineers* **120,** 281. ISSN: 00203270. https://digital-library.theiet.org/content/journals/10.1049/piee.1973.0061 (2022) (1973).

90. Dobelle, W. H., Mladejovsky, M. G. & Girvin, J. P. Artificial Vision for the Blind: Electrical Stimulation of Visual Cortex Offers Hope for a Functional Prosthesis. *Science* **183,** 440–444. ISSN: 0036-8075, 1095-9203. https://www.science.org/doi/10.1126/science.183.4123.440 (2022) (Feb. 1974).

91. Dobelle, W. H., Mladejovsky, M. G., Evans, J. R., Roberts, T. S. & Girvin, J. P. 'Braille' reading by a blind volunteer by visual cortex stimulation. *Nature* **259,** 111–112. ISSN: 0028-0836, 1476-4687. http://www.nature.com/articles/259111a0 (2022) (Jan. 1976).

92. Dobelle, W. H., Stensaas, S. S., Mladejovsky, M. G. & Smith, J. B. A Prosthesis for the Deaf Based on Cortical Stimulation. *Annals of Otology, Rhinology & Laryngology* **82,** 445–463. ISSN: 0003-4894, 1943-572X. http://journals.sagepub.com/doi/10.1177/000348947308200404 (2022) (July 1973).

93. Fernandes, R. A. B., Diniz, B., Ribeiro, R. & Humayun, M. Artificial vision through neuronal stimulation. *Neuroscience Letters* **519,** 122–128. ISSN: 03043940. https://linkinghub.elsevier.com/retrieve/pii/S0304394012001449 (2022) (June 2012).

94. Maynard, E. M. Visual Prostheses, 28 (2001).

95. Mateos-Aparicio, P. & Rodríguez-Moreno, A. The Impact of Studying Brain Plasticity. *Frontiers in Cellular Neuroscience* **13,** 66. ISSN: 1662-5102. https://www.frontiersin.org/article/10.3389/fncel.2019.00066/full (2022) (Feb. 27, 2019).

96. Fernandez, E. Development of visual Neuroprostheses: trends and challenges. *Bioelectronic Medicine* **4,** 12. ISSN: 2332-8886. https://bioelecmed.biomedcentral.com/articles/10.1186/s42234-018-0013-8 (2021) (Dec. 2018).

97. Beauchamp, M. S. *et al.* Dynamic Stimulation of Visual Cortex Produces Form Vision in Sighted and Blind Humans. *Cell* **181,** 774–783.e5. ISSN: 00928674. https://linkinghub.elsevier.com/retrieve/pii/S0092867420304967 (2021) (May 2020).

98. Meikle, S. J. & Wong, Y. T. Neurophysiological considerations for visual implants. *Brain Structure and Function.* ISSN: 1863-2653, 1863-2661. https://link.springer.com/10.1007/s00429-021-02417-2 (2022) (Nov. 13, 2021).

99. Schmidt, E. M. *et al.* Feasibility of a visual prosthesis for the blind based on intracortical micro stimulation of the visual cortex. *Brain* **119,** 507–522. ISSN: 0006-8950, 1460-2156. https://academic.oup.com/brain/article-lookup/doi/10.1093/brain/119.2.507 (2022) (1996).

100. Chen, X., Wang, F., Fernandez, E. & Roelfsema, P. R. Shape perception via a high-channel-count neuroprosthesis in monkey visual cortex. *Science* **370,** 1191–1196. ISSN: 0036-8075, 1095-9203. https://www.science.org/doi/10.1126/science.abd7435 (2021) (Dec. 4, 2020).

101. Caspi, A. *et al.* Eye movements and the perceived location of phosphenes generated by intracranial primary visual cortex stimulation in the blind. *Brain Stimulation* **14,** 851–860. ISSN: 1935861X. https://linkinghub.elsevier.com/retrieve/pii/S1935861X21000899 (2022) (July 2021).

102. Schira, M. M., Tyler, C. W. & Rosa, M. G. Brain mapping: the (un) folding of striate cortex. *Current Biology* **22.** ISBN: 0960-9822 Publisher: Elsevier, R1051–R1053 (2012).

103. Kosta, P. *et al.* Electromagnetic safety assessment of a cortical implant for vision restoration. *IEEE Journal of Electromagnetics, RF and Microwaves in Medicine and Biology* **2.** ISBN: 2469-7249 Publisher: IEEE, 56–63 (2018).

104. Barry, M. P. *et al.* Video-mode percepts are smaller than sums of single-electrode phosphenes with the Orion® visual cortical prosthesis. *Investigative Ophthalmology & Visual Science* **61.** ISBN: 1552-5783 Publisher: The Association for Research in Vision and Ophthalmology, 927–927 (2020).

105. Rosenfeld, J. V. *et al.* Tissue response to a chronically implantable wireless, intracortical visual prosthesis (Gennaris array). *Journal of Neural Engineering.* ISSN: 1741-2560, 1741-2552. https://iopscience.iop.org/article/10.1088/1741-2552/ab9e1c (2022) (June 18, 2020).

106. Fernández, E. *et al.* Visual percepts evoked with an intracortical 96-channel microelectrode array inserted in human occipital cortex. *Journal of Clinical Investigation* **131,** e151331. ISSN: 1558-8238. https://www.jci.org/articles/view/151331 (2022) (Dec. 1, 2021).

107. Troyk, P. R. in *Artificial Vision* 203–214 (Springer, 2017).

108. Niketeghad, S. & Pouratian, N. Brain Machine Interfaces for Vision Restoration: The Current State of Cortical Visual Prosthetics. *Neurotherapeutics* **16,** 134–143. ISSN: 1933-7213, 1878-7479. http://link.springer.com/10.1007/s13311-018-0660-1 (2022) (Jan. 2019).

109. Pio-Lopez, L., Poulkouras, R. & Depannemaecker, D. Visual cortical prosthesis: an electrical perspective. *Journal of Medical Engineering & Technology* **45,** 394–407. ISSN: 0309-1902, 1464-522X. https://www.tandfonline.com/doi/full/10.1080/03091902.2021.1907468 (2022) (July 4, 2021).

110. Luo, Y. H.-L., Zhong, J. J., Clemo, M. & da Cruz, L. Long-term Repeatability and Reproducibility of Phosphene Characteristics in Chronically Implanted Argus II Retinal Prosthesis Subjects. *American Journal of Ophthalmology* **170,** 100–109. ISSN: 00029394. https://linkinghub.elsevier.com/retrieve/pii/S0002939416303671 (2022) (Oct. 2016).

111. Muqit, M. M. *et al.* Six-month safety and efficacy of the intelligent retinal implant system II device in retinitis pigmentosa. *Ophthalmology* **126.** ISBN: 0161-6420 Publisher: Elsevier, 637–639 (2019).

112. Geruschat, D. R., Turano, K. A. & Stahl, J. W. Traditional Measures of Mobility Performance and Retinitis Pigmentosa: *Optometry and Vision Science* **75,** 525–537. ISSN: 1040-5488. http://journals.lww.com/00006324-199807000-00022 (2022) (July 1998).

113. Szlyk, J. P. Relationship Between Difficulty in Performing Daily Activities and Clinical Measures of Visual Function in Patients With Retinitis Pigmentosa. *Archives of Ophthalmology* **115,** 53. ISSN: 0003-9950. http://archopht.jamanetwork.com/article.aspx?doi=10.1001/archopht.1997.01100150055009 (2022) (Jan. 1, 1997).

114. Haymes, S. A., Johnston, A. W. & Heyes, A. D. Relationship between vision impairment and ability to perform activities of daily living. *Ophthalmic and Physiological Optics* **22,** 79–91. ISSN: 0275-5408, 1475-1313. http://doi.wiley.com/10.1046/j.1475-1313.2002.00016.x (2022) (Mar. 2002).

115. Sugawara, T. *et al.* Relationship between peripheral visual field loss and vision-related quality of life in patients with retinitis pigmentosa. *Eye* **24,** 535–539. ISSN: 0950-222X, 1476-5454. http://www.nature.com/articles/eye2009176 (2022) (Apr. 2010).

116. Subhi, H., Latham, K., Myint, J. & Crossland, M. D. Functional visual fields: relationship of visual field areas to self-reported function. *Ophthalmic and Physiological Optics* **37,** 399–408. ISSN: 02755408. https://onlinelibrary.wiley.com/doi/10.1111/opo.12362 (2022) (July 2017).

117. Pérez Fornos, A., Sommerhalder, J., Pittard, A., Safran, A. B. & Pelizzone, M. Simulation of artificial vision: IV. Visual information required to achieve simple pointing and manipulation tasks. *Vision Research* **48,** 1705–1718. ISSN: 00426989. https://linkinghub.elsevier.com/retrieve/pii/S0042698908002368 (2022) (July 2008).

118. Dagnelie, G. *et al.* Real and virtual mobility performance in simulated prosthetic vision. *Journal of Neural Engineering* **4,** S92–S101. ISSN: 1741-2560, 1741-2552. https://iopscience.iop.org/article/10.1088/1741-2560/4/1/S11 (2022) (Mar. 1, 2007).

119. Cha, K., Horch, K. W. & Normann, R. A. Mobility performance with a pixelized vision system. *Vision Research* **32,** 1367–1372. ISSN: 00426989 (July 1992).

120. *Artificial Vision* (ed Gabel, V. P.) (Springer International Publishing, Cham, 2017). ISBN: 978-3-319-41874-2 978-3-319-41876-6. http://link.springer.com/10.1007/978-3-319-41876-6 (2021).

121. Beyeler, M., Rokem, A., Boynton, G. M. & Fine, I. Learning to see again: biological constraints on cortical plasticity and the implications for sight restoration technologies. *Journal of Neural Engineering* **14,** 051003. ISSN: 1741-2560, 1741-2552. https://iopscience.iop.org/article/10.1088/1741-2552/aa795e (2022) (Oct. 1, 2017).

122. Chen, S. C., Suaning, G. J., Morley, J. W. & Lovell, N. H. Simulating prosthetic vision: II. Measuring functional capacity. *Vision Research* **49,** 2329–2343. ISSN: 00426989. https://linkinghub.elsevier.com/retrieve/pii/S0042698909003253 (2022) (Sept. 2009).

123. Waschkowski, F. *et al.* Development of very large electrode arrays for epiretinal stimulation (VLARS). *BioMedical Engineering OnLine* **13,** 11. ISSN: 1475-925X (2014).

124. Lorach, H. *et al.* Photovoltaic restoration of sight with high visual acuity. *Nature medicine* **21.** ISBN: 1546-170X Publisher: Nature Publishing Group, 476–482 (2015).

125. Ghezzi, D. *et al.* A polymer optoelectronic interface restores light sensitivity in blind rat retinas. *Nature Photonics* **7,** 400–406. ISSN: 1749-4885, 1749-4893. http://www.nature.com/articles/nphoton.2013.34 (2022) (May 2013).

126. Maya-Vetencourt, J. F. *et al.* A fully organic retinal prosthesis restores vision in a rat model of degenerative blindness. *Nature Materials* **16,** 681–689. ISSN: 1476-1122 (2017).

127.    Tang, J. *et al.* Nanowire arrays restore vision in blind mice. *Nature Communications* **9,** 786. ISSN: 2041-1723 (Dec. 2018).

128.    Airaghi Leccardi, M. J. & Ghezzi, D. Organic electronics for neuroprosthetics. *Healthcare Technology Letters* **7,** 52–57. ISSN: 20533713 (2020).

129.    Chenais, N. A. L., Airaghi Leccardi, M. J. I. & Ghezzi, D. Naturalistic spatiotemporal modulation of epiretinal stimulation increases the response persistence of retinal ganglion cell. *Journal of Neural Engineering* **18,** 016016. ISSN: 1741-2560, 1741-2552. https://iopscience.iop.org/article/10.1088/1741-2552/abcd6f (2022) (Feb. 1, 2021).

130.    Nanduri, D., Humayun, M., Greenberg, R., McMahon, M. & Weiland, J. *Retinal prosthesis phosphene shape analysis* in *2008 30th Annual International Conference of the IEEE Engineering in Medicine and Biology Society* 2008 30th Annual International Conference of the IEEE Engineering in Medicine and Biology Society (IEEE, Vancouver, BC, Aug. 2008), 1785–1788. ISBN: 978-1-4244-1814-5. http://ieeexplore.ieee.org/document/4649524/ (2022).

131.    Beyeler, M. *et al.* A model of ganglion axon pathways accounts for percepts elicited by retinal implants. *Scientific Reports* **9,** 9199. ISSN: 2045-2322. http://www.nature.com/articles/s41598-019-45416-4 (2022) (Dec. 2019).

132.    Gogliettino, A. R. *et al. High-fidelity restoration of visual signals by electrical stimulation in the central primate retina* preprint (Neuroscience, May 25, 2022). http://biorxiv.org/lookup/doi/10.1101/2022.05.24.493162 (2022).

133.    Chenais, N. A. L., Leccardi, M. J. I. A. & Ghezzi, D. Capacitive-like photovoltaic epiretinal stimulation enhances and narrows the network-mediated activity of retinal ganglion cells by recruiting the lateral inhibitory network. *Journal of Neural Engineering* **16.** ISBN: 1741-2552 Publisher: IOP Publishing, 066009 (2019).

134.    Corna, A. *et al.* Discrimination of simple objects decoded from the output of retinal ganglion cells upon sinusoidal electrical stimulation. *Journal of Neural Engineering* **18,** 046086. ISSN: 1741-2560, 1741-2552. https://iopscience.iop.org/article/10.1088/1741-2552/ac0679 (2022) (Aug. 1, 2021).

135.    Chenais, N. A. L., Airaghi Leccardi, M. J. I. & Ghezzi, D. Photovoltaic retinal prosthesis restores high-resolution responses to single-pixel stimulation in blind retinas. *Communications Materials* **2,** 28. ISSN: 2662-4443 (Dec. 2021).

136.    Wilke, R. *et al.* Spatial Resolution and Perception of Patterns Mediated by a Subretinal 16-Electrode Array in Patients Blinded by Hereditary Retinal Dystrophies. *Investigative Opthalmology & Visual Science* **52,** 5995. ISSN: 1552-5783. http://iovs.arvojournals.org/article.aspx?doi=10.1167/iovs.10-6946 (2022) (July 30, 2011).

137.    Sinclair, N. C. *et al.* The Appearance of Phosphenes Elicited Using a Suprachoroidal Retinal Prosthesis. *Investigative Opthalmology & Visual Science* **57,** 4948. ISSN: 1552-5783. http://iovs.arvojournals.org/article.aspx?doi=10.1167/iovs.15-18991 (2022) (Sept. 21, 2016).

138.  Behrend, M. R., Ahuja, A. K., Humayun, M. S., Chow, R. H. & Weiland, J. D. Resolution of the Epiretinal Prosthesis is not Limited by Electrode Size. *IEEE Transactions on Neural Systems and Rehabilitation Engineering* **19,** 436–442. ISSN: 1534-4320, 1558-0210. http://ieeexplore.ieee.org/document/5752253/ (2022) (Aug. 2011).

139.  Ferlauto, L. *et al.* Design and validation of a foldable and photovoltaic wide-field epiretinal prosthesis. *Nature Communications* **9,** 992. ISSN: 2041-1723. http://www.nature.com/articles/s41467-018-03386-7 (2021) (Dec. 2018).

140.  Shivdasani, M. N. *et al.* Factors Affecting Perceptual Thresholds in a Suprachoroidal Retinal Prosthesis. *Investigative Opthalmology & Visual Science* **55,** 6467. ISSN: 1552-5783. http://iovs.arvojournals.org/article.aspx?doi=10.1167/iovs.14-14396 (2022) (Oct. 14, 2014).

141.  Ho, E. *et al.* Characteristics of prosthetic vision in rats with subretinal flat and pillar electrode arrays. *Journal of Neural Engineering* **16,** 066027. ISSN: 1741-2552. https://iopscience.iop.org/article/10.1088/1741-2552/ab34b3 (2021) (Oct. 30, 2019).

142.  Pezaris, J. S. & Reid, R. C. Demonstration of artificial visual percepts generated through thalamic microstimulation. *Proceedings of the National Academy of Sciences* **104,** 7670–7675. ISSN: 0027-8424. http://www.pnas.org/lookup/doi/10.1073/pnas.0608563104 (2022) (May 1, 2007).

143.  Histed, M. H., Bonin, V. & Reid, R. C. Direct Activation of Sparse, Distributed Populations of Cortical Neurons by Electrical Microstimulation. *Neuron* **63,** 508–522. ISSN: 08966273. https://linkinghub.elsevier.com/retrieve/pii/S0896627309005455 (2022) (Aug. 2009).

144.  Moleirinho, S., Whalen, A. J., Fried, S. I. & Pezaris, J. S. The impact of synchronous versus asynchronous electrical stimulation in artificial vision. *Journal of Neural Engineering* **18,** 051001. ISSN: 1741-2560, 1741-2552. https://iopscience.iop.org/article/10.1088/1741-2552/abecf1 (2021) (Oct. 1, 2021).

145.  Hokanson, J. A., Gaunt, R. A. & Weber, D. J. Effects of Synchronous Electrode Pulses on Neural Recruitment During Multichannel Microstimulation. *Scientific Reports* **8,** 13067. ISSN: 2045-2322. http://www.nature.com/articles/s41598-018-31247-2 (2022) (Dec. 2018).

146.  Cicione, R., Fallon, J. B., Rathbone, G. D., Williams, C. E. & Shivdasani, M. N. Spatiotemporal Interactions in the Visual Cortex Following Paired Electrical Stimulation of the Retina. *Investigative Ophthalmology & Visual Science* **55,** 7726–7738. ISSN: 0146-0404. http://iovs.arvojournals.org/Article.aspx?doi=10.1167/iovs.14-14754 (2021) (Dec. 1, 2014).

147.  Pérez Fornos, A. *et al.* Temporal Properties of Visual Perception on Electrical Stimulation of the Retina. *Investigative Opthalmology & Visual Science* **53,** 2720. ISSN: 1552-5783. http://iovs.arvojournals.org/article.aspx?doi=10.1167/iovs.11-9344 (2022) (May 4, 2012).

148. Stronks, H. C. & Dagnelie, G. The functional performance of the Argus II retinal prosthesis. *Expert Review of Medical Devices* **11,** 23–30. ISSN: 1743-4440, 1745-2422. http://www.tandfonline.com/doi/full/10.1586/17434440.2014.862494 (2021) (Jan. 2014).

149. Stingl, K. *et al.* Artificial vision with wirelessly powered subretinal electronic implant alpha-IMS. *Proceedings of the Royal Society B: Biological Sciences* **280,** 20130077. ISSN: 0962-8452, 1471-2954. https://royalsocietypublishing.org/doi/10.1098/rspb.2013.0077 (2021) (Apr. 22, 2013).

150. Greschner, M., Bongard, M., Rujan, P. & Ammermüller, J. Retinal ganglion cell synchronization by fixational eye movements improves feature estimation. *Nature Neuroscience* **5,** 341–347. ISSN: 1097-6256, 1546-1726. http://www.nature.com/articles/nn821 (2022) (Apr. 2002).

151. Kagan, I., Gur, M. & Snodderly, D. M. Saccades and drifts differentially modulate neuronal activity in V1: Effects of retinal image motion, position, and extraretinal influences. *Journal of Vision* **8,** 19–19. ISSN: 1534-7362. http://jov.arvojournals.org/Article.aspx?doi=10.1167/8.14.19 (2022) (Nov. 1, 2008).

152. Thorn, J. T., Chenais, N. A. L., Hinrichs, S., Chatelain, M. & Ghezzi, D. Virtual reality validation of naturalistic modulation strategies to counteract fading in retinal stimulation. *Journal of Neural Engineering.* ISSN: 1741-2560, 1741-2552. https://iopscience.iop.org/article/10.1088/1741-2552/ac5a5c (2022) (Mar. 3, 2022).

153. Chenais, N. A. L., Airaghi Leccardi, M. J. I. & Ghezzi, D. Photovoltaic retinal prosthesis restores high-resolution responses to single-pixel stimulation in blind retinas. *Communications Materials* **2,** 28. ISSN: 2662-4443 (Dec. 2021).

154. Hafed, Z. M., Stingl, K., Bartz-Schmidt, K.-U., Gekeler, F. & Zrenner, E. Oculomotor behavior of blind patients seeing with a subretinal visual implant. *Vision Research* **118,** 119–131. ISSN: 00426989. https://linkinghub.elsevier.com/retrieve/pii/S0042698915001510 (2022) (Jan. 2016).

155. Davuluri, N. S. & Weiland, J. D. *Time-varying pulse trains limit retinal desensitization caused by continuous electrical stimulation* in *2014 36th Annual International Conference of the IEEE Engineering in Medicine and Biology Society* 2014 36th Annual International Conference of the IEEE Engineering in Medicine and Biology Society (EMBC) (IEEE, Chicago, IL, Aug. 2014), 414–417. ISBN: 978-1-4244-7929-0. http://ieeexplore.ieee.org/document/6943616/ (2022).

156. Soto-Breceda, A., Kameneva, T., Meffin, H., Maturana, M. & Ibbotson, M. R. Irregularly timed electrical pulses reduce adaptation of retinal ganglion cells. *Journal of Neural Engineering* **15,** 056017. ISSN: 1741-2560, 1741-2552. https://iopscience.iop.org/article/10.1088/1741-2552/aad46e (2022) (Oct. 1, 2018).

157. Thorn, J. T., Chenais, N. A. L., Hinrichs, S., Chatelain, M. & Ghezzi, D. *Virtual reality validation of naturalistic modulation strategies to counteract fading in retinal stimulation* preprint (Bioengineering, Nov. 19, 2021). http://biorxiv.org/lookup/doi/10.1101/2021.11.17.468930 (2022).

158. Woeppel, K., Yang, Q. & Cui, X. T. Recent advances in neural electrode–tissue interfaces. *Current Opinion in Biomedical Engineering* **4,** 21–31. ISSN: 24684511. https://linkinghub. elsevier.com/retrieve/pii/S2468451117300478 (2022) (Dec. 2017).

159. Wu, N. *et al.* Electrode materials for brain–machine interface: A review. *InfoMat* **3,** 1174–1194. ISSN: 2567-3165, 2567-3165. https://onlinelibrary.wiley.com/doi/10.1002/ inf2.12234 (2022) (Nov. 2021).

160. Song, E., Li, J., Won, S. M., Bai, W. & Rogers, J. A. Materials for flexible bioelectronic systems as chronic neural interfaces. *Nature Materials* **19,** 590–603. ISSN: 1476-1122, 1476-4660. http://www.nature.com/articles/s41563-020-0679-7 (2022) (June 2020).

161. Wang, X.-S., Tang, H.-P., Li, X.-D. & Hua, X. Investigations on the Mechanical Properties of Conducting Polymer Coating-Substrate Structures and Their Influencing Factors. *International Journal of Molecular Sciences* **10,** 5257–5284. ISSN: 1422-0067. http://www. mdpi.com/1422-0067/10/12/5257 (2022) (Dec. 8, 2009).

162. Hassarati, R. T. *et al.* Stiffness quantification of conductive polymers for bioelectrodes. *Journal of Polymer Science Part B: Polymer Physics* **52,** 666–675. ISSN: 08876266. https: //onlinelibrary.wiley.com/doi/10.1002/polb.23465 (2022) (May 1, 2014).

163. Ferlauto, L. *et al.* Development and Characterization of PEDOT:PSS/Alginate Soft Microelectrodes for Application in Neuroprosthetics. *Frontiers in Neuroscience* **12,** 648. ISSN: 1662-453X. https://www.frontiersin.org/article/10.3389/fnins.2018.00648/full (2021) (Sept. 19, 2018).

164. Damle, S. *et al.* Minimizing Iridium Oxide Electrodes for High Visual Acuity Subretinal Stimulation. *eneuro* **8,** ENEURO.0506–20.2021. ISSN: 2373-2822. https://www.eneuro. org/lookup/doi/10.1523/ENEURO.0506-20.2021 (2022) (Nov. 2021).

165. Corna, A., Herrmann, T. & Zeck, G. Electrode-size dependent thresholds in subretinal neuroprosthetic stimulation. *Journal of Neural Engineering* **15,** 045003. ISSN: 1741-2560, 1741-2552. https://iopscience.iop.org/article/10.1088/1741-2552/aac1c8 (2022) (Aug. 1, 2018).

166. Fanelli, A. & Ghezzi, D. Transient electronics: new opportunities for implantable neurotechnology. *Current Opinion in Biotechnology* **72,** 22–28. ISSN: 09581669. https:// linkinghub.elsevier.com/retrieve/pii/S0958166921001567 (2022) (Dec. 2021).

167. Medagoda, D. I. & Ghezzi, D. Organic semiconductors for light-mediated neuromodulation. *Communications Materials* **2,** 111. ISSN: 2662-4443. https://www.nature.com/ articles/s43246-021-00217-z (2022) (Dec. 2021).

168. Cuttaz, E. *et al.* Conductive elastomer composites for fully polymeric, flexible bioelectronics. *Biomaterials science* **7.** Publisher: Royal Society of Chemistry, 1372–1385 (2019).

169. Kostarelos, K., Vincent, M., Hebert, C. & Garrido, J. A. Graphene in the Design and Engineering of Next-Generation Neural Interfaces. *Advanced Materials* **29,** 1700909. ISSN: 09359648. https://onlinelibrary.wiley.com/doi/10.1002/adma.201700909 (2022) (Nov. 2017).

170. Zeng, Q., Li, X., Zhang, S., Deng, C. & Wu, T. Think big, see small—A review of nanomaterials for neural interfaces. *Nano Select,* nano.202100256. ISSN: 2688-4011, 2688-4011. https://onlinelibrary.wiley.com/doi/10.1002/nano.202100256 (2022) (Nov. 14, 2021).

171. Anderson, J. M., Rodriguez, A. & Chang, D. T. Foreign body reaction to biomaterials. *Seminars in Immunology* **20,** 86–100. ISSN: 10445323. https://linkinghub.elsevier.com/retrieve/pii/S1044532307000966 (2022) (Apr. 2008).

172. Lacour, S. P, Courtine, G. & Guck, J. Materials and technologies for soft implantable neuroprostheses. *Nature Reviews Materials* **1,** 16063. ISSN: 2058-8437. http://www.nature.com/articles/natrevmats201663 (2021) (Oct. 2016).

173. Fallegger, F., Schiavone, G. & Lacour, S. P. Conformable Hybrid Systems for Implantable Bioelectronic Interfaces. *Advanced Materials* **32,** 1903904. ISSN: 0935-9648, 1521-4095. https://onlinelibrary.wiley.com/doi/10.1002/adma.201903904 (2021) (Apr. 2020).

174. Vachicouras, N. Soft Microfabricated Neural Implants : A Path Towards Translational Implementation, 1–184 (2019).

175. Lee, J. M. *et al.* Nanoenabled Direct Contact Interfacing of Syringe-Injectable Mesh Electronics. *Nano Letters* **19,** 5818–5826. ISSN: 1530-6984, 1530-6992. https://pubs.acs.org/doi/10.1021/acs.nanolett.9b03019 (2022) (Aug. 14, 2019).

176. Vanhoestenberghe, A. & Donaldson, N. Corrosion of silicon integrated circuits and lifetime predictions in implantable electronic devices. *Journal of Neural Engineering* **10,** 031002. ISSN: 1741-2560, 1741-2552. https://iopscience.iop.org/article/10.1088/1741-2560/10/3/031002 (2022) (June 1, 2013).

177. Humayun, M. *et al. Preliminary 6 month results from the argus$^{tm}$ ii epiretinal prosthesis feasibility study* in *2009 Annual International Conference of the IEEE Engineering in Medicine and Biology Society* 2009 Annual International Conference of the IEEE Engineering in Medicine and Biology Society (IEEE, Minneapolis, MN, Sept. 2009), 4566–4568. http://ieeexplore.ieee.org/document/5332695/ (2022).

178. Shire, D. B. *et al. ASIC design and data communications for the Boston retinal prosthesis* in *2012 Annual International Conference of the IEEE Engineering in Medicine and Biology Society* 2012 34th Annual International Conference of the IEEE Engineering in Medicine and Biology Society (EMBC) (IEEE, San Diego, CA, Aug. 2012), 292–295. ISBN: 978-1-4577-1787-1 978-1-4244-4119-8. http://ieeexplore.ieee.org/document/6345927/ (2022).

179. Barnes, N. *et al.* Vision function testing for a suprachoroidal retinal prosthesis: effects of image filtering. *Journal of Neural Engineering* **13,** 036013. ISSN: 1741-2560, 1741-2552. https://iopscience.iop.org/article/10.1088/1741-2560/13/3/036013 (2022) (June 1, 2016).

180. Wang, J. *et al.* The application of computer vision to visual prosthesis. *Artificial Organs* **45,** 1141–1154. ISSN: 0160-564X, 1525-1594. https://onlinelibrary.wiley.com/doi/10.1111/aor.14022 (2022) (Oct. 2021).

181. Li, H. *et al.* Image processing strategies based on saliency segmentation for object recognition under simulated prosthetic vision. *Artificial Intelligence in Medicine* **84,** 64–78. ISSN: 09333657. https://linkinghub.elsevier.com/retrieve/pii/S0933365716304195 (2022) (Jan. 2018).

182. Li, H. *et al.* A real-time image optimization strategy based on global saliency detection for artificial retinal prostheses. *Information Sciences* **415-416,** 1–18. ISSN: 00200255. https://linkinghub.elsevier.com/retrieve/pii/S0020025516317571 (2022) (Nov. 2017).

183. Guo, F., Yang, Y. & Gao, Y. Optimization of Visual Information Presentation for Visual Prosthesis. *International Journal of Biomedical Imaging* **2018,** 1–12. ISSN: 1687-4188, 1687-4196. https://www.hindawi.com/journals/ijbi/2018/3198342/ (2022) (2018).

184. Guo, F., Yang, Y., Xiao, Y., Gao, Y. & Yu, N. Recognition of Moving Object in High Dynamic Scene for Visual Prosthesis. *IEICE Transactions on Information and Systems* **E102.D,** 1321–1331. ISSN: 0916-8532, 1745-1361. https://www.jstage.jst.go.jp/article/transinf/E102.D/7/E102.D_2018EDP7405/_article (2022) (July 1, 2019).

185. Sanchez-Garcia, M., Martinez-Cantin, R. & Guerrero, J. *Indoor Scenes Understanding for Visual Prosthesis with Fully Convolutional Networks:* in *Proceedings of the 14th International Joint Conference on Computer Vision, Imaging and Computer Graphics Theory and Applications* 14th International Conference on Computer Vision Theory and Applications (SCITEPRESS - Science and Technology Publications, Prague, Czech Republic, 2019), 218–225. ISBN: 978-989-758-354-4. http://www.scitepress.org/DigitalLibrary/Link.aspx?doi=10.5220/0007257602180225 (2022).

186. Lozano, A. *et al.* Neurolight: A Deep Learning Neural Interface for Cortical Visual Prostheses. *International Journal of Neural Systems* **30,** 2050045. ISSN: 0129-0657, 1793-6462. https://www.worldscientific.com/doi/abs/10.1142/S0129065720500458 (2021) (Sept. 2020).

187. De Ruyter van Steveninck, J., Güçlü, U., van Wezel, R. & van Gerven, M. *End-to-end optimization of prosthetic vision* preprint (Bioengineering, Dec. 21, 2020). http://biorxiv.org/lookup/doi/10.1101/2020.12.19.423601 (2022).

188. Romeni, S., Zoccolan, D. & Micera, S. A machine learning framework to optimize optic nerve electrical stimulation for vision restoration. *Patterns* **2,** 100286. ISSN: 26663899. https://linkinghub.elsevier.com/retrieve/pii/S2666389921001197 (2022) (July 2021).

189. Lozano, A. M. *et al.* Deep brain stimulation: current challenges and future directions. *Nature Reviews Neurology* **15,** 1. ISSN: 1759-4766 (2019).

190. Krook-Magnuson, E., Gelinas, J. N., Soltesz, I. & Buzsáki, G. Neuroelectronics and Biooptics: Closed-Loop Technologies in Neurological Disorders. *JAMA Neurology* **72,** 823. ISSN: 2168-6149. http://archneur.jamanetwork.com/article.aspx?doi=10.1001/jamaneurol.2015.0608 (2022) (July 1, 2015).

191. Shah, N. P. & Chichilnisky, E. J. Computational challenges and opportunities for a bidirectional artificial retina. *Journal of Neural Engineering* **17,** 055002. ISSN: 1741-2552. https://iopscience.iop.org/article/10.1088/1741-2552/aba8b1 (2022) (Oct. 22, 2020).

192. Guo, T. *et al.* Closed-Loop Efficient Searching of Optimal Electrical Stimulation Parameters for Preferential Excitation of Retinal Ganglion Cells. *Frontiers in Neuroscience* **12,** 168. ISSN: 1662-453X. http://journal.frontiersin.org/article/10.3389/fnins.2018.00168/full (2022) (Mar. 19, 2018).

193. Rincón Montes, V. *et al.* Development and in vitro validation of flexible intraretinal probes. *Scientific Reports* **10,** 19836. ISSN: 2045-2322. http://www.nature.com/articles/s41598-020-76582-5 (2022) (Dec. 2020).

194. Rincón Montes, V. *et al.* Toward a Bidirectional Communication Between Retinal Cells and a Prosthetic Device – A Proof of Concept. *Frontiers in Neuroscience* **13,** 367. ISSN: 1662-453X. https://www.frontiersin.org/article/10.3389/fnins.2019.00367/full (2022) (Apr. 30, 2019).

195. Rotermund, D., Ernst, U. A. & Pawelzik, K. R. Open Hardware for neuro-prosthesis research: A study about a closed-loop multi-channel system for electrical surface stimulations and measurements. *HardwareX* **6,** e00078. ISSN: 24680672. https://linkinghub.elsevier.com/retrieve/pii/S2468067218301202 (2022) (Oct. 2019).

196. Caspi, A., Roy, A., Dorn, J. D. & Greenberg, R. J. Retinotopic to spatiotopic mapping in blind patients implanted with the Argus II retinal prosthesis. *Investigative Ophthalmology & Visual Science* **58.** ISBN: 1552-5783 Publisher: The Association for Research in Vision and Ophthalmology, 119–127 (2017).

197. Barbruni, G. L., Ros, P. M., Demarchi, D., Carrara, S. & Ghezzi, D. Miniaturised Wireless Power Transfer Systems for Neurostimulation: A Review. *IEEE Transactions on Biomedical Circuits and Systems* **14,** 1160–1178. ISSN: 1932-4545, 1940-9990. https://ieeexplore.ieee.org/document/9262058/ (2022) (Dec. 2020).

198. Wong, Y. T. *et al.* CMOS stimulating chips capable of wirelessly driving 473 electrodes for a cortical vision prosthesis. *Journal of Neural Engineering* **16,** 026025. ISSN: 1741-2560, 1741-2552. https://iopscience.iop.org/article/10.1088/1741-2552/ab021b (2022) (Apr. 1, 2019).

199. Merabet, L. B., Rizzo, J. F., Amedi, A., Somers, D. C. & Pascual-Leone, A. What blindness can tell us about seeing again: Merging neuroplasticity and neuroprostheses. *Nature Reviews Neuroscience* **6,** 71–77. ISSN: 1471003X (2005).

200. Majji, A. B. *et al.* Long-term histological and electrophysiological results of an inactive epiretinal electrode array implantation in dogs. *Investigative ophthalmology & visual science* **40.** ISBN: 1552-5783 Publisher: The Association for Research in Vision and Ophthalmology, 2073–2081 (1999).

201. Sachs, H. G. *et al.* Subretinal implantation and testing of polyimide film electrodes in cats. *Graefe's Archive for Clinical and Experimental Ophthalmology* **243.** ISBN: 1435-702X Publisher: Springer, 464–468 (2005).

202. Schwahn, H. N. *et al.* Studies on the feasibility of a subretinal visual prosthesis: data from Yucatan micropig and rabbit. *Graefe's archive for clinical and experimental ophthalmology* **239.** ISBN: 1435-702X Publisher: Springer, 961–967 (2001).

203. Chenais, N. A. L., Airaghi Leccardi, M. J. I. & Ghezzi, D. Naturalistic spatiotemporal modulation of epiretinal stimulation increases the response persistence of retinal ganglion cell. *Journal of Neural Engineering*. ISSN: 1741-2560, 1741-2552. https://iopscience.iop.org/article/10.1088/1741-2552/abcd6f (Nov. 24, 2020).

204. Jones, B. W. *et al.* Retinal remodeling triggered by photoreceptor degenerations. *The Journal of Comparative Neurology* **464,** 1–16. ISSN: 0021-9967 (Sept. 8, 2003).

205. Santos, A. *et al.* Preservation of the inner retina in retinitis pigmentosa. A morphometric analysis. *Archives of ophthalmology (Chicago, Ill. : 1960)* **115,** 511–5. ISSN: 0003-9950 (1997).

206. Medeiros, N. E. & Curcio, C. A. Preservation of ganglion cell layer neurons in age-related macular degeneration. *Investigative ophthalmology & visual science* **42,** 795–803. ISSN: 0146-0404 (2001).

207. Jones, B. *et al.* Retinal remodeling in human retinitis pigmentosa. *Experimental Eye Research* **150,** 149–165. ISSN: 0014-4835 (2016).

208. Jones, B. W. *et al.* Retinal remodeling. *Japanese Journal of Ophthalmology* **56,** 289–306. ISSN: 1613-2246 (July 2012).

209. Sullivan, R. K. P., WoldeMussie, E. & Pow, D. V. Dendritic and Synaptic Plasticity of Neurons in the Human Age-Related Macular Degeneration Retina. *Investigative Opthalmology & Visual Science* **48,** 2782. ISSN: 1552-5783. http://iovs.arvojournals.org/article.aspx?doi=10.1167/iovs.06-1283 (2022) (June 1, 2007).

210. Vargas-Martín, F. & Peli, E. Eye Movements of Patients with Tunnel Vision While Walking. *Investigative Opthalmology & Visual Science* **47,** 5295. ISSN: 1552-5783. http://iovs.arvojournals.org/article.aspx?doi=10.1167/iovs.05-1043 (2022) (Dec. 1, 2006).

211. Dulin, D., Hatwell, Y., Pylyshyn, Z. & Chokron, S. Effects of peripheral and central visual impairment on mental imagery capacity. *Neuroscience & Biobehavioral Reviews* **32,** 1396–1408. ISSN: 01497634. https://linkinghub.elsevier.com/retrieve/pii/S0149763408000572 (2022) (Oct. 2008).

212. Merabet, L. B., Rizzo, J. F., Pascual-Leone, A. & Fernandez, E. 'Who is the ideal candidate?': decisions and issues relating to visual neuroprosthesis development, patient testing and neuroplasticity. *Journal of Neural Engineering* **4,** S130–S135. ISSN: 1741-2560, 1741-2552. https://iopscience.iop.org/article/10.1088/1741-2560/4/1/S15 (2022) (Mar. 1, 2007).

213. Erickson-Davis, C. & Korzybska, H. What do blind people "see" with retinal prostheses? Observations and qualitative reports of epiretinal implant users. *PLOS ONE* **16** (ed Price, N. S. C.) e0229189. ISSN: 1932-6203. https://dx.plos.org/10.1371/journal.pone.0229189 (2022) (Feb. 10, 2021).

214. Childs, C. R., Fujiyama, T., Brown, I. E. W. & Tyler, N. *Pedestrian accessibility and movement environment laboratory* in (Walk21, 2005).

215. Cooper-Martin, E. Measures of cognitive effort. *Marketing Letters* **5,** 43–56. ISSN: 0923-0645, 1573-059X. http://link.springer.com/10.1007/BF00993957 (2022) (Jan. 1994).

216. Vetencourt, J. F. M. *et al.* The Antidepressant Fluoxetine Restores Plasticity in the Adult Visual Cortex. *Science* **320,** 385–388. ISSN: 0036-8075, 1095-9203. https://www.science.org/doi/10.1126/science.1150516 (2022) (Apr. 18, 2008).

217. Rokem, A. & Silver, M. A. The benefits of cholinergic enhancement during perceptual learning are long-lasting. *Frontiers in Computational Neuroscience* **7.** ISSN: 1662-5188. http://journal.frontiersin.org/article/10.3389/fncom.2013.00066/abstract (2022) (2013).

218. Chamoun, M. *et al.* Cholinergic Potentiation Improves Perceptual-Cognitive Training of Healthy Young Adults in Three Dimensional Multiple Object Tracking. *Frontiers in Human Neuroscience* **11.** ISSN: 1662-5161. http://journal.frontiersin.org/article/10.3389/fnhum.2017.00128/full (2022) (Mar. 21, 2017).

219. Allen, P. J. Retinal prostheses: Where to from here? *Clinical & Experimental Ophthalmology* **49,** 418–429. ISSN: 1442-6404, 1442-9071. https://onlinelibrary.wiley.com/doi/10.1111/ceo.13950 (2022) (July 2021).

220. Grover, S. *et al.* Visual acuity impairment in patients with retinitis pigmentosa at age 45 years or older. *Ophthalmology* **106,** 1780–1785. ISSN: 01616420. https://linkinghub.elsevier.com/retrieve/pii/S0161642099903421 (2022) (Sept. 1999).

221. Strickland, E. Health care algorithms show racial bias - [News]. *IEEE Spectrum* **57,** 6–7. ISSN: 0018-9235, 1939-9340. https://ieeexplore.ieee.org/document/8946292/ (2022) (Jan. 2020).

222. Chevrie, K. *Navigating the regulatory pathway for an innovative bionic vision system* in *Advanced Biomedical and Clinical Diagnostic and Surgical Guidance Systems XVIII* Advanced Biomedical and Clinical Diagnostic and Surgical Guidance Systems XVIII (ed Mahadevan-Jansen, A.) (SPIE, San Francisco, United States, Feb. 21, 2020), 70. ISBN: 978-1-5106-3221-9 978-1-5106-3222-6. https://www.spiedigitallibrary.org/conference-proceedings-of-spie/11229/2560182/Navigating-the-regulatory-pathway-for-an-innovative-bionic-vision-system/10.1117/12.2560182.full (2022).

223. *Their Bionic Eyes Are Now Obsolete and Unsupported* ieeespectrum. https://spectrum.ieee.org/bionic-eye-obsolete (2022).

224. Jonas, J. B., Schmidt, A. M., Müller-Bergh, J. A., Schlötzer-Schrehardt, U. M. & Naumann, G. O. Human optic nerve fiber count and optic disc size. *Investigative Ophthalmology & Visual Science* **33,** 2012–2018. ISSN: 1552-5783 (May 1, 1992).

225. Salazar, J. J. *et al.* Anatomy of the human optic nerve: Structure and function. *Optic Nerve.* ISBN: 1789849675 Publisher: IntechOpen (2018).

226. Dreyer, E. B., Zurakowski, D., Schumer, R. A., Podos, S. M. & Lipton, S. A. Elevated glutamate levels in the vitreous body of humans and monkeys with glaucoma. *Archives of ophthalmology* **114.** ISBN: 0003-9950 Publisher: American Medical Association, 299–305 (1996).

227. RAMÍREZ, J. M., TRIVIÑO, A., RAMÍREZ, A. I., SALAZAR, J. J. & GARCÍA-SANCHEZ, J. Structural specializations of human retinal glial cells. *Vision research* **36.** ISBN: 0042-6989 Publisher: Elsevier, 2029–2036 (1996).

228. Di Polo, A., Aigner, L. J., Dunn, R. J., Bray, G. M. & Aguayo, A. J. Prolonged delivery of brain-derived neurotrophic factor by adenovirus-infected Müller cells temporarily rescues injured retinal ganglion cells. *Proceedings of the National Academy of Sciences* **95.** ISBN: 0027-8424 Publisher: National Acad Sciences, 3978–3983 (1998).

229. Gehrmann, J., Matsumoto, Y. & Kreutzberg, G. W. Microglia: intrinsic immuneffector cell of the brain. *Brain research reviews* **20.** ISBN: 0165-0173 Publisher: Elsevier, 269–287 (1995).

230. Perry, V. H., Bell, M. D., Brown, H. C. & Matyszak, M. K. Inflammation in the nervous system. *Current opinion in neurobiology* **5.** ISBN: 0959-4388 Publisher: Elsevier, 636–641 (1995).

231. Aloisi, F. Immune function of microglia. *Glia* **36.** ISBN: 0894-1491 Publisher: Wiley Online Library, 165–179 (2001).

232. Gallego, B. I. *et al.* IOP induces upregulation of GFAP and MHC-II and microglia reactivity in mice retina contralateral to experimental glaucoma. *Journal of neuroinflammation* **9.** ISBN: 1742-2094 Publisher: BioMed Central, 1–18 (2012).

233. Campbell, W. W. & DeJong, R. N. *DeJong's the neurologic examination* Issue: 2005. ISBN: 0-7817-2767-7 (Lippincott Williams & Wilkins, 2005).

234. Sigal, I. A. & Ethier, C. R. Biomechanics of the optic nerve head. *Experimental Eye Research* **88,** 799–807. ISSN: 00144835. https://linkinghub.elsevier.com/retrieve/pii/S0014483509000359 (2022) (Apr. 2009).

235. Kline, L. B. & Bajandas, F. J. *Neuro-ophthalmology review manual* ISBN: 1-55642-789-1 (Slack Incorporated, 2008).

236. Trattler, W. B., Kaiser, P. K. & Friedman, N. J. *Review of ophthalmology E-book: Expert consult-online and print* ISBN: 1-4557-3773-9 (Elsevier Health Sciences, 2012).

237. Giolli, R. A. & Guthrie, M. D. The primary optic projections in the rabbit. An experimental degeneration study. *Journal of Comparative Neurology* **136.** ISBN: 0021-9967 Publisher: Wiley Online Library, 99–125 (1969).

238. Barham, H. P., Ramakrishnan, V. R. & Kingdom, T. T. in *Atlas of Endoscopic Sinus and Skull Base Surgery* 157–164 (Elsevier, 2019). ISBN: 978-0-323-47664-5. https://linkinghub.elsevier.com/retrieve/pii/B9780323476645000195 (2021).

239.  *Visual and Auditory anomalies associated with albinism. Donell J. Creel* Webvision. http : / / webvision . org . es / part - xii - the - electroretinogram - erg / 12 - 3 - visual - and - auditory-anomalies-associated-with-albinism/ (2022).

240.  Minckler, D. S. Nerve fiber layer of the macaque retina: Retinotopic organization: by TE Ogden. Invest Ophthalmol Vis Sci 24: 85–98, 1983. *Survey of Ophthalmology* **28.** ISBN: 0039-6257 Publisher: Elsevier, 138–139 (1983).

241.  Ogden, T. E. Nerve fiber layer of the owl monkey retina: retinotopic organization. *Investigative Ophthalmology & Visual Science* **24.** ISBN: 1552-5783 Publisher: The Association for Research in Vision and Ophthalmology, 265–269 (1983).

242.  Naito, J. Retinogeniculate projection fibers in the monkey optic nerve: A demonstration of the fiber pathways by retrograde axonal transport of WGA-HRP. *Journal of Comparative Neurology* **284.** ISBN: 0021-9967 Publisher: Wiley Online Library, 174–186 (1989).

243.  Fitzgibbon, T. & Taylor, S. F. Retinotopy of the human retinal nerve fibre layer and optic nerve head. *Journal of Comparative Neurology* **375.** ISBN: 0021-9967 Publisher: Wiley Online Library, 238–251 (1996).

244.  Forrester, J. V., Dick, A. D., McMenamin, P. G., Roberts, F. & Pearlman, E. in *The Eye* 269–337.e2 (Elsevier, 2016). ISBN: 978-0-7020-5554-6. https://linkinghub.elsevier.com/retrieve/pii/B9780702055546000058 (2022).

245.  Lashley, K. S. The mechanism of vision. VII. The projection of the retina upon the primary optic centers in the rat. *Journal of Comparative Neurology* **59.** ISBN: 0021-9967 Publisher: Wiley Online Library, 341–373 (1934).

246.  Tsuruga, H., Murata, H., Aihara, M. & Araie, M. Retinotopy in the Optic Nerve Using CFP-Expressing Transgenic Mouse. *Investigative Ophthalmology & Visual Science* **50.** ISBN: 1552-5783 Publisher: The Association for Research in Vision and Ophthalmology, 5828–5828 (2009).

247.  Brouwer, B., Zeeman, W. P. C. & Houwer, A. M. Experimentell-anatomische Untersuchungen über die Projektion der Retina auf die primären Opticuszentren. *Schweiz. Arch. Neurol. Psychiat.* **13,** 118–137 (1923).

248.  Hughes, A. Topographical relationships between the anatomy and physiology of the rabbit visual system. *Documenta Ophthalmologica* **30.** ISBN: 1573-2622 Publisher: Springer, 33–159 (1971).

249.  Picanço-Diniz, C. W., Rocha, E. G., Silveira, L. C. L., Elston, G. & Oswaldo-Cruz, E. Cortical representation of the horizon in V1 and peripheral scaling in mammals with lateral eyes. *Psychology & Neuroscience* **4,** 19–27. ISSN: 1983-3288, 1984-3054. http://doi.apa.org/getdoi.cfm?doi=10.3922/j.psns.2011.1.004 (2022) (Jan. 2011).

250.  Picanço-Diniz, C. W., Rocha, E. G., Silveira, L. C. L., Elston, G. & Oswaldo-Cruz, E. Cortical representation of the horizon in V1 and peripheral scaling in mammals with lateral eyes. *Psychology & Neuroscience* **4,** 19–27. ISSN: 1983-3288, 1984-3054. http://doi.apa.org/getdoi.cfm?doi=10.3922/j.psns.2011.1.004 (2022) (Jan. 2011).

251.  Loeb, G. & Peck, R. Cuff electrodes for chronic stimulation and recording of peripheral nerve activity. *Journal of Neuroscience Methods* **64,** 95–103. ISSN: 01650270. https://linkinghub.elsevier.com/retrieve/pii/0165027095001239 (2021) (Jan. 1996).

252.  Tyler, D. & Durand, D. Functionally selective peripheral nerve stimulation with a flat interface nerve electrode. *IEEE Transactions on Neural Systems and Rehabilitation Engineering* **10,** 294–303. ISSN: 1534-4320, 1558-0210. https://ieeexplore.ieee.org/document/1178100/ (2021) (Dec. 2002).

253.  Spearman, B. S. *et al.* Tissue-engineered peripheral nerve interfaces. *Advanced Functional Materials* **28.** ISBN: 1616-301X Publisher: Wiley Online Library, 1701713 (2018).

254.  Davis, T. S. *et al.* Restoring motor control and sensory feedback in people with upper extremity amputations using arrays of 96 microelectrodes implanted in the median and ulnar nerves. *Journal of Neural Engineering* **13,** 036001. ISSN: 1741-2560, 1741-2552. https://iopscience.iop.org/article/10.1088/1741-2560/13/3/036001 (2021) (June 1, 2016).

255.  Del Valle, J. & Navarro, X. in *International Review of Neurobiology* 63–83 (Elsevier, 2013). ISBN: 978-0-12-420045-6. https://linkinghub.elsevier.com/retrieve/pii/B978012420045600002X (2022).

256.  Cutrone, A. *et al.* A three-dimensional self-opening intraneural peripheral interface (SELINE). *Journal of Neural Engineering* **12,** 016016. ISSN: 1741-2560, 1741-2552. https://iopscience.iop.org/article/10.1088/1741-2560/12/1/016016 (2021) (Feb. 1, 2015).

257.  Wurth, S. *et al.* Long-term usability and bio-integration of polyimide-based intra-neural stimulating electrodes. *Biomaterials* **122,** 114–129. ISSN: 18785905. http://dx.doi.org/10.1016/j.biomaterials.2017.01.014 (2017).

258.  Valle, G. *et al.* Biomimetic intraneural sensory feedback enhances sensation naturalness, tactile sensitivity, and manual dexterity in a bidirectional prosthesis. *Neuron* **100.** ISBN: 0896-6273 Publisher: Elsevier, 37–45. e7 (2018).

259.  Petrini, F. M. *et al.* Enhancing functional abilities and cognitive integration of the lower limb prosthesis. *Science translational medicine* **11.** ISBN: 1946-6234 Publisher: American Association for the Advancement of Science, eaav8939 (2019).

260.  Petrini, F. M. *et al.* Six-month assessment of a hand prosthesis with intraneural tactile feedback. *Annals of neurology* **85.** ISBN: 0364-5134 Publisher: Wiley Online Library, 137–154 (2019).

261. Badia, J., Raspopovic, S., Carpaneto, J., Micera, S. & Navarro, X. Spatial and Functional Selectivity of Peripheral Nerve Signal Recording With the Transversal Intrafascicular Multichannel Electrode (TIME). *IEEE Transactions on Neural Systems and Rehabilitation Engineering* **24,** 20–27. ISSN: 1534-4320, 1558-0210. https://ieeexplore.ieee.org/document/7123655/ (2022) (Jan. 2016).

262. Grill, W. M. & Mortimer, J. T. Stimulus waveforms for selective neural stimulation. *IEEE Engineering in Medicine and Biology Magazine* **14.** ISBN: 0739-5175 Publisher: IEEE, 375–385 (1995).

263. Rapeaux, A., Nikolic, K., Williams, I., Eftekhar, A. & Constandinou, T. G. *Fiber size-selective stimulation using action potential filtering for a peripheral nerve interface: A simulation study* in *2015 37th Annual International Conference of the IEEE Engineering in Medicine and Biology Society (EMBC)* (IEEE, 2015), 3411–3414. ISBN: 1-4244-9271-8.

264. Patel, Y. A. & Butera, R. J. Challenges associated with nerve conduction block using kilohertz electrical stimulation. *Journal of neural engineering* **15.** ISBN: 1741-2552 Publisher: IOP Publishing, 031002 (2018).

265. Sweeney, J., Ksienski, D. & Mortimer, J. A nerve cuff technique for selective excitation of peripheral nerve trunk regions. *IEEE Transactions on Biomedical Engineering* **37,** 706–715. ISSN: 00189294. http://ieeexplore.ieee.org/document/55681/ (2022) (July 1990).

266. Veraart, C., Grill, W. & Mortimer, J. Selective control of muscle activation with a multipolar nerve cuff electrode. *IEEE Transactions on Biomedical Engineering* **40,** 640–653. ISSN: 00189294. http://ieeexplore.ieee.org/document/237694/ (2022) (July 1993).

267. Plachta, D. T. T. *et al.* Blood pressure control with selective vagal nerve stimulation and minimal side effects. *Journal of Neural Engineering* **11,** 036011. ISSN: 1741-2560, 1741-2552. https://iopscience.iop.org/article/10.1088/1741-2560/11/3/036011 (2022) (June 1, 2014).

268. Minev, I. R. *et al.* Electronic dura mater for long-term multimodal neural interfaces. *Science* **347,** 159–163. ISSN: 0036-8075, 1095-9203. https://www.science.org/doi/10.1126/science.1260318 (2021) (Jan. 9, 2015).

269. Tybrandt, K. *et al.* High-Density Stretchable Electrode Grids for Chronic Neural Recording. *Advanced Materials* **30,** 1706520. ISSN: 09359648. https://onlinelibrary.wiley.com/doi/10.1002/adma.201706520 (2021) (Apr. 2018).

270. Lienemann, S., Zötterman, J., Farnebo, S. & Tybrandt, K. Stretchable gold nanowire-based cuff electrodes for low-voltage peripheral nerve stimulation. *Journal of Neural Engineering* **18.** ISBN: 1741-2552 Publisher: IOP Publishing, 045007 (2021).

271. Vachicouras, N. *et al.* Microstructured thin-film electrode technology enables proof of concept of scalable, soft auditory brainstem implants. *Science Translational Medicine* **11,** eaax9487. ISSN: 1946-6234, 1946-6242. https://www.science.org/doi/10.1126/scitranslmed.aax9487 (2021) (Oct. 16, 2019).

272.  Čvančara, P. *et al.* Stability of flexible thin-film metallization stimulation electrodes: analysis of explants after first-in-human study and improvement of in vivo performance. *Journal of Neural Engineering* **17,** 046006. ISSN: 1741-2560, 1741-2552. https://iopscience.iop.org/article/10.1088/1741-2552/ab9a9a (2022) (Aug. 1, 2020).

273.  Kuliasha, C. A. & Judy, J. W. The Materials Science Foundation Supporting the Microfabrication of Reliable Polyimide–Metal Neuroelectronic Interfaces. *Advanced Materials Technologies* **6,** 2100149. ISSN: 2365-709X, 2365-709X. https://onlinelibrary.wiley.com/doi/10.1002/admt.202100149 (2022) (June 2021).

274.  Airaghi Leccardi, M. J. I., Vagni, P. & Ghezzi, D. Multilayer 3D electrodes for neural implants. *Journal of Neural Engineering* **16,** 026013. ISSN: 1741-2560, 1741-2552. https://iopscience.iop.org/article/10.1088/1741-2552/aae191 (2021) (Apr. 1, 2019).

275.  Carlborg, C. F., Haraldsson, T., Öberg, K., Malkoch, M. & van der Wijngaart, W. Beyond PDMS: off-stoichiometry thiol–ene (OSTE) based soft lithography for rapid prototyping of microfluidic devices. *Lab on a Chip* **11,** 3136. ISSN: 1473-0197, 1473-0189. http://xlink.rsc.org/?DOI=c1lc20388f (2021) (2011).

276.  Afanasenkau, D. *et al.* Rapid prototyping of soft bioelectronic implants for use as neuromuscular interfaces. *Nature Biomedical Engineering* **4,** 1010–1022. ISSN: 2157-846X. https://www.nature.com/articles/s41551-020-00615-7 (2022) (Oct. 2020).

277.  Khan, Y. *et al.* Inkjet-Printed Flexible Gold Electrode Arrays for Bioelectronic Interfaces. *Advanced Functional Materials* **26,** 1004–1013. ISSN: 1616301X. https://onlinelibrary.wiley.com/doi/10.1002/adfm.201503316 (2022) (Feb. 2016).

278.  Borda, E. *et al.* All-Printed Electrocorticography Array for In Vivo Neural Recordings. *Advanced Engineering Materials* **22,** 1901403. ISSN: 1438-1656, 1527-2648. https://onlinelibrary.wiley.com/doi/10.1002/adem.201901403 (2022) (Mar. 2020).

279.  Bourne, R. R. *et al.* Causes of vision loss worldwide, 1990–2010: a systematic analysis. *The Lancet Global Health* **1,** e339–e349. ISSN: 2214-109X (2013).

280.  Hamel, C. Retinitis pigmentosa. *Orphanet Journal of Rare Diseases* **1,** 40. ISSN: 1750-1172. https://ojrd.biomedcentral.com/articles/10.1186/1750-1172-1-40 (2022) (Dec. 2006).

281.  Ghezzi, D. Retinal prostheses: Progress towards the next generation implants. *Frontiers in Neuroscience* **9,** 1–6. ISSN: 1662453X (JUL 2015).

282.  Prévot, P.-H. *et al.* Behavioural responses to a photovoltaic subretinal prosthesis implanted in non-human primates. *Nature Biomedical Engineering* **4,** 172–180. ISSN: 2157-846X (Feb. 2020).

283.  Ronzani, C. *et al.* High-Frequency Stimulation of Normal and Blind Mouse Retinas Using TiO2 Nanotubes. *Advanced Functional Materials* **28,** 1804639. ISSN: 1616-301X, 1616-3028 (Dec. 2018).

284.  Cruz, d. L. *et al.* The Argus II epiretinal prosthesis system allows letter and word reading and long-term function in patients with profound vision loss. *The British journal of ophthalmology* **97,** 632–6. ISSN: 0007-1161 (2013).

285. Stingl, K. *et al. Interim results of a multicenter trial with the new electronic subretinal implant alpha AMS in 15 patients blind from inherited retinal degenerations* 445 pp. ISBN: 978-3-319-41874-2 (2017).

286. Stingl, K. *et al.* Subretinal visual implant alpha IMS–clinical trial interim report. *Vision research* **111.** ISBN: 0042-6989 Publisher: Elsevier, 149–160 (2015).

287. Hartong, D. T., Berson, E. L. & Dryja, T. P. Retinitis pigmentosa. *Lancet* **368,** 1795–809. ISSN: 0140-6736 (2006).

288. Humayun *et al.* Morphometric analysis of the extramacular retina from postmortem eyes with retinitis pigmentosa. *Investigative ophthalmology & visual science* **40,** 143–8. ISSN: 0146-0404 (1999).

289. Gargini, C., Terzibasi, E., Mazzoni, F. & Strettoi, E. Retinal organization in the retinal degeneration 10 (rd10) mutant mouse: A morphological and ERG study. *Journal of Comparative Neurology* **500,** 222–238. ISSN: 1096-9861 (2007).

290. Mazzoni, F., Novelli, E. & Strettoi, E. Retinal Ganglion Cells Survive and Maintain Normal Dendritic Morphology in a Mouse Model of Inherited Photoreceptor Degeneration. *Journal of Neuroscience* **28,** 14282–14292. ISSN: 0270-6474, 1529-2401 (Dec. 24, 2008).

291. Jones, B. W. & Marc, R. E. Retinal remodeling during retinal degeneration. *Experimental eye research* **81,** 123–37. ISSN: 0014-4835 (2005).

292. Watt, C., Jones, B., Yang, J.-H., Marc, R. & LaVail, M. Complex Rewiring In Retinal Remodeling. *Investigative Ophthalmology & Visual Science* **45,** 777–777. ISSN: 1552-5783 (May 1, 2004).

293. Marc, R. E. & Jones, B. W. Retinal Remodeling in Inherited Photoreceptor Degenerations. *Molecular Neurobiology* **28,** 139–148. ISSN: 0893-7648 (2003).

294. Margolis, D. J. & Detwiler, P. B. Cellular Origin of Spontaneous Ganglion Cell Spike Activity in Animal Models of Retinitis Pigmentosa. *Journal of Ophthalmology* **2011,** 507037. ISSN: 2090-004X (2011).

295. Goetz, G. A. & Palanker, D. V. Electronic approaches to restoration of sight. *Reports on progress in physics. Physical Society (Great Britain)* **79,** 096701. ISSN: 1361-6633. http://www.ncbi.nlm.nih.gov/pubmed/27502748 (2016).

296. Fang, X. *et al.* Direct stimulation of optic nerve by electrodes implanted in optic disc of rabbit eyes. **243.** ISSN: 0721-832X. http://dx.doi.org/10.1007/s00417-004-0957-0 (2004).

297. Fang, X. *et al.* Electrophysiological and histological studies of chronically implanted intrapapillary microelectrodes in rabbit eyes. *Graefe's Archive for Clinical and Experimental Ophthalmology* **244,** 364–375. ISSN: 0721-832X (2006).

298. Lohmann, T. K. *et al.* The very large electrode array for retinal stimulation (VLARS)—A concept study. *Journal of Neural Engineering* **16,** 066031. ISSN: 1741-2560, 1741-2552. https://iopscience.iop.org/article/10.1088/1741-2552/ab4113 (2022) (Dec. 1, 2019).

299. Brelén, M. E., Vince, V., Gérard, B., Veraart, C. & Delbeke, J. Measurement of Evoked Potentials after Electrical Stimulation of the Human Optic Nerve. *Investigative Opthalmology & Visual Science* **51,** 5351. ISSN: 1552-5783. http://iovs.arvojournals.org/article.aspx?doi=10.1167/iovs.09-4346 (2021) (Oct. 1, 2010).

300. Dubey, A. & Ray, S. Cortical Electrocorticogram (ECoG) Is a Local Signal. *The Journal of Neuroscience* **39,** 4299–4311. ISSN: 0270-6474, 1529-2401 (May 29, 2019).

301. Fischer, B., Schander, A., Kreiter, A. K., Lang, W. & Wegener, D. Visual epidural field potentials possess high functional specificity in single trials. *Journal of Neurophysiology* **122,** 1634–1648. ISSN: 0022-3077, 1522-1598 (Oct. 1, 2019).

302. Sun, J. *et al.* Spatiotemporal Properties of Multipeaked Electrically Evoked Potentials Elicited by Penetrative Optic Nerve Stimulation in Rabbits. *Investigative Opthalmology & Visual Science* **52,** 146. ISSN: 1552-5783. http://iovs.arvojournals.org/article.aspx?doi=10.1167/iovs.09-4024 (2021) (Jan. 5, 2011).

303. Thompson, J. M., Woolsey, C. N. & Talbot, S. A. Visual areas I and II of cerebral cortex of rabbit. *Journal of Neurophysiology* **13,** 277–288. ISSN: 0022-3077 (July 1950).

304. Choudhury, B. P. Visual cortex in the albino rabbit. *Experimental Brain Research* **66,** 565–571. ISSN: 0014-4819, 1432-1106. http://link.springer.com/10.1007/BF00270689 (2021) (May 1987).

305. Shannon, R. V. A model of safe levels for electrical stimulation. *IEEE transactions on bio-medical engineering* **39,** 424–426. ISSN: 0018-9294 (Apr. 1992).

306. Wong, Y. T. *et al.* Spectral distribution of local field potential responses to electrical stimulation of the retina. *Journal of Neural Engineering* **13,** 036003. ISSN: 1741-2560, 1741-2552. https://iopscience.iop.org/article/10.1088/1741-2560/13/3/036003 (2021) (June 1, 2016).

307. Edwards, C. A., Kouzani, A., Lee, K. H. & Ross, E. K. *Neurostimulation devices for the treatment of neurologic disorders* in *Mayo Clinic Proceedings* **92.** Issue: 9 (Elsevier, 2017), 1427–1444. ISBN: 0025-6196.

308. Steigerwald, F., Matthies, C. & Volkmann, J. Directional Deep Brain Stimulation. *Neurotherapeutics* **16,** 100–104. ISSN: 1933-7213, 1878-7479. http://link.springer.com/10.1007/s13311-018-0667-7 (2022) (Jan. 2019).

309. Dhanasingh, A. & Jolly, C. An overview of cochlear implant electrode array designs. *Hearing Research* **356,** 93–103. ISSN: 03785955. https://linkinghub.elsevier.com/retrieve/pii/S0378595517302940 (2022) (Dec. 2017).

310. Luo, Y. & Cruz, d. L. The Argus® II Retinal Prosthesis System. *Progress in Retinal and Eye Research* **50,** 89–107. ISSN: 1350-9462 (2016).

311. Stieglitz, T. *et al.* Development of a neurotechnological system for relieving phantom limb pain using transverse intrafascicular electrodes (TIME). *Biomedizinische Technik/Biomedical Engineering* **57.** ISSN: 1862-278X, 0013-5585. https://www.degruyter.com/document/doi/10.1515/bmt-2011-0140/html (2022) (Jan. 1, 2012).

312. Khalili Moghadam, G., Wilke, R., Suaning, G. J., Lovell, N. H. & Dokos, S. Quasi-Monopolar Stimulation: A Novel Electrode Design Configuration for Performance Optimization of a Retinal Neuroprosthesis. *PLoS ONE* **8** (ed Ohlmann, A.) e73130. ISSN: 1932-6203. https://dx.plos.org/10.1371/journal.pone.0073130 (2021) (Aug. 26, 2013).

313. Li, M. *et al.* A simulation of current focusing and steering with penetrating optic nerve electrodes. *Journal of Neural Engineering* **10,** 066007. ISSN: 1741-2560, 1741-2552. https://iopscience.iop.org/article/10.1088/1741-2560/10/6/066007 (2021) (Dec. 1, 2013).

314. Hodgkin, A. L. & Huxley, A. F. A quantitative description of membrane current and its application to conduction and excitation in nerve. *The Journal of Physiology* **117,** 500–544. ISSN: 0022-3751, 1469-7793. https://onlinelibrary.wiley.com/doi/10.1113/jphysiol.1952.sp004764 (2022) (Aug. 28, 1952).

315. Oozeer, M., Veraart, C., Legat, V. & Delbeke, J. A model of the mammalian optic nerve fibre based on experimental data. *Vision Research* **46,** 2513–2524. ISSN: 00426989. https://linkinghub.elsevier.com/retrieve/pii/S0042698906000563 (2022) (Aug. 2006).

316. Oka, H., Shimono, K., Ogawa, R., Sugihara, H. & Taketani, M. A new planar multielectrode array for extracellular recording: application to hippocampal acute slice. *Journal of Neuroscience Methods* **93,** 61–67. ISSN: 01650270. https://linkinghub.elsevier.com/retrieve/pii/S0165027099001132 (2022) (Oct. 1999).

317. Flores, T., Goetz, G., Lei, X. & Palanker, D. Optimization of return electrodes in neurostimulating arrays. *Journal of Neural Engineering* **13.** ISSN: 17412552 (2016).

318. Spencer, T. C., Fallon, J. B., Thien, P. C. & Shivdasani, M. N. Spatial Restriction of Neural Activation Using Focused Multipolar Stimulation With a Retinal Prosthesis. *Investigative Opthalmology & Visual Science* **57,** 3181. ISSN: 1552-5783. http://iovs.arvojournals.org/article.aspx?doi=10.1167/iovs.16-19325 (2021) (June 16, 2016).

319. Matteucci, P. B. *et al.* Current steering in retinal stimulation via a quasimonopolar stimulation paradigm. *Investigative Ophthalmology and Visual Science* **54,** 4307–4320. ISSN: 01460404 (2013).

320. Bendali, A. *et al.* Synthetic 3D diamond-based electrodes for flexible retinal neuroprostheses: Model, production and in vivo biocompatibility. *Biomaterials* **67,** 73–83. ISSN: 01429612. https://linkinghub.elsevier.com/retrieve/pii/S0142961215006006 (2022) (Oct. 2015).

321. Joucla, S. & Yvert, B. Improved Focalization of Electrical Microstimulation Using Microelectrode Arrays: A Modeling Study. *PLoS ONE* **4** (ed Mansvelder, H. D.) e4828. ISSN: 1932-6203. https://dx.plos.org/10.1371/journal.pone.0004828 (2022) (Mar. 12, 2009).

322. Joucla, S., Glière, A. & Yvert, B. Current approaches to model extracellular electrical neural microstimulation. *Frontiers in Computational Neuroscience* **8.** ISSN: 1662-5188. http://journal.frontiersin.org/article/10.3389/fncom.2014.00013/abstract (2022) (2014).

323. *Principal Component Analysis* ISBN: 978-0-387-95442-4. http://link.springer.com/10. 1007/b98835 (2022) (Springer-Verlag, New York, 2002).

324. Ruach, R., Mitelman, R., Sherman, E., Cohen, O. & Prut, Y. An assumption-free quantification of neural responses to electrical stimulations. *Journal of Neuroscience Methods* **254,** 10–17. ISSN: 01650270. https://linkinghub.elsevier.com/retrieve/pii/S0165027015002514 (2022) (Oct. 2015).

325. Wong, Y. *et al.* Focal activation of the feline retina via a suprachoroidal electrode array. *Vision Research* **49,** 825–833. ISSN: 00426989. https://linkinghub.elsevier.com/retrieve/pii/S0042698909000704 (2021) (May 2009).

326. Blaize, K. *et al.* Functional ultrasound imaging of deep visual cortex in awake nonhuman primates. *Proceedings of the National Academy of Sciences* **117,** 14453–14463. ISSN: 0027-8424, 1091-6490. https://pnas.org/doi/full/10.1073/pnas.1916787117 (2022) (June 23, 2020).

327. Aristovich, K. Y. *et al.* Imaging fast electrical activity in the brain with electrical impedance tomography. *NeuroImage* **124,** 204–213. ISSN: 10959572. http://dx.doi.org/10.1016/j. neuroimage.2015.08.071 (2016).

328. Vallone, F. *et al.* Simultaneous decoding of cardiovascular and respiratory functional changes from pig intraneural vagus nerve signals. *Journal of Neural Engineering* **18,** 0460a2. ISSN: 1741-2560, 1741-2552. https://iopscience.iop.org/article/10.1088/1741-2552/ac0d42 (2022) (Aug. 1, 2021).

329. Fitchett, A., Mastitskaya, S. & Aristovich, K. Selective Neuromodulation of the Vagus Nerve. *Frontiers in Neuroscience* **15,** 685872. ISSN: 1662-453X. https://www.frontiersin.org/articles/10.3389/fnins.2021.685872/full (2022) (May 24, 2021).

330. Kumar*, R. *et al.* MP54-01 SOFT SILICONE ELECTRODE NET FOR MODULATING BLADDER FUNCTION: *The Journal of Urology* **203,** e791. ISSN: 0022-5347. http://journals.lww.com/10.1097/JU.0000000000000916.01 (2022) (Apr. 2020).

331. Hong, G. & Lieber, C. M. Novel electrode technologies for neural recordings. *Nature Reviews Neuroscience* **20,** 330–345. ISSN: 1471-003X, 1471-0048. http://www.nature.com/articles/s41583-019-0140-6 (2021) (June 2019).

332. Won, S. M., Cai, L., Gutruf, P. & Rogers, J. A. Wireless and battery-free technologies for neuroengineering. *Nature Biomedical Engineering*. ISSN: 2157-846X. http://www.nature.com/articles/s41551-021-00683-3 (2022) (Mar. 8, 2021).

333. Luan, L. *et al.* Recent Advances in Electrical Neural Interface Engineering: Minimal Invasiveness, Longevity, and Scalability. *Neuron* **108,** 302–321. ISSN: 08966273. https://linkinghub.elsevier.com/retrieve/pii/S0896627320308072 (2022) (Oct. 2020).

334. Vázquez-Guardado, A., Yang, Y., Bandodkar, A. J. & Rogers, J. A. Recent advances in neurotechnologies with broad potential for neuroscience research. *Nature Neuroscience* **23,** 1522–1536. ISSN: 1097-6256, 1546-1726. http://www.nature.com/articles/s41593-020-00739-8 (2022) (Dec. 2020).

335.   Bonaccini Calia, A. *et al.* Full-bandwidth electrophysiology of seizures and epileptiform activity enabled by flexible graphene microtransistor depth neural probes. *Nature Nanotechnology* **17,** 301–309. ISSN: 1748-3387, 1748-3395. https://www.nature.com/articles/s41565-021-01041-9 (2022) (Mar. 2022).

336.   Wagner, F. B. *et al.* Targeted neurotechnology restores walking in humans with spinal cord injury. *Nature* **563,** 65–71. ISSN: 0028-0836, 1476-4687. https://www.nature.com/articles/s41586-018-0649-2 (2022) (Nov. 1, 2018).

337.   Oxley, T. J. *et al.* Motor neuroprosthesis implanted with neurointerventional surgery improves capacity for activities of daily living tasks in severe paralysis: first in-human experience. *Journal of neurointerventional surgery* **13.** ISBN: 1759-8478 Publisher: British Medical Journal Publishing Group, 102–108 (2021).

338.   Willett, F. R., Avansino, D. T., Hochberg, L. R., Henderson, J. M. & Shenoy, K. V. High-performance brain-to-text communication via handwriting. *Nature* **593,** 249–254. ISSN: 0028-0836, 1476-4687. http://www.nature.com/articles/s41586-021-03506-2 (2022) (May 13, 2021).

339.   Moses, D. A. *et al.* Neuroprosthesis for Decoding Speech in a Paralyzed Person with Anarthria. *New England Journal of Medicine* **385,** 217–227. ISSN: 0028-4793, 1533-4406. http://www.nejm.org/doi/10.1056/NEJMoa2027540 (2022) (July 15, 2021).

340.   Salatino, J. W., Ludwig, K. A., Kozai, T. D. Y. & Purcell, E. K. Glial responses to implanted electrodes in the brain. *Nature Biomedical Engineering* **1,** 862–877. ISSN: 2157-846X. http://www.nature.com/articles/s41551-017-0154-1 (2021) (Nov. 2017).

341.   Renz, A. F., Reichmuth, A. M., Stauffer, F., Thompson-Steckel, G. & Vörös, J. A guide towards long-term functional electrodes interfacing neuronal tissue. *Journal of Neural Engineering* **15,** 061001. ISSN: 1741-2560, 1741-2552. https://iopscience.iop.org/article/10.1088/1741-2552/aae0c2 (2021) (Dec. 1, 2018).

342.   Michelson, N. J. *et al.* Multi-scale, multi-modal analysis uncovers complex relationship at the brain tissue-implant neural interface: new emphasis on the biological interface. *Journal of Neural Engineering* **15,** 033001. ISSN: 1741-2560, 1741-2552. https://iopscience.iop.org/article/10.1088/1741-2552/aa9dae (2022) (June 1, 2018).

343.   Wellman, S. M. *et al.* A Materials Roadmap to Functional Neural Interface Design. *Advanced Functional Materials* **28,** 1701269. ISSN: 1616-301X, 1616-3028. https://onlinelibrary.wiley.com/doi/10.1002/adfm.201701269 (2022) (Mar. 2018).

344.   Barrese, J. C. *et al.* Failure mode analysis of silicon-based intracortical microelectrode arrays in non-human primates. *Journal of Neural Engineering* **10,** 066014. ISSN: 1741-2560, 1741-2552. https://iopscience.iop.org/article/10.1088/1741-2560/10/6/066014 (2022) (Dec. 1, 2013).

345.   Sridharan, A., Rajan, S. D. & Muthuswamy, J. Long-term changes in the material properties of brain tissue at the implant–tissue interface. *Journal of Neural Engineering* **10,** 066001. ISSN: 1741-2560, 1741-2552. https://iopscience.iop.org/article/10.1088/1741-2560/10/6/066001 (2022) (Dec. 1, 2013).

346. Jorfi, M., Skousen, J. L., Weder, C. & Capadona, J. R. Progress towards biocompatible intracortical microelectrodes for neural interfacing applications. *Journal of Neural Engineering* **12,** 011001. ISSN: 1741-2560, 1741-2552. https://iopscience.iop.org/article/10.1088/1741-2560/12/1/011001 (2022) (Feb. 1, 2015).

347. Feiner, R. & Dvir, T. Tissue–electronics interfaces: from implantable devices to engineered tissues. *Nature Reviews Materials* **3,** 17076. ISSN: 2058-8437. http://www.nature.com/articles/natrevmats201776 (2022) (Jan. 2018).

348. Araki, T. *et al.* Flexible neural interfaces for brain implants—the pursuit of thinness and high density. *Flexible and Printed Electronics* **5,** 043002. ISSN: 2058-8585. https://iopscience.iop.org/article/10.1088/2058-8585/abc3ca (2022) (Nov. 27, 2020).

349. Vomero, M. *et al.* On the longevity of flexible neural interfaces: Establishing biostability of polyimide-based intracortical implants. *Biomaterials* **281,** 121372. ISSN: 01429612. https://linkinghub.elsevier.com/retrieve/pii/S0142961222000114 (2022) (Feb. 2022).

350. Yoon, E. *et al.* An implantable microelectrode array for chronic in vivo epiretinal stimulation of the rat retina. *Journal of Micromechanics and Microengineering* **30,** 124001. ISSN: 0960-1317, 1361-6439. https://iopscience.iop.org/article/10.1088/1361-6439/abbb7d (2022) (Dec. 1, 2020).

351. De la Oliva, N., Mueller, M., Stieglitz, T., Navarro, X. & del Valle, J. On the use of Parylene C polymer as substrate for peripheral nerve electrodes. *Scientific Reports* **8,** 5965. ISSN: 2045-2322. http://www.nature.com/articles/s41598-018-24502-z (2022) (Dec. 2018).

352. Luan, L. *et al.* Ultraflexible nanoelectronic probes form reliable, glial scar–free neural integration. *Science Advances* **3,** e1601966. ISSN: 2375-2548. https://www.science.org/doi/10.1126/sciadv.1601966 (2022) (Feb. 3, 2017).

353. Vomero, M. *et al.* Conformable polyimide-based μECoGs: Bringing the electrodes closer to the signal source. *Biomaterials* **255,** 120178. ISSN: 01429612. https://linkinghub.elsevier.com/retrieve/pii/S0142961220304245 (2021) (Oct. 2020).

354. He, F., Lycke, R., Ganji, M., Xie, C. & Luan, L. Ultraflexible Neural Electrodes for Long-Lasting Intracortical Recording. *iScience* **23,** 101387. ISSN: 25890042. https://linkinghub.elsevier.com/retrieve/pii/S2589004220305757 (2022) (Aug. 2020).

355. Tringides, C. M. & Mooney, D. J. Materials for implantable surface electrode arrays: current status and future directions. *Advanced Materials,* 2107207. ISSN: 0935-9648, 1521-4095. https://onlinelibrary.wiley.com/doi/10.1002/adma.202107207 (2022) (Oct. 30, 2021).

356. Yu, D. Y. W. & Spaepen, F. The yield strength of thin copper films on Kapton. *Journal of Applied Physics* **95,** 2991–2997. ISSN: 0021-8979, 1089-7550. http://aip.scitation.org/doi/10.1063/1.1644634 (2022) (Mar. 15, 2004).

357.  Fekete, Z. & Pongrácz, A. Multifunctional soft implants to monitor and control neural activity in the central and peripheral nervous system: A review. *Sensors and Actuators, B: Chemical* **243,** 1214–1223. ISSN: 09254005. http://dx.doi.org/10.1016/j.snb.2016.12.096 (2017).

358.  Fallegger, F. *et al.* MRI-Compatible and Conformal Electrocorticography Grids for Translational Research. *Advanced Science* **8,** 2003761. ISSN: 2198-3844, 2198-3844. https://onlinelibrary.wiley.com/doi/10.1002/advs.202003761 (2022) (May 2021).

359.  Renz, A. F. *et al.* Opto-E-Dura: A Soft, Stretchable ECoG Array for Multimodal, Multiscale Neuroscience. *Advanced Healthcare Materials* **9,** 1–11. ISSN: 21922659 (2020).

360.  Lee, K. Y. *et al.* Development of a Polydimethylsiloxane-Based Electrode Array for Electrocorticography. *Advanced Materials Interfaces* **7,** 2001152. ISSN: 2196-7350, 2196-7350. https://onlinelibrary.wiley.com/doi/10.1002/admi.202001152 (2021) (Dec. 2020).

361.  Tringides, C. M. *et al.* Viscoelastic surface electrode arrays to interface with viscoelastic tissues. *Nature Nanotechnology* **16,** 1019–1029. ISSN: 1748-3387, 1748-3395. https://www.nature.com/articles/s41565-021-00926-z (2022) (Sept. 2021).

362.  Liu, Y. *et al.* Soft and elastic hydrogel-based microelectronics for localized low-voltage neuromodulation. *Nature Biomedical Engineering* **3,** 58–68. ISSN: 2157-846X. http://www.nature.com/articles/s41551-018-0335-6 (2021) (Jan. 2019).

363.  Tafazoli, S. *et al.* Learning to control the brain through adaptive closed-loop patterned stimulation. *Journal of Neural Engineering* **17,** 056007. ISSN: 1741-2552. https://iopscience.iop.org/article/10.1088/1741-2552/abb860 (2021) (Oct. 13, 2020).

364.  Lee, H. C. *et al.* Histological evaluation of flexible neural implants; Flexibility limit for reducing the tissue response? *Journal of Neural Engineering* **14.** ISSN: 17412552 (2017).

365.  Sandström, N. *et al.* Reaction injection molding and direct covalent bonding of OSTE+ polymer microfluidic devices. *Journal of Micromechanics and Microengineering* **25,** 075002. ISSN: 0960-1317, 1361-6439. https://iopscience.iop.org/article/10.1088/0960-1317/25/7/075002 (2022) (July 1, 2015).

366.  Hansson, J., Karlsson, J. M., Carlborg, C. F., van der Wijngaart, W. & Haraldsson, T. *Low gas permeable and non-absorbent rubbery OSTE&#x002B; for pneumatic microvalves* in *2014 IEEE 27th International Conference on Micro Electro Mechanical Systems (MEMS)* 2014 IEEE 27th International Conference on Micro Electro Mechanical Systems (MEMS) (IEEE, San Francisco, CA, USA, Jan. 2014), 987–990. ISBN: 978-1-4799-3509-3. http://ieeexplore.ieee.org/document/6765809/ (2022).

367.  Carlborg, C. F. *et al.* Functional off-stoichiometry thiol-ene-epoxy thermosets featuring temporally controlled curing stages via an UV/UV dual cure process. *Journal of Polymer Science Part A: Polymer Chemistry* **52,** 2604–2615. ISSN: 0887624X. https://onlinelibrary.wiley.com/doi/10.1002/pola.27276 (2021) (Sept. 15, 2014).

368.  Ejserholm, F. *et al. A polymer neural probe with tunable flexibility* in *2013 6th International IEEE/EMBS Conference on Neural Engineering (NER)* 2013 6th International IEEE/EMBS Conference on Neural Engineering (NER) (IEEE, San Diego, CA, USA, Nov. 2013), 691–694. ISBN: 978-1-4673-1969-0. http://ieeexplore.ieee.org/document/6696028/ (2021).

369.  Ferlauto, L. *et al.* All-polymeric transient neural probe for prolonged in-vivo electrophysiological recordings. *Biomaterials* **274,** 120889. ISSN: 01429612. https://linkinghub.elsevier.com/retrieve/pii/S0142961221002453 (2022) (July 2021).

370.  Haraldsson, T., Carlborg, C. F. & van der Wijngaart, W. OSTE: a novel polymer system developed for Lab-on-Chip. **897608,** 897608. ISSN: 1996756X. http://proceedings.spiedigitallibrary.org/proceeding.aspx?doi=10.1117/12.2041918 (March 2014 2014).

371.  Ejserholm, F. *et al.* Biocompatibility of a polymer based on Off-Stoichiometry Thiol-Enes + Epoxy (OSTE+) for neural implants. *Biomaterials Research* **19,** 19. ISSN: 2055-7124. http://www.biomaterialsres.com/content/19/1/19 (2021) (Dec. 2015).

372.  Graudejus, O. *et al.* A soft and stretchable bilayer electrode array with independent functional layers for the next generation of brain machine interfaces. *Journal of Neural Engineering* **17,** 056023. ISSN: 1741-2552. https://iopscience.iop.org/article/10.1088/1741-2552/abb4a5 (2021) (Oct. 14, 2020).

373.  Ware, T., Simon, D., Rennaker, R. L. & Voit, W. Smart Polymers for Neural Interfaces. *Polymer Reviews* **53,** 108–129. ISSN: 1558-3724, 1558-3716. http://www.tandfonline.com/doi/abs/10.1080/15583724.2012.751924 (2022) (Jan. 2013).

374.  Fuentes, M. d. C., Pérez, N. & Ayerdi, I. Metallization and electrical characterization of platinum thin film microelectrodes on biocompatible polydimethylsiloxane substrates for neural implants. *Thin Solid Films* **636,** 438–445. ISSN: 00406090. https://linkinghub.elsevier.com/retrieve/pii/S0040609017304522 (2022) (Aug. 2017).

375.  Bowden, N., Brittain, S., Evans, A. G., Hutchinson, J. W. & Whitesides, G. M. Spontaneous formation of ordered structures in thin films of metals supported on an elastomeric polymer. *nature* **393.** ISBN: 1476-4687 Publisher: Nature Publishing Group, 146–149 (1998).

376.  Lacour, S. P., Wagner, S., Huang, Z. & Suo, Z. Stretchable gold conductors on elastomeric substrates. *Applied Physics Letters* **82,** 2404–2406. ISSN: 0003-6951, 1077-3118. http://aip.scitation.org/doi/10.1063/1.1565683 (2022) (Apr. 14, 2003).

377.  Ware, T. *et al.* Thiol-ene/acrylate substrates for softening intracortical electrodes. *Journal of Biomedical Materials Research Part B: Applied Biomaterials* **102.** ISBN: 1552-4973 Publisher: Wiley Online Library, 1–11 (2014).

378.  Ware, T. *et al.* Three-Dimensional Flexible Electronics Enabled by Shape Memory Polymer Substrates for Responsive Neural Interfaces. *Macromolecular Materials and Engineering* **297,** 1193–1202. ISSN: 14387492. https://onlinelibrary.wiley.com/doi/10.1002/mame.201200241 (2022) (Dec. 2012).

379. Stiller, A. *et al.* Chronic Intracortical Recording and Electrochemical Stability of Thiol-ene/Acrylate Shape Memory Polymer Electrode Arrays. *Micromachines* **9,** 500. ISSN: 2072-666X. http://www.mdpi.com/2072-666X/9/10/500 (2022) (Sept. 29, 2018).

380. Reit, R. *et al.* Thiol–epoxy/maleimide ternary networks as softening substrates for flexible electronics. *Journal of Materials Chemistry B* **4,** 5367–5374. ISSN: 2050-750X, 2050-7518. http://xlink.rsc.org/?DOI=C6TB01082B (2022) (2016).

381. Sheng, H. *et al.* Neural interfaces by hydrogels. *Extreme Mechanics Letters* **30,** 100510. ISSN: 23524316. https://linkinghub.elsevier.com/retrieve/pii/S235243161930046X (2022) (July 2019).

382. Bou, S. J. M. C. & Ellis, A. V. *Microfluidic devices using thiol-ene polymers* in. SPIE Micro+Nano Materials, Devices, and Applications (eds Friend, J. & Tan, H. H.) (Melbourne, Victoria, Australia, Dec. 7, 2013), 89232B. http://proceedings.spiedigitallibrary.org/proceeding.aspx?doi=10.1117/12.2032608 (2022).

383. Brydon, H. L., Hayward, R., Harkness, W. & Bayston, R. Physical properties of cerebrospinal fluid of relevance to shunt function. 2: The effect of protein upon CSF surface tension and contact angle. *British Journal of Neurosurgery* **9,** 645–652. ISSN: 0268-8697, 1360-046X. http://www.tandfonline.com/doi/full/10.1080/02688699550040936 (2022) (Jan. 1995).

384. Hirsch, S. *et al.* In vivo measurement of volumetric strain in the human brain induced by arterial pulsation and harmonic waves. *Magnetic Resonance in Medicine* **70,** 671–683. ISSN: 07403194. https://onlinelibrary.wiley.com/doi/10.1002/mrm.24499 (2022) (Sept. 2013).

385. Jiang, Y., Xu, H., Liu, J., Li, P. & Wu, Y. Biomechanical analysis of optic nerve injury treated by compound light granules and ciliary neurotrophic factor. *Neural Regeneration Research* **7.** Publisher: Wolters Kluwer–Medknow Publications, 2889 (2012).

386. Gonzalez, M. *et al.* Design of metal interconnects for stretchable electronic circuits. *Microelectronics Reliability* **48,** 825–832. ISSN: 00262714. https://linkinghub.elsevier.com/retrieve/pii/S0026271408000760 (2021) (June 2008).

387. Carta, R. *et al.* Design and implementation of advanced systems in a flexible-stretchable technology for biomedical applications. *Sensors and Actuators A: Physical* **156.** ISBN: 0924-4247 Publisher: Elsevier, 79–87 (2009).

388. Axisa, F., Bossuyt, F., Vervust, T. & Vanfleteren, J. *Laser based fast prototyping methodology of producing stretchable and conformable electronic systems* in *2008 2nd Electronics System-Integration Technology Conference* (IEEE, 2008), 1387–1390. ISBN: 1-4244-2813-0.

389. Lüttjohann, A., Fabene, P. F. & van Luijtelaar, G. A revised Racine's scale for PTZ-induced seizures in rats. *Physiology & Behavior* **98,** 579–586. ISSN: 00319384. https://linkinghub.elsevier.com/retrieve/pii/S0031938409003047 (2022) (Dec. 2009).

390.	Javadian, N., Rahimi, N., Javadi-Paydar, M., Doustimotlagh, A. H. & Dehpour, A. R. The modulatory effect of nitric oxide in pro- and anti-convulsive effects of vasopressin in PTZ-induced seizures threshold in mice. *Epilepsy Research* **126,** 134–140. ISSN: 09201211. https://linkinghub.elsevier.com/retrieve/pii/S0920121116301152 (2022) (Oct. 2016).

391.	Yonekawa, W. D., Kupferberg, H. J. & Woodbury, D. M. Relationship between pentylenetetrazol-induced seizures and brain pentylenetetrazol levels in mice. *Journal of Pharmacology and Experimental Therapeutics* **214.** ISBN: 0022-3565 Publisher: ASPET, 589–593 (1980).

392.	Yadav, A. P. & Nicolelis, M. A. L. Electrical Stimulation of the Dorsal Columns of the Spinal Cord for Parkinson ' s Disease Spinal Cord Stimulation Low-Frequency Neuronal Oscillations Are Correlated With PD. **00,** 1–13 (2017).

393.	Fedor, F. Z. *et al.* Soft, Thiol-ene/Acrylate-Based Electrode Array for Long-Term Recording of Intracranial EEG Signals with Improved Biocompatibility in Mice. *Advanced Materials Technologies,* 2100942. ISSN: 2365-709X, 2365-709X. https://onlinelibrary.wiley.com/doi/10.1002/admt.202100942 (2022) (Oct. 10, 2021).

394.	Ware, T. *et al.* Fabrication of Responsive, Softening Neural Interfaces. *Advanced Functional Materials* **22,** 3470–3479. ISSN: 1616301X. https://onlinelibrary.wiley.com/doi/10.1002/adfm.201200200 (2022) (Aug. 21, 2012).

395.	Spira, M. E. & Hai, A. Multi-electrode array technologies for neuroscience and cardiology. *Nature nanotechnology* **8,** 83–94. ISSN: 1748-3387 (2013).

396.	Reynolds, D. *et al.* A Leadless Intracardiac Transcatheter Pacing System. *The New England Journal of Medicine* **374,** 533–541. ISSN: 0028-4793 (2016).

397.	Rubinstein, J. T. Paediatric cochlear implantation: prosthetic hearing and language development. *The Lancet* **360,** 483–485. ISSN: 0140-6736 (2002).

398.	Chuang, A. T., Margo, C. E. & Greenberg, P. B. Retinal implants: a systematic review. *British Journal of Ophthalmology* **98,** bjophthalmol–2013. ISSN: 0007-1161 (2014).

399.	Schuettler, M., Stiess, S., King, B. V. & Suaning, G. J. Fabrication of implantable microelectrode arrays by laser cutting of silicone rubber and platinum foil. *Journal of Neural Engineering* **2,** S121–S128. ISSN: 1741-2560, 1741-2552 (Mar. 1, 2005).

400.	Geddes, L. A. & Roeder, R. Criteria for the Selection of Materials for Implanted Electrodes. *Annals of Biomedical Engineering* **31,** 879–890. ISSN: 0090-6964 (July 2003).

401.	Cogan, S. F. Neural Stimulation and Recording Electrodes. *Annual Review of Biomedical Engineering* **10,** 275–309. ISSN: 1523-9829. http://www.annualreviews.org/doi/10.1146/annurev.bioeng.10.061807.160518 (2008).

402.	Bachmann, B. *et al.* All-inkjet-printed gold microelectrode arrays for extracellular recording of action potentials. *Flexible and Printed Electronics* **2,** 035003. ISSN: 2058-8585 (2017).

403.	Swisher, S. L. *et al.* Impedance sensing device enables early detection of pressure ulcers in vivo. *Nature Communications* **6,** 6575. ISSN: 2041-1723 (2015).

404.  Lochner, C. M., Khan, Y., Pierre, A. & Arias, A. C. All-organic optoelectronic sensor for pulse oximetry. *Nature Communications* **5,** 5745. ISSN: 2041-1723 (2014).

405.  Roberts, T. *et al.* Flexible Inkjet-Printed Multielectrode Arrays for Neuromuscular Cartography. *Advanced healthcare materials* **5,** 1462–70. ISSN: 2192-2659 (2016).

406.  Aristovich, K. *et al.* Imaging fast neural traffic at fascicular level with electrical impedance tomography: proof of principle in rat sciatic nerve. *Journal of Neural Engineering* **15,** 056025. ISSN: 1741-2560, 1741-2552. https://iopscience.iop.org/article/10.1088/1741-2552/aad78e (2022) (Oct. 1, 2018).

407.  Shivdasani, M. N. *et al.* Evaluation of stimulus parameters and electrode geometry for an effective suprachoroidal retinal prosthesis. *Journal of neural engineering* **7,** 036008. ISSN: 17412552 (2010).

408.  Cicione, R. *et al.* Visual cortex responses to suprachoroidal electrical stimulation of the retina: Effects of electrode return configuration. *Journal of Neural Engineering* **9.** ISSN: 17412560 (2012).

409.  Provansal, M. *et al.* Functional ultrasound imaging of the spreading activity following optogenetic stimulation of the rat visual cortex. *Scientific reports* **11.** ISBN: 2045-2322 Publisher: Nature Publishing Group, 1–12 (2021).

410.  Nguyen, D. *et al.* Novel Graphene Electrode for Retinal Implants: An in vivo Biocompatibility Study. *Frontiers in Neuroscience* **15,** 615256. ISSN: 1662-453X. https://www.frontiersin.org/articles/10.3389/fnins.2021.615256/full (2022) (Mar. 4, 2021).

411.  Fornos, A. P., Sommerhalder, J., Rappaz, B., Safran, A. B. & Pelizzone, M. Simulation of Artificial Vision, III: Do the Spatial or Temporal Characteristics of Stimulus Pixelization Really Matter? *Investigative Opthalmology & Visual Science* **46,** 3906. ISSN: 1552-5783. http://iovs.arvojournals.org/article.aspx?doi=10.1167/iovs.04-1173 (2022) (Oct. 1, 2005).

412.  Yan, D. *et al.* *Ultra-flexible and Stretchable Intrafascicular Peripheral Nerve Recording Device with Axon-dimension, Cuff-less Microneedle Electrode Array* preprint (Neuroscience, Jan. 21, 2022). http://biorxiv.org/lookup/doi/10.1101/2022.01.19.476928 (2022).

413.  Pearre, B. W., Michas, C., Tsang, J.-M., Gardner, T. J. & Otchy, T. M. Fast micron-scale 3D printing with a resonant-scanning two-photon microscope. *Additive Manufacturing* **30,** 100887. ISSN: 22148604. https://linkinghub.elsevier.com/retrieve/pii/S2214860418303944 (2022) (Dec. 2019).

414.  Otchy, T. M. *et al.* Printable microscale interfaces for long-term peripheral nerve mapping and precision control. *Nature Communications* **11,** 4191. ISSN: 2041-1723. https://www.nature.com/articles/s41467-020-18032-4 (2022) (Dec. 2020).

415. Neely, R. M., Piech, D. K., Santacruz, S. R., Maharbiz, M. M. & Carmena, J. M. Recent advances in neural dust: towards a neural interface platform. *Current Opinion in Neurobiology* **50,** 64–71. ISSN: 09594388. https://linkinghub.elsevier.com/retrieve/pii/S0959438817302386 (2022) (June 2018).

# ELEONORA BORDA

Chemin du Mont-Tendre 6,
1007 Lausanne, CH

borda.eleonora@gmail.com

+41788856846

www.linkedin.com/in/eleonora-borda

## Profile

Bionengineer focused on the application of micro-nanotechnologies for the
development medical devices, specifically neural interfaces.
Juggling different projects every day,
from lab experiments to business development calls
Love connecting those in my network when I see a matching need.

## Education

| | |
|---|---|
| **10.2017 - 05.2022 (exp)** | EPF Lausanne, Switzerland<br>PhD in Bioengineering, Campus Biotech, Geneva |
| **09.2015 - 09.2017** | EPF Lausanne, Switzerland<br>M.Sc. in Bioengineering & Minor in Neuroprosthetics |
| **09.2012 - 09.2015** | Politecnico di Milano, Milan, Italy<br>B.Sc. in Biomedical Engineering |

## Work Experience

| | |
|---|---|
| **10.2021 - Present** | Byosen Limited, London UK<br>CTO & Co-Founder, part-time<br>- **Main tasks**: Developing the company's strategy for using technological resources<br>- **Communication tasks**: Communicate technology strategy to partners and stakeholders |
| **10.2017 - 05.2022 (exp)** | Campus Biotech, Geneva, Switzerland<br>PhD candidate in Bioengineering, Laboratory of Neuroengineering<br>- **Experimental work:** development and optimization of process flows for new materials and electrodes designs, fabrication and testing of microfabricated devices for neural interfaces, performed animal experiemnts, collected and analysed data.<br>- **Team management:** supervision of 5 master students during their short or long lab experience regarding operative tasks,<br>- **Teaching tasks**: Teaching assistant for Analysis I (Bachelor), Material Science for Bioengineers (Bachelor), Biomaterials (Master), Neuroengineering for vision restoration (Master). Lecture on material processing (Bachelor) and on novel organic and flexible visual prostheses (Master).<br>- **Communication tasks**: team meetings, research updates presentations, conference presentations and posters |
| **02.2016 - 08.2017** | Duke University Medical Center, USA<br>Master Thesis, Nicolelis Lab led by Professor Miguel Nicolelis<br>- **Experimental work:** performed animal experiments, collected and analysed data |

| 06.2015 - 09.2015 | Second Sight Medical, Lausanne, Switzerland |
| | Intership Project |
| | - **Main task:** implementation of an image processing pipeline to evaluate patients data in a faster, easier and automatic way. |
| | - **Team management**: coordination with ophtalmologists from different centers to collect patients data. |

## Additional Experience

| 01.2022 - Present | "What to do next?" Podcast |
| | - Searching for speakers, creating visual identity, posting on social-media |
| 09.2020 - Present | Innovation Forum Lausanne, Lausanne Switzerland |
| | Co-President |
| | - Team managment, events design and organization, marketing strategy, fundraising and sponsorship |
| 09.2020 - Present | Volunteer member of the Fédération Suisse des aveugles et malvoyants FSA (Geneva section) |

## Professional Expertise

| Computer Languages | Python - basic coding skills |
| Engineering Software | LaTex - basic coding skills |
| | MATLAB - intermediate coding skills |
| | Autodesk (AUTOCAD, Fusion 360) - intermediate user skills |
| | COMSOL Multiphysics - basic user skills |
| Microfabrication | Thin film processing, wet and dry etching, photplithography, scanning electron microscopy |
| Electrochemistry | Electrochemical characterization of electrode arrays in-vitro |
| In-vivo Experimentation | Resal module 1, hands-on experience in handling of rodents, experimentation for electrical stimulation and recording of neural tissue in rodents |
| Basic Tools | Outlook |
| | Microsoft package (Word, Excel, Powerpoint) |
| | Adobe Illustrator for academic posters and marketing material for the association |
| | Canva for the podcast communication on social media |

## Language

| Italian | Mother tongue |
| English | Oral fluent; written fluent |
| French | Oral fluent; written intermediate |
| German | Oral basic; written basic |

## Scholarship

Master Thesis Grant from ZENO KARL SCHINDLER Foundation 2016-2017

# Publications

- Eleonora Borda  et al., (2022), Three-dimensional multilayer concentric bipolar electrodes enhance the selectivity of optic nerve stimulation. bioRxiv
doi: https://doi.org/10.1101/2022.03.21.485100

- Vivien Gaillet et al., (2021), A machine-learning algorithm correctly classifies cortical evoked potentials from both visual stimulation and electrical stimulation of the optic nerve. J. Neural Eng. 18 046031
https://doi.org/10.1088/1741-2552/abf523

- Borda et al., (2020), All-Printed Electrocorticography Array for In Vivo  Neural Recordings. Adv. Eng. Mater..
doi:10.1002/adem.201901403

# Conferences

- Soft Three-dimensional self-opening intraneural peripheral interface for optic nerve stimulation.
Poster Presentation. NanoBioTech-Montreux 2018, Montreux, Switzerland , October 29-31, 2018

- Off-Stoichiometry-Thiol-Ene Epoxy Polymers for Soft Implantable Electrode Array.
Poster Presentation. 2020 Virtual MRS Spring/Fall Meeting & Exhibit. 27th November - 4th December.

- Optic nerve stimulation via a three-dimensional multilayer concentric bipolar electrode array.
Oral Presentation. Virtual NER, Visual Prosthesis session, May 5th 2021.

- Off-Stoichiometry-Thiol-Ene Epoxy Polymers for conformable ECoG Array.
Poster Presentation. GRS & GRC Conference 12th March - 18th March 2022